AN ABSTRACT OF THE DISSERTATION OF

Jordan E. Lubbers for the degree of Doctor of Philosophy in Geology presented on September 2, 2021.

Title: Thermochemical Storage Conditions of Caldera Forming Magmatic Systems Revealed by Diffusion Chronometry

Abstract approved:

Adam J.R. Kent

Large silicic magmatic systems are responsible for producing the largest explosive volcanic eruptions on earth. These phenomena, although infrequent (i.e., 1 per 100,000 years), impact the global climate, deposit ash over continent sized regions, and significantly alter landscapes. Silicic magmatism also plays important roles in the formation and ongoing evolution of continental crust. This makes understanding the processes that generate, transport, store, and erupt large volumes of silicic magma extremely important.

In this dissertation, I present two case studies that explore the long-term thermal evolution of two caldera forming magmatic systems: Cerro Galán in NW Argentina and Toba in Sumatra. In them, I quantify the amount of time that the system experiences thermochemical conditions (i.e., temperatures > 750°C) sufficient to produce and store large volumes of eruptible magma (i.e., < ~50 % crystals and at a viscosity below the magma extrusion limit of 10^6 - 10^8 Pa·s). This eruptible time window, or *thermal history*, is recorded by the minerals (i.e., plagioclase) that crystallize within the reservoir and can be quantified by fitting forward models of trace element diffusion (i.e., Sr in plagioclase, Mg in plagioclase, Sr in hornblende) to the observed trace element profiles within the grain. We find that both the Cerro Galán and Toba magmatic systems experience relatively short time intervals (e.g., decades to centuries) during their overall history in which the thermal state of the magmatic system is sufficient to produce and store the large volumes of eruptible magma that constitute their eruptive products. This implies that these systems were dominantly stored in relatively cool, crystal-rich

conditions and were only remobilized shortly before eruption. In addition, all the other processes that occur in the formation and evolution of large bodies of silicic magma – such as melting, recharge etc. also all need to fall within this "thermal budget". This is also consistent with the dearth of geophysically resolved liquid-rich magma bodies under active volcanoes.

A large part of the work described above uses the chemical variations within minerals to study magmatic processes, and by necessity much of this is done on 2D sections of minerals. However, the 3D distribution of elements in minerals is also important to evaluate, and thus the second part of this study investigates chemical zoning in sanidine, a common volcanic mineral, in 3D using micro computed tomography (microCT). We show that X-ray attenuation is largely a function of Ba concentration in sanidine and from this develop a method to quantify Ba zoning in 3D. We also show that this method can help mitigate problems in diffusion modeling caused by sectioning effects (i.e., apparent diffusion widths) by allowing for the true chemical gradient to be extracted from a 3D volume rather than interpreted from a random 2D section. Furthermore, we show that true zoning geometries can be observed in 3D, allowing for the interpretations that come from studying them to be more completely understood.

Thermochemical Storage Conditions of Caldera Forming Magmatic Systems Revealed by Diffusion Chronometry

by
Jordan E. Lubbers

A DISSERTATION

submitted to

Oregon State University

in partial fulfillment of
the requirements for the
degree of

Doctor of Philosophy

Presented September 2, 2021
Commencement June 2022

Doctor of Philosophy dissertation of Jordan E. Lubbers presented on September 2, 2021

APPROVED:

Major Professor, representing Geology

Dean of the College of Earth, Ocean, and Atmospheric Sciences

Dean of the Graduate School

I understand that my dissertation will become part of the permanent collection of Oregon State University libraries. My signature below authorizes release of my dissertation to any reader upon request.

Jordan E. Lubbers, Author

ACKNOWLEDGEMENTS

This has been the hardest I have ever worked on anything in my entire life. That being said, I truly could not have made it to this point alone. This document and all the science that created it is the result of a team effort that I had the honor of writing up at the "end". First and foremost, I would like to thank my advisor, Adam Kent. His mentorship and encouragement allowed me to freely explore my scientific interests no matter how strange they may have seemed at the time. It was this sort of encouragement that directly led to the genesis of Chapter 4 in this dissertation. His comments and advice throughout my degree were a welcome guide in a seemingly endless sea of data and complexities, ultimately making my research much better than it would have been had I been left to my own ideas. I'd also like to thank the rest of my committee: Frank Tepley, Shan de Silva, Christy Till, and my GCR Matt Evans. All your guidance has been extremely helpful over the last four years, and I look forward to continuing to work with you in the future.

I would like to express my deepest admiration and gratitude to Chris Russo. Thank you for teaching me everything I know about analytical chemistry, having patience as I learn along the way, and being a fantastic mentor. I feel fortunate to have been able to learn from you the last few years. It truly has been a wild ride, but we've managed to get through it with the help of plenty of coffee breaks and post-work beers. I look forward to continuing to work together and keeping this friendship alive for years to come.

To my colleagues in the VIPER group. You are the reason I came to OSU in the first place, and I cherish the relationships I have made with you all along the way. Pete, I'm going to miss our office, but I'm grateful for all the times we've shared together and look forward to the many more to come. To all my other friends I have made along the way here in Oregon, your camaraderie has made this part of my life all the more memorable and I'll take that with me wherever I go. Arielle, thank you for being an incredible partner and helping me keep my chin up when it felt heavy.

To my family: thank you for all your love and support. These words can never actually express how thankful I am to have you in my corner all these years, but just know that without you none of this would ever be possible.

And finally, to me: Thank you for seeing this through. No matter the challenges the last four years presented, you overcame them and got the job done.

CONTRIBUTION OF AUTHORS

Adam Kent was involved in the design, interpretation, and writing of all chapters in this dissertation. Shan de Silva was involved in the design, field work, and interpretation of data for Chapter 2 as well as providing samples and interpretation of data for Chapter 3. Dorthe Wildenschild and Douglas Meisenheimer (College of Engineering at OSU) are responsible for partaking in the design, data collection, and data processing for Chapter 4. Chris Russo was involved in the design and discussion for Chapter 5.

TABLE OF CONTENTS

Page

CHAPTER ONE: GENERAL INTRODUCTION 1

REFERENCES 6

CHAPTER TWO: THERMAL BUDGETS OF MAGMA STORAGE CONSTRAINED BY DIFFUSION CHRONOMETRY: THE CERRO GALÁN IGNIMBRITE 11

ABSTRACT 12
INTRODUCTION 12
Geologic Background 14
METHODS 15
Bulk Rock Geochemistry 15
Electron Probe Micro Analysis 16
Laser Ablation Inductively Coupled Plasma Mass Spectrometry (LA-ICP-MS) 16
Diffusion Chronometry 17
RESULTS 20
Geochemistry 20
Whole Rock 20
Plagioclase 20
DISCUSSION 21
Diffusion of Mg and Sr in plagioclase 21
Thermal history of magma storage 22
Plagioclase as a recorder of magma reservoir conditions 23
Constraints from zircon 25
Periodic recharge 26
Long term thermochemical conditions 27
CONCLUSION 28
REFERENCES 30

CHAPTER THREE: THERMAL HISTORY OF THE TOBA MAGMATIC SYSTEM AND ITS SOURCES: INSIGHT FROM MULTI-PHASE DIFFUSION CHRONOMETRY 51

ABSTRACT 52
INTRODUCTION 52
Geologic Background 52
METHODS 54
Samples 54
EPMA 55
LA-ICP-MS 55
Diffusion Chronometry 56
RESULTS 56
Plagioclase 57
Amphibole 58
Glass chemistry 58
DISCUSSION 58
Diffusion of Sr and Mg in plagioclase 58
Amphibole thermometry 61
Diffusion of Sr in Amphibole 61
Compositionally heterogeneous but thermally homogenous sources 62

TABLE OF CONTENTS (Continued)

Page

Long-term storage conditions of the Toba magmatic system 63
REFERENCES 66

CHAPTER FOUR: 3D ZONING OF BARIUM IN ALKALI FELDSPAR 85

ABSTRACT 86
INTRODUCTION 86
X-ray micro tomography 88
Sanidine 89
METHODS 90
Samples 90
MicroCT 90
Electron Probe MicroAnalyzer 91
Image Processing 91
RESULTS 92
DISCUSSION 93
Geochemical controls on X-ray attenuation in sanidine 93
Observing chemical zoning in 3D 95
IMPLICATIONS FOR MINERAL ZONING STUDIES 96
Gradient Variability Between Two Zones 96
Beyond sanidine – barium 97
ACKNOWLEDGEMENTS 98
REFERENCES 99

CHAPTER FIVE: OPEN-SOURCE DATA PROCESSING FOR LA-ICP-MS SPOT DATA: LASERTRAM AND LASERCALC 120

ABSTRACT 121
INTRODUCTION 121
GOVERNING EQUATIONS 122
DETERMINING NORMALIZED RATIOS 123
DRIFT CORRECTION 124
UNCERTAINTIES 125
USING LASERTRAM AND LASERCALC 125
LaserTRAM 125
LaserCalc 129
REFERENCES 132

CHAPTER SIX: GENERAL CONCLUSIONS 133

BIBLIOGRAPHY 133

APPENDICES 151

Appendix A: 152
Appendix B: 166
Appendix C: 177

LIST OF FIGURES

Figure Page

Figure 2.1: Digital elevation map (DEM) of the Cerro Galán Caldera and its location within the Central Andean Volcanic Zone (CAVZ). 36

Figure 2.2: A) Total alkalis vs silica (TAS) diagram for CGI pumice compared to other CAVZ volcanics from the last 10Ma. 37

Figure 2.3 : Panel of selected trace elements in CGI plagioclase filtered by what pumice type they are from (i.e., gray or white). 38

Figure 2.4: Plagioclase from the CGI exhibiting high-An cores. 39

Figure 2.5: Strontium and Mg vs An in CGI plagioclase in both observed data (A, C) and calculated equilibrated data (B, D). 40

Figure 2.6: (A) Cumulative distribution plot of diffusion modeling for both Sr and Mg in CGI plagioclase. 41

Figure 2.7: Representative plagioclase from the CGI and their corresponding Mg diffusion models. 42

Figure 2.8: Representative plagioclase from the CGI and their corresponding Sr diffusion models. 43

Figure 2.9: Example of grain where multiple LA-ICP-MS transects were measured. 44

Figure 2.10: Comparing various trace elements to An profiles in plagioclase. 45

Figure 2.11: Magnesium diffusion model for grain 1-7-1 in both Mg vs distance (A) and Mg vs An (B) 46

Figure 2.12: Comparing melt compositions in equilibrium with CGI plagioclase (colormapped circles) to observed glass compositions (red circles) for Ba, Sr, and Mg. 47

Figure 2.13: Schematic of different Ba – An relationships in CGI plagioclase with observed examples side by side. 48

Figure 2.14: Results from MELTS and zircon saturation modeling. 49

Figure 3.1: Map of Toba caldera and its location within the larger Sunda arc (inset). 70

Figure 3.2: Plagioclase trace element vs. An relationships for all samples studied represented by 2D kernel density estimates (KDEs) 71

Figure 3.3: A) Sr vs. Zr for all amphiboles studied 72

Figure 3.4: Selected trace elements for YTT pumice glass 73

LIST OF FIGURES (Continued)

Figure Page

Figure 3.5: Summary of diffusion results for each chronometer used in this study shown using a cumulative distribution plot 74

Figure 3.6: A) Strontium diffusion model for profile LT22 from sample LT_001 showing that the observed Sr data for this profile closely resembles its calculated equilibrium profile, suggesting that it has spent prolonged periods of time at high (> 750°C) temperatures. 75

Figure 3.7: Representative diffusion models for Sr and Mg in plagioclase 76

Figure 3.8: Comparing the influence of temperature on best fit diffusion time 77

Figure 3.9: Summary of amphibole only and amphibole – plagioclase thermometry completed in this study. 78

Figure 3.10: Comparing amphibole composition with crystallization temperature 79

Figure 3.11: Representative diffusion models for Sr in amphibole 80

Figure 3.12: A) Comparing YTT glass chemistry with that of the OTT and MTT 81

Figure 3.13: Results from modeling fractional crystallization over a range of initial liquid compositions 82

Figure 4.1: Schematic of the sample setup used in the microtomographic scanning. Sanidine grains were mounted vertically in a thin epoxy rod and placed in the sample holder on the helical rotation stage. This allowed for a source to sample distance of 5mm, and the helical trajectory subsequently allowed for numerous grains to be scanned in one single (long) scan at high resolution 104

Figure 4.2: Individual CT slices extracted from the 3D dataset and their corresponding histograms 105

Figure 4.3: 3D rendering of a segmented sanidine from the Kneeling Nun Tuff and the same grain shown in Figure 1KNT 106

Figure 4.4: Representative sanidine grains from each system studied comparing BSE (left) and CT (middle) grayscale images for similar 2D slices through the same grain 107

Figure 4.5: Calculated linear attenuation coefficient (μ) plotted against major element compositions for each analysis 108

Figure 4.6: Observed CT grayscale for the same location on a given sanidine that EPMA analyses were completed, plotted against major element compositions for the same location 109

Figure 4.7: Comparison of BSE image and CT grayscale image for the same plane through a KNT sanidine 110

LIST OF FIGURES (Continued)

Figure Page

Figure 4.8 A) Regression for Ba vs. CT relationship for all sanidines studied in this experiment 111

Figure 4.9: R2 and Root Mean Squared Error (RMSE) of predicted CT grayscale results of a Monte Carlo simulation in which each machine learning algorithm for predicting CT values was run 1000 times 112

Figure 4.10 A) scatter plot of predicted vs. observed CT grayscale values from the ERT (left) and random forest (right) algorithms for one of the random iterations of the Monte Carlo simulation shown in Figure 8 illustrating that they: 1) accurately predict the observed CT values (e.g., falls along a 1:1 predicted vs. observed line); 2) produces low RMSE values relative to the overall attenuation signal (i.e., < 3%) 113

Figure 4.11 3D volume reconstructions of chosen sanidines segmented in this study.....114

Figure 4.12: Selected random slices and their corresponding CT grayscale profile perpendicular to observed zoning from grain LCTB – 1 shown in Figure 10E 115

Figure 4.13: Stereonet of 150 random slices through crystal LCTB – 1 shown in Figure 10E, where each pole to the plane for a given random slice is a spot on the stereonet.....116

Figure 4.14: Breakdown of random slicing exercise in which 35, 75, and 150 random slices were generated through the center of grain LCTB-1, shown in Figure 10E.....117

Figure 5.1: Example of raw data for a single spot analysis from standard reference material BCR-2G showing the possibility of measuring > 25 analytes in a given experiment 122

Figure 5.2: Drift correction test for selected analytes in Figure 5.1 illustrating analytes that are both drift corrected and not drift corrected in LaserCalc.....125

Figure 5.3: Empty LaserTRAM window upon opening the program.....126

Figure 5.4: Example of data format required for LaserTRAM.....126

Figure 5.5: LaserTRAM interface with populated graphs after choosing a spot analysis from the dropdown menu.....127

Figure 5.6: Toolbar used for manipulating graphs in LaserTRAM. 127

Figure 5.7: Example of the table generated as the user saves information for each spot. 128

Figure 5.8: Example output generated from LaserTRAM. This completely mimics the data table generated in the GUI. 129

Figure 5.9: LaserCalc interface upon loading the program. 129

LIST OF FIGURES (Continued)

Figure Page

Figure 5.10: Populated Internal Std. Concentrations table after output from LaserTRAM is loaded into LaserCalc. 130

Figure 5.11: Populated Calculated Concentrations table after "Calculate!" button is clicked. 131

LIST OF TABLES

Table Page

Table 2.1: Accepted and measured values for plagioclase standard reference material (LABR) used in this study. 50

Table 3.1: Sample names, types, and locations used in this study. 83

Table 3.2: Results of 2 sided Kolmogorov-Smirnov test for each chronometer used in this study, which tests the null hypothesis that two samples (e.g., Sr diffusion model times and Mg diffusion model times) are drawn from the same distribution. 84

Table 4.1: Standards utilized in EPMA experiment calibration for each element measured, along with the relative standard error and detection limit for each element measured 118

Table 4.2 List of programs/software used in this research and what each was used for. 119

LIST OF APPENDIX FIGURES

Figure Page

Figure A.1: Comparing partition coefficients calculated using Bindeman et al., (1998) and Nielsen et al., (2017) 152

Figure A.2 Plagioclase BSE images 153

Figure A.3: Individual Mg diffusion models for each grain shown in A.1 155

Figure A.4: Individual Sr diffusion models for each grain shown in A.1 161

Figure B.1: Plagioclase BSE images 166

Figure B.2: Amphibole BSE images 167

Figure B.3: Individual Mg in plagioclase diffusion models for grains shown in B.1 168

Figure B.4: Individual Sr in plagioclase diffusion models for all the grains shown in B.1 ... 172

Figure B.5: Individual Sr in amphibole diffusion models for grains shown in B.2 176

Figure C.1: Raw data histograms for all grains in this study 177

CHAPTER ONE: GENERAL INTRODUCTION

Silicic magmatic systems play a vital role in the formation and evolution of continental crust, and are the primary cause of explosive volcanic activity (e.g., Dingwell, 1998; Petford *et al.*, 2000; Rudnick and Fountain, 1995; Taylor and McLennan, 1995). Although infrequent (i.e., 1 per 100,000 years), the largest explosive silicic eruptions (e.g., supereruptions) produce 1-2 orders of magnitude more erupted material than any historic explosive eruption (Wilson et al., 2021). These perilous phenomena have been shown to influence global temperatures for years after the eruption takes place (e.g. Sigl *et al.*, 2015), deposit ash over continent-sized areas, and significantly alter landscapes with pyroclastic flows (e.g., Self, 2006). This makes understanding the timescales of processes that generate, transport, store, and erupt large volumes of silicic magma extremely important (Mason et al., 2004).

Silicic magma production is widely considered to be the result of two end member processes: 1) partial melting of pre-existing crust (e.g., Glazner et al., 2008; Ratajeski et al., 2005; Streck and Grunder, 2008); 2) differentiation by fractional crystallization (± assimilation) of a less evolved magma (e.g., Bachmann and Bergantz, 2004; Hildreth, 1981; Lubbers et al., 2020) or some combination of these (e.g., Annen et al., 2006; Deering et al., 2008; Hildreth, 1981). Numerical and petrologic evidence also suggests that silicic magmas can exist at or above the solidus for long periods of time (10^4-10^5 years) prior to eruption (e.g., Bachmann and Bergantz, 2004; Bacon and Lowenstern, 2005; Claiborne et al., 2010; Folkes et al., 2011a; Gelman et al., 2013; Kaiser et al., 2017; Kern et al., 2016; Szymanowski et al., 2019, 2017; Tierney et al., 2016; Wotzlaw et al., 2013) in the mid to upper crust (Gualda et al., 2018; Huber et al., 2019) with facilitation by changes in upper crustal rheology (de Silva and Gregg, 2014).

Despite this potentially long residence, the thermochemical conditions at which these systems exist may be highly variable due to individual magma reservoirs being the amalgamation of many complex and, sometimes, simultaneous processes (e.g., recharge, eruption, second boiling, thermal buffering, magma ascent etc.). Furthermore, crystallization of magmas plays a large role in determining their physical properties (Marsh, 1981). Crystallization causes an increase in the viscosity of the melt (Giordano et al., 2008), and also the overall magma (Scaillet et al., 1998) such that at approximately 40 – 60% crystallinity the viscosity of a magma drastically changes with small changes in crystal fraction (Caricchi and Blundy, 2015). The observation that large volumes of magma are erupted in caldera systems requires that this volume of magma exists within the shallow crust prior to eruption (Huber et al., 2019) and has a viscosity that allows it to move along fractures and conduits to the surface

(Takeuchi, 2004). This implies a 'magma extrusion limit' whereby magmas are too viscous to be erupted (i.e., 10^6 – 10^8 Pa·s; Takeuchi, 2011). Bradshaw (2017) found that for many large caldera-forming magmatic systems, this limit is reached at temperatures near 750°C. Producing and storing large volumes of eruptible magma therefore requires that these reservoirs experience temperatures above 750°C with for durations long enough to reduce the crystallinity below 40-60%. Thus, a key issue in understanding how some of the largest volcanic eruptions in the geologic record are produced is determining whether these large volumes of eruptible magma are ephemeral or long-lived.

Recently it has been proposed that crustal magma reservoirs spend most of their time in a state where they are not eruptible and experience punctuated thermal events that generate eruptible volumes of magma (e.g. Cooper and Kent, 2014; Rubin et al., 2017; Szymanowski et al., 2017). This view is also supported by geophysical approaches, which rarely observe melt-dominated (greater than 50%) magma reservoirs (Lundstrom and Glazner, 2016). Conversely, it has been argued that magma reservoirs spend the vast majority of their time at temperatures which allow for a significant and eruptible melt fraction throughout much of their history to be present (e.g., Barboni et al., 2016; Kaiser et al., 2017; Tierney et al., 2016). These scenarios imply distinctly different behavior within the associated magmatic plumbing system and impact how volcano monitoring data are interpreted.

In the last several decades numerical modeling studies have investigated the processes responsible for generating, storing, and erupting large volumes of magma (e.g., Annen et al., 2006; Gelman et al., 2013; Jellinek and DePaolo, 2003; Karakas et al., 2017), however the current state of petrologic tools makes discerning between different modeling scenarios challenging. Furthermore, while there are many tools in the petrology toolkit to gather both crystallization ages (Cooper and Reid, 2008 and references therein) and temperatures (e.g., Putirka, 2008 and references therein) of magmatic mineral phases, none of these tools quantify the *thermal history* – or time interval a given mineral has spent at a given temperature, and typically allow researchers to only look at brief snapshots of the P-T-X-fO_2 conditions of a magma system at the time that specific mineral and melt systems equilibrate. Analytical uncertainties also limit the effectiveness of existing geochronology to define thermal histories (e.g., Kent and Cooper, 2018). This ultimately limits our understanding of how the thermochemical conditions of magma storage evolve through time.

Modeling the diffusion of trace elements in volcanic crystals has emerged as a useful tool for quantifying timescales of magmatic processes leading up to eruption (see reviews by Chakraborty, 2008; Costa et al., 2008; Zhang, 2010 for an in depth discussion on the

background of diffusion in minerals). Although much of the existing diffusion work is aimed at understanding the shorter timescales associate with eruptions (e.g., Couperthwaite et al., 2020; Rubin et al., 2017; Ruth et al., 2018) the thermal dependence of diffusivity also means that diffusion can also be used to address the question of *"How long has a mineral spent at or above a certain temperature?"* This is done by estimating how much diffusional equilibration could have occurred with observed trace element distributions at a specified temperature. Adding to this utility is the observation that there are mineral – element pairs that span many orders of magnitude (Costa et al., 2020), illustrating that: 1) a wide compositional range of volcanic systems containing diverse crystal cargoes can be studied and 2) both short and long duration volcanic processes may be potentially be quantified.

Modeling diffusion generally requires *in situ* mineral data that either directly (i.e., electron probe, laser ablation ICP-MS) or indirectly (i.e., cathodoluminescence, back scattered electron, micro computed tomography) quantify elemental abundances. These data are then compared to forward models of diffusive equilibration for a specific element to find a best fit model to the observed data. Best fit models are then used to assign a duration that a grain or portion of a grain has spent at or above the selected temperature. When measured across enough grains so as to be representative of the magmatic system being investigated (Shea et al., 2015), important inferences about its thermal history (i.e., time – temperature path) may be discerned (Bradshaw, 2017).

Throughout this dissertation I use diffusion modeling (colloquially known as diffusion chronometry or geospeedometry) to constrain the long-term thermal evolution of caldera forming magmatic systems. Specifically, I predominantly use diffusion of Mg and Sr in plagioclase (Costa et al., 2003) to quantify the amount of time that plagioclase grains in erupted magmas spend at or above 750°C in their host reservoir prior to eruption. As mentioned above, this is roughly the temperature during cooling at which many large silicic magmatic systems experience an increase in viscosity such that they become uneruptible. Results from these diffusion models can then be used to infer how long a given grain has experienced temperatures required to produce and store large volumes of eruptible magma. When combined with other data that provide insight into the overall crystallization duration for the magmatic system (e.g., geothermobarometry, mineral and glass trace element contents, and zircon crystallization ages), we can infer whether the magma system was experiencing dominantly near solidus (e.g., cold; Cooper and Kent, 2014), liquid-dominated (e.g., warm; Barboni et al., 2016), or more complex (e.g., some combination of the two; Andersen et al., 2017; Bradshaw, 2017) storage conditions throughout its residence in the crust.

In Chapter 2, I investigate the thermal history of the 2.06 Ma, 630 km^3 Cerro Galán Ignimbrite (CGI; Folkes et al., 2011b). I use diffusion modeling of Sr and Mg in plagioclase combined with high-resolution core to rim changes in other petrogenetically significant elements in silicic magmas (e.g., Ba) and Rhyolite-MELTS (Gualda et al., 2012) modeling. This addresses not only the duration of time individual plagioclase are experiencing magma reservoir conditions at or above 750°C but also where they existed on the liquid line of descent relative to other phases observed in CGI pumice. I demonstrate that this combination of diffusion chronometry and trace element mapping can help distinguish whether a grain is experiencing longer durations of magma storage or is the result of later stage growth. This is crucial in providing context for diffusion model results and allows for us to develop a long-term thermal history for the CGI magmatic system.

Chapter 3 explores the thermal evolution of the cataclysmic 74 ka, 2800 km^3 Youngest Toba Tuff (YTT; Rose and Chesner, 1987). I use Sr and Mg diffusion modeling in plagioclase, Sr diffusion in amphibole, amphibole thermometry, and pumice glass trace element chemistry to quantify a thermal history of the magmatic system in a similar fashion to what was done in Chapter 2. However, the presence of amphibole in the YTT allows better constraint on reservoir temperatures. Furthermore, amphibole in the YTT have been found to be xenocrystic and only incorporated into the YTT magma system decades prior to eruption (Gardner et al., 2002), ultimately allowing us to not only quantify thermal histories of the YTT system but also the magma system stratigraphically below the YTT responsible for initially crystallizing amphibole. This study also provides one of the first attempts at modeling Sr diffusion in amphibole, demonstrating the potential for another useful chronometer to the petrology community.

Chapter 4 focuses on developing a method to quantify Ba concentrations in sanidine in 3D using non-destructive micro-computed tomography (microCT). Barium in sanidine has many useful petrologic applications ranging from being a chronometer for diffusion (Chamberlain et al., 2014; Morgan and Blake, 2006; Shamloo et al., 2021; Till et al., 2015) to being an indicator of cumulate remelting and remobilization (Lubbers et al., 2020; Wolff, 2017; Wolff et al., 2020, 2015). Therefore, quantifying both absolute abundance and spatial distribution of Ba in sanidine is of importance to many petrologic studies. This has conventionally been done using 2D sections, but it has been shown numerically, however, that when using conventional *in situ* methods for gathering elemental concentrations, sectioning effects greatly influence the shape of concentration gradients observed in 1D (Krimer and Costa, 2017; Shea et al., 2015). The 'apparent' diffusion times produced from 1D profiles, if

not carefully screened, may then cause an overestimation of the duration at which a mineral has experienced a given thermal history. This chapter shows that it is now possible to use microCT to extract 3D Ba concentration information in sanidine allowing for observation of: 1) the true shape of Ba concentration gradients between mineral zones; 2) complex zoning morphologies not otherwise viewable from 2D sections (e.g., back scattered electron imaging).

The final chapter, Chapter 5, presents an open-source, user friendly, and web-hosted graphical user interface for the reduction of laser ablation inductively coupled plasma mass spectrometry (LA-ICP-MS) data. A collaboration with the W.M. Keck Collaboratory for Plasma Spectrometry, it will soon be deployed as the primary method for reducing LA-ICP-MS data for visiting researchers and, as such, includes both a written demonstration and links to videos detailed how to use the software.

REFERENCES

Andersen, N.L., Jicha, B.R., Singer, B.S., Hildreth, W., 2017. Incremental heating of Bishop Tuff sanidine reveals preeruptive radiogenic Ar and rapid remobilization from cold storage 114, 12407–12412. https://doi.org/10.1073/pnas.1709581114

Annen, C., Blundy, J.D., Sparks, R.S.J., 2006. The genesis of intermediate and silicic magmas in deep crustal hot zones. J. Petrol. 47, 505–539. https://doi.org/10.1093/petrology/egi084

Bachmann, O., Bergantz, G.W., 2004. On the Origin of Crystal-poor Rhyolites: Extracted from Batholithic Crystal Mushes. J. Petrol. 45, 1565–1582. https://doi.org/10.1093/petrology/egh019

Bacon, C.R., Lowenstern, J.B., 2005. Late Pleistocene granodiorite source for recycled zircon and phenocrysts in rhyodacite lava at Crater Lake, Oregon. Earth Planet. Sci. Lett. 233, 277–293. https://doi.org/10.1016/j.epsl.2005.02.012

Barboni, M., Boehnke, P., Schmitt, A.K., Harrison, T.M., Shane, P., Bouvier, A.-S., Baumgartner, L., 2016. Warm storage for arc magmas. Proc. Natl. Acad. Sci. 113, 13959–13964. https://doi.org/10.1073/pnas.1616129113

Bradshaw, R.W., 2017. Crystal Records of the Origin, Evolution, and Thermal Histories of Magmas. Oregon State University.

Caricchi, L., Blundy, J., 2015. Experimental petrology of monotonous intermediate magmas. Geol. Soc. Spec. Publ. 422, 105–130. https://doi.org/10.1144/SP422.9

Chakraborty, S., 2008. Diffusion in Solid Silicates: A Tool to Track Timescales of Processes Comes of Age. Annu. Rev. Earth Planet. Sci. 36, 153–190. https://doi.org/10.1146/annurev.earth.36.031207.124125

Chamberlain, K.J., Morgan, D.J., Wilson, C.J.N., 2014. Timescales of mixing and mobilisation in the Bishop Tuff magma body : perspectives from diffusion chronometry. Contrib. to Mineral. Petrol. https://doi.org/10.1007/s00410-014-1034-2

Claiborne, L.L., Miller, C.F., Flanagan, D.M., Clynne, M.A., Wooden, J.L., 2010. Zircon reveals protracted magma storage and recycling beneath Mount St. Helens. Geology 38, 1011–1014. https://doi.org/10.1130/G31285.1

Cooper, K.M., Kent, A.J.R., 2014. Rapid remobilization of magmatic crystals kept in cold storage. Nature 506, 480–3. https://doi.org/10.1038/nature12991

Cooper, K.M., Reid, M.R., 2008. Uranium-series Crystal Ages. Rev. Mineral. Geochemistry 69, 479–544. https://doi.org/10.2138/rmg.2008.69.13

Costa, F., Chakraborty, S., Dohmen, R., 2003. Diffusion coupling between major and trace elements and a model for the calculation of magma chamber residence times using plagioclase. Geochim. Cosmochim. Acta 67, 2189–2200. https://doi.org/10.1016/S0016-7037(00)01345-5

Costa, F., Dohmen, R., Chakraborty, S., 2008. Time Scales of Magmatic Processes from Modeling the Zoning Patterns of Crystals. Rev. Mineral. Geochemistry 69, 545–594. https://doi.org/10.2138/rmg.2008.69.14

Costa, F., Shea, T., Ubide, T., 2020. Diffusion chronometry and the timescales of magmatic processes. Nat. Rev. Earth Environ. 1, 201–214. https://doi.org/10.1038/s43017-020-0038-x

Couperthwaite, F.K., Thordarson, T., Morgan, D.J., Harvey, J., Wilson, M., 2020. Diffusion Timescales of Magmatic Processes in the Moinui Lava Eruption at Mauna Loa, Hawai`i, as Inferred from Bimodal Olivine Populations. J. Petrol. 61. https://doi.org/10.1093/petrology/egaa058

de Silva, S.L., Gregg, P.M., 2014. Thermomechanical feedbacks in magmatic systems: Implications for growth, longevity, and evolution of large caldera-forming magma reservoirs and their supereruptions. J. Volcanol. Geotherm. Res. 282, 77–91. https://doi.org/10.1016/j.jvolgeores.2014.06.001

Deering, C.D., Cole, J.W., Vogel, T.A., 2008. A rhyolite compositional continuum governed by lower crustal source conditions in the taupo volcanic zone, New Zealand. J. Petrol. 49, 2245–2276. https://doi.org/10.1093/petrology/egn067

Dingwell, D.B., 1998. Recent experimental progress in the physical description of silicic magma relevant to explosive volcanism. Geol. Soc. London, Spec. Publ. 145, 9–26. https://doi.org/10.1144/GSL.SP.1996.145.01.02

Folkes, C.B., De Silva, S.L., Schmitt, A.K., Cas, R.A.F., 2011a. A reconnaissance of U-Pb zircon ages in the Cerro Galán system, NW Argentina: Prolonged magma residence, crystal recycling, and crustal assimilation. J. Volcanol. Geotherm. Res. 206, 136–147. https://doi.org/10.1016/j.jvolgeores.2011.06.001

Folkes, C.B., Wright, H.M., Cas, R.A.F., de Silva, S.L., Lesti, C., Viramonte, J.G., 2011b. A re-appraisal of the stratigraphy and volcanology of the Cerro Galán volcanic system, NW Argentina. Bull. Volcanol. 73, 1427–1454. https://doi.org/10.1007/s00445-011-0459-y

Gardner, J.E., Layer, P.W., Rutherford, M.J., 2002. Phenocrysts versus xenocrysts in the youngest Toba Tuff: Impications for the petrogenesis of 2800 km3 of magma. Geology 30, 347–350. https://doi.org/10.1130/0091-7613(2002)030<0347:PVXITY>2.0.CO;2

Gelman, S.E., Gutiérrez, F.J., Bachmann, O., 2013. On the longevity of large upper crustal silicic magma reservoirs. Geology 41. https://doi.org/10.1130/G34241.1

Giordano, D., Russell, J.K., Dingwell, D.B., 2008. Viscosity of magmatic liquids : A model 271, 123–134. https://doi.org/10.1016/j.epsl.2008.03.038

Glazner, A.F., Coleman, D.S., Bartley, J.M., 2008. The tenuous connection between high-silica rhyolites and granodiorite plutons. Geology 36, 183–186. https://doi.org/10.1130/G24496A.1

Gualda, G.A.R., Ghiorso, M.S., Lemons, R. V., Carley, T.L., 2012. Rhyolite-MELTS: A modified calibration of MELTS optimized for silica-rich, fluid-bearing magmatic systems. J. Petrol. 53, 875–890. https://doi.org/10.1093/petrology/egr080

Gualda, G.A.R., Gravley, D.M., Connor, M., Hollmann, B., Pamukcu, A.S., Bégué, F., Ghiorso, M.S., Deering, C.D., 2018. Climbing the crustal ladder: Magma storage-depth evolution during a volcanic flare-up. Sci. Adv. 4, 1–10. https://doi.org/10.1126/sciadv.aap7567

Hildreth, W., 1981. Gradients in Silicic Magma Chambers Implications for Lithospheric Magmatism. J. Geophys. Res. 86, 10153–10192.

Huber, C., Townsend, M., Degruyter, W., Bachmann, O., 2019. Optimal depth of subvolcanic magma chamber growth controlled by volatiles and crust rheology. Nat. Geosci. 12, 762–768. https://doi.org/10.1038/s41561-019-0415-6

Jellinek, A.M., DePaolo, D.J., 2003. A model for the origin of large silicic magma chambers: Precursors of caldera-forming eruptions. Bull. Volcanol. 65, 363–381. https://doi.org/10.1007/s00445-003-0277-y

Kaiser, J.F., de Silva, S., Schmitt, A.K., Economos, R., Sunagua, M., 2017. Million-year melt–presence in monotonous intermediate magma for a volcanic–plutonic assemblage in the Central Andes: Contrasting histories of crystal-rich and crystal-poor super-sized silicic magmas. Earth Planet. Sci. Lett. 457, 73–86. https://doi.org/10.1016/j.epsl.2016.09.048

Karakas, O., Degruyter, W., Bachmann, O., Dufek, J., 2017. Lifetime and size of shallow magma bodies controlled by crustal-scale magmatism. Nat. Geosci. 10, 446–450. https://doi.org/10.1038/ngeo2959

Kent, A.J.R., Cooper, K.M., 2018. How well do zircons record the thermal evolution of magmatic systems ? 46, 1–4. https://doi.org/doi.org/10.1130/G39690.1

Kern, J.M., de Silva, S.L., Schmitt, A.K., Kaiser, J.F., Iriarte, A.R., Economos, R., 2016. Geochronological imaging of an episodically constructed subvolcanic batholith: U-Pb in

zircon chronochemistry of the Altiplano-Puna Volcanic Complex of the Central Andes. Geosphere 12, 1054–1077. https://doi.org/10.1130/GES01258.1

Krimer, D., Costa, F., 2017. Evaluation of the effects of 3D diffusion, crystal geometry, and initial conditions on retrieved time-scales from Fe–Mg zoning in natural oriented orthopyroxene crystals. Geochim. Cosmochim. Acta 196, 271–288. https://doi.org/10.1016/j.gca.2016.09.037

Laumonier, M., Karakas, O., Bachmann, O., Gaillard, F., Lukács, R., Seghedi, I., Menand, T., Harangi, S., 2019. Evidence for a persistent magma reservoir with large melt content beneath an apparently extinct volcano. Earth Planet. Sci. Lett. 521, 79–90. https://doi.org/10.1016/j.epsl.2019.06.004

Lubbers, J., Deering, C., Bachmann, O., 2020. Genesis of rhyolitic melts in the upper crust : Fractionation and remobilization of an intermediate cumulate at Lake City caldera, Colorado, USA. J. Volcanol. Geotherm. Res. 392. https://doi.org/10.1016/j.jvolgeores.2019.106750

Lundstrom, C.C., Glazner, A.F., 2016. Silicic magmatism and the volcanic-plutonic connection. Elements 12. https://doi.org/10.2113/gselements.12.2.91

Marsh, B.D., 1981. On the crystallinity, probability of occurrence, and rheology of lava and magma. Contrib. to Mineral. Petrol. 78, 85–98. https://doi.org/10.1007/BF00371146

Mason, B.G., Pyle, D.M., Oppenheimer, C., 2004. The size and frequency of the largest explosive eruptions on Earth. Bull. Volcanol. 66, 735–748. https://doi.org/10.1007/s00445-004-0355-9

Morgan, D.J., Blake, S., 2006. Magmatic residence times of zoned phenocrysts: Introduction and application of the binary element diffusion modeling (BEDM) technique. Contrib. to Mineral. Petrol. 151, 58–70. https://doi.org/10.1007/s00410-005-0045-4

Petford, N., Cruden, A.R., McCaffrey, K.J.W., Vigneresse, J.L., 2000. Granite magma formation , transport and emplacement in the Earth ' s crust 408, 1–15.

Putirka, K.D., 2008. Thermometers and Barometers for Volcanic Systems. Rev. Mineral. Geochemistry 69, 61–120. https://doi.org/10.2138/rmg.2008.69.3

Ratajeski, K., Sisson, T.W., Glazner, A.F., 2005. Experimental and geochemical evidence for derivation of the El Capitan Granite, California, by partial melting of hydrous gabbroic lower crust. Contrib. to Mineral. Petrol. 149, 713–734. https://doi.org/10.1007/s00410-005-0677-4

Rose, Wi., Chesner, C., 1987. Dispersal of ash in the great Toba eruption, 75 ka. Geology 15, 913–917.

Rubin, A.E., Cooper, K.M., Till, C.B., Kent, A.J.R., Costa, F., Bose, M., Gravley, D., Deering, C., Cole, J., 2017. Rapid cooling and cold storage in a silicic magma reservoir recorded in Individual Crystals. Science (80-.). 356, 1154–1156. https://doi.org/10.1126/science.aam8720

Rudnick, R.L., Fountain, D.M., 1995. Nature and composition of the continental crust: A lower-crustal perspective. Rev. Geophys. 33, 267–309. https://doi.org/Doi 10.1029/95rg01302

Ruth, D.C.S., Costa, F., Bouvet De Maisonneuve, C., Franco, L., Cortés, J.A., Calder, E.S., 2018. Crystal and melt inclusion timescales reveal the evolution of magma migration before eruption. Nat. Commun. 9. https://doi.org/10.1038/s41467-018-05086-8

Scaillet, B., Holtz, F., Pichavant, M., 1998. Phase equilibrium constraints on the viscosity of silicic magmas: 1. Volcanic-plutonic comparison. J. Geophys. Res. Solid Earth 103, 27257–27266. https://doi.org/10.1029/98jb02469

Self, S., 2006. The effects and consequences of very large explosive volcanic eruptions. Philos. Trans. R. Soc. A Math. Phys. Eng. Sci. 364, 2073–2097. https://doi.org/10.1098/rsta.2006.1814

Shamloo, H.I., Till, C.B., Hervig, R.L., 2021. Multi-mode Magnesium Diffusion in Sanidine:

Applications for Geospeedometry in Magmatic Systems. Geochim. Cosmochim. Acta 298, 55–69. https://doi.org/10.1016/j.gca.2021.01.044

Shea, T., Costa, F., Krimer, D., Hammer, J.E., 2015. Accuracy of timescales retrieved from diffusion modeling in olivine: A 3D perspective. Am. Mineral. 100, 2026–2042. https://doi.org/10.2138/am-2015-5163

Sigl, M., Winstrup, M., McConnell, J.R., Welten, K.C., Plunkett, G., Ludlow, F., Büntgen, U., Caffee, M., Chellman, N., Dahl-Jensen, D., Fischer, H., Kipfstuhl, S., Kostick, C., Maselli, O.J., Mekhaldi, F., Mulvaney, R., Muscheler, R., Pasteris, D.R., Pilcher, J.R., Salzer, M., Schüpbach, S., Steffensen, J.P., Vinther, B.M., Woodruff, T.E., 2015. Timing and climate forcing of volcanic eruptions for the past 2,500 years. Nature 523, 543–549. https://doi.org/10.1038/nature14565

Streck, M.J., Grunder, A.L., 2008. Phenocryst-poor rhyolites of bimodal, tholeiitic provinces: The Rattlesnake Tuff and implications for mush extraction models. Bull. Volcanol. 70, 385–401. https://doi.org/10.1007/s00445-007-0144-3

Szymanowski, D., Ellis, B.S., Wotzlaw, J.-F., Bachmann, O., 2019. Maturation and rejuvenation of a silicic magma reservoir: High-resolution chronology of the Kneeling Nun Tuff. Earth Planet. Sci. Lett. 510, 103–115. https://doi.org/10.1016/j.epsl.2019.01.007

Szymanowski, D., Wotzlaw, J.-F., Ellis, B.S., Bachmann, O., Guillong, M., von Quadt, A., 2017. Protracted near-solidus storage and pre-eruptive rejuvenation of large magma reservoirs. Nat. Geosci. 10. https://doi.org/10.1038/ngeo3020

Takeuchi, S., 2011. Preeruptive magma viscosity: An important measure of magma eruptibility. J. Geophys. Res. Solid Earth 116. https://doi.org/10.1029/2011JB008243

Takeuchi, S., 2004. Precursory dike propagation control of viscous magma eruptions. Geology 32, 1001–1004. https://doi.org/10.1130/G20792.1

Taylor, S., McLennan, S., 1995. The Geochemical Evolution of the Continental Crust. Rev. Geophys. 33, 241–265. https://doi.org/10.1029/95RG00262

Tierney, C.R., Schmitt, A.K., Lovera, O.M., de Silva, S.L., 2016. Voluminous plutonism during volcanic quiescence revealed by thermochemical modeling of zircon. Geology 44, 683–686. https://doi.org/10.1130/G37968.1

Till, C.B., Vazquez, J.A., Boyce, J.W., 2015. Months between rejuvenation and volcanic eruption at Yellowstone caldera, Wyoming Supplementary Data. Geology 3–7. https://doi.org/10.1038/ngeo1638.Kuiper

Wilson, C.J.N., Cooper, G.F., Chamberlain, K.J., Barker, S.J., Myers, M.L., Kemp, F.I.-, Farrell, J., 2021. No single model for supersized eruptions and their magma bodies. Nat. Rev. Earth Environ. https://doi.org/10.1038/s43017-021-00191-7

Wolff, J.A., 2017. On the syenite-trachyte problem 45, 1067–1070.

Wolff, J.A., Ellis, B.S., Ramos, F.C., Starkel, W.A., Boroughs, S., Olin, P.H., Bachmann, O., 2015. Remelting of cumulates as a process for producing chemical zoning in silicic tuffs: A comparison of cool, wet and hot, dry rhyolitic magma systems. Lithos 236–237, 275–286. https://doi.org/10.1016/j.lithos.2015.09.002

Wolff, J.A., Forni, F., Ellis, B.S., Szymanowski, D., 2020. Europium and barium enrichments in compositionally zoned felsic tuffs: A smoking gun for the origin of chemical and physical gradients by cumulate melting. Earth Planet. Sci. Lett. 540, 116251. https://doi.org/10.1016/j.epsl.2020.116251

Wotzlaw, J.F., Schaltegger, U., Frick, D.A., Dungan, M.A., Gerdes, A.G., Günther, D., 2013. Tracking the evolution of large-volume silicic magma reservoirs from assembly to supereruption. Geology 41, 867–870. https://doi.org/10.1130/G34366.1

Zhang, Y., 2010. Diffusion in minerals and melts: Theoretical background. Rev. Mineral. Geochemistry 72, 5–59. https://doi.org/10.2138/rmg.2010.72.2

CHAPTER TWO: THERMAL BUDGETS OF MAGMA STORAGE CONSTRAINED BY DIFFUSION CHRONOMETRY: THE CERRO GALÁN IGNIMBRITE

Jordan Lubbers
Adam Kent
Shan de Silva

Manuscript in preparation for submission to:
Journal of Petrology
Oxford Journals

ABSTRACT

The long-term thermochemical conditions at which large bodies of silicic magma are stored in the crust is integral to our understanding of the timing, frequency, and intensity of volcanic eruptions and helps provide context for volcano monitoring data. Despite this realization, however, individual magmatic systems also may have unique time-temperature paths, or thermal histories, that are the result of many complex and, sometimes, simultaneous/competing processes, ultimately leading to an incomplete understanding of their long-term thermal evolution. Of recent interest to the volcanology community is the length of time large volumes of eruptible magma exist within the crust prior to their eruption. Here we use a combination of diffusion chronometry, trace element, and thermodynamic modeling to quantify the thermal history of the 2.08 Ma, 630km^3 Cerro Galán Ignimbrite (CGI) in NW Argentina, one of the largest explosive volcanic eruptions in the geologic record. We find that diffusion of both Mg and Sr in plagioclase indicate that the system only spent decades to centuries at or above temperatures (~750°C) required to produce and store significant volumes of eruptible magma. We utilize high-resolution trace element transects to also show that some plagioclase record time periods of co-crystallization with biotite and sanidine, while others do not, providing evidence for their long-term storage. Further evidence for long-term storage comes from calculated plagioclase equilibrium liquid compositions representing an array that is controlled by fractionation of plagioclase + biotite + sanidine. Despite this long-term storage, we find diffusion models record a unimodal distribution which, when combined with prior work revealing zircon residence times of ~10^5 years and calculated zircon saturation temperatures of 786 ± 14°C, provide compelling evidence that the CGI magmatic system spent most of its upper crustal residence in an uneruptible state and was ultimately remobilized shortly before eruption.

INTRODUCTION

Large silicic magma reservoirs, responsible for producing the biggest explosive volcanic eruptions in the geologic record (Mason et al., 2004; Wilson et al., 2021), exist as local thermal anomalies in the otherwise cold mid to upper continental crust (Huber et al., 2019; Turcotte and Schubert, 2002). Maintaining magma volumes that are sufficiently liquid-rich to erupt reflects a balance between conductive cooling, advective gain or loss of heat via eruption and addition recharge magma, and latent heat of crystallization (e.g., Degruyter and Huber, 2014). Because of this, rapid addition of magma is thought to be necessary to grow and sustain large volumes of magma in the crust (Annen et al., 2015; de Silva and Gregg, 2014; Gelman et al.,

2013). However, individual magma systems (and different regions with a single magma system) may also have unique time-temperature paths, or thermal histories, that are the amalgamation of many complex and, sometimes, simultaneous processes (e.g., recharge, eruption, second boiling, thermal buffering, magma ascent, etc.). Despite these complexities, quantifying the thermal state and evolution of a magma reservoir remains important as it has been shown to be responsible for controlling eruption timing, frequency, and dynamics (e.g., Degruyter and Huber, 2014) and thus an understanding of the thermal history of a crustal magma reservoir is important for understanding volcanic processes.

The thermal histories of crustal magma systems, and the conditions that give rise to large bodies of eruptible magma, have been investigated for several decades using numerical modeling (e.g., Annen et al., 2006; de Silva and Gregg, 2014; Gelman et al., 2013; Jellinek and DePaolo, 2003; Karakas et al., 2017) and also more recently these issues have been investigated by petrological and geochemical techniques. The latter are based on a range of approaches, including single mineral geochronology (Andersen et al., 2017; Barboni et al., 2016; Klemetti et al., 2011; Szymanowski et al., 2017), thermobarometry and phase equilibria (e.g., Walker et al., 2013) or a combination of these approaches. In addition, in recent years, diffusion chronometry in a range of different mineral phases (e.g., Bradshaw, 2017; Cooper and Kent, 2014; Rubin et al., 2017; Shamloo and Till, 2019) has also emerged as a powerful way to constrain the thermal evolution of magmas. Although diffusion chronometry is more often used to quantify timescales of short duration magmatic processes – typically those associated with the buildup to eruption (e.g., Couperthwaite et al., 2020; Ruth et al., 2018; Shamloo and Till, 2019), mineral element pairs with slower diffusivities at temperatures relevant to silicic magmatic systems can also be used to study longer term magmatic processes (e.g. Cooper and Kent, 2014; Bradshaw, 2017; Rubin et al., 2017).

Based on these studies two broad end-member models have emerged. In the first scenario crustal magma reservoirs spend the vast majority of their time in a state of near solidus temperatures, where they are not eruptible, and experience punctuated thermal events that generate and/or erupt eruptible volumes of magma (e.g. Cooper and Kent, 2014; Rubin et al., 2017; Szymanowski et al., 2017). This view is also supported by geophysical approaches, which rarely observe melt-dominated (greater than 50%) magma reservoirs (Lundstrom and Glazner, 2016), although some exceptions to this may exist (Laumonier et al., 2019). In contrast it has also been argued that magma reservoirs spend the vast majority of their time at temperatures which allow for a significant and eruptible melt fraction throughout much of their history to be present (e.g. Barboni et al., 2016; Kaiser et al., 2017; Tierney et al., 2016).

These alternatives imply distinctly different behavior within the associated magmatic plumbing systems and are thus important to constrain. However, considering these scenarios as a simple binary is also likely to obscure important details about the complexity of magmatic systems, and larger magmatic reservoirs may exhibit both of these storage types within a single system (e.g., Andersen et al., 2017; Bradshaw, 2017). Many thermal history investigations have also focused on systems that erupt relatively small volumes of magma (e.g., less than 10^{1-2} km^3; Barboni et al., 2016; Cooper and Kent, 2014; Rubin et al., 2017; Tierney et al., 2016; Till et al., 2015). Larger systems have also been studied (e.g., greater than 500 km^3; Andersen et al., 2017; Bradshaw, 2017; Shamloo and Till, 2019; Szymanowski et al., 2017), although many of the available constraints utilize relatively small data sets, and thus are less suitable to see if there is complexity in the thermal histories experienced by different magmatic components within an individual magma reservoir.

One way to investigate this issue further is to conduct more detailed studies of a single large eruption, and to combine diffusional constraints with other petrologic approaches to provide additional context within which to interpret results. In addition, use of multiple trace elements for diffusion modeling can also make diffusion constraints more robust (e.g., Chamberlain et al., 2014; Morgan and Blake, 2006; Shamloo and Till, 2019; Till et al., 2015). Here we utilize diffusion modeling of Sr and Mg in plagioclase and detailed documentation of core to rim changes in plagioclase chemistry in the 2.08 Ma, 630 km^3 Cerro Galán Ignimbrite (Folkes et al., 2011c; Kay et al., 2011). We also combine these results with thermodynamic modeling (e.g., Rhyolite-MELTS; Gualda et al. 2012) and other petrological observations to constrain the long-term thermal evolution in this system.

Geologic Background

The Cerro Galán caldera, located in northwest Argentina on the eastern edge of the Puna plateau, is a part of the larger Central Volcanic Zone of the South American Andes (Figure 2.1). Between 5.6 and 2.08 Ma the Cerro Galán magmatic system produced >1200km^3 of high-K, crystal rich (40-50%), chemically homogenous (68-71wt% SiO_2) rhyodacite (Folkes et al., 2011a, 2011c) that have been classified as a 'monotonous intermediates' (Hildreth, 1981). The largest and most recent eruption, the 2.08 Ma Cerro Galán Ignimbrite (CGI), produced 630km^3 of ignimbrite that extends outward from the caldera 40km in all directions and up to 80km north of the caldera (Folkes et al., 2011c).

The CGI is a massive, crystal-rich (40-50% crystals), and generally pumice poor ignimbrite with a mineral assemblage of plagioclase + sanidine + quartz + biotite + Fe-Ti oxides + apatite + zircon. The majority of pumice have between 69-71 wt% SiO_2, however two

types of pumice are evident (Wright et al., 2011): 1) the majority of pumice (~95%) are "white pumice" that contain 44 – 57% crystals, no microlites, > 76 wt.% SiO_2 groundmass, and higher Ba concentrations; 2) a volumetrically small proportion of pumice (~5%) are "grey pumice" that contain 35 – 59% crystals, abundant microlites, groundmass SiO_2 concentrations of 69 – 74 wt.%, and ~150ppm lower Ba concentrations at equivalent SiO_2 concentrations as white pumice. Fe-Ti oxide geothermometry on white pumice record temperatures of 790-820°C (Wright et al., 2011), however Folkes et al., (2011) note that due to the high fO_2 (+1-1.7 NNO) calculated for the CGI these temperature estimates may have uncertainties of 50-100 °C. Trace element ratios in the CGI, when compared to previous ignimbrites from the Galán magmatic system, indicate magmas that experience closed system evolution (Folkes et al., 2011b). Appearance of sanidine in the CGI, coupled with the disappearance of amphibole present in previous eruptions from the Cerro Galán system has been experimentally demonstrated to be the result of a shallowing of the magmatic system over time, and this is also supported by volatile contents in quartz-hosted melt inclusions (Grocke et al., 2017). Previous reconnaissance studies (e.g., Folkes et al., 2011b; Wright et al., 2011) of the thermal evolution of the Cerro Galán Ignimbrite indicate that there are multiple populations of plagioclase with one population recording magma storage for long durations at high temperature (> 750 °C; type 1), while the other (and more common) records short time at high temperature (type 2). Additionally, these different plagioclase populations contain unique trace element signatures with type 1 plagioclase exhibiting a positive correlation between Ba and An, while type 2 exhibits a negative correlation. This has been interpreted as being the result of plagioclase recording crystallizing environments in which the magma system switches from conditions that inhibit sanidine crystallization (type 2) to those that promote it (type 1) as the magma system shallows with time (Bradshaw, 2017). It is also possible, however, that these trends may be heavily influenced by the presence of biotite (found up to 15 vol% vs. 1.5 vol% sanidine in the CGI) and reflect a magma reservoir with diverse crystallization conditions, further establishing the need for an in depth, multidisciplinary assessment of the time-temperature evolution of the Cerro Galán magmatic system.

METHODS

Bulk Rock Geochemistry

Eight samples from representative locations around the Cerro Galán caldera were chosen for bulk rock geochemical analysis. Samples were turned into billets at Oregon State University, then went to Washington State University where they were processed and analyzed for both major (SiO_2, TiO_2, Al_2O_3, FeO, MnO, MgO, CaO, Na_2O, K_2O, P_2O_5) and trace element

(La, Ce, Pr, Nd, Sm, Eu, Gd, Tb, Dy, Ho, Er, Tm, Yb, L, Ba, Th, Nb, Y, Hf, Ta, U, Pb, Rb, Cs, Sr, Sc, Zr, V, Cr, Ni, Cu, Zn, Ga) analyses. Major elements, high field strength elements (HFSE), and their corresponding uncertainties were characterized using a ThermoARL AdvantXP XRF following the method of Johnson et al 1999. Rare earth elements (REE) and remaining trace elements along with their uncertainties were measured by inductively coupled plasma mass spectrometry (ICP-MS) using an Agilent 7700 Q-ICP-MS according to Knaack et al., (1994). Bulk rock major and trace element concentrations, along with their uncertainties can be found in online supplementary material.

Electron Probe Micro Analysis

Major element (Na, Si, Al, Fe, Ca, K, Mg, Ti) spot analyses and backscattered electron (BSE) images were conducted using Cameca SX100 electron probe microanalyzer (EPMA) at Oregon State University with a focused beam of 5μm, 15kV accelerating voltage, and 30nA current were used. Uncertainties were calculated by repeated measurement of standard reference materials. Measured accepted values along with their uncertainties can be found in Table 2.1.

Laser Ablation Inductively Coupled Plasma Mass Spectrometry (LA-ICP-MS)

Trace element (^{7}Li,^{24}Mg,^{27}Al,^{43}Ca,^{57}Fe,^{88}Sr,^{138}Ba,^{139}La,^{140}Ce,^{153}Eu,^{208}Pb) analyses of plagioclase were conducted using a Photon Machines Analyte G2193 ArF Excimer laser system connected to a ThermoFisher Scientific iCAP-RQ ICP-MS at the W.M. Keck Collaboratory for Plasma Spectrometry at Oregon State University. Analyses were conducted as a line of spots with dimensions 5 by 50 μm with 5 μm between spot centers, pulse rate of 50 Hz, and analysis time of 10 seconds per spot. This approach allows for high spatial resolution to be maintained in the direction of the transect, while still allowing for higher count rates to improve precision. All total, 81 plagioclase transects across 9 samples were gathered. Profile locations within individual plagioclase were chosen following the advice provided in Shea et al., (2015) to mitigate the influence of sectioning effects and merging diffusion fronts in our diffusion models.

Ablated material was carried to the mass spectrometer using an Aerosol Rapid Introduction System (ARIS; Teledyne Photon Machines Inc., Bozeman MT, USA) microcapillary tube to decrease washout time, allow for easier ablation peak identification, and help improve detection of low concentration elements. Analyzed isotopes were converted to elemental concentrations using the methodology of Kent and Ungerer, (2006) and Longerich et al., (1996) using ^{43}Ca as the internal standard and BCR-2G as the calibration standard. Anorthite contents of plagioclase were calculated using measured Ca/Si ratios similar to the

method of (Kent et al., 2007). ATHO-G and BCR-2G standards were analyzed every 5 profiles as well as at the beginning and end of each experiment along with NIST-612 and BHVO-2G to monitor for drift in the mass spectrometer. Concentrations of all measured secondary standards can be found in the appendix.

Diffusion Chronometry

This study utilizes Mg and Sr diffusion in plagioclase to quantify the duration that a given crystal (or area of a crystal) has experienced a certain temperature. Trace element partitioning in plagioclase is dependent on An content (Bindeman et al., 1998; Dohmen and Blundy, 2014; Nielsen et al., 2017) and follows an Arrhenius relationship such that:

$$1. \quad RT\, ln(K_D) = AX_{An} + B$$

Where R is the gas constant, T is temperature, X_{An} is the molar fraction of anorthite, and both A and B are constants (Bindeman et al., 1998; Nielsen et al., 2017). Likewise, the rate at which self-diffusion of both Mg and Sr occurs within plagioclase is dependent on An content (Cherniak and Watson, 1994; Costa et al., 2003; Giletti and Casserly, 1994; LaTourrette and Wasserburg, 1998; Van Orman et al., 2014). Having both the partition and diffusion coefficient values dependent on An content then necessitates a diffusion equation that incorporates these observations. As such we utilize the solutions from Costa et al. (2003) to model how Mg and Sr profiles will change with time:

$$2. \quad \frac{\delta C}{\delta t} = \left(\frac{\delta D}{\delta x}\frac{\delta C}{\delta x} + D\frac{\delta^2 C}{\delta x^2}\right) - \frac{A}{RT}\left(D\frac{\delta C}{\delta x}\frac{\delta X_{An}}{\delta x} + C\frac{\delta D}{\delta x}\frac{\delta X_{An}}{\delta x} + DC\frac{\delta^2 X_{An}}{\delta x^2}\right)$$

Where D is the diffusion coefficient of the trace element being modeled, C is the concentration of that trace element measured at a given point, and A is the thermodynamic constant from Equation 1. This solution to the diffusion equation proceeds towards an equilibrium profile that is dictated by the observed An profile as well as the composition of plagioclase that is in equilibrium with the melt at the time of eruption (e.g., the rim). Over the range of An values observed in CGI plagioclase (~40-75), we find the choice of partitioning model is not extremely important, as they all produce similar partition coefficients for both Sr and Mg (Figure A.1).

We model the modification of Sr and Mg contents in plagioclase via diffusion using a finite difference forward model following the method of Costa et al., (2008) adapted to Equation 2. Diffusion coefficients for Mg and Sr were taken from Van Orman et al., (2014) and Giletti and Casserly (1994), respectively. Equilibrium profiles were calculated by using Equation 1 and the composition of the most rimward analysis in the transect used to calculate an equilibrium liquid composition. We then assume that this liquid composition is what the plagioclase in the measured profile is striving to equilibrate with. While these analyses are not

always exactly at the rim of the grain, we find that calculated equilibrium liquids for each profile are broadly consistent with one another (i.e., 0.4 ± .1 wt% Mg; 157 ± 37 ppm Sr), regardless of whether or not they are at the core or rim of a given grain. Furthermore, as long as the observed trace element profile in the plagioclase is trying to equilibrate with a single liquid composition (real or hypothetical) this assumption is valid (Costa et al., 2003).

Boundary conditions used as starting profiles for diffusion models were chosen using An profile shapes as a guide. This is justified for two reasons: 1) NaSi – CaAl interdiffusion in plagioclase is extremely slow (e.g., Grove et al., 1984; Liu and Yund, 1992) such that it does not change appreciably on magmatic timescales at 750°C; 2) Anorthite profile shapes are approximately the inverse of the calculated equilibrium profiles as partition coefficient is inversely related to An (e.g., Bindeman et al., 1998; Nielsen et al., 2017). This then means that if a diffusion profile at t = $>10^4$ years was tracked back through time to t = 0 years, it produces an initial boundary condition that mimics the width and height of an An profile. Applying this logic, we create either a step-function profile or profile that closely mimics the shape of the An profile, and focus on regions where there are large changes (steps) in An concentration. While not as numerically complex as other models for estimating initial boundary conditions that require assumptions about the initial magma composition and how it evolves with time (e.g., Costa et al., 2003; Druitt et al., 2012; Mutch et al., 2021), we find that these boundary conditions accurately approach calculated equilibrium conditions and are therefore suitable for the purposes of this study. Furthermore, after a number of attempts we concluded that forward models of both Sr and Mg evolution in the CGI magmatic system were unable to reproduce the observed relationships between Sr, Mg, and An and if used for calculating initial Sr and Mg profiles in plagioclase, would introduce considerable additional uncertainty into our diffusion models. The benefit of using step function-like initial profiles is then two-fold in this situation: 1) less uncertainty introduced by inaccurate trace element evolution models; 2) diffusion model results reflect diffusion times that are maxima as it assumes that compositional changes in plagioclase are instantaneous relative to crystal growth.

The rate at which diffusion occurs is strongly dependent on temperature. As such, temperature is a critically important input in all diffusion models. In the case of long-term magma storage, it is difficult to accurately assign a temperature and storage conditions are unlikely to be isothermal in any case. We instead follow the approach of Cooper and Kent (2014) where we constrain the maximum time that a given crystal could spend at a given temperature. We further use the relationship between viscosity and temperature (Marsh, 1981) to constrain the maximum time that magma could spend in a state where it was mobile.

Bradshaw (2017) used Rhyolite-MELTS modeling to show that the CGI system reaches 40-60% crystals at 750 ± 10 °C. This change in crystallinity corresponds to an abrupt change in magma viscosity found in magmas from other large silicic systems such as the Fish Canyon Tuff (Caricchi and Blundy, 2015). Importantly, this increase in viscosity results in a magma that is near the magma extrusion limit between 10^6-10^8 Pa·s (Scaillet et al., 1998; Takeuchi, 2011). Thus, at temperatures cooler than ~750°C, the CGI magmatic system is at rheological conditions such that it cannot be erupted. As we are primarily concerned with the duration at which the CGI magmatic system spent at temperatures where there were large volumes of eruptible melt, we set our diffusion model temperatures at 750°C. Our diffusion model results, then, quantify the maximum duration a given grain, or portion of that grain, resided in a magma that was hotter than 750°C, and thus was in eruptible magma.

The best fit diffusion model to the observed trace element profile was assessed using a standard chi-squared test that assigns a 'goodness of fit' for each iteration of the model. The smallest chi-squared value for a given model is then deemed to be the best fit diffusion time based on the input parameters. Uncertainties for each diffusion model were evaluated using a Monte Carlo approach where 1000 random profiles were generated for each modeled profile. Random profiles were based on the analytical uncertainty at each analyzed point (i.e., for each point in the profile a normally distributed random number was generated based on the observed mean analysis value and its 1 sigma uncertainty). Best fit diffusion times were then fit to each random profile in the Monte Carlo simulation keeping the initial boundary conditions and temperature fixed. As we are quantifying a duration above 750°C (for reasons listed above) and not a measured temperature with an uncertainty, we keep this fixed as well. Overall uncertainties for a given diffusion model were calculated by taking the mean and standard deviation for the Monte Carlo simulation. Most of the distributions from Monte Carlo simulations were determined to be log-normal, so prior to taking the mean and standard deviation they were first transformed such that they fit a normal distribution. Calculated means and standard deviations from the transformed distribution were then back transformed so that they were in correct time units (e.g., years and not log[years]). For a more complete explanation of the diffusion modeling process and the intricacies of the model, we have created a Jupyter notebook (https://github.com/jlubbersgeo/diffusion_chronometry) that is available for download.

RESULTS

Geochemistry

Whole Rock

Bulk rock major and trace element data for our samples are consistent with previous work (e.g., Folkes et al., 2011b; Wright et al., 2011). Pumice found within the CGI is relatively homogenous in SiO_2 and other major elements (Figure 2.2A), but has been interpreted to be the result of fractional crystallization (Folkes et al., 2011b). Wright and others (2011) note, however, that there is a less dominant pumice species found within the CGI that displays elevated Ba concentrations, lower Sr/Ba, and Eu/Eu^*. Rare earth element diagrams for the CGI show shallow Eu anomalies and middle - heavy rare earth concentrations of 10x chondrite consistent with other large silicic eruptions that have been interpreted to be from cold, wet, and oxidizing conditions (Bachmann and Bergantz, 2008; Deering et al., 2008, 2010). Although there are some more subtle differences in Eu/Eu*, overall REE trends are similar for both pumice types (Figure 2.2B).

Plagioclase

Plagioclase from the CGI An values that are normally distributed around $An_{36\pm4}$. There are, however, small numbers of analyses that display $An_{>60}$ and $An_{<25}$. High An values are exclusively found in plagioclase cores. Plagioclase trace element compositions from the CGI, like An, show mostly unimodal trace element distributions and plagioclase compositions largely overlap between white and gray pumice (Figure 2.3). When plagioclase analyses are observed incorporating spatial information, however, we find that there are small geochemical heterogeneities on the intracrystalline scale (see section below on Ba-An distributions). Furthermore, we find that, although most plagioclase display Mg concentrations and 30-50 μg/g and have a mean composition of An_{35}, some restricted zones in plagioclase cores contain concentrations up to 200 - 400 μg/g and are An_{55} or greater (Figure 2.4). Strontium and Mg in plagioclase from the CGI also exhibit a positive relationship with An (Figure 2.5 A, C). This contrasts with negative correlations between Mg, Sr and An that would result from equilibrium partitioning with a single liquid composition, or from complete diffusive equilibrium (Figure 2.5B, D). Thus, the Sr and Mg profiles in plagioclase must lie somewhere between their initial state (the composition when that part of the mineral formed) and full diffusive equilibration.

DISCUSSION

Diffusion of Mg and Sr in plagioclase

As discussed above, both Sr and Mg in plagioclase appear to be out of diffusive equilibrium with their plagioclase host. This is shown by the observation that both Sr and Mg profiles are significantly different from calculated equilibrium profiles (e.g., Figure 2.4), and by the positive correlations between An - Sr and An - Mg in individual crystals and in the CGI system as a whole (Figure 2.5) which are antithetic to trends expected from full diffusive equilibration. The positive correlations between Sr, Mg and An reflect petrogenetic processes during the crystallization of plagioclase whereby Sr and Mg are removed from the melt by crystallization of plagioclase and mafic phases (e.g., Cooper and Kent, 2014) as progressively lower An plagioclase forms, producing the observed positive trends.

Magnesium in plagioclase diffusion models were completed for 44 grains and best fits range in duration from <1.5 to 358 years (Figure 2.6). While a large range, 95% of times are less than 108 years. Strontium in plagioclase diffusion models were completed for 34 grains and range in duration from <10 years to 969 years with 95% of times being less than 452 years. Diffusion coefficient and analytical resolution dictate the lower limit of resolvable timescales achievable when modeling 1D diffusion (Bradshaw and Kent, 2017). This effectively puts a lower 'resolution' boundary on all diffusion models, regardless of what the 'best fit' model suggests. At An_{50} (CGI 3 sigma upper value) this is 1.5 years for Mg and 10 years for Sr. Two grains modeled for Mg diffusion and one grain modeled for Sr diffusion return times less than these respective limits, and we simply report these as < 1.5 and < 10 years.

Representative diffusion models for Mg and Sr in plagioclase can be found in Figure 2.7 and Figure 2.8 respectively and illustrate: 1) Variations of both Mg and Sr, for the most part, mimic the width and magnitude of An profile shapes and, as such, are much more similar to observed An profiles in form than the calculated equilibrium profiles; 2) Using these initial Sr and Mg distributions and at a temperature of 750°C, our diffusion models report decadal to centennial timescales for transects that are in both the cores and rims of grains. For grains where multiple transects were measured throughout, core transects consistently record longer diffusion timescales than rim transects (Figure 2.9).

There is significant overlap in the ranges of apparent timescales recorded by Mg and Sr (Figure 2.6A), however there are also some significant discrepancies between the Sr and Mg best fit diffusion times in individual crystals (Figure 2.6B). We find that as Mg diffusion times increase, Sr diffusion times do not increase in a predictable way (e.g., Figure 2.6C), implying that this observation is likely not the result of either systematic differences in partition or

diffusion coefficients. Furthermore, despite Mg diffusing roughly 5 times faster than Sr at the appropriate CGI An content and at 750°C, Mg profiles consistently match the profiles of An and other slow diffusing elements (e.g., Ba) profiles more closely than Sr profiles (Figure 2.7, Figure 2.10). This observation alone suggests that little diffusion has occurred.

One explanation for the differences between Sr and Mg diffusion models might be differences in the variation of Sr and Mg that occurs with changes in An content during plagioclase formation. Elements that have large discrepancies in diffusion rates should produce noticeably different diffusion widths after a sufficiently long period of time (e.g., Morgan and Blake, 2006). Conversely, when their diffusion widths and magnitudes appear similar, they will yield different diffusion times reflecting their individual diffusion rates, subsequently leading to the interpretation that diffusion has not progressed significantly from initial boundary conditions (Shamloo and Till, 2019; Till et al., 2015). While CaAl – NaSi diffuses so slowly (Cherniak, 2010 and references therein) that it is not useful in quantifying timescales of volcanic processes, we apply similar logic to Till et al. (2015) inasmuch as Mg profiles in the CGI plagioclase simply could not have existed for $>10^3$ years at 750°C while still resembling the observed An profile more than equilibrium profile shapes (Figure 2.11A) and maintaining a positive correlation with An (Figure 2.11B). As some Sr diffusion models record diffusion times up to 1500 years, we suggest that initial step functions based on the shape of the An profile may be an overestimation of boundary conditions for Sr profiles in some instances and, since the Sr diffusion coefficient is significantly slower than Mg, lead to overestimations in the time a given grain has experienced at a certain temperature. We hypothesize that this may be the result of Sr and Mg partitioning in plagioclase having different sensitivities to changes in An (i.e., the "A" parameter in Equation 2; Bindeman et al., 1998; Nielsen et al., 2017). Furthermore, the faster diffusion of Mg means that overestimation of the diffusion times are likely to be smaller with incorrect boundary conditions, and thus Mg diffusion models are likely to: 1) be less sensitive in inaccuracies of diffusion model boundary conditions; 2) more accurately represent the duration at which the CGI magma existed at or above 750°C.

Thermal history of magma storage

The eruption that produced the Cerro Galán Ignimbrite evacuated 630 km^3 of crystal rich (40-50% crystals) volcanic material from Cerro Galán caldera (Folkes et al., 2011c). Bradshaw (2017) modelled crystallization in the CGI magma system using Rhyolite-MELTS (Gualda et al., 2012). Liquid compositions and crystal fractions predicted by Rhyolite-MELTS were then used to calculate melt and magma viscosities using Giordano et al., (2008) and Scaillet et al., (1998), respectively. As with many silicic magmas, the CGI system experienced

a drastic increase in magma viscosity as it reached crystallinities of 30-40% and temperatures of 750 ± 10°C, such that it reached values near or exceeding the magma extrusion limit (e.g., 10^6-10^8 Pa·s; Scaillet et al., 1998; Takeuchi, 2011), implying that this temperature and crystallinity approximates an inflection point whereby the magma changes from being rheologically mobile to immobile (e.g., uneruptible). While we note that highly crystalline magmas experience non-Newtonian behavior (Mader et al., 2013), and these viscosities are approximations of complex multi-phase fluid dynamics problems, further evidence to suggest that 30-40% crystallinity may be at the upper limit of magma eruptible magma viscosities is the observation that crystallinities of erupted volcanic rocks are rarely above 45-50% (Marsh, 1981), and that the crystallinities of Cerro Galán rocks themselves are only as high as 40-50% crystals. Thus, when calculated at 750°C our best fit diffusion timescales for both Mg and Sr in plagioclase correspond to the maximum amount of time that an individual grain, or portion of a grain, could have spent at magma reservoir conditions sufficient for the magma to be mobile. In addition, each grain is recording its own individual thermal history, and as diffusion is continuous from the moment a given chemical potential (i.e., zone boundary) within the mineral forms, then the calculated timescale provides a "thermal budget" for all the processes that might impact the thermal state of the crystal. This includes initial crystal growth – which can occur over a wide range of temperatures in the Cerro Galán magmatic system (Bradshaw, 2017), including temperatures over 750°C, as well as long term storage, and transient reheating events associated with magma recharge (e.g., Rubin et al., 2017).

Despite this potential complexity, our results collectively indicate that the population of CGI plagioclase we have examined, from the moment plagioclase began crystallizing in the CGI magmatic system, only spent decades to centuries at temperatures required to produce large volumes of eruptible melt. Moreover, despite analysis of a much larger number of crystals than previous studies we see broadly unimodal timescale distributions (Figure 2.6A) with little evidence for plagioclase populations that have experienced systematically different thermal histories. This may relate to the relatively high uncertainties in our diffusion chronology estimates, but also may reflect that diffusion of heat in silicic magmas is relatively rapid (e.g., Jaeger, 1964). Our Sr and Mg diffusion in plagioclase diffusion results also align with other plagioclase diffusion studies that investigated storage conditions of caldera forming eruptions (Bradshaw, 2017; Druitt et al., 2012).

Plagioclase as a recorder of magma reservoir conditions

Plagioclase is a solid solution found in virtually all igneous rocks. It displays a myriad of growth, dissolution, and zoning textures, is capable of preserving long crystallization and

mixing histories (e.g., Cooper et al., 2001; Davidson et al., 2001; Singer et al., 1995), and crystallizes over a wide P-T-X-fO_2 range (e.g., Bowen, 1915, 1913; Drake, 1976), making it a key mineral to study for observing long-term magma reservoir processes. It also has many useful geochemical applications such as U-series dating (e.g. Cooper and Reid 2003), diffusion modeling (e.g. Costa et al. 2003; Druitt et al. 2012), and thermometry (e.g., Putirka 2008 and references therein). In the following section we explore how plagioclase can be used to infer long-term magma reservoir thermochemical histories using a combination of trace element partitioning and diffusion chronometry.

Plagioclase crystallizes over a wide range of temperatures in the CGI magma system (Bradshaw, 2017), suggesting that it should reflect crystallization from a melt that is becoming more progressively depleted with elements such as Sr and Mg that are compatible in plagioclase (e.g., Bindeman et al., 1998; Nielsen et al., 2017) or compatible in phases that are co-crystallizing with plagioclase. Using partition coefficients from Nielsen et al., (2017) and our measured plagioclase compositions we have calculated melt compositions in equilibrium with observed plagioclase compositions and compared these to the erupted pumice glass compositions (Figure 12). Except for the lowest An compositions, the erupted glass composition for the CGI and the liquid compositions in equilibrium with CGI plagioclase do not overlap, and the vast majority of plagioclase equilibrium melt compositions are less evolved than the observed pumice glasses. While a decrease in temperature to near solidus (e.g., ~650-680) temperatures shifts plagioclase equilibrium melt compositions to lower Sr and Mg abundances, even at these low temperatures most calculated equilibrium compositions are still less evolved than the erupted glass compositions. Assuming the K_d values used are broadly correct this suggests that most plagioclase crystallized at a relatively early stage of magmatic evolution and are in equilibrium with melts that are more enriched in both Sr and Mg (which is also consistent with the observed Sr-An and Mg-An relations we observe). Although there are always uncertainties associated with any partitioning model for any phase, however we find most calculated plagioclase equilibrium liquids and erupted glass compositions do not overlap within 2-sigma uncertainty. These observations are also true when using partition coefficients from Bindeman et al., (1998), suggesting that calculated partition coefficients, themselves, are not a significant source of error. Rather, we propose that the wide array of melt compositions in equilibrium with plagioclase compositions are the result of plagioclase recording magma reservoir conditions that do not reflect those immediately prior to eruption, but longer-term magma storage that is evolving due to fractionation of predominantly plagioclase and biotite. Figure 2.12B also illustrates that nearly all CGI plagioclase formed in equilibrium with a liquid

that was much more enriched in Mg. As biotite is the only phase within the CGI in which Mg is a major component (Mg# 58-66; Folkes et al., 2011b), we take this observation to imply that the majority of CGI plagioclase crystallized from a magma that was either absent of biotite or had crystallized less biotite than what is observed in erupted pumice.

Trace element contents also provide constraints the thermochemical conditions that CGI plagioclase are recording. Barium is less compatible in plagioclase compared to lower temperature phases in the CGI (i.e., biotite, sanidine). Barium also diffuses sufficiently slowly (Cherniak, 2002) that measured Ba contents have not been significantly modified by diffusion. Looking at the Ba-An relationship in a single grain allows us to determine whether or not biotite or sanidine were present as that portion of the plagioclase was growing, as a decrease in Ba with mineral growth implies a co-crystallization with a Ba compatible phase. Barium-An relationships reveal a diversity of behavior and can broadly be grouped into 6 categories (fractionation with Ba compatible phases, fractionation without Ba compatible phases, recharge with Ba compatible phases present, recharge without Ba compatible phases present, little to no fractionation, and some combination of these trends; Figure 2.13) revealing that individual plagioclase crystals are not only recording different crystallization environments, but also have the potential to record multiple crystallization/dissolution events prior to their evacuation from the reservoir(s) in which they grew. This is also in contrast to the bulk rock major and trace element chemistry which suggest a more chemically homogeneous system (This study; Folkes et al., 2011b). To determine if there are statistically significant differences recorded in diffusion timescales between groups, we performed a two-sample Kolmogorov-Smirnov (KS) test which tests the null hypothesis if two samples are drawn from the same distribution. In this case our samples were plagioclase that show signs of co-crystallization with biotite/sanidine and plagioclase that do not. We find that despite plagioclase recording very different chemical environments, there is no statistically significant difference in diffusion timescales between groups (i.e., KS statistic below critical value and p-value >> 0.05). These results hold for both Mg and Sr diffusion results. Collectively these data are interpreted to show that although the magma system from which the CGI was erupted contained significant reservoir scale chemical heterogeneities through time, and that individual plagioclase experienced and recorded quite different petrologic environments, there are no substantive differences recorded in thermal history between these crystals.

Constraints from zircon

To further help quantify the long-term thermal state of the Cerro Galán magmatic system, we also compare zircon residence times (Folkes et al., 2011a), zircon saturation

temperatures (Boehnke et al., 2013; Watson and Harrison, 1983), and plagioclase diffusive equilibration times. Folkes et al., (2011a) found that many zircons from the CGI have cores that crystallized at > 10^5 but < 10^6 years prior to eruption. This implies that parts of the CGI magmatic system must have been below zircon saturation temperatures for at least that duration of time. To calculate zircon saturation temperatures throughout the evolution of the CGI magmatic system we utilized Rhyolite MELTS for Excel (Gualda et al., 2012; Gualda and Ghiorso, 2015) as it quantifies many extensive properties of a magmatic system while it crystallizes from fully liquid to solid. The CGI has been interpreted as the result of fractionation of a parent magma that is a 50:50 mix of mantle derived basalts and local basement (Kay et al., 2011) and, using this as a guide, we create a starting composition for MELTS models. Basement compositions were taken from Ortiz et al., (2019) and basalt compositions were taken from Drew et al., (2009) as well as Kay et al., (1994). Log fO_2 is constrained between +1 – 1.7 NNO (Folkes et al., 2011b). For each down temperature step in a given MELTS model a M parameter, [(Na + K + 2Ca)/(Al*Si)], was calculated for the remaining liquid composition. Zircon saturation temperatures were then calculated using (Boehnke et al., 2013) and we find that across all MELTS models zircon saturation occurs at 786 ± 14°C (Figure 2.14). Calculating zircon saturation temperatures from measured glass data yields somewhat higher zircon saturation temperatures of 807 ± 5°C. While generally regarded as a robust and faithful recorder of magma reservoir processes in silicic systems, Bindeman and Melnik (2016) show that when exposed to temperatures above the zircon saturation temperature, even larger zircons (e.g., 200μm diameter) will dissolve in 10^3 – 10^4 years. Therefore, for the CGI zircons to record such long residence times, while also remaining hundreds of microns in length, they could not have been above zircon saturation temperatures for a significant period. This also puts a limit on the thermal state of the CGI magmatic system, and when combined with plagioclase diffusion timescales, provides compelling evidence that the CGI magmatic system spent most its time at sufficiently low temperatures such that stored magmas were unlikely to be at an eruptible viscosity.

Periodic recharge

Plagioclase from the CGI exhibit mean An values of An_{35}, however display frequent $An_{>55}$ zones throughout many analyzed grains (Figure 2.4). While an increase in An of this magnitude may due to a multitude of processes such as temperature or pressure increase Streck (2008) or rapid ascent of water saturated magmas Blundy et al., (2006), we propose that this increase in An is due to recharge of a less evolved magma, as increases in An are typically not found at the rims of a given grain. The high An zones are also associated with significantly

higher concentrations of Mg (Figure 2.4) which may be indicative of influence from a less evolved magma. These observations effectively rule out rapid ascent of water saturated magmas as a likely cause, as rapid ascent driven changes in An would also likely be one of the last things a plagioclase experiences prior to eruption and be found at the rims of grains or as infilled sieved textures, both of which we do not see.

Our diffusion chronometry of Mg also puts thermal and temporal limits on these recharge events, as our data provide an estimate of the total time that a crystal could have been at temperatures in excess of 750°C. Thus, diffusion data define a thermal "budget" within which the analyzed plagioclase must form, be stored, and then erupted. Given the relatively short durations we estimate for residence at temperatures >= 750°C, it implies that although recharge events clearly occur, they may have had relatively little thermal input to the system overall, and are mainly reflected in changes in composition, not temperature.

Our data also show that grains that experience recharge occur throughout the systems fractionation history (i.e., some profiles have Ba-An relationships indicating co crystallization with biotite, where others have Ba-An relationships indicating crystallization without biotite). Rhyolite-MELTS models predict that biotite begins crystallizing with quartz relatively late in the CGI crystallization sequence (i.e., ~850-820°C and ~30-50% crystallinity), but before sanidine. We use this to delineate between plagioclase that record relatively late stage (post-biotite saturation), and longer-term magma reservoir processes that occur prior to biotite saturation. We take the ubiquity of high-An zones in both these groups of plagioclase to imply that the Cerro Galán magmatic system has been periodically recharged with a magma that produces plagioclase of at least An_{60} and potentially as high as An_{75} composition. This idea is also supported by: 1) the presence of a volumetrically minor, less evolved, pumice population (i.e., gray pumice) that Wright et al., (2011) used to suggest that there was a second, less evolved melt reservoir deeper in the crust that briefly interacted with CGI magmas prior to eruption; 2) volatile zoning in apatite indicating recharge of a volatile-rich magma shortly before eruption into a reservoir that contained local variations in composition (Boyce and Hervig, 2008).

Long term thermochemical conditions

The results from our plagioclase trace element and diffusion modeling show that the plagioclase measured in this study are recording a range of longer-term and later stage magma reservoir processes within the Cerro Galán magmatic system, and that overall, eruptible magmas are only present for periods of decades to centuries or less, regardless of whether or not plagioclase show signs of long-term residence (i.e., crystallization without biotite and

sanidine) or later-stage crystallization (i.e., co-crystallizing with biotite and sanidine). This is important as it implies that short diffusion times are not simply reflective of young crystals and that the long-term thermal history of the CGI magmatic system was one was dominated by storage temperatures below 750°C. Below, we address how these timescales fit with previous literature on magma remobilization timescales and what it means for the long-term thermochemical state of the magma system.

Previously, the Cerro Galán magmatic system has been classified as homogenous on the basis of bulk rock and major phase chemistry (Folkes et al., 2011b). While homogeneity of a given system is ultimately defined by the scale of investigation (e.g., Fish Canyon Tuff, Bachmann et al., 2002), the CGI is homogenous inasmuch as it does not display bulk rock major element zoning characteristic of many large silicic eruptions (e.g., Carpenter Ridge Tuff, Bachmann et al., 2014; Youngest Toba Tuff, Chesner and Rose, 1991; Kneeling Nun Tuff, Szymanowski et al., 2019). The CGI, however, also has been interpreted as the result of fractionation of a 50-50 mix of local metamorphic basement and mantle derived basalts (Folkes et al., 2011b; Kay et al., 2011), suggesting that there may have been large scale thermochemical zoning related to progressive differentiation at some point in its history (Bachmann and Bergantz, 2008). Huber et al., (2012) find that these reservoir scale heterogeneities may be removed in crystal rich, eutectoid, systems with high degrees of exsolved volatiles on the order of years or less, which is significantly shorter than the time required to reactivate a given mush body via repeated injection of hotter magmas. While longer than homogenization times, other numerical models suggest that reactivation times for a hydrous, crystal rich, magma systems may be on the order of hundreds to thousands of years (Hartung et al., 2019). These results align with our diffusion modeling results that show CGI plagioclase spent only decades to centuries at or above temperatures required for production of eruptible magma. Based on heterogeneous crystal cargo that display frequent zoning (Figure 2.4, Figure 2.7, Figure 2.8), evidence for long term storage with repeated recharge of less evolved, volatile rich material (Boyce and Hervig, 2008; Wright et al., 2011; Figure 2.13), and short times at remobilizing temperatures (Figure 2.6, Figure 2.10, Figure 2.11), we argue it is highly plausible then, that the Cerro Galán magma system was in a chemically heterogeneous but uneruptible state for a significant portion of its history and was only homogenized and remobilized shortly before eruption.

CONCLUSION

We applied diffusion modeling of Mg and Sr in plagioclase from the 2.08 Ma, 630 km^3, Cerro Galán Ignimbrite (CGI) to investigate the long-term thermochemical magma

storage conditions of large silicic magma reservoirs. Our results indicate that, although bulk-rock geochemistry implies a magmatic system that is chemically homogeneous at the time of eruption, plagioclase are recording diverse crystallization environments (i.e., late stage co-crystallization with Ba-compatible phases such as biotite and sanidine as well as earlier crystallization without Ba-compatible phases) throughout their crystallization history that largely do not reflect those at the time of eruption. Furthermore, despite this evidence for long-term storage within the reservoir, CGI plagioclase are only recording timescales of decades to centuries at temperatures required to produce eruptible volumes of magma. Combined with evidence for periodic recharge of a less evolved magma, we take these results to mean that the CGI magmatic system existed in a predominantly immobile, but chemically heterogeneous state for most of its residence within the crust. These results help to further constrain the long-term thermochemical storage conditions of magma systems capable of producing catastrophic caldera forming eruptions.

REFERENCES

Andersen, N.L., Jicha, B.R., Singer, B.S., Hildreth, W., 2017. Incremental heating of Bishop Tuff sanidine reveals preeruptive radiogenic Ar and rapid remobilization from cold storage 114, 12407–12412. https://doi.org/10.1073/pnas.1709581114

Annen, C., Blundy, J.D., Leuthold, J., Sparks, R.S.J., 2015. Construction and evolution of igneous bodies: Towards an integrated perspective of crustal magmatism. Lithos 230, 206–221. https://doi.org/10.1016/j.lithos.2015.05.008

Annen, C., Blundy, J.D., Sparks, R.S.J., 2006. The genesis of intermediate and silicic magmas in deep crustal hot zones. J. Petrol. 47, 505–539. https://doi.org/10.1093/petrology/egi084

Bachmann, Olivier, Bergantz, G.W., 2008. Rhyolites and their source mushes across tectonic settings. J. Petrol. 49, 2277–2285. https://doi.org/10.1093/petrology/egn068

Bachmann, O., Bergantz, G.W., 2008. Deciphering Magma Chamber Dynamics from Styles of Compositional Zoning in Large Silicic Ash Flow Sheets. Rev. Mineral. Geochemistry 69, 651–674. https://doi.org/10.2138/rmg.2008.69.17

Bachmann, O., Deering, C.D., Lipman, P.W., Plummer, C., 2014. Building zoned ignimbrites by recycling silicic cumulates: insight from the 1,000 km3 Carpenter Ridge Tuff, CO. Contrib. to Mineral. Petrol. 167, 1025. https://doi.org/10.1007/s00410-014-1025-3

Bachmann, O., Dungan, M.A., Lipman, P.W., 2002. The Fish Canyon Magma Body , San Juan Volcanic Field , Colorado : Rejuvenation and Eruption of an Upper-Crustal Batholith 43, 1469–1503.

Barboni, M., Boehnke, P., Schmitt, A.K., Harrison, T.M., Shane, P., Bouvier, A.-S., Baumgartner, L., 2016. Warm storage for arc magmas. Proc. Natl. Acad. Sci. 113, 13959–13964. https://doi.org/10.1073/pnas.1616129113

Bindeman, I.N., Davis, A.M., Drake, M.J., 1998. Ion microprobe study of plagioclase- basalt partition experiments at natural concentration levels of trace elements. Geochim. Cosmochim. Acta 62, 1175–1193. https://doi.org/10.1016/S0016-7037(98)00047-7

Bindeman, I.N., Melnik, O.E., 2016. Zircon survival, rebirth and recycling during crustal melting, magma crystallization, and mixing based on numerical modeling. J. Petrol. 57, 437–460. https://doi.org/10.1093/petrology/egw013

Blundy, J., Cashman, K., Humphreys, M., 2006. Magma heating by decompression-driven crystallization beneath andesite volcanoes. Nature 443, 76–80. https://doi.org/10.1038/nature05100

Boehnke, P., Watson, E.B., Trail, D., Harrison, T.M., Schmitt, A.K., 2013. Zircon saturation re-revisited. Chem. Geol. 351, 324–334. https://doi.org/10.1016/j.chemgeo.2013.05.028

Bowen, N.L., 1915. The Later Stages of the Evolution of the Igneous Rocks 23.

Bowen, N.L., 1913. The Melting Phenomena of the Plagioclase Feldspars. Am. J. Sci.

Boyce, J.W., Hervig, R.L., 2008. Magmatic degassing histories from apatite volatile stratigraphy. Geology 36, 63–66. https://doi.org/10.1130/G24184A.1

Bradshaw, R.W., 2017. Crystal Records of the Origin, Evolution, and Thermal Histories of Magmas. Oregon State University.

Bradshaw, R.W., Kent, A.J.R., 2017. The analytical limits of modeling short diffusion timescales. Chem. Geol. 466, 667–677. https://doi.org/10.1016/j.chemgeo.2017.07.018

Caricchi, L., Blundy, J., 2015. Experimental petrology of monotonous intermediate magmas. Geol. Soc. Spec. Publ. 422, 105–130. https://doi.org/10.1144/SP422.9

Chamberlain, K.J., Morgan, D.J., Wilson, C.J.N., 2014. Timescales of mixing and mobilisation in the Bishop Tuff magma body : perspectives from diffusion chronometry. Contrib. to Mineral. Petrol. https://doi.org/10.1007/s00410-014-1034-2

Cherniak, D.J., 2010. Cation diffusion in feldspars. Rev. Mineral. Geochemistry 72, 691–733. https://doi.org/10.2138/rmg.2010.72.15

Cherniak, D.J., 2002. Ba diffusion in feldspar. Geochim. Cosmochim. Acta 66, 1641–1650. https://doi.org/10.1016/S0016-7037(01)00866-3

Cherniak, D.J., Watson, E.B., 1994. A study of strontium diffusion in plagioclase using Rutherford backscattering spectroscopy. Geochim. Cosmochim. Acta 58, 5179–5190. https://doi.org/10.1016/0016-7037(94)90303-4

Chesner, C., Rose, Wi., 1991. Stratigraphy of the Toba Tuffs and the evolution of the Toba Caldera Complex, Sumatra, Indonesia. Bull. Volcanol. 53, 343–356.

Cooper, K., Reid, M., Murrell, M., D.a., C., 2001. Crystal and magma residence at Kilauea Volcano. Earth Planet. Sci. Lett. 184, 703–718.

Cooper, K.M., Kent, A.J.R., 2014. Rapid remobilization of magmatic crystals kept in cold storage. Nature 506, 480–3. https://doi.org/10.1038/nature12991

Cooper, K.M., Reid, M.R., 2003. Re-examination of crystal ages in recent Mount St. Helens lavas: Implications for magma reservoir processes. Earth Planet. Sci. Lett. 213, 149–167. https://doi.org/10.1016/S0012-821X(03)00262-0

Costa, F., Chakraborty, S., Dohmen, R., 2003. Diffusion coupling between major and trace elements and a model for the calculation of magma chamber residence times using plagioclase. Geochim. Cosmochim. Acta 67, 2189–2200. https://doi.org/10.1016/S0016-7037(00)01345-5

Costa, F., Dohmen, R., Chakraborty, S., 2008. Time Scales of Magmatic Processes from Modeling the Zoning Patterns of Crystals. Rev. Mineral. Geochemistry 69, 545–594. https://doi.org/10.2138/rmg.2008.69.14

Couperthwaite, F.K., Thordarson, T., Morgan, D.J., Harvey, J., Wilson, M., 2020. Diffusion Timescales of Magmatic Processes in the Moinui Lava Eruption at Mauna Loa, Hawai`i, as Inferred from Bimodal Olivine Populations. J. Petrol. 61. https://doi.org/10.1093/petrology/egaa058

Davidson, J., Tepley, F., Palacz, Z., Meffan-Main, S., 2001. Magma recharge, contamination and residence times revealed by in situ laser ablation isotopic analysis of feldspar in volcanic rocks. Earth Planet. Sci. Lett. 184, 427–442. https://doi.org/10.1016/S0012-821X(00)00333-2

de Silva, S.L., Gregg, P.M., 2014. Thermomechanical feedbacks in magmatic systems: Implications for growth, longevity, and evolution of large caldera-forming magma reservoirs and their supereruptions. J. Volcanol. Geotherm. Res. 282, 77–91. https://doi.org/10.1016/j.jvolgeores.2014.06.001

Deering, C.D., Cole, J.W., Vogel, T.A., 2008. A rhyolite compositional continuum governed by lower crustal source conditions in the taupo volcanic zone, New Zealand. J. Petrol. 49, 2245–2276. https://doi.org/10.1093/petrology/egn067

Deering, C.D., Gravley, D.M., Vogel, T.A., Cole, J.W., Leonard, G.S., 2010. Origins of cold-wet-oxidizing to hot-dry-reducing rhyolite magma cycles and distribution in the Taupo Volcanic Zone, New Zealand. Contrib. to Mineral. Petrol. 160, 609–629. https://doi.org/10.1007/s00410-010-0496-0

Degruyter, W., Huber, C., 2014. A model for eruption frequency of upper crustal silicic magma chambers. Earth Planet. Sci. Lett. 403, 117–130. https://doi.org/10.1016/j.epsl.2014.06.047

Dohmen, R., Blundy, J., 2014. A PREDICTIVE THERMODYNAMIC MODEL FOR ELEMENT PARTITIONING BETWEEN PLAGIOCLASE AND MELT AS A FUNCTION OF PRESSURE , TEMPERATURE AND COMPOSITION 314, 1319–1372. https://doi.org/10.2475/09.2014.04

Drake, M.J., 1976. Plagioclase-melt equilibria. Geochim. Cosmochim. Acta 40, 457–465.

Drew, S.T., Ducea, M.N., Schoenbohm, L.M., 2009. Mafic volcanism on the Puna Plateau, NW Argentina: Implications for lithospheric composition and evolution with an emphasis on lithospheric foundering. Lithosphere 1, 305–318.

https://doi.org/10.1130/L54.1
Druitt, T.H., Costa, F., Deloule, E., Dungan, M., Scaillet, B., 2012. Decadal to monthly timescales of magma transfer and reservoir growth at a caldera volcano. Nature 482, 77–80. https://doi.org/10.1038/nature10706
Folkes, C.B., De Silva, S.L., Schmitt, A.K., Cas, R.A.F., 2011a. A reconnaissance of U-Pb zircon ages in the Cerro Galán system, NW Argentina: Prolonged magma residence, crystal recycling, and crustal assimilation. J. Volcanol. Geotherm. Res. 206, 136–147. https://doi.org/10.1016/j.jvolgeores.2011.06.001
Folkes, C.B., de Silva, S.L., Wright, H.M., Cas, R.A.F., 2011b. Geochemical homogeneity of a long-lived, large silicic system; evidence from the Cerro Galán caldera, NW Argentina. Bull. Volcanol. 73, 1455–1486. https://doi.org/10.1007/s00445-011-0511-y
Folkes, C.B., Wright, H.M., Cas, R.A.F., de Silva, S.L., Lesti, C., Viramonte, J.G., 2011c. A re-appraisal of the stratigraphy and volcanology of the Cerro Galán volcanic system, NW Argentina. Bull. Volcanol. 73, 1427–1454. https://doi.org/10.1007/s00445-011-0459-y
Gelman, S.E., Gutiérrez, F.J., Bachmann, O., 2013. On the longevity of large upper crustal silicic magma reservoirs. Geology 41. https://doi.org/10.1130/G34241.1
Giletti, B.J., Casserly, J.E.D., 1994. Strontium diffusion kinetics in plagioclase feldspars. Geochim. Cosmochim. Acta 58, 3785–3793. https://doi.org/10.1016/0016-7037(94)90363-8
Giordano, D., Russell, J.K., Dingwell, D.B., 2008. Viscosity of magmatic liquids : A model 271, 123–134. https://doi.org/10.1016/j.epsl.2008.03.038
Grocke, S.B., Andrews, B.J., de Silva, S.L., 2017. Experimental and petrological constraints on long-term magma dynamics and post-climactic eruptions at the Cerro Galán caldera system, NW Argentina. J. Volcanol. Geotherm. Res. 347, 296–311. https://doi.org/10.1016/j.jvolgeores.2017.09.021
Grove, T.L., Baker, M.B., Kinzler, R.J., 1984. Coupled CaAl-NaSi diffusion in plagioclase feldspar: Experiments and applications to cooling rate speedometry. Geochim. Cosmochim. Acta 48, 2113–2121. https://doi.org/10.1016/0016-7037(84)90391-0
Gualda, G.A.R., Ghiorso, M.S., 2015. MELTS-Excel: A Microsoft Excel-based MELTS interface for research and teaching of magma properties and evolution. Geochemistry, Geophys. Geosystems 16, 315–324. https://doi.org/10.1002/2014GC005545
Gualda, G.A.R., Ghiorso, M.S., Lemons, R. V., Carley, T.L., 2012. Rhyolite-MELTS: A modified calibration of MELTS optimized for silica-rich, fluid-bearing magmatic systems. J. Petrol. 53, 875–890. https://doi.org/10.1093/petrology/egr080
Hartung, E., Weber, G., Caricchi, L., 2019. The role of H2O on the extraction of melt from crystallising magmas. Earth Planet. Sci. Lett. 508, 85–96. https://doi.org/10.1016/j.epsl.2018.12.010
Hildreth, W., 1981. Gradients in Silicic Magma Chambers Implications for Lithospheric Magmatism. J. Geophys. Res. 86, 10153–10192.
Huber, C., Bachmann, O., Dufek, J., 2012. Crystal-poor versus crystal-rich ignimbrites: A competition between stirring and reactivation. Geology 40, 115–118. https://doi.org/10.1130/G32425.1
Huber, C., Townsend, M., Degruyter, W., Bachmann, O., 2019. Optimal depth of subvolcanic magma chamber growth controlled by volatiles and crust rheology. Nat. Geosci. 12, 762–768. https://doi.org/10.1038/s41561-019-0415-6
Jaeger, J.C., 1964. Thermal Effects of Intrusions. Rev. Geophys. 2.
Jellinek, A.M., DePaolo, D.J., 2003. A model for the origin of large silicic magma chambers: Precursors of caldera-forming eruptions. Bull. Volcanol. 65, 363–381. https://doi.org/10.1007/s00445-003-0277-y
Kaiser, J.F., de Silva, S., Schmitt, A.K., Economos, R., Sunagua, M., 2017. Million-year

melt–presence in monotonous intermediate magma for a volcanic–plutonic assemblage in the Central Andes: Contrasting histories of crystal-rich and crystal-poor super-sized silicic magmas. Earth Planet. Sci. Lett. 457, 73–86. https://doi.org/10.1016/j.epsl.2016.09.048

Karakas, O., Degruyter, W., Bachmann, O., Dufek, J., 2017. Lifetime and size of shallow magma bodies controlled by crustal-scale magmatism. Nat. Geosci. 10, 446–450. https://doi.org/10.1038/ngeo2959

Kay, S.M., Coira, B., Viramonte, J., 1994. Young mafic back arc volcanic rocks as indicators of continental lithospheric delamination beneath the Argentine Puna plateau, central Andes 99.

Kay, S.M., Coira, B., Wörner, G., Kay, R.W., Singer, B.S., 2011. Geochemical, isotopic and single crystal 40Ar/39Ar age constraints on the evolution of the Cerro Galán ignimbrites. Bull. Volcanol. 73, 1487–1511. https://doi.org/10.1007/s00445-010-0410-7

Kent, A.J.R., Blundy, J., Cashman, K. V., Copper, K.M., Donnelly, C., Pallister, J.S., Reagan, M., Rowe, M.C., Thornber, C.R., 2007. Vapor transfer prior to the October 2004 eruption of Mount St. Helens, Washington. Geology 35, 231–234. https://doi.org/10.1130/G22809A.1

Kent, A.J.R., Ungerer, C.A., 2006. Analysis of light lithophile elements (Li, Be, B) by laser ablation ICP-MS: Comparison between magnetic sector and quadrupole ICP-MS. Am. Mineral. 91, 1401–1411. https://doi.org/10.2138/am.2006.2030

Klemetti, E.W., Deering, C.D., Cooper, K.M., Roeske, S.M., 2011. Magmatic perturbations in the Okataina Volcanic Complex, New Zealand at thousand-year timescales recorded in single zircon crystals. Earth Planet. Sci. Lett. 305, 185–194. https://doi.org/10.1016/j.epsl.2011.02.054

Knaack, C., Cornelius, S., Hooper, P., 1994. Trace element analyses of rocks and minerals by ICP-MS.

LaTourrette, T., Wasserburg, G.J., 1998. Mg diffusion in anorthite: implications for the formation of early solar system planetesimals. Earth Planet. Sci. Lett. 158, 91–108. https://doi.org/10.1016/S0012-821X(98)00048-X

Laumonier, M., Karakas, O., Bachmann, O., Gaillard, F., Lukács, R., Seghedi, I., Menand, T., Harangi, S., 2019. Evidence for a persistent magma reservoir with large melt content beneath an apparently extinct volcano. Earth Planet. Sci. Lett. 521, 79–90. https://doi.org/10.1016/j.epsl.2019.06.004

Liu, M., Yund, R.A., 1992. NaSi-CaAl interdiffusion in plagioclase. Am. Mineral. 77, 275–283.

Longerich, H.P., Jackson, S.E., Günther, D., 1996. Laser ablation inductively coupled plasma mass spectrometric transient signal data acquisition and analyte concentration calculation. J. Anal. At. Spectrom. 11, 899–904. https://doi.org/10.1039/JA9961100899

Lundstrom, C.C., Glazner, A.F., 2016. Silicic magmatism and the volcanic-plutonic connection. Elements 12. https://doi.org/10.2113/gselements.12.2.91

Mader, H.M., Llewellin, E.W., Mueller, S.P., 2013. The rheology of two-phase magmas: A review and analysis. J. Volcanol. Geotherm. Res. 257, 135–158. https://doi.org/10.1016/j.jvolgeores.2013.02.014

Marsh, B.D., 1981. On the crystallinity, probability of occurrence, and rheology of lava and magma. Contrib. to Mineral. Petrol. 78, 85–98. https://doi.org/10.1007/BF00371146

Mason, B.G., Pyle, D.M., Oppenheimer, C., 2004. The size and frequency of the largest explosive eruptions on Earth. Bull. Volcanol. 66, 735–748. https://doi.org/10.1007/s00445-004-0355-9

Morgan, D.J., Blake, S., 2006. Magmatic residence times of zoned phenocrysts: Introduction and application of the binary element diffusion modeling (BEDM) technique. Contrib. to Mineral. Petrol. 151, 58–70. https://doi.org/10.1007/s00410-005-0045-4

Mutch, E.J.F., Maclennan, J., Shorttle, O., Rudge, J.F., Neave, D.A., 2021. DFENS: Diffusion Chronometry Using Finite Elements and Nested Sampling. Geochemistry, Geophys. Geosystems 22, 1–28. https://doi.org/10.1029/2020GC009303

Nielsen, R., Ustunisik, G., Weinsteiger, A., Tepley, F., Johnston, D., Kent, A.J.R., 2017. Trace element partitioning between plagioclase and melt: An investigation of the impact of experimental and analytical procedures. Geochemistry, Geophys. Geosystems 18, 1580–1593. https://doi.org/10.1002/2017GC006821

Ortiz, A., Suzaño, N., Hauser, N., Becchio, R., Nieves, A., 2019. New hints on the evolution of the Eastern Magmatic Belt, Puna Argentina. SW Gondwana margin: Zircon U-Pb ages and Hf isotopes in the Pachamama Igneous-Metamorphic Complex. J. South Am. Earth Sci. 94, 102246. https://doi.org/10.1016/j.jsames.2019.102246

Putirka, K.D., 2008. Thermometers and Barometers for Volcanic Systems. Rev. Mineral. Geochemistry 69, 61–120. https://doi.org/10.2138/rmg.2008.69.3

Rubin, A.E., Cooper, K.M., Till, C.B., Kent, A.J.R., Costa, F., Bose, M., Gravley, D., Deering, C., Cole, J., 2017. Rapid cooling and cold storage in a silicic magma reservoir recorded in Individual Crystals. Science (80-.). 356, 1154–1156. https://doi.org/10.1126/science.aam8720

Ruth, D.C.S., Costa, F., Bouvet De Maisonneuve, C., Franco, L., Cortés, J.A., Calder, E.S., 2018. Crystal and melt inclusion timescales reveal the evolution of magma migration before eruption. Nat. Commun. 9. https://doi.org/10.1038/s41467-018-05086-8

Scaillet, B., Holtz, F., Pichavant, M., 1998. Phase equilibrium constraints on the viscosity of silicic 103.

Shamloo, H.I., Till, C.B., 2019. Decadal transition from quiescence to supereruption: petrologic investigation of the Lava Creek Tuff, Yellowstone Caldera, WY. Contrib. to Mineral. Petrol. 174, 1–18. https://doi.org/10.1007/s00410-019-1570-x

Shea, T., Costa, F., Krimer, D., Hammer, J.E., 2015. Accuracy of timescales retrieved from diffusion modeling in olivine: A 3D perspective. Am. Mineral. 100, 2026–2042. https://doi.org/10.2138/am-2015-5163

Singer, B.S., Dungan, M.A., Layne, G.D., 1995. Textures and Sr,Ba,Mg,Fe,K, and Ti compositional profiles in volcanic plagioclase: Clues to the dynamics of calc-alkaline magma chambers. Am. Mineral. 80, 833–840. https://doi.org/10.2138/am-1995-7-819

Streck, M.J., 2008. Mineral Textures and Zoning as Evidence for Open System Processes. Rev. Mineral. Geochemistry 69, 595–622. https://doi.org/10.2138/rmg.2008.69.15

Szymanowski, D., Ellis, B.S., Wotzlaw, J.-F., Bachmann, O., 2019. Maturation and rejuvenation of a silicic magma reservoir: High-resolution chronology of the Kneeling Nun Tuff. Earth Planet. Sci. Lett. 510, 103–115. https://doi.org/10.1016/j.epsl.2019.01.007

Szymanowski, D., Wotzlaw, J.-F., Ellis, B.S., Bachmann, O., Guillong, M., von Quadt, A., 2017. Protracted near-solidus storage and pre-eruptive rejuvenation of large magma reservoirs. Nat. Geosci. 10. https://doi.org/10.1038/ngeo3020

Takeuchi, S., 2011. Preeruptive magma viscosity: An important measure of magma eruptibility. J. Geophys. Res. Solid Earth 116. https://doi.org/10.1029/2011JB008243

Tierney, C.R., Schmitt, A.K., Lovera, O.M., de Silva, S.L., 2016. Voluminous plutonism during volcanic quiescence revealed by thermochemical modeling of zircon. Geology 44, 683–686. https://doi.org/10.1130/G37968.1

Till, C.B., Vazquez, J.A., Boyce, J.W., 2015. Months between rejuvenation and volcanic eruption at Yellowstone caldera, Wyoming. Geology 43, 695–698. https://doi.org/10.1130/G36862.1

Turcotte, D., Schubert, G., 2002. Geodynamics, 2nd ed. Cambridge University Press.

Van Orman, J.A., Cherniak, D.J., Kita, N.T., 2014. Magnesium diffusion in plagioclase: Dependence on composition, and implications for thermal resetting of the 26Al-26Mg

early solar system chronometer. Earth Planet. Sci. Lett. 385, 79–88. https://doi.org/10.1016/j.epsl.2013.10.026

Walker, B.A., Klemetti, E.W., Grunder, A.L., Dilles, J.H., Tepley, F.J., Giles, D., 2013. Crystal reaming during the assembly, maturation, and waning of an eleven-million-year crustal magma cycle: Thermobarometry of the Aucanquilcha Volcanic Cluster. Contrib. to Mineral. Petrol. 165, 663–682. https://doi.org/10.1007/s00410-012-0829-2

Watson, E.B., Harrison, T.M., 1983. Zircon saturation revisited: temperature and composition effects in a variety of crustal magma types. Earth Planet. Sci. Lett. 64, 295–304. https://doi.org/10.1016/0012-821X(83)90211-X

Wilson, C.J.N., Cooper, G.F., Chamberlain, K.J., Barker, S.J., Myers, M.L., Kemp, F.I.-, Farrell, J., 2021. No single model for supersized eruptions and their magma bodies. Nat. Rev. Earth Environ. https://doi.org/10.1038/s43017-021-00191-7

Wright, H.M.N., Folkes, C.B., Cas, R.A.F., Cashman, K. V., 2011. Heterogeneous pumice populations in the 2.08-Ma Cerro Galán Ignimbrite: Implications for magma recharge and ascent preceding a large-volume silicic eruption. Bull. Volcanol. 73, 1513–1533. https://doi.org/10.1007/s00445-011-0525-5

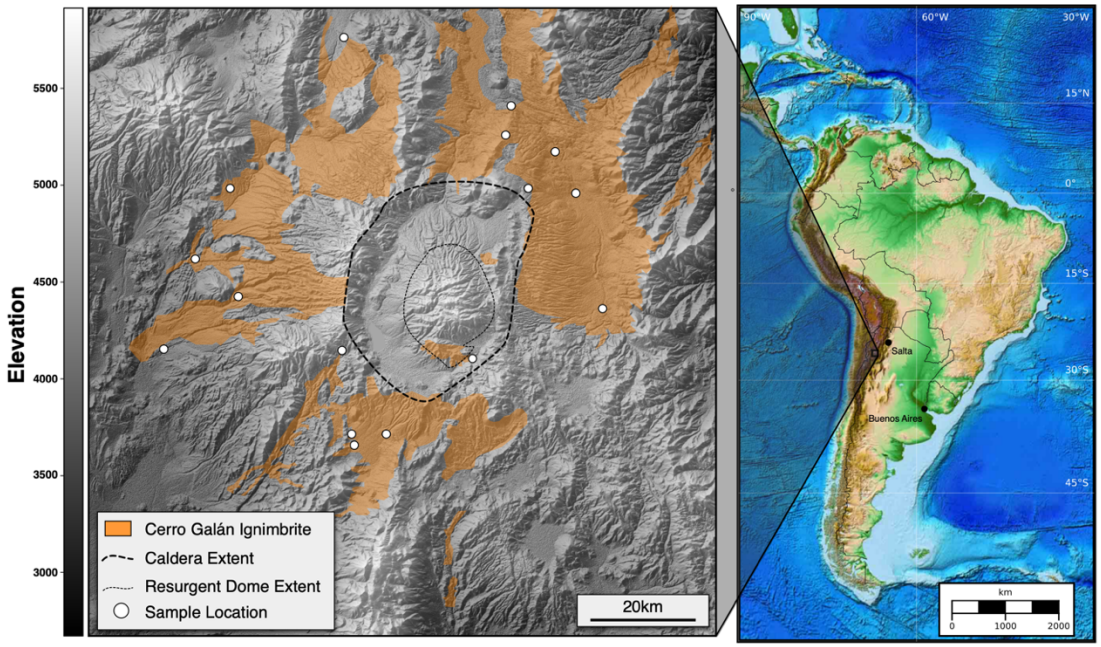

Figure 2.1: Digital elevation map (DEM) of the Cerro Galán Caldera and its location within the Central Andean Volcanic Zone (CAVZ). Orange shading represents the extent of the Cerro Galán Ignimbrite and white dots are sampling locations for this experiment.

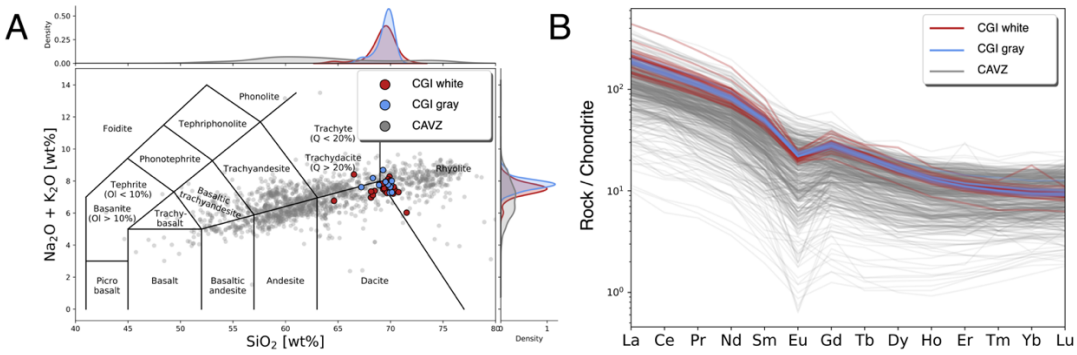

Figure 2.2: A) Total alkalis vs silica (TAS) diagram for CGI pumice compared to other CAVZ volcanics from the last 10Ma. Note the overlapping between the two pumice types as well as the unimodal distribution of data in both silica and total alkalis. B) REE diagram for CGI pumice (gray and white) compared to other CAVZ volcanics from the last 10 Ma. It can be seen here that CGI pumice have REE trends that are more consistent with cold, wet, oxidizing than hot, dry, reducing rhyolites from other large volcanic eruptions (Deering et al., 2010).

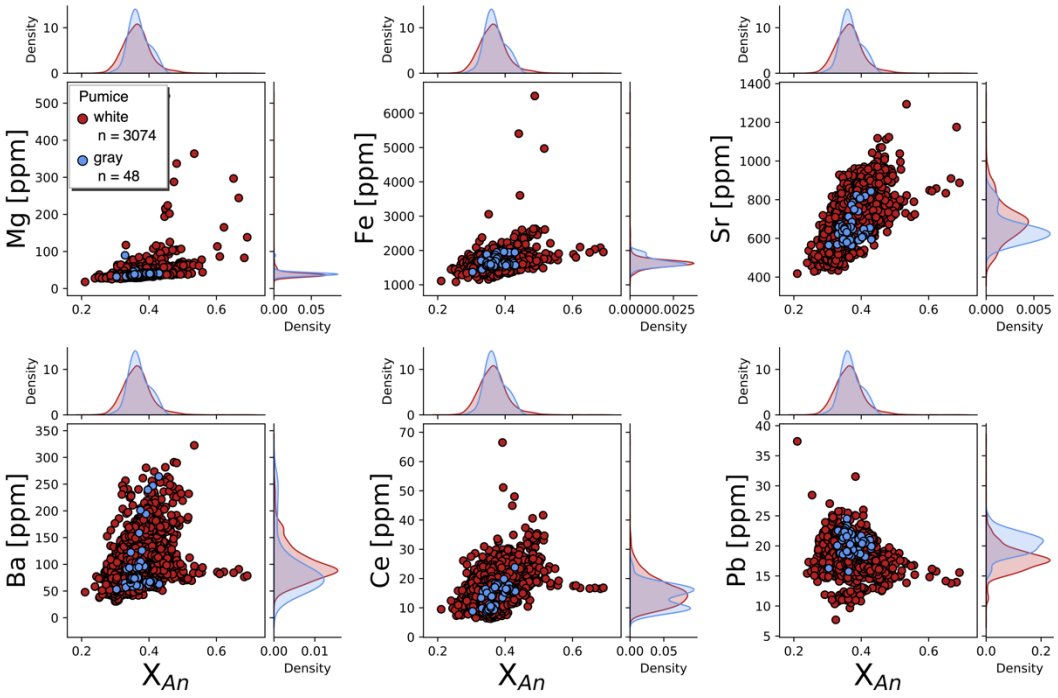

Figure 2.3 : Panel of selected trace elements in CGI plagioclase filtered by what pumice type they are from (i.e., gray or white). Similar to bulk rock pumice data, plagioclase from the CGI overlap in composition for all trace elements measured and show unimodal distributions. Note, however, the elevated Mg concentrations found at An_{60} *and above.*

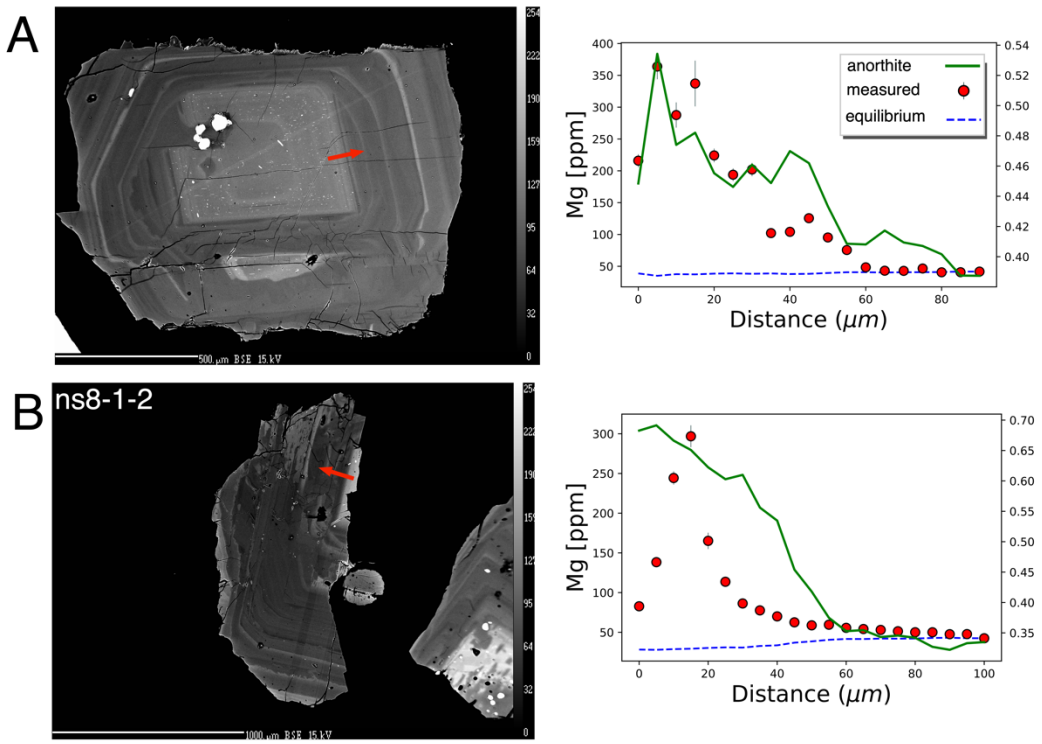

Figure 2.4: Plagioclase from the CGI exhibiting high-An cores. High-An cores in CGI plagioclase also consistently contain significantly higher Mg concentrations (e.g., > 200 µg/g). Some high-An core boundaries have Mg profile that also mimic the shape of the An profile well suggesting little to no diffusive equilibration (A), while others show significant deviation from the shape of the An profile (B).

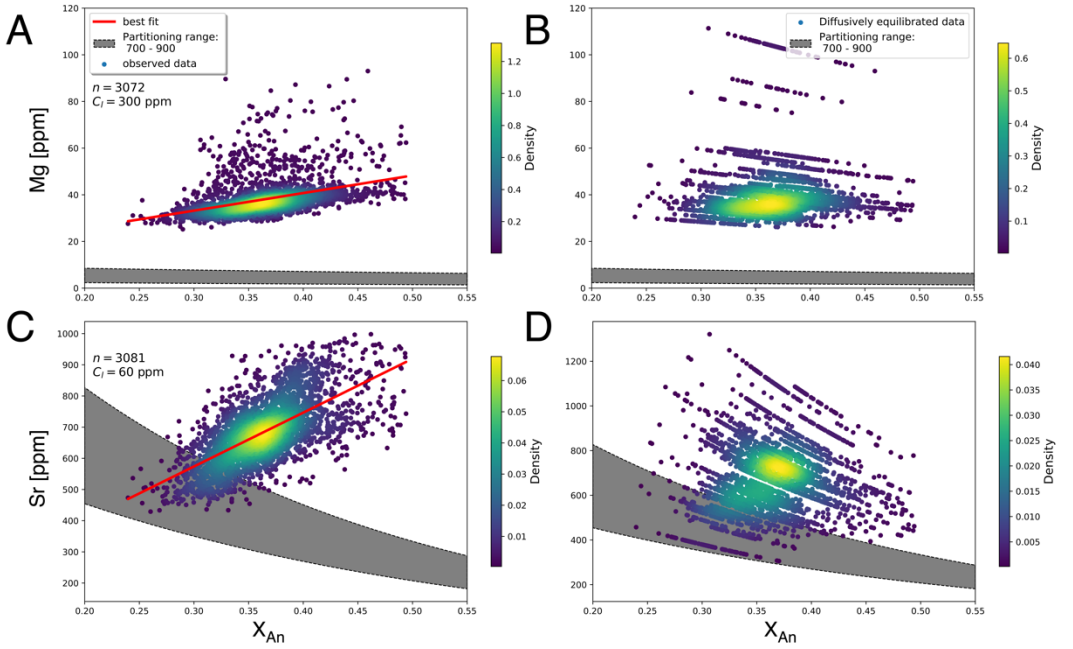

*Figure 2.5: Strontium and Mg vs An in CGI plagioclase in both observed data (A, C) and calculated equilibrated data (B, D). Gray area is the range that would be predicted using Cs = Kd*Cl where Kd is calculated using Equation 1 and observed median glass composition. Based on the observed global positive correlations between Sr and Mg vs. An, CGI plagioclase are not in diffusive equilibration. Note, that even though diffusively equilibrated plagioclase do not fall within the gray region in (B, D), their slope still broadly matches that of the gray region. Gray region location on the charts is ultimately determined by an assumed liquid composition. B and D then suggest that CGI plagioclase have formed in a liquid that is elevated in Sr and Mg relative to erupted glass compositions.*

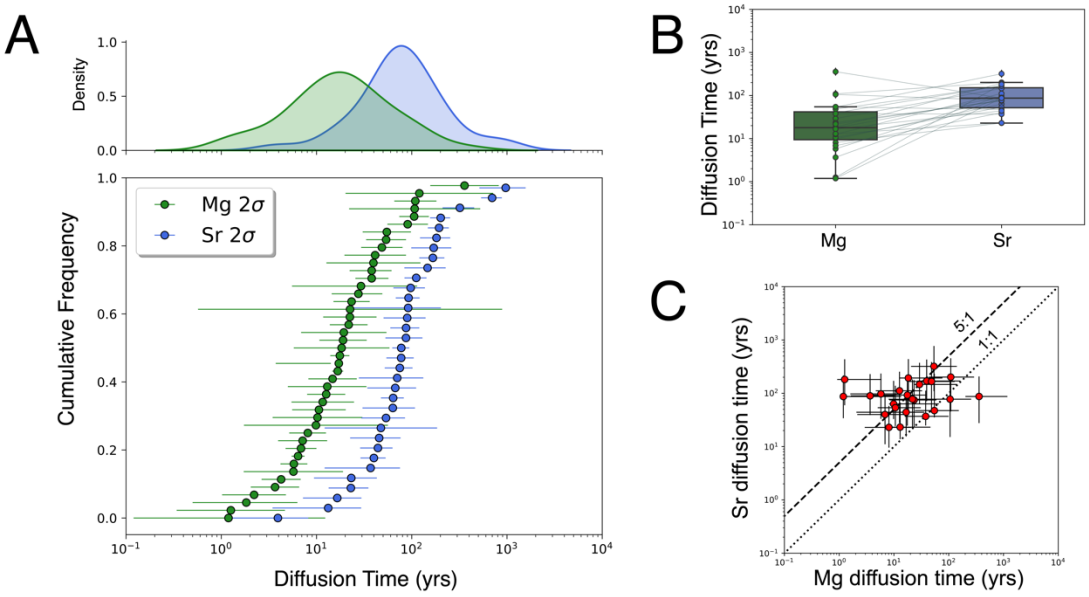

Figure 2.6: (A) Cumulative distribution plot of diffusion modeling for both Sr and Mg in CGI plagioclase. Note there is significant overlap between distributions (top). (B) Box and whisker plots for Sr and Mg diffusion in plagioclase results. Gray lines between points connect diffusion timescales for the same transect. C) Comparing Sr and Mg diffusion results for the same grain. While most of the Sr diffusion times are longer than Mg, there is no systematic relationship between grains (i.e., it is not diffusion coefficient related).

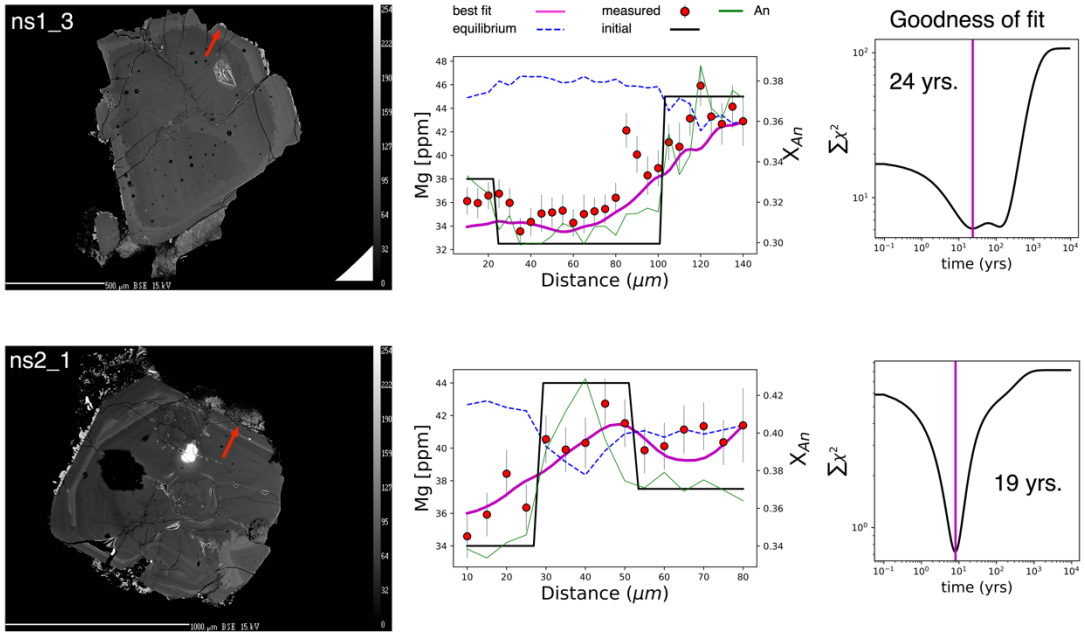

Figure 2.7: Representative plagioclase from the CGI and their corresponding Mg diffusion models. Red arrows on BSE images show the approximate length of the transect. Middle column plots show the observed Mg and An data, the initial boundary conditions for the diffusion model, and the best fit diffusion model (magenta curve). The farthest right column shows the goodness of fit for each diffusion model as time increases. The minimum value is the best fit.

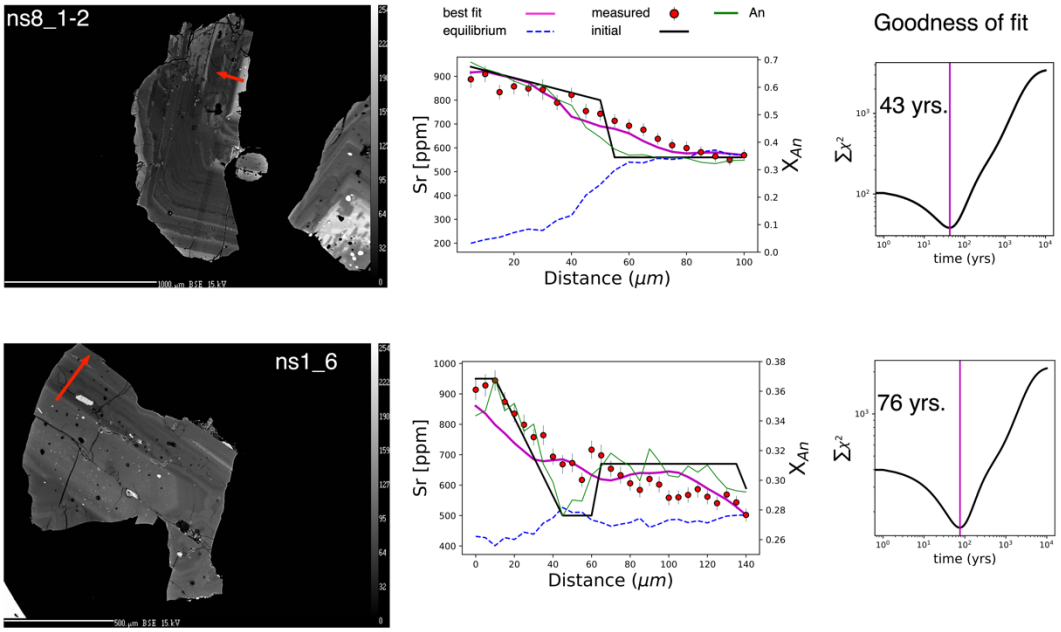

Figure 2.8: Representative plagioclase from the CGI and their corresponding Sr diffusion models. Red arrows on BSE images show the approximate length of the transect. Middle column plots show the observed Mg and An data, the initial boundary conditions for the diffusion model, and the best fit diffusion model (magenta curve). The farthest right column shows the goodness of fit for each diffusion model as time increases. The minimum value is the best fit.

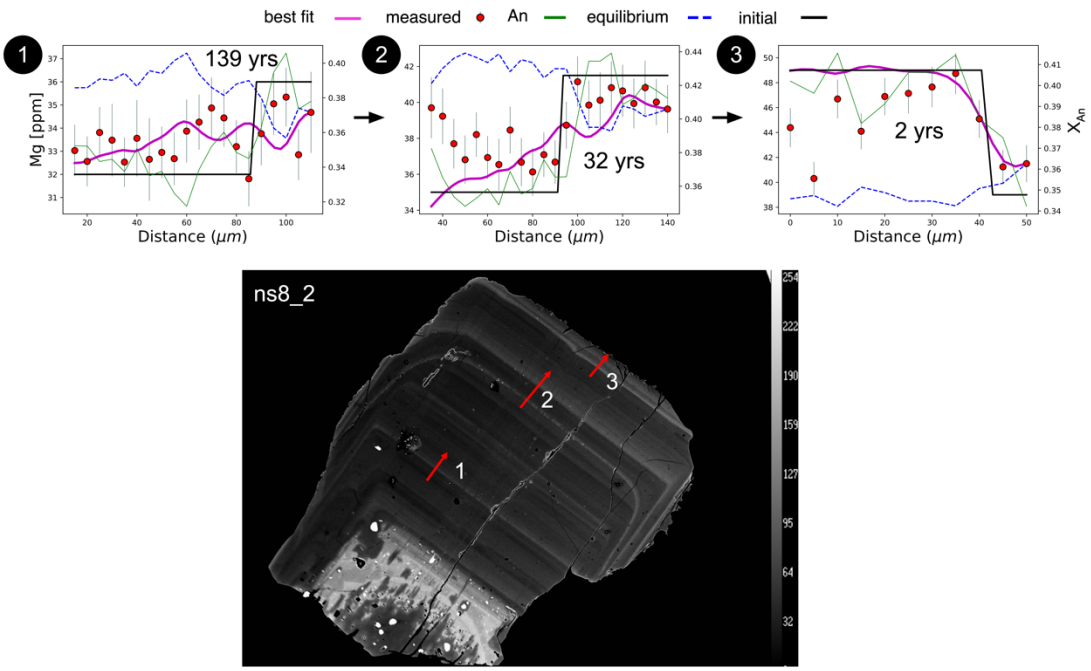

Figure 2.9: Example of grain where multiple LA-ICP-MS transects were measured. From core to rim diffusion model time decreases, which is what would be expected from progressive growth of a mineral during fractionation as the magma cooled.

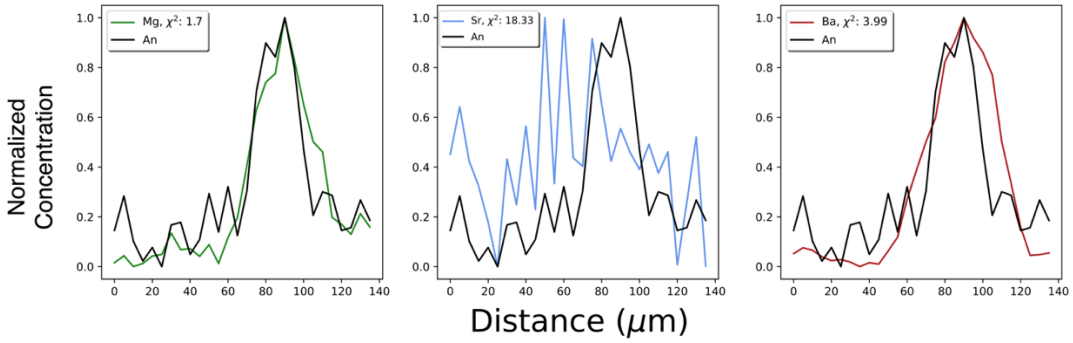

Figure 2.10: Comparing various trace elements to An profiles in plagioclase. For elements that have positive correlations with An, we expect any large deviations from An profile shape to be diffusion related. Example here is from CGI plagioclase 5-8-3 showing how Sr looks more 'diffused' than Mg if we take the An profile to be the initial boundary conditions. The similarity between Mg and Ba suggests that little if any diffusive modification of Mg contents has occurred in this profile at all. However, if only Sr is considered it gives the impression that larger amounts of diffusion have transpired.

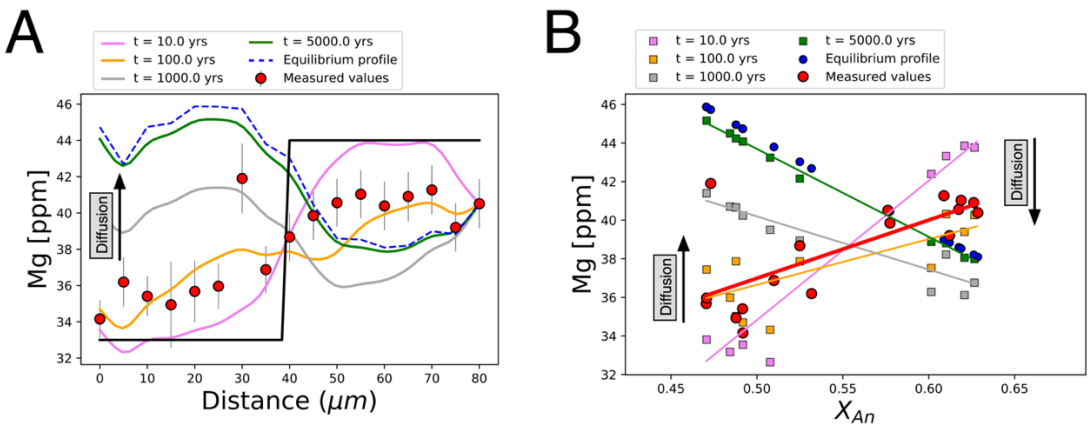

Figure 2.11: Magnesium diffusion model for grain 1-7-1 in both Mg vs distance (A) and Mg vs An (B). Different colored lines (A) and symbols with regression lines (B) indicate different durations of diffusion ranging from initial boundary conditions to equilibrium and illustrate that as Mg profiles near equilibrium (e.g., long durations of time at high temperature), they begin to have a negative correlation with An. As negative correlations are never observed between Mg and An in CGI plagioclase, we take this to mean that 1) initial Mg profiles based off An profiles accurately represent the initial Mg concentration at the time of plagioclase formation (i.e., initial profiles in diffusion models) 2) CGI plagioclase thermal histories are more accurately recorded by Mg diffusion than Sr diffusion 3) CGI plagioclase have not spent long durations of time at or above 750 °C.

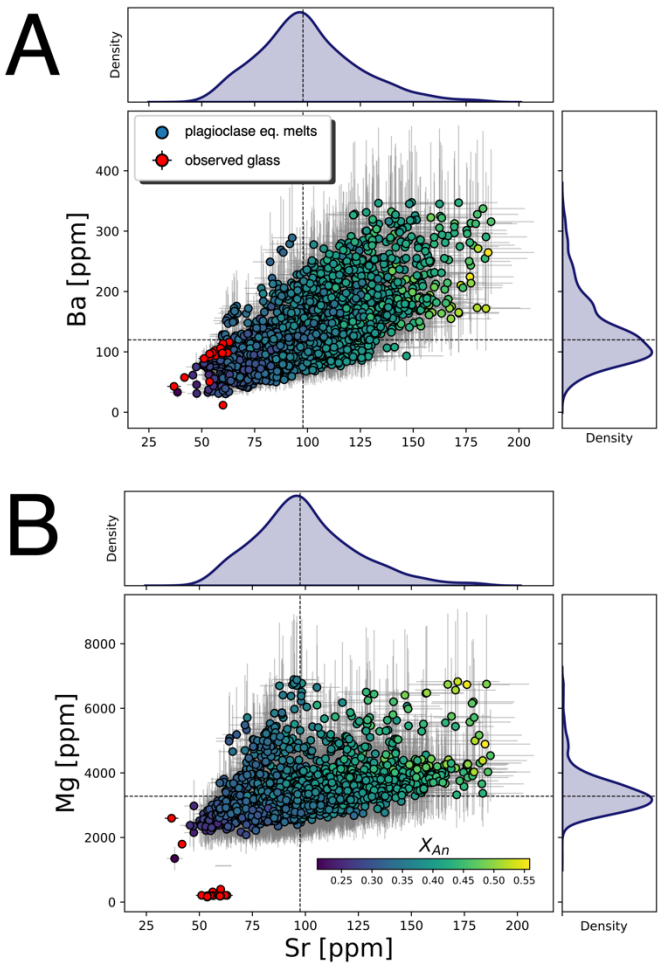

Figure 2.12: Comparing melt compositions in equilibrium with CGI plagioclase (colormapped circles) to observed glass compositions (red circles) for Ba, Sr, and Mg. Equilibrium melt compositions are calculated using Equation 1 for the plagioclase partition coefficient. We can see that the observed glass is much more depleted in Sr (from plag fractionation), Mg (from biotite fractionation), and Ba (from biotite, sanidine, and, to a lesser degree plagioclase, fractionation). The elevated Mg equilibrium liquid comps suggest that much of the plagioclase that we analyzed crystallized (at least partially) before biotite fractionation. As biotite in the CGI are typically greater than a couple of mm and euhedral we interpret this as evidence for plagioclase experiencing extended periods of time in the magma reservoir.

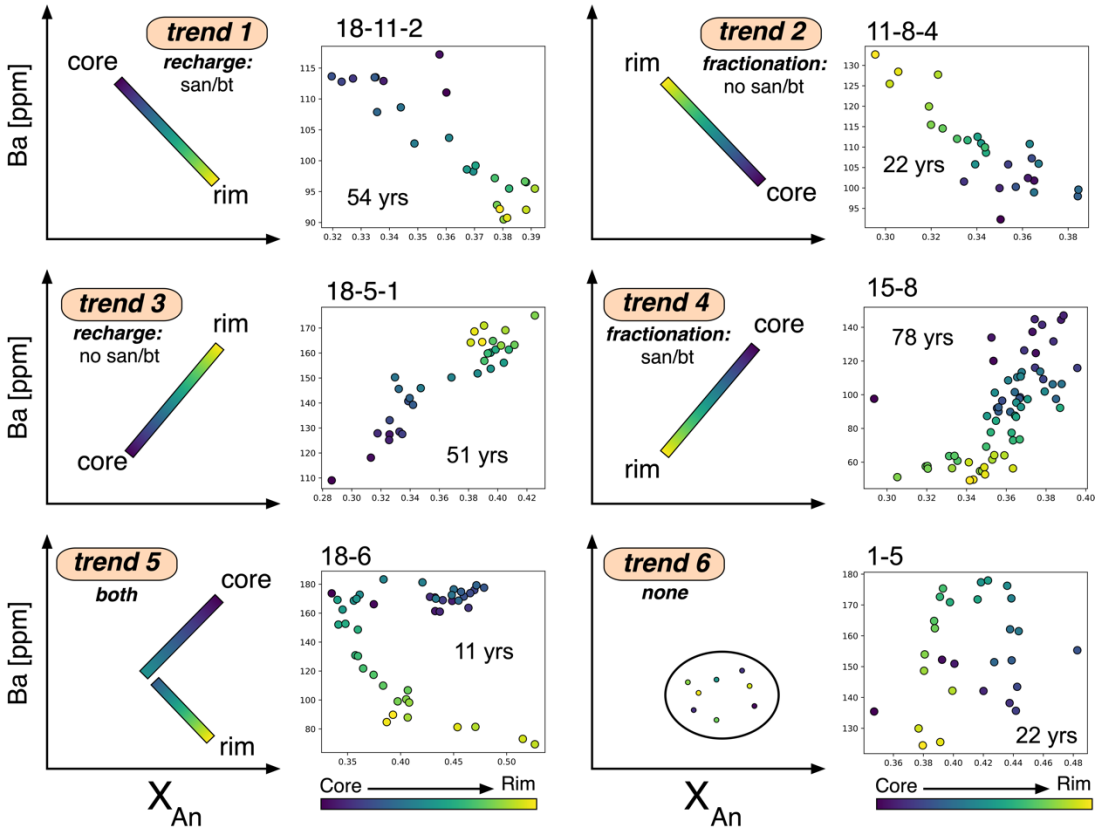

Figure 2.13: Schematic of different Ba – An relationships in CGI plagioclase with observed examples side by side. Magnesium diffusion times are included with observed examples. We can see in this wide array of trends that plagioclase is crystallizing in multiple environments; some with Ba compatible phases (e.g., biotite and sanidine), and some without. Combined with Figure 12, this suggests that while most of the plagioclase equilibrium liquid compositions at the time of transect formation are less evolved (potentially pre biotite), individual grains are experiencing heterogeneous chemical environments where biotite/sanidine are coming in and out of the liquidus.

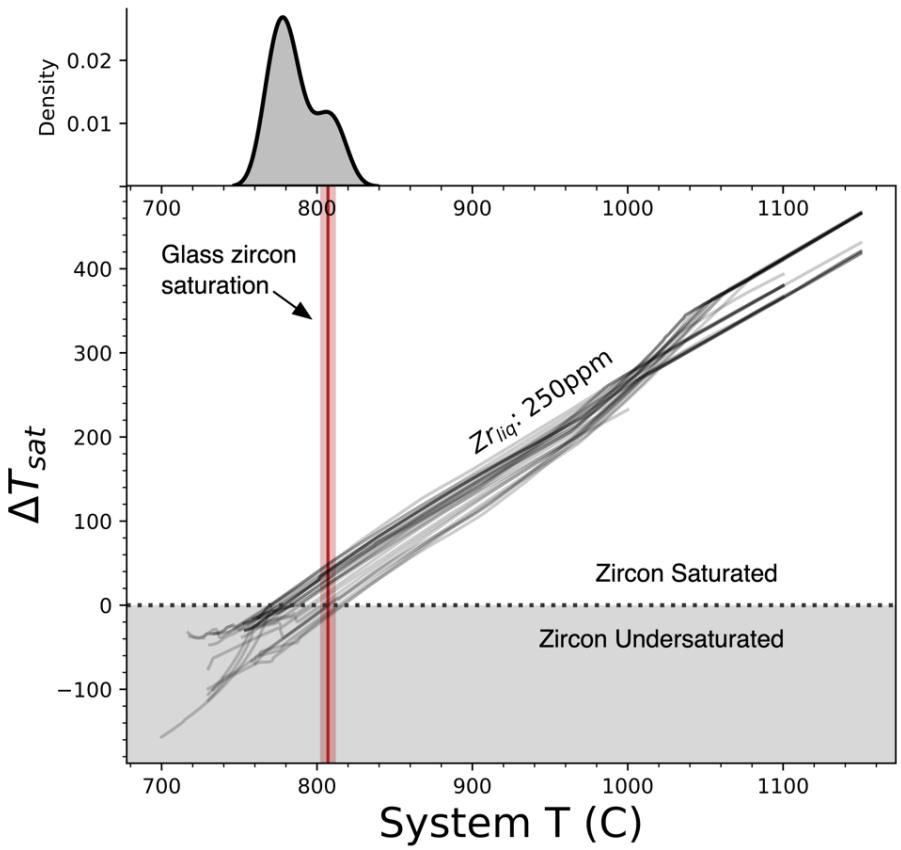

Figure 2.14: Results from MELTS and zircon saturation modeling. For each down temperature step, a given MELTS model's remaining liquid is either zircon undersaturated ($\Delta T_{sat} < 0$) or saturated ($\Delta T_{sat} > 0$), where ΔT_{sat} is the difference between the system temperature and the calculated zircon saturation temperature. MELTS models suggest zircon saturation temperature of the CGI is 787 ± 14 and for our observed glass data this is 807 ± 5. This suggests two things: 1) MELTS models are accurately (within error) portraying zircon saturation temperatures for the CGI magmatic system and 2) zircon saturation in the CGI magmatic system is relatively low temperature.

Table 2.1: Accepted and measured values for plagioclase standard reference material (LABR) used in this study.

Element	Accepted (wt%)	Avg. Measured (wt%)	1 std. dev. (wt%)	RSD (%)
Na	2.56	2.63	0.04	1.50
Si	23.958	23.96	0.15	0.64
Al	16.36	16.26	0.12	0.71
Fe	0.36	0.34	0.01	3.80
Ca	9.748	9.65	0.01	0.11
K	0.15	0.09	0.01	10.78
Mg	0.08	0.08	0.00	3.23
Ti	0.03	0.02	0.00	12.86
O	47.61	46.72	0.14	0.31

CHAPTER THREE: THERMAL HISTORY OF THE TOBA MAGMATIC SYSTEM AND ITS SOURCES: INSIGHT FROM MULTI-PHASE DIFFUSION CHRONOMETRY

Jordan Lubbers
Adam Kent
Shan de Silva

Manuscript in preparation for submission to:
Earth and Planetary Science Letters
Elsevier Inc.

ABSTRACT

Large silicic magma reservoirs are responsible for producing the largest explosive eruptions in the geologic record. Petrologic data provide evidence for these systems spending significant periods of time (10^3-10^5 yrs) within the upper crust prior to eruption, however their long-term thermochemical evolution is not fully understood, as existing petrologic data make it challenging to quantify a time interval a magmatic system has spent at certain temperatures, or its thermal history. Here we investigate the 74 ka, Youngest Toba Tuff (YTT), one of the largest explosive eruptions in the geologic record, to better constrain the long-term thermal evolution of magmatic systems capable of producing the world's largest explosive volcanic eruptions. We combine diffusion of Sr and Mg in plagioclase, diffusion of Sr in hornblende, mineral thermometry, and trace element evolution models to quantify the thermochemical evolution of the YTT magmatic system. We find that plagioclase records decades of storage at temperatures (~750°C) capable of producing and storing large volumes of eruptible magma, while xenocrystic hornblende records up to 2000 years at the same temperatures. Hornblende crystallizes at temperatures around 800°C and adjusting our diffusion results to this temperature results in no more than 400 years at initial crystallization temperatures. Trace element modeling shows that the large diversity of pumice glass compositions observed from YTT samples can be explained by fractionation of discrete melt bodies that have compositions reflecting influence from local country rock and previous eruptions. Together these results suggest that although there was extreme chemical diversity for long durations in the YTT magma system sufficient to produce unique composition eruptive products, the entire system was experiencing a relatively similar thermal history that did not allow for large bodies of eruptible magma to be present for much of the system's history. Rather, we suggest the YTT experienced dominantly uneruptible conditions and was only remobilized in the decades prior to eruption.

INTRODUCTION

Silicic magmatic activity plays an important role in the differentiation of continental crust, the rates at which it evolves, and is the primary cause of explosive volcanic activity (e.g., Dingwell, 1998; Petford et al., 2000; Rudnick and Fountain, 1995; Taylor and McLennan, 1995). Existing data shows that silicic magmas may spend significant periods of time (10^3-10^5) in the crust prior to eruption (e.g., Claiborne et al., 2010; Reid and Vazquez, 2017). Thus, the thermochemical conditions (i.e., P-T-X, fO_2) within the reservoirs that store silicic magma prior to eruption, have been of great interest to the petrology community in recent years, and a wide

array of techniques have been used to constrain these, including: diffusion chronometry (e.g., Bradshaw, 2017; Cooper and Kent, 2014; Druitt et al., 2012; Shamloo and Till, 2019), numerical modeling (e.g., Annen et al., 2015; Karakas et al., 2017), and radiometric dating combined with geochemical modeling (e.g., Andersen et al., 2017; Barboni et al., 2016; Szymanowski et al., 2017; Tierney et al., 2019; Wotzlaw et al., 2013).

Despite this progress, important questions remain, specifically with regards to what the dominant thermochemical conditions (i.e., "thermal state") of a given magma reservoir is throughout its lifetime. This has colloquially become known as either "cold" (i.e., near solidus; Cooper and Kent, 2014) or "warm" (i.e., large proportions of melt present; Barboni et al., 2016) storage of magmas, but can ultimately be thought of as constraining the overall thermal budget for a given magma and magmatic system into which everything the it experiences (e.g., recharge, crystallization, storage, growth, etc.) must fit (Lubbers et al., 2021 *in prep*). These are the processes that build crustal magma systems (e.g., Annen et al., 2006; Cashman et al., 2017). It is also likely that for a single magmatic system – particularly those capable of producing large eruptions – there may be portions of a single reservoir that experience quite different thermal histories than others (Andersen et al., 2017; Szymanowski et al., 2017). Thus, understanding the thermal history experienced by different magmatic components within one system and coupling that with other petrological information (e.g., compositional and thermobarometric information), has great potential for constraining the processes that control the development and evolution of crustal magma systems, a major goal of petrological research. Moreover, understanding the thermal state of magma storage has important implications for the behavior of volcanic systems, and for the hazards that they can produce. For example, recently it has been shown that magma reservoirs, under the right conditions, can undergo a series of thermomechanical feedbacks that help promote growth rather than eruption (de Silva and Gregg, 2014) and that can ultimately lead to very large eruptions, further demonstrating the importance of understanding the thermal state of the system if frequency, timing, and magnitude of future volcanic eruptions are to be fully understood.

To explore the thermal state of magma storage in one of the largest known eruptions in history (and one of the Earth's most recent "super-eruptions"; Mason et al., 2004; Wilson et al., 2021), herein we use a combination of diffusion chronometry, mineral thermometry, and glass trace element chemistry to constrain the thermal budget and long-term thermochemical evolution of the 74 ka Youngest Toba Tuff (YTT). This research shows that use of these tools, when combined, can provide important constraints on the evolution of magmatic systems capable of producing the largest explosive volcanic eruptions.

Geologic Background

Toba caldera (Figure 3.1) is located in northern Sumatra, Indonesia in the Barisan Mountains and is responsible for four caldera forming eruptions in the last 1.2 Ma (Chesner and Rose, 1991). The 74 ka Youngest Toba Tuff (YTT) is the most recent caldera activity at Toba and produced 2800km^3 (Rose and Chesner, 1987) of high-K magma ranging in composition from 68-77 wt% SiO_2 (Chesner, 1998). The YTT is crystal rich (up to 40%) and contains a mineral assemblage of quartz + plagioclase + sanidine + biotite + amphibole + orthopyroxene + magnetite + allanite + zircon + ilmenite. General characteristics of the YTT as SiO_2 increases are (Chesner, 1998): 1) crystallinity decreases; 2) sanidine abundance increases; 3) the biotite to amphibole ratio increases drastically; 4) orthopyroxene decreases to where it is non-existent at higher SiO_2 contents. Zircon ages for the YTT show that the magma reservoir underwent a 200 ka period of growth prior to eruption (Reid and Vazquez, 2017). Chesner (1998) suggest that this allowed sufficient time for a zoned magma reservoir to form via crystal fractionation and is also supported by observations that mineral and whole rock geochemical variations form a continuous array. Geographic distribution of the YTT shows that much of the outflow is high SiO_2, while intracaldera tuff is low SiO_2 (Chesner, 2012). Chesner (1998) used a combination of Fe-Ti oxide thermometry and amphibole barometry to determine that YTT magmas crystallized between 701-780°C at a pressures of ~3 kbar, although the experimental study of Gardner et al., (2002) found that amphibole is not a stable phase in in Toba magmas, implying that it is xenocrystic in origin. Furthermore, dating of YTT amphiboles indicates that they were included into YTT magmas from rocks as old as 1.5 Ma (Gardner et al., 2002). Chesner and Luhr (2010) used quartz hosted melt inclusions to show that YTT magmas contained 4.0 – 5.5 wt% H_2O and formed at shallower pressures of 1 – 1.5 kbar, while Jaxybulatov et al., (2014) use seismic tomography beneath Toba caldera to suggest a fine-scale layering of partially molten sills at depths below 7km. When combined with other petrologic data (e.g., bulk rock and glass chemistry, phase abundances, etc.), these data indicate that the YTT magmatic system was chemically and thermally zoned. Diverse late-stage geochemical environments are also recorded in discrete glass populations (Pearce et al., 2020), and zircon surface chemistry (Tierney et al., 2019) ,and suggest that the YTT magmatic system consists of multiple reservoirs staged at similar depths.

METHODS

Samples

Three pumice samples were utilized in this study: 1) LT_001: pumice from nonwelded ignimbrite north of the caldera; 2) LT_012: pumice from nonwelded ignimbrite east of the

caldera; 3) MQ: both nonwelded and banded pumice from ignimbrite found at Merek Quarry. All nonwelded pumice display the same textural characteristics, however the banded pumice contains both light and dark pumice, is less porous, and contains fewer crystals than nonwelded pumice. Sampling and mineral separation methods for samples can be found in Mucek et al., (2017). Approximate locations for each sample can be found in Table 3.1.

EPMA

Backscattered electron (BSE) images and major element (Si, Ti, Al, Fe, Mg, Na, Ca, K) spot analyses for plagioclase, amphibole, and amphibole mineral inclusions were conducted using a Cameca SX100 electron probe microanalyzer (EPMA) at Oregon State University. For all analyses, a focused beam of 5μm, 15 kV accelerating voltage and 30 nA current were used. Uncertainties for each element measured can be found in the online Supplementary Data and are typically < 1-2% for major (i.e., > 1 wt%) elements.

LA-ICP-MS

Trace element analyses of pumice glass, plagioclase and amphibole were conducted using a Photon Machines Analyte G2193 ArF Excimer laser system connected to a ThermoFisher Scientific iCAP-RQ ICP-MS at the Oregon State University W.M. Keck Collaboratory for Plasma Spectrometry. Analyses used the following isotopes: plagioclase - ^{7}Li, ^{24}Mg, ^{27}Al, ^{29}Si, ^{43}Ca, ^{48}Ti, ^{57}Fe, ^{88}Sr, ^{138}Ba, ^{139}La, ^{140}Ce, ^{153}Eu, ^{208}Pb; and amphibole - ^{7}Li, ^{43}Ca, ^{51}V, ^{59}Co, ^{85}Rb, ^{86}Sr, ^{88}Sr, ^{89}Y, ^{90}Zr, ^{93}Nb, ^{133}Cs, ^{13}7Ba, ^{139}La, ^{140}Ce, ^{141}Pr, ^{146}Nd, ^{147}Sm, ^{153}Eu, ^{157}Gd, ^{163}Dy, ^{166}Er, ^{172}Yb; pumice glass - ^{24}Mg, ^{43}C, ^{48}Ti, ^{59}Co, ^{85}Rb, ^{88}Sr, ^{89}Y, ^{90}Zr, ^{93}Nb, ^{137}Ba, ^{139}La, ^{140}Ce, ^{141}Pr, ^{146}Nd, ^{147}Sm, ^{153}Eu, ^{157}Gd, ^{163}Dy, ^{166}Er, ^{172}Yb, ^{178}Hf, ^{208}Pb, ^{232}Th, ^{238}U. Analyses of plagioclase and amphibole were conducted two ways: 1) as a line of spots with dimensions 5 by 50 μm with 5 μm between spot centers, pulse rate of 15 Hz, laser energy of 8.16 J·cm^{-2}, and analysis time of 10 seconds per spot, 2) individual spots with dimensions 30 by 30 μm, pulse rate of 15 Hz, laser energy of 8.16 J·cm^{-2}, and analysis time of 30 seconds per spot. The line of spots approach was used to produce the high-resolution trace element profiles used as the basis for diffusion modeling, as it allows for high spatial resolution to be maintained in the direction of the transect, while still allowing for higher count rates to improve precision. Trace element analyses of pumice glass, plagioclase and amphibole were conducted using 30 μm diameter circular spots, a pulse rate of 7 Hz, laser energy of 6.42 J·cm^{-2}, and analysis time of 30 seconds per spot. A total of 45 plagioclase transects, 174 plagioclase spots, 22 amphibole transects, 105 amphibole spots, and 270 pumice glass spots were measured in this study.

Elemental concentrations were calculated from analytes using the methodology of Kent and Ungerer, (2006) and Longerich et al., (1996). Anorthite contents of plagioclase were

calculated using measured Ca/Si ratios similar to the method of (Kent et al., 2008). BCR-2G was used as the calibration standard and was analyzed every 5 profiles or 10 spot analyses (i.e., ~15 minutes) along with ATHO-G to monitor for drift in the mass spectrometer. BCR-2G, ATHO-G, NIST-612, and BHVO-2G were run as standard blocks at the beginning, middle, and end of each experiment. Their concentrations and uncertainties can be found in the Supplementary Data. Analyses suggest precision for trace elements measurements in all materials are < 5% except for heavy rare earths, Co, and V in glass analyses.

Diffusion Chronometry

We model Sr and Mg diffusion in plagioclase using a forward model that applies the finite difference method outlined in Appendix 1 of Costa et al., (2008) adapted to Equation 7 from Costa et al., (2003). Diffusion coefficients for Sr and Mg were taken from Giletti and Casserly (1994) and Van Orman et al., (2014), respectively. Trace element partitioning in plagioclase was calculated from Nielsen et al., (2017). The choice of specific partitioning model in this regard is less important, as both Nielsen et al., (2017) and Bindeman et al., (1998) partition models produce results that are within uncertainty of one another for intermediate An values (Lubbers et al., 2021 *in prep*). Other ways to calculate partition coefficients in plagioclase (e.g., Dohmen and Blundy, 2014) also produce similar results to Nielsen et al. (2017), but require explicit knowledge of the melt composition, and are therefore not used here. Diffusion modeling and estimates of associated uncertainties using a Monte Carlo approach follow the method of Lubbers et al., (2021 *in prep*).

Strontium diffusion modeling in hornblende was completed using a forward model applying the finite difference method to Fick's 2nd Law (e.g., Equation A1 from Costa et al., 2008). While there is an analytical solution to Fick's 2nd Law in which the diffusion coefficient is constant (e.g., Crank, 1975), employing the finite difference method ultimately allows for more freedom in choosing model boundary conditions (i.e., initial profiles that are not step functions or profiles that have multiple steps) and is the preferred method in this study. The diffusion coefficient for Sr in hornblende was taken from (Brabander and Giletti, 1995) and has been shown to be isotropic with no compositional dependence on diffusivity within the uncertainty of the Arrhenius relation (e.g., activation energy, pre-exponential factor) parameters, negating the need to incorporate diffusion coefficient corrections for crystallographic axis. Initial boundary conditions for diffusion models were chosen by comparing the shape of Sr profiles with profiles of slower diffusing elements (i.e., Zr, REEs), as these elements are assumed to have not diffused appreciably since that part of the grain has formed. When this was not possible, it was assumed that initial Sr profiles took the shape of an

either one- or two-sided step function. We also evaluated the uncertainties associated with the selection of initial geometry.

The rate at which diffusion occurs is strongly dependent on temperature. As such, temperature is a critically important input in all diffusion models. For long term magma storage conditions, the temperature is not clear, and is unlikely to be isothermal. Thus to relate calculated diffusion timescales we calculate to a useful temperature we follow the approach Cooper and Kent (2014) and Bradshaw (2017) whereby we use Rhyolite-MELTS modeling to estimate the temperature at which silicic magma systems reach 40-60%. At this temperature the increasing crystallinity and concomitant increase in viscosity results in a magma that is now at values near the magma extrusion limit between 10^6-10^8 Pa·s (Scaillet et al., 1998a; Takeuchi, 2011). Bradshaw (2017) modelled the change in crystallinity of a number of large silicic eruptions and found that this transition occurred at ~750°C, and this is also consistent with experimental studies on the Fish Canyon Tuff (Caricchi and Blundy, 2015). This suggests that at temperatures cooler than 750°C, large silicic magmatic systems are at rheological conditions such that they are not mobile and cannot be erupted. Thus, using a temperature of 750°C for our diffusion models provides an estimate of the maximum duration at which the YTT magmatic system spent at temperatures capable of producing large volumes of eruptible melt. We note that we are not sensitive to the use of 40-60% crystals as the crystallinity at which rheological lockup occurs during this stage of the crystallization sequence increases in crystallinity very rapidly with little or no temperature change.

RESULTS

Plagioclase

Plagioclase from YTT pumice range in composition from An_{27} to An_{58}, with most analyses being between An_{32} and An_{42} (Figure 3.2). Strontium, magnesium, and iron show positive correlations with An and fall along an array (Figure 3.2), consistent with trace element trends in plagioclase from other large silicic magma systems (Bradshaw, 2017, Lubbers et al., 2021 *in prep*). There is no significant difference in composition between samples for major elements and most trace elements, with the one exception being Ba. Barium for sample LT001 displays a positive correlation with An similar to Sr, Mg, and Fe, however in sample MQ we see two populations of data: one around An_{32} that overlaps with sample LT001; one at compositions > An_{35} that shows a negative correlation with An. Plagioclase inclusions found in amphibole range between An_{40} and An_{50} and overlap in trace element composition with phenocrysts of similar An content from both samples.

Amphibole

Amphibole from the YTT are calcic and can broadly be classified as magnesiohornblendes using the criteria of Leake et al., (1997). This is different from the ferro-edenitic hornblende classification of Chesner (1998), however we justify this based on three pieces of evidence: 1) all amphibole analyses have Ca B-site values > 1.50; 2) 97% of amphibole analyses have alkali A-site values < 0.5; 3) 94% of amphibole analyses have an Mg# ($Mg/[Mg+Fe^{2+}]$) > 0.5. They contain inclusions of plagioclase, pyroxene, apatite, and Fe-Ti oxides. Areas of amphibole with higher proportions of inclusions also contain abundant sieve textures and are commonly found near the rims of the grain. Despite major element analyses showing little variation, using trace elements amphibole analyses from the YTT can further be separated into two groups: 1) high Sr (>80 ppm) – low (<150 ppm) Y; 2) low Sr – high Y (Figure 3.3). While there are amphiboles from banded and normal pumice in both groups, the high Sr – low Y group is predominantly comprised of amphibole from banded pumice. These analyses also display a negative correlation between Sr and Zr (Figure 3.3), whereas the low Sr – high Y group displays a positive correlation.

Glass chemistry

Glass trace element compositions from YTT pumice span a wide range of compositions between samples and correspond to discrete populations identified in YTT tephra from Pearce et al., (2020), hereafter referred to as "Pearce groups (PG)" (Figure 3.4). Sample LT_012 corresponds most to PG1, sample LT_001 corresponds most to PG3 with small amounts belonging to PG1-2, and sample MQ most resembles PG4-5 (Figure 3.4).

DISCUSSION

Diffusion of Sr and Mg in plagioclase

Modelling diffusive equilibration of trace elements within volcanic minerals has been shown to be a useful tool at constraining the rates of volcanic processes (e.g., Costa et al., 2020 and references therein). This study models Sr and Mg diffusion in plagioclase as well as Sr diffusion in hornblende to constrain the amount of time a given grain, or portion of a grain, has experienced at or above a given temperature. As both plagioclase and hornblende have different proposed origins in the Toba magmatic system (Gardner et al., 2002), utilizing both phases for diffusion chronometry offers the possibility of quantifying the thermal evolution of the magmatic system from multiple viewpoints.

In addition, relatively few diffusion studies compare timescales from multiple phases for the same system, and even fewer utilize diffusion in hornblende, making this approach novel. Furthermore, as the hornblende have already been dated (e.g., ~1.5Ma) and their

duration in the YTT magma calculated to be decades prior to eruption using diffusive radiogenic Ar loss (Gardner et al., 2002), we have important context for interpreting hornblende diffusion times. Conversely, while not directly dated, it has been shown that context for plagioclase diffusion times can be gathered from their inferred equilibrium liquid compositions at the time of formation coupled with spatial variations in certain trace elements (e.g., Ba), allowing for their position on the liquid line of descent to be determined (Lubbers et al., 2021 *in prep*). Combining diffusion results from these two phases, then, allows us to not only make interpretations about the YTT magmatic system, but also the system responsible for introducing amphibole into the YTT magma system, furthering our understanding of the transcrustal magma system beneath Toba caldera.

Results from all diffusion models can be found in Figure 3.5. Magnesium in plagioclase diffusion models were completed for 30 profiles and best fit diffusion times range from 1.34 to 953 years, with 95% of times recording less than 325 years residence at 750°C. Strontium in plagioclase diffusion models were completed for 30 profiles and range in duration from less than 4.4 years 1148 years, with 95% of times recording less than 174 years. Furthermore, we find that Sr and Mg diffusion in plagioclase models produce statistically identical distributions (Table 3.2). Based on analytical resolution and diffusion coefficient we determined one Sr profile to have a best fit time that was below the lower limit (4.4 years) that is resolvable using the relationship described in Bradshaw and Kent (2017), making diffusion unquantifiable.

We also found one profile that appeared to match the calculated equilibrium profile (Figure 3.6A), making a best fit profile indistinguishable (i.e., once it has reached equilibrium, it is not possible to quantify how long the profile has spent there as increases in model time do not result in significant changes of the model profile). This suggests it is either fully equilibrated from spending an extended period at > 750°C or formed an initial Sr distribution that was close to equilibrium, making our diffusion model assumptions about initial Sr distributions invalid and overestimated. In this instance we use the Mg diffusion model to help reconcile between the two scenarios, as it diffuses ~5-7 times faster than Sr in plagioclase (Giletti and Casserly, 1994; Van Orman et al., 2014) and if it has spent long durations at > 750°C, it would also have a profile that closely resembled equilibrium. We find, however, the corresponding Mg diffusion model records short times at > 750°C (Figure 3.6B), suggesting that the Sr diffusion model in this case is misleading. While it is possible to increase Mg diffusion model times by adjusting initial diffusion model boundary conditions (i.e., the black line in Figure 3.6B), it still progresses towards equilibrium in < 1000 years and, when coupled

with the observation that it is still "far" away from the equilibrium profile, makes it unlikely that this grain has experienced extended durations at > 750°C.

Diffusivity of trace elements in minerals is a strong function of temperature and our diffusion modeling estimates the maximum length of time that a given grain, or portion of a grain, spent at or above the specified temperature (e.g., Costa et al., 2020, 2008). Herein we model diffusion at 750°C, as a way to estimate the maximum duration that the crystal (or portion of a crystal) spent at temperatures where the crystallinity of the magma was sufficiently low that the magma was eruptible (Bradshaw, 2017). In silicic and intermediate magmas 750°C approximates the temperature where there is a rapid increase in crystallinity (above 40-60%) as magmas cool. Combined with the increasing SiO_2 of remaining melt, magma viscosity drastically increases with small increases in temperature. Together, these changes reflect an overall magma viscosity that reaches or exceeds the magma extrusion limit of 10^6 – 10^8 Pa·s (Scaillet et al., 1998a; Takeuchi, 2011). This temperature, then, approximates the point whereby the erupted magma goes from being in a rheologically mobile state to one that is not mobile and therefore uneruptible. This ultimately allows us to use the results from our diffusion modeling to quantify the amount of time a given grain (or portion of grain) has spent at temperatures that kept magma viscosity low enough to be erupted. From our results we conclude that YTT plagioclase reveal the magmas erupted for the YTT could not have existed at temperatures greater than 750°C for more than 10^3 years (and probably significantly less) during magma storage and the lead up to eruption (Figure 3.5). Magnesium and Sr in plagioclase give similar best fit diffusion times within two-sigma uncertainty for each grain analyzed (Table 3.2), thus, we have a high degree of confidence in diffusion model timescales being accurate (Figure 3.7).

We also infer, based on the mineral assemblage present and the large size of crystals in the YTT (e.g., Barbee et al., 2020), that it is extremely likely the magmatic system spent some duration of time at eutectic conditions prior to eruption (e.g., quartz + plag + sanidine). By adjusting the temperature of our diffusion modeling to eutectoid temperatures (e.g., 660 – 680°C), diffusion results also allow us to speculate on the duration that YTT plagioclase existed at or above eutectoid conditions. While it is possible to reactivate sub-solidus plutons, it is costly with respect to both energy (Dufek and Bergantz, 2005) and volatiles (Caricchi and Blundy, 2015), as they are lost to the surrounding country rock when the reservoir completely crystallizes. This necessitates a large degree of heat to be re-added to the system such that compensates for the sensible and latent heat loss that occurred during solidification (Bachmann and Huber, 2016). We argue that this makes it unlikely that YTT plagioclase existed within a

magma reservoir that was at predominantly subsolidus temperatures prior to eruption, therefore making diffusion models at solidus temperatures a proxy for the longest possible amount of time a given plagioclase (or portion of that plagioclase) has spent in the YTT reservoir prior to eruption. Our results suggest that YTT plagioclase could not have spent more than ~10^4 years at eutectoid conditions (Figure 3.8). Combining the results from Figure 3.5 and Figure 3.8A, we calculate a relative duration (i.e., 750°C diffusion time divided by solidus diffusion time) of a given grain's overall history at or above 750°C. We conclude that YTT plagioclase spent < 5% of their time at temperatures responsible for producing and storing large volumes of eruptible magma.

Amphibole thermometry

Amphibole from the YTT, originally thought to be phenocrysts (Chesner, 1998), have since been shown to be xenocrysts as old as 1.5 Ma only incorporated into the YTT magma system decades prior to eruption (Gardner et al., 2002). We utilized the Python package ThermoBar (https://github.com/PennyWieser/Thermobar) to conduct amphibole only thermometry (Putirka, 2016; Eqs. 5, 6, 8) and plagioclase – amphibole thermometry (Holland and Blundy, 1994; Thermometer B), to establish the temperature that not only YTT amphiboles, but also plagioclase inclusions within the amphiboles, formed at. Thermometers were chosen to include a spectrum of thermometer types: amphibole only that is pressure independent (Putirka 2016 Eq. 5); amphibole only that is pressure dependent (Putirka 2016 Eq. 6, 8); and amphibole – plagioclase (Holland and Blundy, 1994) which utilizes multiple phases rather than just relying on amphibole compositions alone. Thermometer B from Holland and Blundy (1994) was chosen over thermometer A, as A requires amphibole and plagioclase to be co-crystallizing with quartz which we do not have definitive evidence for. Holland and Blundy (1994) found that, when applied to amphibole – plagioclase pairs that did not co-crystallize with quartz, Thermometer A produced systematic temperature overestimates (e.g., Bachmann and Dungan, 2002).

Amphibole only thermometry produces a mean temperatures near 800 degrees, while amphibole – plagioclase thermometry produces a slightly higher mean temperature of 845 degrees (Figure 3.9), however both overlap within 1 sigma error of both thermometers (Holland and Blundy, 1994; Putirka, 2016). We find that there is a positive correlation between Mg # and crystallization temperature amongst YTT amphiboles (Figure 3.10), which is also noticed in other large silicic systems (e.g., Bachmann and Dungan, 2002). Using the amphibole groups listed above, we also find that the low Y – high Sr record both lower Mg # and crystallization temperature than high Y – low Sr amphibole compositions (Figure 3.10B). Furthermore, we

use Equation 10 from Putirka (2016) to calculate the SiO_2 content of the melt that YTT amphiboles crystallized from and compare it to the erupted SiO_2 content of the YTT pumice glass. Calculated SiO_2 contents have a mean value of 70.4 and 71 wt% ± 3 wt% for amphibole-only and amphibole – plagioclase thermometers, respectively. Quartz hosted melt inclusion compositions and volatile contents from all Toba Tuffs (i.e., Oldest, Middle, Youngest) display SiO_2 contents of 74 - 77 wt% and crystallization pressures of 1-1.5kbar (Chesner and Luhr, 2010), implying that YTT amphibole and some plagioclase are not only xenocrystic (i.e., Gardner et al., 2002), but also are crystallizing over a range of P-T-X conditions that are not as evolved and hotter than the Toba Tuffs.

Diffusion of Sr in Amphibole

Strontium in amphibole diffusion models were completed for 12 profiles and record best fit times between 222 and 2000 years at 750°C, with 95% of model times being less than 1906 years. These times are roughly an order of magnitude longer than plagioclase (Figure 3.5). This, however, is unsurprising as YTT amphibole are most likely: 1) xenocrystic (This study; Gardner et al., 2002) and therefore older than the majority of YTT plagioclase; 2) crystallized at a higher temperature than most of the YTT plagioclase (This study; Chesner, 1998). Regardless, we find that YTT amphibole record no longer than 2000 years at temperatures greater than 750°C. A shift to 800°C (i.e., a representative temperature for YTT amphibole formation; Figure 3.9) for diffusion models moves this to no longer than 400 years and suggests that although YTT amphibole formed at temperatures > 800°C (Figure 3.9), they spent relatively little time in their 1.5 Ma history at the temperature they were initially crystallized, but instead spent prolonged periods of storage at much lower, and potentially even subsolidus, temperatures.

Compositionally heterogeneous but thermally homogenous sources

Chesner (1998) initially proposed that the YTT and the compositionally zoned magma reservoir that produced it was the result of 27 – 53 % crystal fractionation of the phases observed in its least silicic pumice samples. Modelling allanite fractionation, Vazquez and Reid (2004) similarly showed that YTT allanites record long storage times (> 150,000 years) and up to 45% crystal fractionation of a plagioclase-sanidine-biotite-quartz assemblage as described in Chesner (1998). They concluded that, as the Toba magmatic system grew, mixing became less efficient and diverse crystallization conditions developed resulting in localized areas within the reservoir that were fractionated to different degrees. Pearce et al., (2020), noted the wide variety of glass compositions observed in the YTT and recognized five distinct populations. In combination with glass barometry, Pearce et al. (2020) hypothesized that the

magma system responsible for the eruption of the YTT was not actually one reservoir, but 5 discrete reservoirs at similar depths within the crust that contained chemical signatures of both the OTT and MTT.

Our glass trace element from pumice samples data overlap closely with tephra glass data from Pearce et al., (2020) (Figure 3.4) and thus also agree with their interpretation that pumice from north of the YTT caldera (e.g., those that largely plot in group 1) have chemical signatures more similar to the OTT (e.g., sample LT012), while pumice from the east and south of the YTT caldera (e.g., those that plot more in groups 3 – 5) have chemical signatures more similar to the MTT (e.g., samples LT01 and MQ) (Figure 3.12A). To test the hypothesis put forth by Vazquez and Reid (2004), we model crystal fractionation of a similar mineral assemblage (i.e., plagioclase, sanidine, quartz, zircon, biotite) and compare it to the observed glass data. We find that the observed trace element compositions and trends in YTT glass can largely be explained by fractionation of 25 – 55% of plagioclase, sanidine, quartz, zircon, and biotite (Figure 3.13). We omit amphibole from this assemblage, as it was most likely introduced into the Toba reservoir decades to years prior to eruption (Gardner et al., 2002) and did not contribute significantly to the long – term trace element evolution of the system. We also find that although all largely explained by crystal fractionation, the different glass populations as identified by Pearce et al., (2020) must have had different compositions from which fractionation began (Figure 3.13). Distinguishing whether or not these different compositions are discrete magma reservoirs, or one heterogeneous reservoir is beyond the scope of this study, however below we further explore the origin of different compositional sources and their influence on the observed YTT magma chemistry.

When plotted in La/Yb vs. Sr/Y space, we find that our YTT pumice data fall along a linear array with samples from the north of the caldera being much more depleted in La/Yb and Sr/Y ratios than samples from the south of the caldera (Figure 3.12B). Changes in these ratios can be due to a multitude of petrogenetic processes (e.g., Castillo, 2012 Table 2), specifically crystallization of phases that are compatible with heavy rare earth elements (HREE) such as amphibole or garnet. For YTT pumice, changes in La/Yb ratios are largely driven by depletion of Yb, leading to the interpretation that YTT samples from south of the caldera (e.g., those that are more influenced by the MTT magma system) are significantly more depleted in HREEs than those from the north (e.g., pumice more influenced by the OTT magma system). Since both the OTT and MTT have similar mineralogy, effectively ruling out crystallization of a distinct phase influencing trace element chemistry, we propose differences in initial melt composition as the reason for the observed spatial difference in YTT pumice chemistry. Further

evidence to support this comes from O isotope evidence indicating the incorporation of hydrothermally altered granitoid composition roof material during late stage YTT petrogenesis (Budd et al., 2017) and the MTT having distinctly higher Sr isotope values than other Toba caldera eruptions (Chesner, 1998). Since the hydrothermally altered country rock within the boundaries of the Toba caldera likely consists of previous Toba caldera eruptions (e.g., HDT, OTT, and MTT), the spatial distribution of these units will have a local effect on magma composition when they are incorporated into the magma reservoir via assimilation. If the reservoir is at a viscosity such that it is not convecting (e.g., Scaillet et al., 1998; Vigneresse et al., 1996), these local compositional changes will persist until eruption.

Despite pumice samples recording unique and heterogeneous trace element chemistry (Figure 3.4; Figure 3.12), the plagioclase contained within these pumice are recording similar diffusion times (Figure 3.5). More specifically, we find no relationship between which composition glass a plagioclase came from and its diffusion time. We interpret this to imply that the magma system that produced the YTT, although heterogeneous in composition, was experiencing similar long-term thermal conditions within the precision of our diffusion models, as large-scale heterogeneities in temperature would lead to different samples recording unique populations of diffusion times. Moreover, our data collectively suggest that the magma system was not vertically extensive as initially hypothesized by (Chesner, 1998), but was more likely laterally distributed, as a vertically extensive magma system would inherit temperature gradients that reflect the local geothermal gradient (Turcotte and Schubert, 2002) and ultimately be reflected in diffusion timescales. This conclusion is also in agreement with previous work that shows all pumice recording similar extraction pressures (Pearce et al., 2020), and also with geophysical imaging outlining a laterally extensive low velocity region around 7km depth (Jaxybulatov et al., 2014).

Long-term storage conditions of the Toba magmatic system

The YTT magmatic system produced 2800km^3 of chemically heterogeneous ignimbrite (e.g., Chesner, 1998; Pearce et al., 2020). In combining diffusion of trace elements in plagioclase and hornblende, hornblende thermometry, and pumice glass trace element chemistry we can quantify the long-term thermochemical state of the YTT magma reservoir. Trace element modeling of observed YTT phases and comparison with YTT pumice glass suggests that the YTT: 1) is dominantly produced by 20-60% fractionation of a plagioclase + quartz + sanidine + biotite + zircon assemblage; 2) contained discrete composition zones that produced individual liquid lines of descent that were influenced by previous eruption (i.e., OTT and MTT) compositions. Despite this heterogeneity, however, the reservoir(s) from which all

YTT plagioclase were crystallized experienced a relatively homogenous thermal history. More specifically, we find that plagioclase spent more than 95% of their time in magma that was uneruptible as diffusion of trace elements in plagioclase are only recording decades to centuries at or above 750°C. Hornblende, despite being xenocrystic and recording ages up to 1.5Ma, (Gardner et al., 2002), only records up to 2000 years at 750°C and centuries at its initial crystallization temperature of around 800°C. We take this to imply that not only was the magma system that produced the YTT predominantly uneruptible for much of its storage in the crust, but so was the system responsible for initially crystallizing YTT amphibole. Therefore, in order to produce the observed erupted volume of ignimbrite, the YTT magmatic system must have underwent a relatively rapid period of remobilization similar to what is observed in other large caldera-forming eruptions (e.g., Shamloo and Till, 2019). Collectively, these data help provide insight into the long-term thermochemical conditions of large silicic magma reservoirs: the systems responsible for producing the largest explosive eruptions in the geologic record.

REFERENCES

Andersen, N.L., Jicha, B.R., Singer, B.S., Hildreth, W., 2017. Incremental heating of Bishop Tuff sanidine reveals preeruptive radiogenic Ar and rapid remobilization from cold storage 114, 12407–12412. https://doi.org/10.1073/pnas.1709581114

Annen, C., Blundy, J.D., Leuthold, J., Sparks, R.S.J., 2015. Construction and evolution of igneous bodies: Towards an integrated perspective of crustal magmatism. Lithos 230, 206–221. https://doi.org/10.1016/j.lithos.2015.05.008

Annen, C., Blundy, J.D., Sparks, R.S.J., 2006. The genesis of intermediate and silicic magmas in deep crustal hot zones. J. Petrol. 47, 505–539. https://doi.org/10.1093/petrology/egi084

Bachmann, O., Dungan, M.A., 2002. Temperature-induced Al-zoning in hornblendes of the Fish Canyon magma, Colorado. Am. Mineral. 87, 1062–1076. https://doi.org/10.2138/am-2002-8-903

Bachmann, O., Huber, C., 2016. Silicic magma reservoirs in the Earth's crust. Am. Mineral. 101, 2377–2404. https://doi.org/10.2138/am-2016-5675

Barbee, O., Chesner, C., Deering, C., 2020. Quartz in Toba rhyolites show textures symptomatic of rapid crystallization. Am. Mineral. 105, 194–226. https://doi.org/10.2138/am-2020-6947

Barboni, M., Boehnke, P., Schmitt, A.K., Harrison, T.M., Shane, P., Bouvier, A.-S., Baumgartner, L., 2016. Warm storage for arc magmas. Proc. Natl. Acad. Sci. 113, 13959–13964. https://doi.org/10.1073/pnas.1616129113

Bindeman, I.N., Davis, A., Drake, M., 1998. Ion microprobe study of plagioclase-basalt partition experiments at natural concentration levels of trace elements 62, 1175–1193.

Boehnke, P., Watson, E.B., Trail, D., Harrison, T.M., Schmitt, A.K., 2013. Zircon saturation re-revisited. Chem. Geol. 351, 324–334. https://doi.org/10.1016/j.chemgeo.2013.05.028

Brabander, D.J., Giletti, B.J., 1995. Strontium diffusion kinetics in amphiboles and significance to thermal history determinations. Geochim. Cosmochim. Acta 59, 2223–2238. https://doi.org/10.1016/0016-7037(95)00102-6

Bradshaw, R.W., 2017. Crystal Records of the Origin, Evolution, and Thermal Histories of Magmas. Oregon State University.

Bradshaw, R.W., Kent, A.J.R., 2017. The analytical limits of modeling short diffusion timescales. Chem. Geol. 466, 667–677. https://doi.org/10.1016/j.chemgeo.2017.07.018

Budd, D.A., Troll, V.R., Deegan, F.M., Jolis, E.M., Smith, V.C., Whitehouse, M.J., Harris, C., Freda, C., Hilton, D.R., Halldórsson, S.A., Bindeman, I.N., 2017. Magma reservoir dynamics at Toba caldera, Indonesia, recorded by oxygen isotope zoning in quartz. Sci. Rep. 7, 1–11. https://doi.org/10.1038/srep40624

Caricchi, L., Blundy, J., 2015. Experimental petrology of monotonous intermediate magmas. Geol. Soc. Spec. Publ. 422, 105–130. https://doi.org/10.1144/SP422.9

Cashman, K. V., Sparks, R.S.J., Blundy, J.D., 2017. Vertically extensive and unstable magmatic systems: A unified view of igneous processes. Science (80-.). 355. https://doi.org/10.1126/science.aag3055

Castillo, P.R., 2012. Adakite petrogenesis. Lithos 134–135, 304–316. https://doi.org/10.1016/j.lithos.2011.09.013

Chesner, C., Rose, Wi., 1991. Stratigraphy of the Toba Tuffs and the evolution of the Toba Caldera Complex, Sumatra, Indonesia. Bull. Volcanol. 53, 343–356.

Chesner, C.A., 2012. The Toba Caldera Complex. Quat. Int. 258, 5–18. https://doi.org/10.1016/j.quaint.2011.09.025

Chesner, C.A., 1998. Petrogenesis of the Toba Tuffs, Sumatra, Indonesia. J. Petrol. 39, 397–438. https://doi.org/10.1093/petroj/39.3.397

Chesner, C.A., Luhr, J.F., 2010. A melt inclusion study of the Toba Tuffs, Sumatra, Indonesia. J. Volcanol. Geotherm. Res. 197, 259–278.

https://doi.org/10.1016/j.jvolgeores.2010.06.001
Claiborne, L.L., Miller, C.F., Flanagan, D.M., Clynne, M.A., Wooden, J.L., 2010. Zircon reveals protracted magma storage and recycling beneath Mount St. Helens. Geology 38, 1011–1014. https://doi.org/10.1130/G31285.1
Cooper, K.M., Kent, A.J.R., 2014. Rapid remobilization of magmatic crystals kept in cold storage. Nature 506, 480–3. https://doi.org/10.1038/nature12991
Costa, F., Chakraborty, S., Dohmen, R., 2003. Diffusion coupling between major and trace elements and a model for the calculation of magma chamber residence times using plagioclase. Geochim. Cosmochim. Acta 67, 2189–2200. https://doi.org/10.1016/S0016-7037(00)01345-5
Costa, F., Dohmen, R., Chakraborty, S., 2008. Time Scales of Magmatic Processes from Modeling the Zoning Patterns of Crystals. Rev. Mineral. Geochemistry 69, 545–594. https://doi.org/10.2138/rmg.2008.69.14
Costa, F., Shea, T., Ubide, T., 2020. Diffusion chronometry and the timescales of magmatic processes. Nat. Rev. Earth Environ. 1, 201–214. https://doi.org/10.1038/s43017-020-0038-x
Crank, J., 1975. The Mathematics of Diffusion, Second. ed. Oxford University Press, Oxford, England.
de Silva, S.L., Gregg, P.M., 2014. Thermomechanical feedbacks in magmatic systems: Implications for growth, longevity, and evolution of large caldera-forming magma reservoirs and their supereruptions. J. Volcanol. Geotherm. Res. 282, 77–91. https://doi.org/10.1016/j.jvolgeores.2014.06.001
Dingwell, D.B., 1998. Recent experimental progress in the physical description of silicic magma relevant to explosive volcanism. Geol. Soc. London, Spec. Publ. 145, 9–26. https://doi.org/10.1144/GSL.SP.1996.145.01.02
Dohmen, R., Blundy, J., 2014. A PREDICTIVE THERMODYNAMIC MODEL FOR ELEMENT PARTITIONING BETWEEN PLAGIOCLASE AND MELT AS A FUNCTION OF PRESSURE , TEMPERATURE AND COMPOSITION 314, 1319–1372. https://doi.org/10.2475/09.2014.04
Druitt, T.H., Costa, F., Deloule, E., Dungan, M., Scaillet, B., 2012. Decadal to monthly timescales of magma transfer and reservoir growth at a caldera volcano. Nature 482, 77–80. https://doi.org/10.1038/nature10706
Dufek, J., Bergantz, G.W., 2005. Lower crustal magma genesis and preservation: A stochastic framework for the evaluation of basalt-crust interaction. J. Petrol. 46, 2167–2195. https://doi.org/10.1093/petrology/egi049
Gardner, J.E., Layer, P.W., Rutherford, M.J., 2002. Phenocrysts versus xenocrysts in the youngest Toba Tuff: Impications for the petrogenesis of 2800 km3 of magma. Geology 30, 347–350. https://doi.org/10.1130/0091-7613(2002)030<0347:PVXITY>2.0.CO;2
Giletti, B.J., Casserly, J.E.D., 1994. Strontium diffusion kinetics in plagioclase feldspars. Geochim. Cosmochim. Acta 58, 3785–3793. https://doi.org/10.1016/0016-7037(94)90363-8
Holland, T., Blundy, J., 1994. Non-ideal interactions in calcic amphiboles and their bearing on amphibole-plagioclase thermometry. Contrib. to Mineral. Petrol. 116, 433–447. https://doi.org/10.1007/BF00310910
Jaxybulatov, K., Shapiro, N.M., Koulakov, I., Mordret, A., Landès, M., Sens-Schönfelder, C., 2014. A large magmatic sill complex beneath the Toba caldera. Science (80-.). 346, 617–619. https://doi.org/10.1126/science.1258582
Karakas, O., Degruyter, W., Bachmann, O., Dufek, J., 2017. Lifetime and size of shallow magma bodies controlled by crustal-scale magmatism. Nat. Geosci. 10, 446–450. https://doi.org/10.1038/ngeo2959
Kent, A.J.R., Rowe, M.C., Thornber, C.R., Pallister, J.S., 2008. Trace element and Pb isotope

composition of plagioclase from dome samples from the 2004-2005 eruption of Mount St. Helens, Washington. US Geol. Surv. Prof. Pap. 809–826. https://doi.org/10.3133/pp175035

Kent, A.J.R., Ungerer, C.A., 2006. Analysis of light lithophile elements (Li, Be, B) by laser ablation ICP-MS: Comparison between magnetic sector and quadrupole ICP-MS. Am. Mineral. 91, 1401–1411. https://doi.org/10.2138/am.2006.2030

Leake, B.E., Woolley, A.R., Arps, C.E.S., Birch, W.D., Gilbert, M.C., Grice, J.D., Hawthorne, F.C., Kato, A., Kisch, H.J., Krivovichev, V.G., Linthout, K., Laird, J., Mandarino, J.A., Maresch, W. V., Nickel, E.H., Rock, N.M.S., Schumacher, J.C., Smith, D.C., Stephenson, N.C.N., Ungaretti, L., Whittaker, E.J.W., Youzhi, G., 1997. Nomenclature of amphiboles: Report of the subcommittee on amphiboles of the international mineralogical association, commission on new minerals and mineral names. Can. Mineral. 35, 219–246.

Longerich, H.P., Jackson, S.E., Günther, D., 1996. Laser ablation inductively coupled plasma mass spectrometric transient signal data acquisition and analyte concentration calculation. J. Anal. At. Spectrom. 11, 899–904. https://doi.org/10.1039/JA9961100899

Mason, B.G., Pyle, D.M., Oppenheimer, C., 2004. The size and frequency of the largest explosive eruptions on Earth. Bull. Volcanol. 66, 735–748. https://doi.org/10.1007/s00445-004-0355-9

Mucek, A.E., Danišík, M., De Silva, S.L., Schmitt, A.K., Pratomo, I., Coble, M.A., 2017. Post-supereruption recovery at Toba Caldera. Nat. Commun. 8, 1–9. https://doi.org/10.1038/ncomms15248

Nielsen, R., Ustunisik, G., Weinsteiger, A., Tepley, F., Johnston, D., Kent, A.J.R., 2017. Trace element partitioning between plagioclase and melt: An investigation of the impact of experimental and analytical procedures. Geochemistry, Geophys. Geosystems 18, 1580–1593. https://doi.org/10.1002/2017GC006821

Pearce, N.J.G., Westgate, J.A., Gualda, G.A.R., Gatti, E., Muhammad, R.F., 2020. Tephra glass chemistry provides storage and discharge details of five magma reservoirs which fed the 75 ka Youngest Toba Tuff eruption, northern Sumatra. J. Quat. Sci. 35, 256–271. https://doi.org/10.1002/jqs.3149

Petford, N., Cruden, A.R., McCaffrey, K.J.W., Vigneresse, J.L., 2000. Granite magma formation , transport and emplacement in the Earth ' s crust 408, 1–15.

Putirka, K., 2016. Amphibole thermometers and barometers for igneous systems and some implications for eruption mechanisms of felsic magmas at arc volcanoes. Am. Mineral. 101, 841–858. https://doi.org/10.2138/am-2016-5506

Reid, M.R., Vazquez, J.A., 2017. Fitful and protracted magma assembly leading to a giant eruption, Youngest Toba Tuff, Indonesia. Geochemistry, Geophys. Geosystems 18, 156–177. https://doi.org/10.1002/2016GC006641

Rose, Wi., Chesner, C., 1987. Dispersal of ash in the great Toba eruption, 75 ka. Geology 15, 913–917.

Rudnick, R.L., Fountain, D.M., 1995. Nature and composition of the continental crust: A lower-crustal perspective. Rev. Geophys. 33, 267–309. https://doi.org/Doi 10.1029/95rg01302

Scaillet, B., Holtz, F., Pichavant, M., 1998a. Phase equilibrium constraints on the viscosity of silicic 103.

Scaillet, B., Holtz, F., Pichavant, M., 1998b. Phase equilibrium constraints on the viscosity of silicic magmas: 1. Volcanic-plutonic comparison. J. Geophys. Res. Solid Earth 103, 27257–27266. https://doi.org/10.1029/98jb02469

Shamloo, H.I., Till, C.B., 2019. Decadal transition from quiescence to supereruption: petrologic investigation of the Lava Creek Tuff, Yellowstone Caldera, WY. Contrib. to Mineral. Petrol. 174, 1–18. https://doi.org/10.1007/s00410-019-1570-x

Szymanowski, D., Wotzlaw, J.-F., Ellis, B.S., Bachmann, O., Guillong, M., von Quadt, A., 2017. Protracted near-solidus storage and pre-eruptive rejuvenation of large magma reservoirs. Nat. Geosci. 10. https://doi.org/10.1038/ngeo3020

Takeuchi, S., 2011. Preeruptive magma viscosity: An important measure of magma eruptibility. J. Geophys. Res. Solid Earth 116. https://doi.org/10.1029/2011JB008243

Taylor, S., McLennan, S., 1995. The Geochemical Evolution of the Continental Crust. Rev. Geophys. 33, 241–265. https://doi.org/10.1029/95RG00262

Tierney, C.R., Reid, M.R., Vazquez, J.A., Chesner, C.A., 2019. Diverse late-stage crystallization and storage conditions in melt domains from the Youngest Toba Tuff revealed by age and compositional heterogeneity in the last increment of accessory phase growth. Contrib. to Mineral. Petrol. 174, 1–21. https://doi.org/10.1007/s00410-019-1566-6

Turcotte, D., Schubert, G., 2002. Geodynamics, 2nd ed. Cambridge University Press.

Van Orman, J.A., Cherniak, D.J., Kita, N.T., 2014. Magnesium diffusion in plagioclase: Dependence on composition, and implications for thermal resetting of the 26Al-26Mg early solar system chronometer. Earth Planet. Sci. Lett. 385, 79–88. https://doi.org/10.1016/j.epsl.2013.10.026

Vazquez, J.A., Reid, M.R., 2004. Probing the accumulation history of the voluminous Toba magma. Science (80-.). 305, 991–994. https://doi.org/10.1126/science.1096994

Vigneresse, J.L., Barbey, P., Cuney, M., 1996. Rheological Transitions During Partial Melting and Crystallization with Application to Felsic Magma Segregation and Transfer. J. Petrol. 37, 1579–1600.

Wilson, C.J.N., Cooper, G.F., Chamberlain, K.J., Barker, S.J., Myers, M.L., Kemp, F.I.-, Farrell, J., 2021. No single model for supersized eruptions and their magma bodies. Nat. Rev. Earth Environ. https://doi.org/10.1038/s43017-021-00191-7

Wotzlaw, J.F., Schaltegger, U., Frick, D.A., Dungan, M.A., Gerdes, A.G., G??nther, D., 2013. Tracking the evolution of large-volume silicic magma reservoirs from assembly to supereruption. Geology 41, 867–870. https://doi.org/10.1130/G34366.1

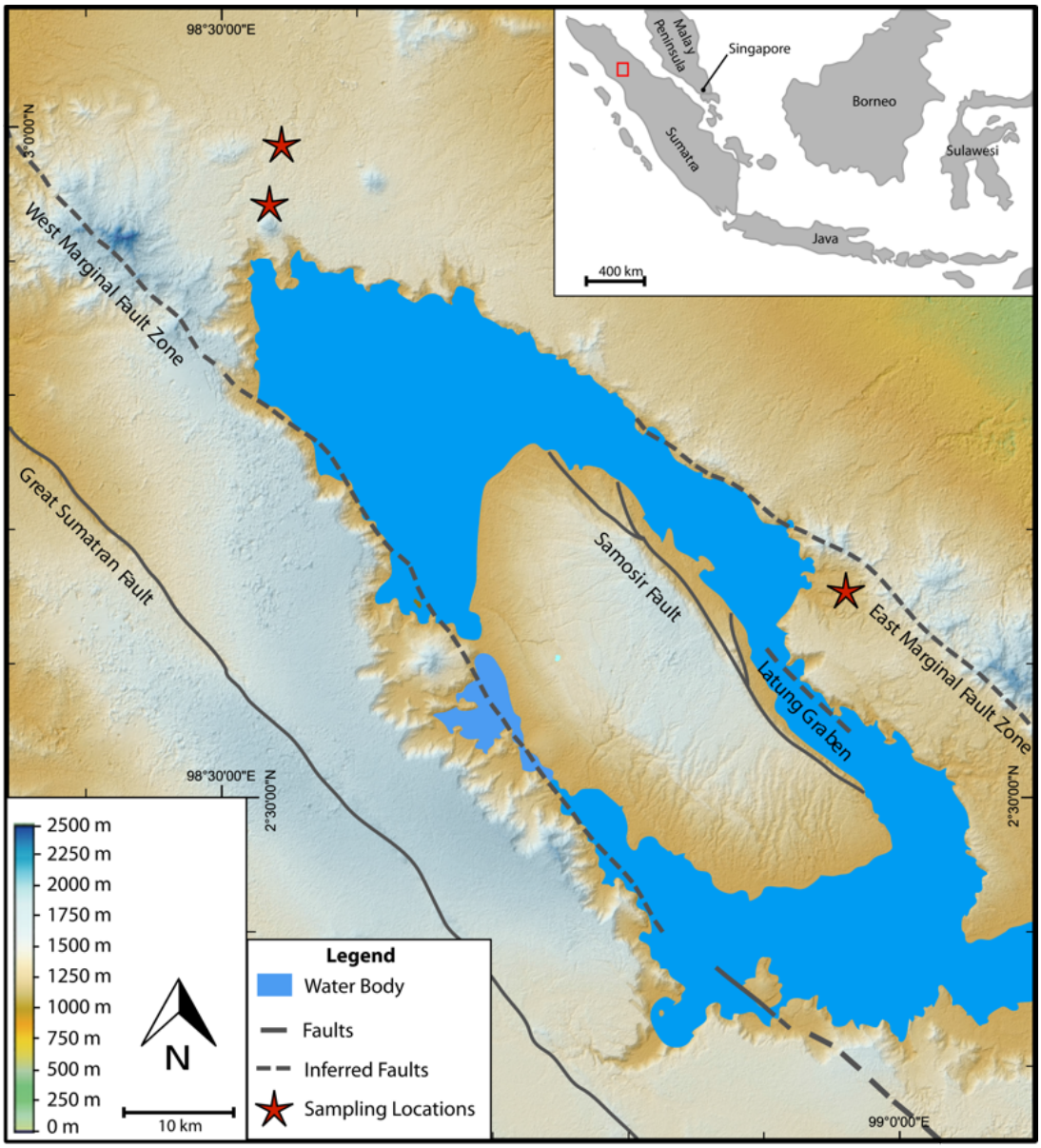

Figure 3.1: Map of Toba caldera and its location within the larger Sunda arc (inset). Sample locations used in this study are represented by red stars.

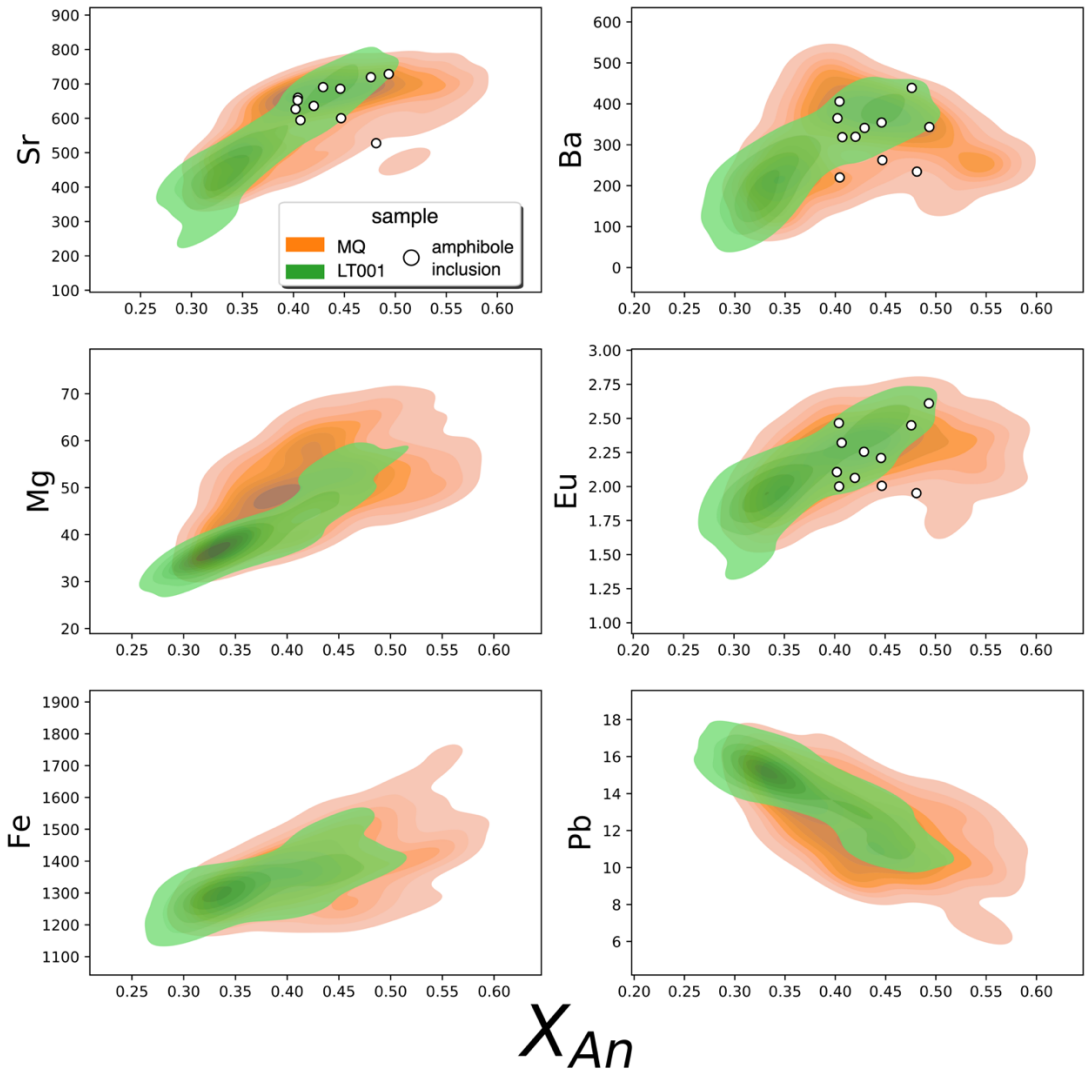

Figure 3.2: Plagioclase trace element vs. An relationships for all samples studied represented by 2D kernel density estimates (KDEs). Darker shades of green and orange correspond to higher densities of data for each sample. Notice the significant overlap between the two samples and plagioclase inclusions found in amphibole (white spots).

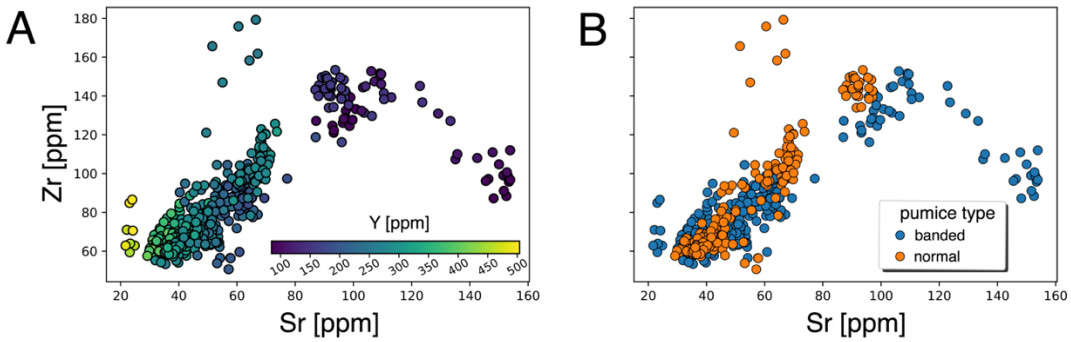

Figure 3.3: A) Sr vs. Zr for all amphiboles studied. Spots are colored according to their Y concentration. From this it can be seen that there are two populations: 1) High Sr – low Y that has a negative correlation with Zr; 2) Low Sr – high Y that has a positive correlation with Zr. B) Same data plotted in A, but now colored by pumice type (i.e., normal or banded). While both pumice types plot in population 2, we find that only banded pumice displays the negative relationship with Zr.

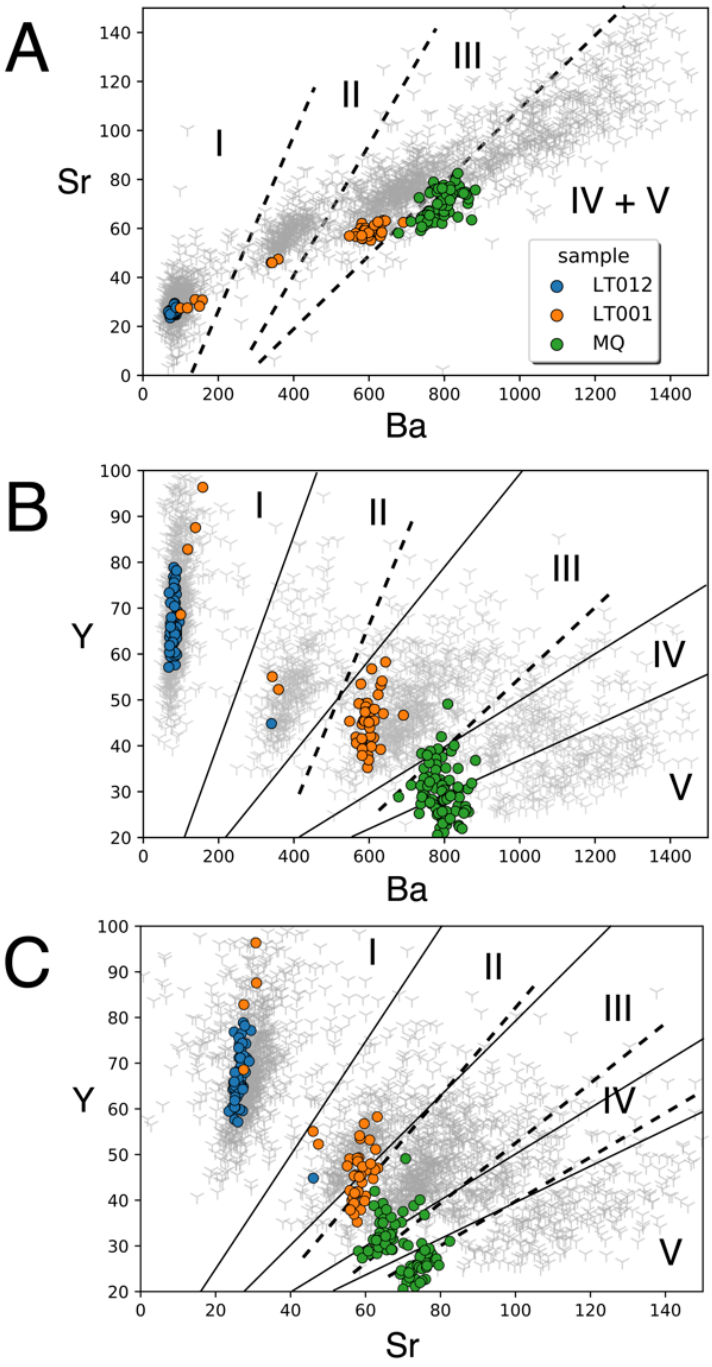

Figure 3.4: Selected trace elements for YTT pumice glass. Spots are colored by which sample they come from. Gray data in the background and population fields are from Pearce et al., (2020)*. It can be seen here that the data gathered in this study overlaps significantly with previously gathered data from* Pearce et al., (2020) *and every population defined there is represented between our three samples. A) Sr vs. Ba; B) Y vs. Ba; C) Y vs. Sr.*

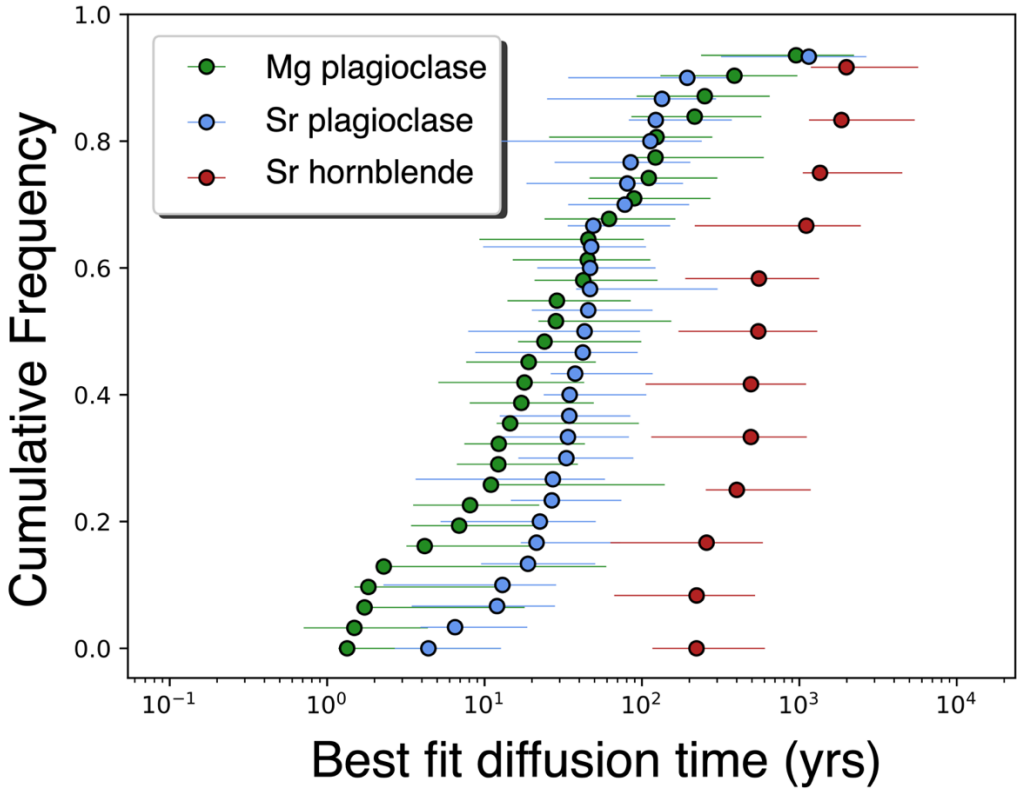

Figure 3.5: Summary of diffusion results for each chronometer used in this study shown using a cumulative distribution plot. 1D KDE for each chronometer plotted above showing that Mg in plagioclase records a wider range in diffusion times than both Sr in plagioclase and Sr in amphibole. Uncertainty bars on each individual point are 95% confidence limits and we see that Sr and Mg largely overlap within uncertainty. Strontium in amphibole, however, does not and records diffusion times that are roughly an order of magnitude longer.

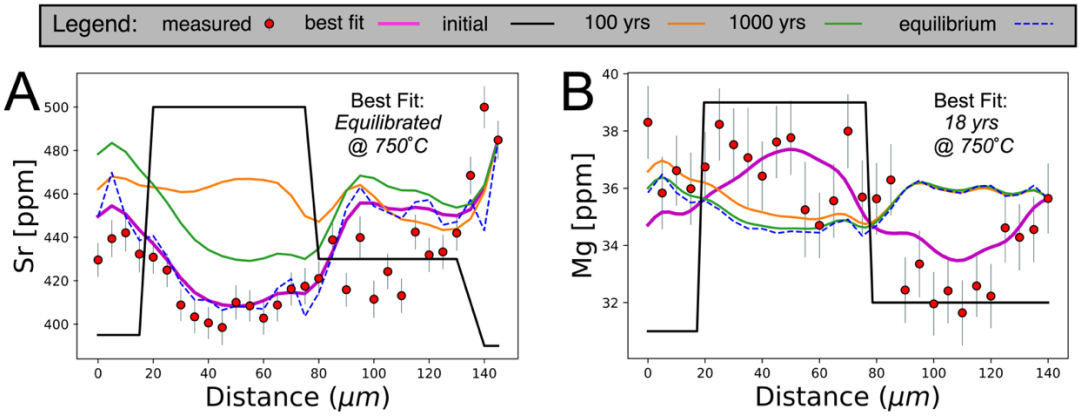

Figure 3.6: A) Strontium diffusion model for profile LT22 from sample LT_001 showing that the observed Sr data for this profile closely resembles its calculated equilibrium profile, suggesting that it has spent prolonged periods of time at high (> 750°C) temperatures. B) Magnesium diffusion model for the same profile in A showing an observed Mg profile that suggests it has spent short durations at 750°C. Collectively, A and B illustrate the of modeling multiple trace elements in plagioclase to get a more complete picture of the magmatic system, as one chronometer alone may skew petrologic interpretations towards inaccurate results.

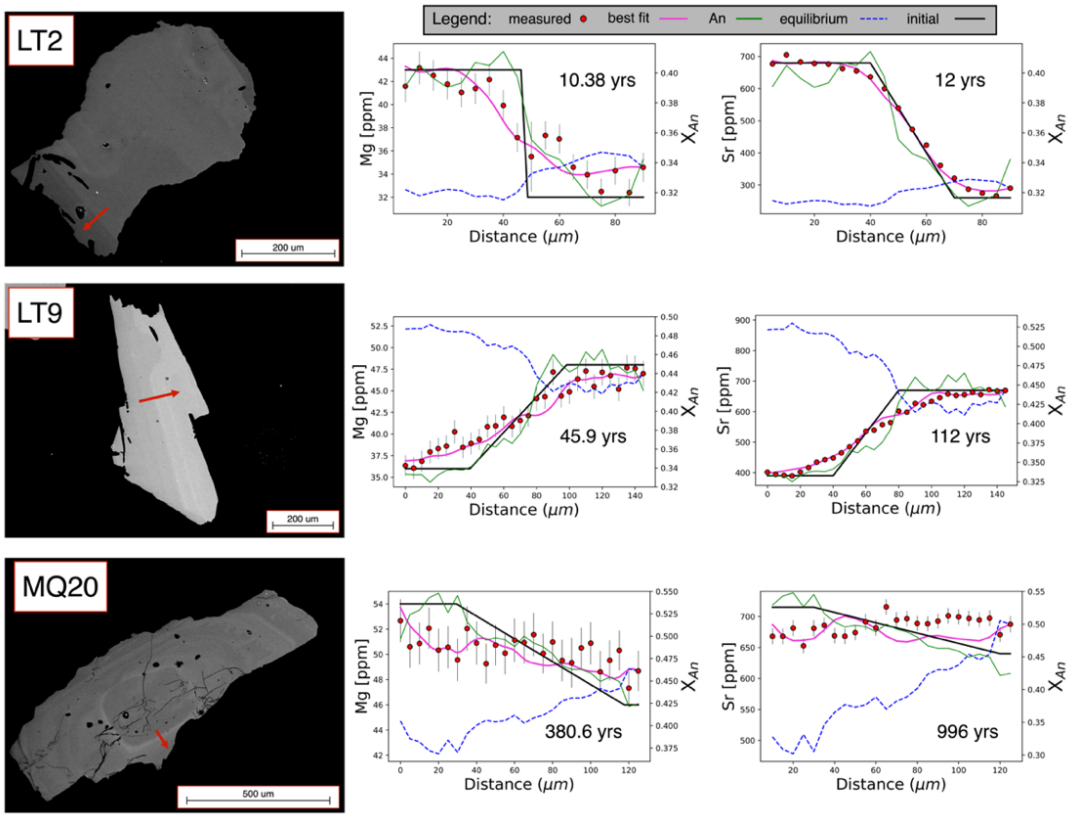

Figure 3.7: Representative diffusion models for Sr and Mg in plagioclase. Left column is a BSE of the grain with red arrows indicating the approximate location of the LA-ICP-MS transect. Middle column shows observed Mg, observed An, initial Mg boundary conditions for the diffusion model, best fit diffusion model, and equilibrium profiles. Right column shows same profiles but for Sr. The striking nature of both Mg and Sr profiles mimicking the observed An rather than equilibrium profiles suggests that diffusion has not significantly progressed from initial boundary conditions.

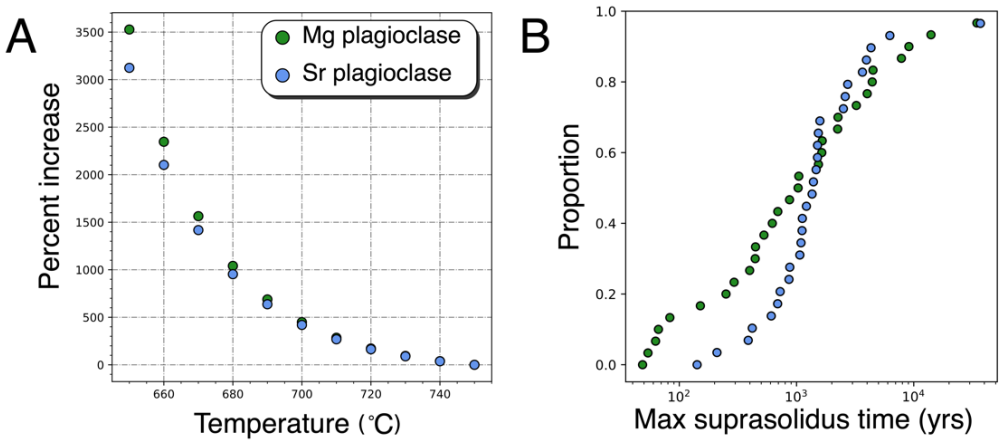

Figure 3.8: Comparing the influence of temperature on best fit diffusion time. A) showing the percent increase in diffusion time if diffusion models were run at different temperatures between 750 and 650 (i.e., rough approximations for granitic solidus temperatures). B) Using a hypothetical solidus temperature of 660, we apply the results of A to our best fit diffusion models for Sr and Mg in plagioclase (i.e., the data shown in Figure 3.5) to show that this is the maximum amount of time that a given profile could've spent above the solidus in the YTT system prior to eruption.

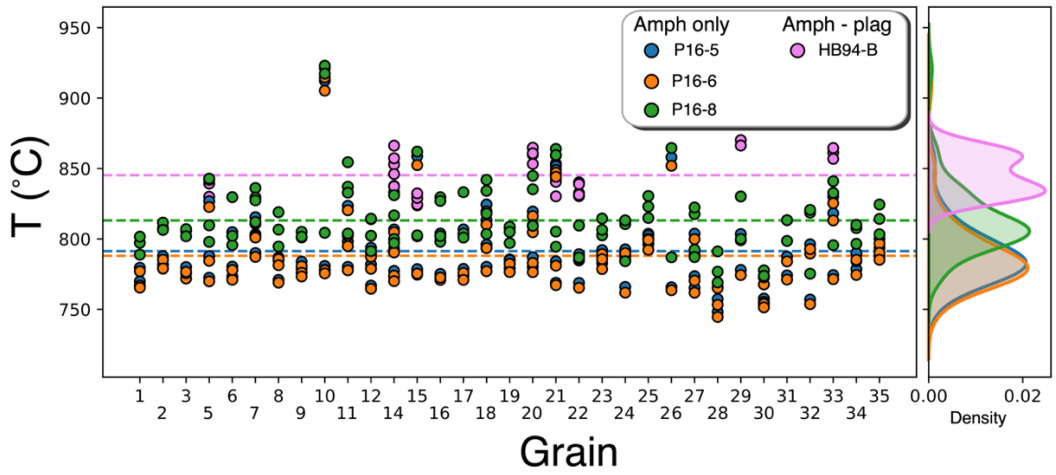

Figure 3.9: Summary of amphibole only and amphibole – plagioclase thermometry completed in this study. We see that amphibole – plagioclase thermometry produces systematically higher temperatures than amphibole only thermometry, however both are within one sigma uncertainty of each other. 1D KDEs for each thermometer's results are shown on the right and display largely unimodal distributions.

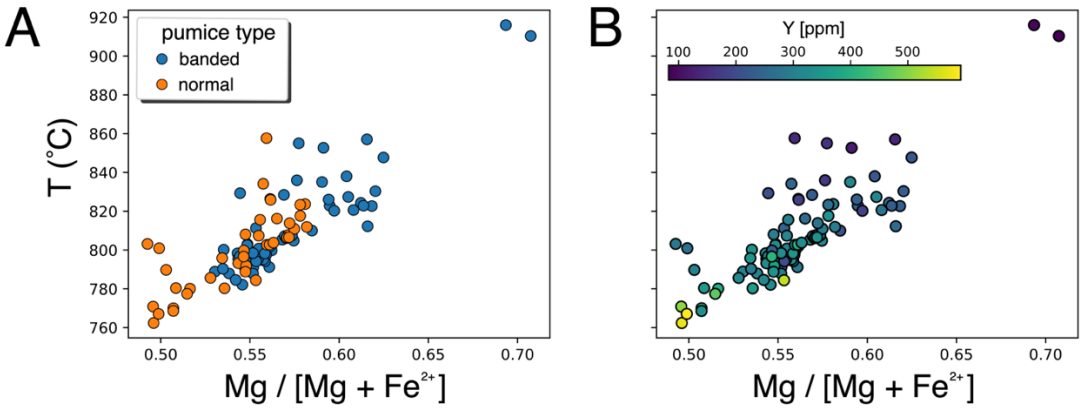

Figure 3.10: Comparing amphibole composition with crystallization temperature. A) comparing Mg # with crystallization temperature where data are colored by pumice type. While there is a lot of overlap, banded pumice are recording higher crystallization temperatures than normal pumice. B) same data plotted in A but colored by Y concentration similar to Figure 3.3 to show that the high Sr – low Y population amphiboles are recording higher temperatures and predominantly from the banded pumice.

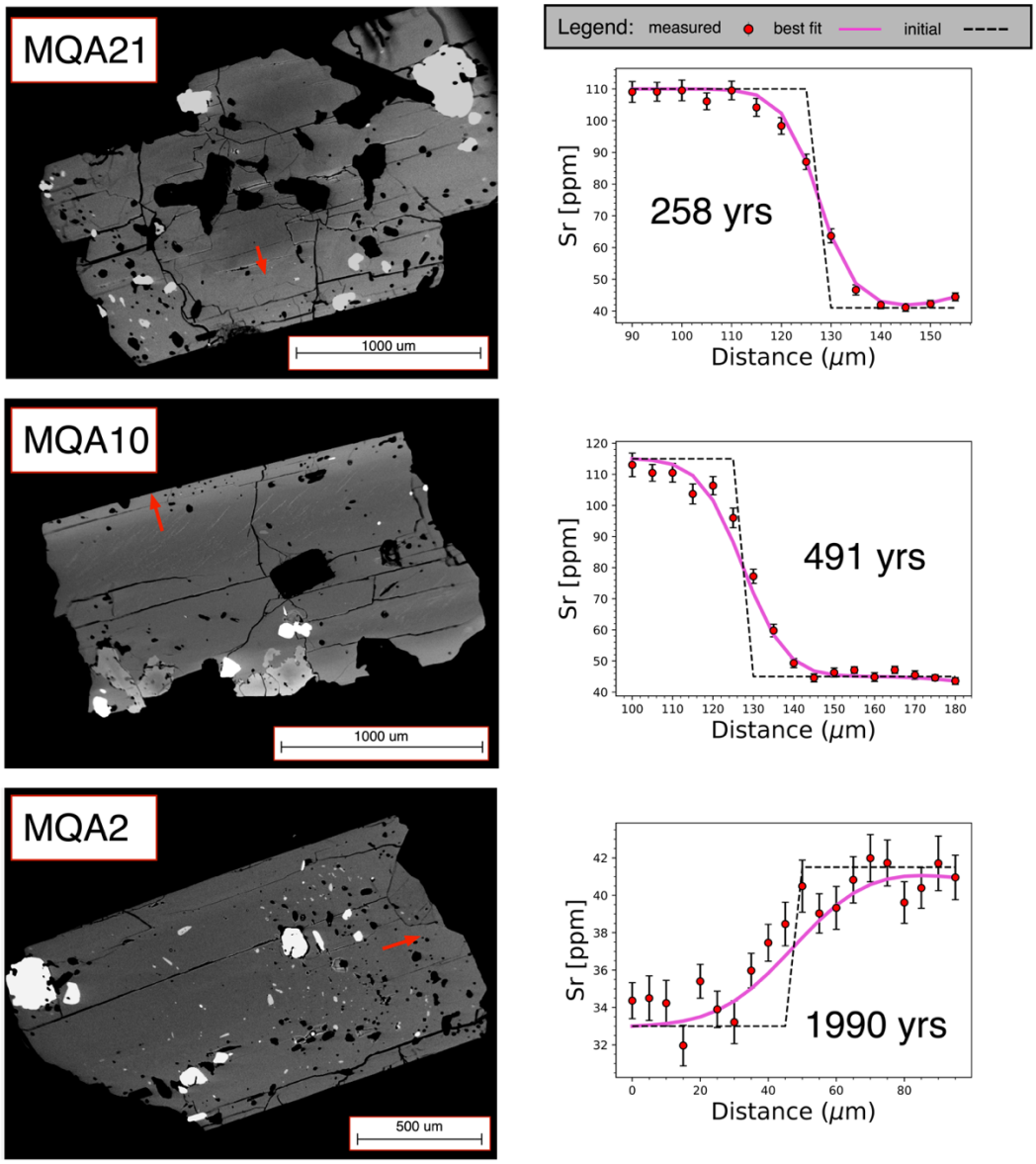

Figure 3.11: Representative diffusion models for Sr in amphibole. Left column is a BSE of the grain with red arrows indicating the approximate location of the LA-ICP-MS transect. Right column shows observed Sr, initial boundary condition Sr, and best fit diffusion profiles. We see here that the observed data when, modeled from step function boundary conditions, are well represented by Fick's 2nd Law (i.e., diffusion curves that are shaped like error functions).

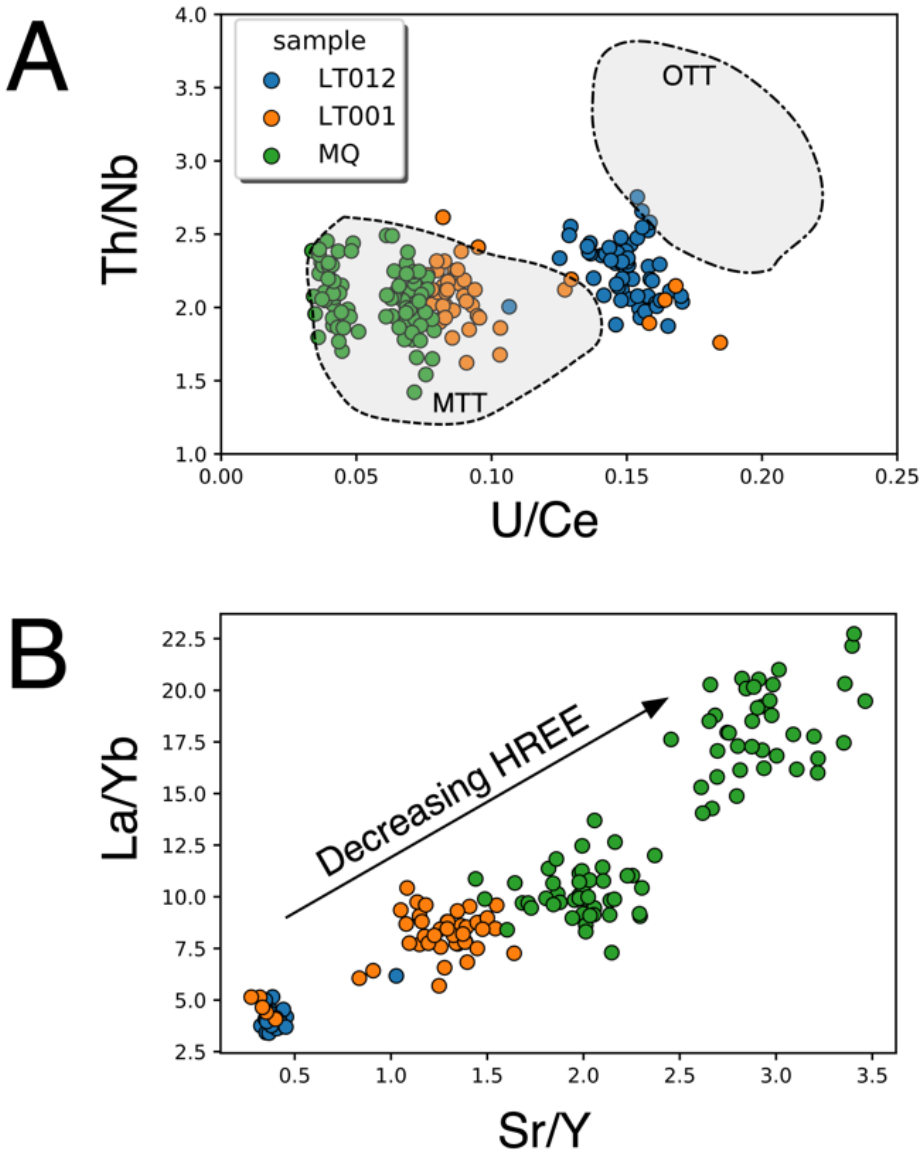

Figure 3.12: A) Comparing YTT glass chemistry with that of the OTT and MTT. Samples from more northward (e.g., LT_001 and MQ) reflect compositions more similar to the MTT, while samples further south (e.g., LT_012) more similarly reflect OTT compositions. B) Plot reflecting the drastic changes in La/Yb amongst YTT pumice glass. This is largely driven by changes in Yb and likely reflects a source magma that is depleted in HREEs to varying degrees. Data plot in 4 clusters similar to the groups proposed in Figure 3.4 and Pearce et al., (2020).

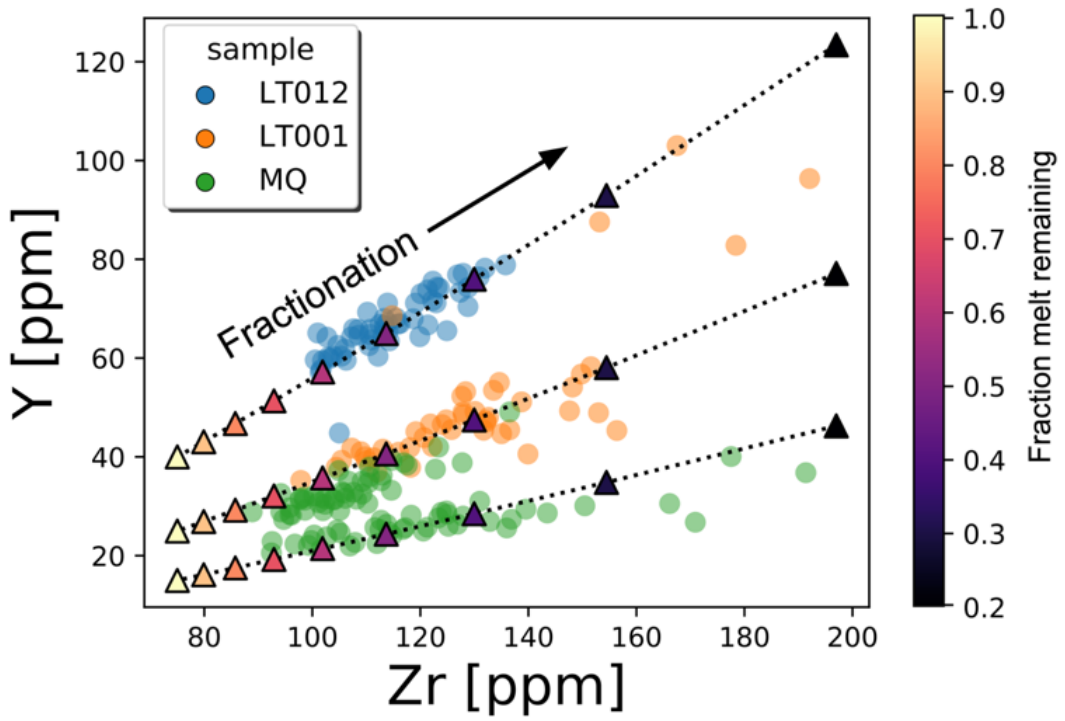

Figure 3.13: Results from modeling fractional crystallization over a range of initial liquid compositions. Each individual line is a fractionation path where triangles represent 10% crystallization increments and are colored according to the fraction of melt remaining in the system (e.g., the F parameter in the Rayleigh Fractionation equation). Partition coefficients for Zr are calculated using Boehnke et al., (2013) *and Y partition coefficient values are from the GERM partition coefficient database. Zircon abundance is assumed to be .01 vol%. Starting compositions were chosen using a range of compositions according to values from Chesner and Luhr, (2010; Table 1). Starting Zr concentrations are 75 ppm and starting Y concentrations are 40, 25, and 15 ppm from top down. Fractionating assemblage is based off hand sample identification and previous literature estimates for phase abundances in the YTT: 40% plagioclase, 20% quartz, 10% biotite, and .01% zircon by volume. Changes in these estimates combined with partition coefficients from GERM result in a Y distribution coefficient of .3 ± .02, where biotite and zircon are the driving factors. These results show that it is possible to create the unique trace element patterns observed in YTT pumice by crystal fractionation of discrete composition magmas that then experience their own liquid lines of descent. This further supports the interpretations put forth by Vazquez and Reid (2004) and Pearce et al., (2020), in which discrete melt bodies are present in the YTT for potentially prolonged periods of time.*

Table 3.1: Sample names, types, and locations used in this study.

Sample name	Pumice type	Location	Latitude (N°)	Longitude (E°)
LT_001	Nonwelded	North of Toba Caldera	02°59.630	098°32.643
LT_012	Nonwelded	East of Toba Caldera	02°39.118	098°57.523
MQ_normal	Nonwelded	North of Toba Caldera	02°57.434	98°31.910
MQ_banded	Banded	North of Toba Caldera	02°57.434	98°31.910

Table 3.2: Results of 2 sided Kolmogorov-Smirnov test for each chronometer used in this study, which tests the null hypothesis that two samples (e.g., Sr diffusion model times and Mg diffusion model times) are drawn from the same distribution. It can be seen here that Sr and Mg in plagioclase produce statistically identical distributions while Sr in amphibole is not statistically identical to either Sr or Mg in plagioclase.

Chronometer pair	$KS_{critical}$	$KS_{observed}$	p-value	Same Distribution ($KS_{observed} < KS_{critical}$; p >=.05)
Mg_{plag} -Sr_{plag}	0.348	0.286	0.116	Yes
Mg_{plag} -Sr_{amph}	0.465	0.871	2.80×10^{-7}	No
Sr_{plag} -Sr_{amph}	0.465	0.933	1.65×10^{-8}	No

CHAPTER FOUR: 3D ZONING OF BARIUM IN ALKALI FELDSPAR

Jordan Lubbers
Adam Kent
Douglas Meisenheimer
Dorthe Wildenschild

Manuscript in review for submission to
American Mineralogist
Mineralogical Society of America

ABSTRACT

Interpretation of chemical zoning within igneous minerals is critical to many petrologic studies. Zoning in minerals, however, is commonly observed in thin sections or grain mounts, which are random 2D slices of a 3D system. Use of these 2D sections to infer 3D geometries requires a set of assumptions, often not directly tested, introducing a number of issues and partial loss of zoning information. Computed X-Ray microtomography (microCT) offers a way to assess 3D zoning in minerals at high resolution. To observe 3D mineral zoning using microCT, however, requires that zoning is observable as differences in X-ray attenuation. Sanidine, with its affinity for Ba in the crystal lattice, can display large, abrupt, variations in Ba that are related to various magma reservoir processes. These changes in Ba also significantly change the X-ray attenuation coefficient of sanidine, ultimately allowing for discrete mineral zones to be mapped in 3D using microCT. Here we utilize microCT to show 3D chemical zoning within natural sanidines from a suite of volcanic eruptions throughout the geologic record. We also show that changes in microCT grayscale in sanidine are largely controlled by changes in Ba. Starting with 3D mineral reconstructions, we simulate thin section making by generating random 2D slices across a mineral zone to show that slicing orientation alone can drastically change the apparent width and slope of composition transitions between different zones. These findings have important implications for tools that rely on the interpretation of chemical zoning within minerals (e.g., diffusion chronometry, timing of eruption triggers, rates of magma mixing/assimilation, etc.) and illustrate a new way to investigate igneous systems, helping to further our understanding of their temporal evolution.

Keywords: computed X-ray microtomography, mineral zoning, sanidine, barium

INTRODUCTION

Chemical zoning is nearly ubiquitous in igneous minerals. The compositions of zoned crystals preserve records of magmatic conditions and compositions when mineral growth occurred, and documenting and interpreting such zoning, and relating compositional variations to textural features is a thus crucial pillar upon which modern igneous petrology is based. Studies of mineral chemical zoning provide important insight into common igneous processes such as: magma mixing (e.g., Streck et al., 2005; Kent et al., 2010; Eichelberger, 1975; Anderson, 1976; Simonetti et al., 1996); frequency and origins of magma recharge (e.g.,Tepley et al., 2000; Davidson et al., 2001; Davidson and Tepley, 1997; Singer et al., 1995); thermal evolution of magma reservoirs (e.g.,Cooper and Kent 2014; Rubin et al. 2017; Shamloo and Till 2019); and the rates of igneous processes (e.g.,Costa and Dungan, 2005; Ruprecht and

Plank, 2013; Costa et al., 2003; Morgan and Blake, 2006). Changes in mineral chemistry can also be used to understand the temporal sequence and evolution of the these and other processes (Cooper 2017). When applied to a sufficiently large and representative population of grains, this approach then allows the long-term physicochemical conditions within a given magmatic system to be constrained.

The vast majority of mineral zoning studies, however, only investigate the interplay between chemical zoning and mineral textures using 2D exposures (i.e., thin sections or mineral mounts). However, use of 2D mineral zoning patterns to represent 3D systems can also introduce a number of artifacts and other issues (e.g., incorrect estimates of mineral size and shape, width of compositional zones, modification of compositional gradients etc.), potentially leading to incomplete and or inaccurate characterization and interpretation of igneous processes (e.g., Higgins 2000). For example, recent studies have numerically investigated the effects of sectioning 3D zoned crystals using modeling approaches for the purposes of documenting diffusion gradients (e.g., Shea et al. 2015; Krimer and Costa 2017). This shows that many 2D sections suffer from partial loss of zoning information, requiring a careful evaluation of each crystal studied to avoid a distorted view of the true concentration gradient between chemical zones and obtain reliable results (e.g., diffusion timescales). Despite this realization, however, studies of 3D zoning in natural mineral examples have been relatively underutilized to address 2D sectioning issues.

To observe natural mineral chemical zoning in 3D, previous studies of have used serial sectioning combined with either electron probe (e.g., Spear and Daniel 2003), focused ion beam time of flight secondary ion mass spectrometry (FIB ToF SIMS; Wirth 2009; Tajčmanová et al. 2012), or atom probe tomography (APT; Reddy et al. 2020; Rickard et al. 2020), however these approaches: 1) often only produce 3D imaging/chemical information for an extremely small volume and are difficult to apply to an entire mineral (e.g., FIB ToF SIMS, APT); 2) can only create coarse 3D reconstructions based on limited 2D slices (electron probe serial sections); 3) necessitate the destruction of the sample being studied; 4) are extremely time consuming making it challenging to be representative of an entire magmatic system.

In recent years, technological developments in high resolution imaging via computed X-ray microtomography (microCT) have provided new opportunities to observe textural and zoning characteristics throughout individual minerals in 3D (e.g., Uesugi et al. 2010; Tsuchiyama et al. 2013; Pankhurst et al. 2018; Mourey and Shea 2019). These studies show there is great potential to further use microCT and related techniques to document and understand compositional zoning in igneous minerals, but there remains a need to develop

greater understanding of the potential for using microCT in different mineral systems, and to establish what the 3D variations in X-ray attenuation revealed by microCT correspond to in terms of compositional variations for specific minerals. In this study we use microCT to document intracrystalline 3D chemical zoning of natural sanidine crystals and explore the geochemical controls responsible for changes in X-ray attenuation throughout this mineral.

X-ray micro tomography

When X-rays interact with a sample they are attenuated according to Lambert-Beer's Law:

1. $I = I_0 exp(-\mu D)$

Where I is the attenuated intensity of X-rays after they pass through a sample of thickness D, I_0 is the incident radiation (X-ray) intensity, and μ is the linear attenuation coefficient of the material the X-rays are interacting with. The linear attenuation coefficient is a constant that describes the fraction of attenuated incident photons in a monoenergetic beam per unit thickness of a material, and varies with beam energy, atomic electron density, and the bulk density of the material (Wildenschild and Sheppard 2013). Although attenuation mechanisms also vary with beam energy (i.e., Compton scattering for $5<I_0<10$ MeV; pair production $I_0 >$ 10 MeV), for geologic materials a beam energy of 50-100 keV is typically used and the photoelectric effect dominates (Mccullough 1975). This is an extremely useful observation as both the photoelectric effect and Compton scattering are sensitive to the atomic number of an element (Van Grieken and Markowicz 2002), allowing for the possibility of correlating changes in linear attenuation coefficient to changes in chemical composition of minerals and other geologic materials. Earlier attempts to use microCT to quantify intracrystalline chemical heterogeneity within olivine and pyroxene from meteorites were successfully made by Uesugi et al. (2010) and Tsuchiyama et al. (2013), respectively, however attempts to apply this methodology to terrestrial igneous systems have been underutilized (Pankhurst et al. 2014, 2018). Thorough reviews further expanding on previous applications of X-ray computed tomography within the geosciences can be found in Hanna and Ketcham (2017) as well as Cnudde and Boone (2013). For a more comprehensive description of photon interaction with matter the reader is referred to Mccullough (1975) and Van Grieken and Markowicz (2002).

In order to create tomographic images of a material, X-rays must pass through the sample from many directions and then be combined through reconstruction methods to produce a stack of 2D "slices". A slice is compiled from X-ray intensity measurements at a given height for a full 360° rotation around the sample and can be thought of as a spatial distribution of linear attenuation coefficient (μ) values (Denison et al. 1997). Each slice represents a finite

thickness based on setup conditions and these slices can then be further combined to construct a 3D rendering of the sample that can then be quantitatively investigated. Although there are a few types of scanning in commercial microCT setups, the method used in this study employs helical scanning from a conical X-ray source which both improves the signal to noise ratio associated with reduced focal spot size, allows for faster scan times, longer specimen scans, and allows for theoretically exact reconstruction of the sample (Varslot et al. 2011). A more in-depth explanation of both microCT equipment configurations and helical scanning reconstruction can be found in Wildenschild and Sheppard (2013) and Varslot et al., (2011) respectively.

Sanidine

Feldspars are the most abundant constituents of igneous rocks and as such, are integral to many petrologic studies. Sanidine ($[K,Na]AlSi_3O_8$; Or_{37-100}) is the dominant alkali feldspar found in volcanic rocks and displays frequent chemical zoning. As it typically equilibrates at higher temperatures than other alkali feldspars, sanidine is prone to having greater amounts of elemental substitution (typically Ba^{+2}, Sr^{+2}, Ti^{+4}, Fe^{+2}, Fe^{+3}, Mg^{+2}) in its crystal structure (Deer et al. 1966). Of these, Ba^{2+} substitution is the most common because of similar atomic radii between K^+ and Ba^{2+} and is accommodated into sanidine in the following substitution (Icenhower and London 1996):

2. $(Ba^{2+}, Sr^{2+}) + K^+ + Al^{3+} = 2Na^+ + Si^{4+}$

Thus, Ba is a highly compatible element in sanidine and is often present at concentrations that range from 100's of µg/g to weight percent levels. Barium zoning is also commonly observed in sanidine and other alkali feldspars from plutonic and volcanic rocks (e.g., Chambers et al. 2020; Rout et al. 2021). Specifically, sanidine populations that display frequent high (>1 wt%) Ba zones occur in many large ignimbrites (e.g., Bachmann et al. 2014; Szymanowski et al. 2017, 2019; Forni et al. 2018; Lubbers et al. 2020) from throughout the geologic record, implying that the processes responsible for forming them is also of importance in understanding the evolution of many silicic systems capable of producing large volcanic eruptions. Commonly proposed mechanisms for formation of these high Ba zones are either localized cumulate melting (e.g., Bachmann et al. 2014; Wolff et al. 2015, 2020), mass transfer from a more mafic magma relatively enriched in Ba (e.g., Ginibre et al., 2004), or temperature cycling (Rout et al. 2021), however reconciling these mechanisms with other types of data (i.e., major element zoning, other trace element zoning, diffusive equilibration timescales, thermodynamic modeling) often introduces additional ambiguity, such that it is difficult to definitively discern between competing models (Shamloo and Till 2019). Interpretations are also complicated by

the relatively slow rates of Ba diffusion in silicate melts (Singer et al. 1995; Zhang 2010), which can result in a decoupling of major and minor element behavior, and also by lack of accurate description of Ba partitioning as a function of P-T-X, reflecting the fact that alter-valent (i.e., 2^+ to 1^+) Ba partitioning into K sites in sanidine is also highly sensitive to changes in melt composition (Mcintire 1963). As a result, although Ba zoning has also been shown to be useful for understanding the timescales associated with recharge leading up to an eruption (Morgan and Blake 2006; Till et al. 2015; Shamloo and Till 2019), the ultimate causes of this zonation remains incompletely understood.

METHODS

Samples

To observe the relationship between CT data and sanidine composition, sanidines from a number of different volcanic rocks have been studied: the 35.3 Ma Kneeling Nun Tuff (Szymanowski et al. 2017) from the Mogollon-Datil Volcanic Field (MDVF); the 27.55 Ma Carpenter Ridge Tuff (Lipman and McIntosh 2008) from the Southern Rocky Mountain Volcanic Field (SRMVF); the 631 ka Lava Creek Tuff (Matthews et al. 2015) from Yellowstone caldera; and recent dome lavas from Taapaca volcano in northern Chile (e.g., Rout et al. 2021). These samples were chosen because they all show significant zoning in Ba contents, and collectively also span a large range in BaO concentrations (0 – ~3.5 wt%). Sanidine grains were mechanically separated and hand-picked using conventional crushing and picking methods. Once picked, selected sanidine grains were then mounted vertically in an epoxy rod (Figure 4.1). This geometry was selected to produce a shorter sample to X-ray source distance compared to 25 mm epoxy round mounts, while still allowing for many grains to be scanned at once using helical scanning. The shorter sample to source distance allows for higher spatial resolution data to be gathered as microCT data voxel size is proportional to sample distance from the X-ray source (Sheppard et al. 2014).

MicroCT

MicroCT scans were acquired using Oregon State University's microCT facility (microct.oregonstate.edu), which uses a Hamamatsu L10711-19 source set at a voltage of 80kV, current of 60μA, and source to sample distance of 5 mm. These settings resulted in a voxel size of 2.1-2.2 μm. Maps of X-ray intensities for each sequential 2D frame, collected as the sample rotates through 360 degrees, were reconstructed to produce 3D volumetric data (a full scan) consisting of digital grayscale images, following the methodology of Varslot et al., (2011). The 3D volumetric data was then further processed, analyzed, and rendered in 3D.

Electron Probe MicroAnalyzer

Backscatter electron (BSE) images and major element analyses of sanidine grains were obtained using a Cameca SX100 electron probe microanalyzer (EPMA) at Oregon State University. For all analyses, a focused beam of 5μm, 15kV accelerating voltage, and 30nA current was used. Standards utilized and detection limits for each element can be found in Table 4.1. Two approaches were taken to facilitate direct comparison of data and 2D images from the EPMA to 3D microCT images. Initially, individual crystals were sectioned, polished and imaged using BSE after microCT images were taken, and we then selected the section in the microCT volume that most closely matched the 2D section. This proved challenging in some cases, however, and for subsequent analyses, crystals were sectioned and analyzed via EPMA prior to microCT in order to locate crystals with the largest amount of variation of Ba contents for analysis. After CT scans, corresponding BSE and CT 2D sections were chosen for comparison.

Image Processing

In microCT data, variations in linear attenuation coefficient of a material are observed as changes in grayscale intensity in the reconstructed 3D volumes (Denison et al. 1997). Linear attenuation coefficients of sanidine areas analyzed by EPMA in this study were also predicted using Mccullough (1975):

3. $\mu_l = \mu_{m(total)}\rho_{mineral}$

Where μ_m is the mass attenuation coefficient and ρ is the density of the mineral. Mass attenuation coefficients of mixtures (i.e., sanidine) were also calculated using (Mccullough 1975):

4. $\mu_{m(total)} = \sum_{i=1}^{n} \omega_i(\mu_m)_i$

Where μ_m is the mass attenuation coefficient and ω is the proportion by weight of stoichiometric component *i*. Chemical zoning in minerals, if sufficiently different, will be observed as changes in X-ray attenuation (Equations 3-4).

The software/coding packages used for image processing in this project are shown in Table 4.2. Datasets generated from the initial 3D volume were cropped into smaller, more manageable sizes that: 1) reflect individual minerals; 2) reduce file size substantially to make subsequent processing achievable on a standard personal laptop. One of the goals of this project was also to make the methodology as open source and accessible as possible. Because of this, all of the image processing besides the cropping and slicing of datasets (Avizo) was done in either Fiji/ImageJ or via scripting in Python. Built on top of the Python package scikit-image

(https://scikit-image.org/; Van Der Walt et al. 2014), we have also created a Python module, CTPy (https://github.com/jlubbersgeo/ctpy; Lubbers 2021), to help make the image segmentation process more streamlined.

To quantify the number of distinct phases or regions within a sample, a histogram was generated where each peak generally corresponds to a specific phase/region. For materials with different attenuation (e.g., sanidine, epoxy, air) the histogram peaks of CT grayscale were typically distinct (e.g., Figure 4.2). When dealing with intracrystalline zoning in minerals, however, we found that although there are observable differences in grayscale within minerals (Figure 4.2A: right) the histogram created from these two zones still overlapped significantly (Figure 4.2A: left). To refine these histograms by removing inherent noise from the data, while still preserving crucial textural information, we used a non-local means (NLM) algorithm (Buades et al. 2005; Van Der Walt et al. 2014). After this filter was applied, we typically observe four peaks in the slice data (background, epoxy, mineral zone 1, mineral zone 2; Figure 2B left) that match what we qualitatively see in grayscale (Figure 4.2B: right). This approach allowed us to better quantify areas and volumes of individual mineral zones via image segmentation (i.e., partitioning the image into distinct regions/segments based on a set of characteristics).

Image segmentation was completed using the watershed algorithm (Vincent and Soille 1991; Roerdink and Meijster 2000; Van Der Walt et al. 2014). Using predefined markers, the watershed algorithm identifies the spatial extent of the two regions of interest. For our sanidine grains, we create these markers by applying the Sobel gradient operator to create an image mask where pixel values correspond to their intensity gradient (Jähne et al. 1999; Van Der Walt et al. 2014). With sanidines segmented into distinct regions based on both grayscale value and location, three dimensional reconstructions of these volumes were made (Figure 4.3A-C).

RESULTS

Histograms for each sanidine crystal can be found in Supplementary Figure 1 and compositional data for each crystal gathered using EPMA can be found in Appendix 1. Most samples display multiple CT grayscale feldspar peaks after passed through the non-local means denoising filter (e.g., Figure 4.3E), except for Lava Creek Tuff (LCT-B) sanidines which typically only display one. Likewise, backscattered electron (BSE) imaging of LCT-B sanidines also shows little to no grayscale zoning, whereas sanidines from the other samples display frequent grayscale zoning (Figure 4.4). BaO concentrations in sanidines measured range from near detection limit (~300 μg/g) to 3.7 wt% and brighter BSE zones correspond to

higher BaO contents in all 2D sections analyzed. In the following section, the relationship between CT grayscale and sanidine composition is further explored.

DISCUSSION

Geochemical controls on X-ray attenuation in sanidine

A first order observation in the denoised histograms of sanidine microCT data is that there are multiple peaks corresponding to regions within the minerals that attenuate X-rays to different degrees (Figure 4.3E). In order to translate this observation to useful 3D compositional information we first need to investigate the controls on X-ray attenuation in sanidine. Equation 3 shows that the mass attenuation coefficient (μ_m), and subsequently linear attenuation coefficient (μ_l), of a mixture can be predicted on the basis of the stoichiometric proportions of all elements within a mixture and individual mass attenuation coefficients for a given energy. Because major element chemistry totals measured via EPMA sum to close to 100 wt.% (Appendix 1), they are sufficient to estimate mass attenuation coefficients. Trace elements present in lower concentrations (e.g., Sr, Mg, REE, Pb, etc.) can also be included in this calculation, although typically the lower concentrations mean that attenuation characteristics will have lesser impact on overall attenuation.

In figures 5, 6 we compare the composition of the sanidine with its calculated linear attenuation coefficients and the observed CT greyscale values, respectively. Calculated linear attenuation values and CT grayscale values correlate strongly with observed sanidine composition (Figure 4.5, Figure 4.6). This is consistent with greyscale intensity being directly related to the linear attenuation coefficient for a given voxel (Denison et al. 1997). Moreover, although calculated linear attenuation coefficients show weak correlations with SiO_2, CaO and Na_2O in some samples, for all samples Ba contents are very strongly correlated (Figure 4.5), suggesting that Ba is the primary control on X-ray attenuation and that changes in Ba contents are reflected in the observed changes in greyscale. Other elements display no clear relationship between changes in concentration and changes in calculated linear attenuation coefficient or voxel greyscale in sanidine (Figure 4.5). Although Ba is present at lower concentrations than other stoichiometrically important components, the relatively high atomic weight and resulting photoelectric X-ray attenuation above the K-shell edge of Ba (particularly relative to the other elements present) coupled with the large variations evident in Ba mean that Ba is the primary control on X-ray attenuation in sanidine.

To further test this conclusion, we have also compared measured CT greyscale and measured Ba contents along transects across regions where Ba contents change substantially (Figure 4.7). In these examples we again observe that CT grayscale is strongly correlated with

Ba contents, and not with other elements. Figure 4.8 quantifies both the global and local relationships observed between BaO in the different sanidines studied for this experiment. The data suggest that overall increases in BaO will result in an increase in CT grayscale (Figure 4.8A) and follows the relationship:

5. $BaO\ (wt\%) = (3.4 \times 10^{-4} \pm 1.28 \times 10^{-5})X - (5.974 \pm 0.25)$

Where X is the CT grayscale value. The RMSE for this relationship is 0.275. Rewritten in terms of μg/g Ba, the relationship is:

6. $Ba\ \left(\frac{ug}{g}\right) = (0.1055 \pm 0.004)X - (1867.067 \pm 78.023)$

With a RMSE of 86. Although a single relationship can be used to define the impact of Ba contents of X-ray attenuation, the relatively high RMSE and the observation that sanidine from different samples fall into distinct regions on the plot of BaO vs. CT greyscale (and define different trends) in Figure 4.8B suggest that there may be additional minor controls on X-ray attenuation. As all CT scans were done with the same setup conditions, we hypothesize that the small variations in the exact relation between BaO and X-ray attenuation are due to other elements also contributing more minor changes to the linear attenuation coefficient. For example, we see in both the LCTB and CRT that CaO and Na_2O also have linear relationships with CT grayscale value (Figure 4.6), however the slope of this relationship is much greater in the CRT than it is in the LCTB.

To further quantify the influence other elements have on the overall CT attenuation, we utilized several supervised machine learning regression algorithms, specifically, the random forest (Breiman 2001) and extremely randomized trees (ERT; Geurts et al., 2006) algorithms as they performed the best out of all algorithms tested (e.g., highest R^2 and lowest RMSE values). These algorithms were employed via the scikit-learn package (https://scikit-learn.org/; Pedregosa et al., 2011) in Python as it is 1) open-source and 2) allows one to easily implement both supervised and unsupervised machine learning algorithms (e.g., Petrelli et al. 2020). In brief, our data was split randomly into both training and test datasets, where they consisted of random subsamples from each system studied in this experiment so as to be representative of a wide range of both geochemical characteristics and geologic settings. Once split into training and test datasets, each was standardized and further separated into features (i.e., wt% oxide measurements) and a target (i.e., CT grayscale value). While multiple linear regression also offers a way to incorporate the influence of multiple features on a given target, we prefer the ERT and random forest algorithms as they have both better performance metrics (Figure 4.9) and allow us to quantify the relative importance each feature has on predicting a target value without having to deal with issues related to multicollinearity (e.g., SiO_2, Al_2O_3) that cause

multiple regression coefficients to have limited predictive power. We find that both ERT and random forest algorithms predict observed CT values well (Figure 4.10A) as well as further reinforce the importance of Ba in controlling attenuation Figure 4.10B.

Observing chemical zoning in 3D

Having established the geochemical controls on X-ray attenuation in sanidine now allows us to both observe and quantify chemical zoning in 3D. Using image segmentation previously outlined in the "Image Processing" section we segment individual sanidine grains into "high" (e.g., Figure 4.3E peak 4) and "low" (e.g., Figure 4.3E peak 3) Ba zones for KNT and LCT-B sanidines (Figure 4.11). While the number of segmented regions is ultimately user defined and specific to individual datasets, the designation of distinct high and low Ba zones are justified based on 1) CT data histograms (e.g., Figure 4.3E); 2) previous literature illustrating high and low Ba zones found in sanidines from many of the systems studied (Bachmann et al. 2014; Shamloo and Till 2019; Szymanowski et al. 2019; Rout et al. 2021).

Defining two zones on the basis of Ba also allows us to study the 3D geometry of these regions, and although our sample set is still somewhat limited, we observe a range of different zoning types. Some high-Ba zones were observed as concentric rims (Figure 4.11A,C), consistent with a simple view of progressive crystal growth from magmas with different Ba contents, but other zones also display more complex geometric relationships, such as in intermediate zones between the crystal core and rim, (Figure 4.11B,D,E). The observation of intermediate high-Ba zones is important, as it implies that the magma reservoir processes responsible for producing these zones are not tied to eruption or initiation of eruption, but rather that they occur within a magma reservoir during ongoing magma storage and evolution. This aligns with recent thermal models, showing that large silicic magma reservoirs can reside in the upper crust long periods of time (Gelman et al. 2013) and accommodate volume/pressure changes related to rejuvenation in order to promote growth rather than eruption (de Silva and Gregg 2014).

We also find that some KNT sanidine crystals have high-Ba zones that were largely discontinuous (i.e., they did not form a zone around/throughout the entire grain), did not have uniform thickness, and were never cores of grains. While we note that the markers used for the watershed algorithm may influence the final geometry of mineral zone reconstructions, these observations hold true for all of the grains scanned from the KNT, suggesting that they are representative of features of the sanidines from this system. Previously, these high-Ba zones have been interpreted as the result of cumulate remelting in a thermally heterogeneous magma reservoir prior to eruption (Szymanowski et al. 2019). Our 3D reconstructions of high-Ba zones

agree with this interpretation, as we argue that progressive mineral growth in a closed system is unlikely to produce the wide array of geometries observed here. Rather, as mineral zoning reflects the thermochemical conditions in which the mineral grew, the heterogeneous mineral zoning geometries observed are most likely the result of reservoir scale heterogeneities. Further CT-based works offer the potential for quantitatively examining the shape and distribution of high Ba zones in these samples and in other igneous rocks to test models for magma genesis and evolution.

IMPLICATIONS FOR MINERAL ZONING STUDIES

Gradient Variability Between Two Zones

Assessing the shape of the concentration gradient between two chemical zones is critical for understanding magma evolution, and also for petrologic approaches such as diffusion chronometry. Commonly this approach utilizes either thin sections or mineral grain mounts to analyze the 1D changes in chemistry across a concentration gradient (i.e., chemical zone boundary) within a mineral. Production of thin sections or grain mounts commonly produces random or near random sectioning of crystals, and this can strongly influence the nature of a given concentration gradient (Shea et al. 2015). Slices that are near perpendicular to compositional zoning will have a steeper gradient between zones than slices that are more oblique. At their extremes, slicing perpendicular to zoning will reflect the true gradient shape, while slicing parallel to zoning will show no zoning at all. This effect has been studied numerically using synthetic crystals (Shea et al. 2015; Krimer and Costa 2017), however our information on the 3D distribution of Ba in sanidine allows us to also study this in natural crystals, and simulate the 2D sectioning process by randomly slicing a 3D CT volume. We can then compare this with the profile extracted from a slice perpendicular to the gradient to see the how the shape of that gradient changes with slicing orientation.

As expected, significant variability can be introduced into the shape of gradients between zones simply by randomly slicing the same mineral through its center (Figure 4.12). When combined with slicing orientation information we see that as slices become more perpendicular to the 2D plane that represents the true gradient, profiles both increase in slope and decrease in width (Figure 4.13). Looking at the distribution of slopes across a range of random slice numbers it becomes clear that the highest number of random slices are not centered around the true slope, but rather much shallower (Figure 4.14C) implying that the majority of 2D section profiles from random slices do not reflect the true shape of the concentration gradient between zones.

Similarly, we find that the width of a given concentration gradient is not accurately represented by the mean of random slices and overestimates the true width (Figure 4.14A). Random slicing of a grain across a concentration gradient, however, does accurately capture the height of a concentration gradient (Figure 4.14B). To accurately obtain concentration gradient information (e.g., slope, width, height), Shea and others (2015) suggest that by following a list of criteria (e.g., discarding small grains, constructing profiles away from crystal corners, avoiding profiles with dipping plateaus, when concentric zoning is present avoid zoning that is asymmetric), constructing profiles from 2D sections can more accurately portray the true gradient shape if ~20 well-chosen analytical profiles are constructed. However, it is also true that when 3D information is available, it is possible to no longer speculate about the shape of the concentration gradient between zones but rather to directly observe it by going into the CT stack and extracting a slice perpendicular to CT grayscale zoning. If CT grayscale is governed by changes in a specific element (e.g., Ba in sanidine, Fe-Mg differences in olivine), then accurate 1D, 2D, and 3D diffusion modeling can be completed without ambiguity as to whether or not we are measuring the true shape of the concentration gradient.

Beyond sanidine – barium

While it has been shown here that 3D chemical zoning in Ba can be observed in sanidine, in theory this methodology should not be limited to just sanidine if chemical zones within minerals have a sufficient difference in linear attenuation coefficient. The absolute difference required to observe chemical zoning using microCT, however, depends on the voxel resolution used for imaging and the machine settings (i.e., voltage, current, exposure time) used, which affect image contrast (signal-to-noise ratio). Because the photoelectric effect (and its sensitivity to atomic number) and density are the dominant attenuation mechanisms for energies used in scanning geologic samples, large changes in heavy elements should be relatively easy to observe. This makes minerals with proportionally high concentrations and zoning of heavier elements, such as rare earth elements, actinides (U, Th) and heavier transition metals (e.g., Pb) likely candidates for observing chemical zoning using microCT if they are present in sufficient quantity. Different Fe-Mg olivine populations have already been successfully identified using both monochromatic (Pankhurst et al. 2018) and polychromatic microCT (Pankhurst et al. 2014), making the intracrystalline investigation of Fe-Mg zoning another worthwhile pursuit (cf. NIST Standard Reference Database 66, Chantler, 2000).

One of the current limitations of industrial microCT devices is that they emit polychromatic radiation and are subject to potential imaging artifacts (e.g., beam hardening) and limitations in X-ray output, requiring longer scan times. To overcome these, synchrotron

sources are typically used (e.g. Hanna and Ketcham 2017). The large amount of energy produced by a synchrotron source allows for beam filtration and fine scale 'tuning' over a given energy range (Willmott 2011). The use of this in the petrology community is minimal (e.g., Gualda and Rivers 2006; Gualda et al. 2010; Pamukcu and Gualda 2010; Pankhurst et al. 2018), however the potential is very high, as it allows for one to theoretically focus in on a given element, and scanning above and below the photoelectric absorption edge for that element to allow for subtraction tomography. If utilized, the benefit of this would be twofold: (i) better elemental resolving power and (ii) a range of lower beam energies to subject the sample to, further increasing the contrast in grayscale between chemical zones. This increased contrast would then lead to more accurate segmentation of geochemically distinct phases and allow us to better view the complexities of mineral zoning in 3D and the interpretations that come from its investigation (e.g., diffusion chronometry, mineral growth/dissolution, glomerocryst formation).

ACKNOWLEDGEMENTS

We would like to thank the many people who provided samples for this study: Dawid Szymanowski and Ben Ellis (Kneeling Nun Tuff); Olivier Bachmann and Chad Deering (Carpenter Ridge Tuff); Hannah Shamloo and Christy Till (Lava Creek Tuff). We would also like to thank Frank Tepley and Marie Takach for their expertise and advice gathering microprobe data. This research was supported by National Science Foundation grant NSF-EAR 1654275.

REFERENCES

Anderson, A.T. (1976) Magma mixing: petrological process and volcanological tool. Journal of Volcanology and Geothermal Research, 1, 3–33.

Bachmann, O., Deering, C.D., Lipman, P.W., and Plummer, C. (2014) Building zoned ignimbrites by recycling silicic cumulates: insight from the 1,000 km3 Carpenter Ridge Tuff, CO. Contributions to Mineralogy and Petrology, 167, 1025.

Breiman, L. (2001) Random forests. In R.E. Schapire, Ed., Machine Learning pp. 5–32. Kluwer Academic Publishers.

Buades, A., Coll, B., and Morel, J.M. (2005) A non-local algorithm for image denoising. In Proceedings - 2005 IEEE Computer Society Conference on Computer Vision and Pattern Recognition, CVPR 2005 Vol. II, pp. 60–65.

Chambers, M., Memeti, V., Eddy, M.P., and Schoene, B. (2020) Half a million years of magmatic history recorded in a K-feldspar megacryst of the tuolumne intrusive complex, California, USA. Geology, 48, 400–404.

Chantler, C.T. (2000) Detailed Tabulation of Atomic Form Factors, Photoelectric Absorption and Scattering Cross Section, and Mass Attenuation Coefficients in the Vicinity of Absorption Edges in the Soft X-Ray (Z=30-36,Z=60-89,E=0.1 keV-10 keV), Addressing Convergence Issues of. J. Phys. Chem. Ref. Data, 29, 597–1048.

Cnudde, V., and Boone, M.N. (2013) High-resolution X-ray computed tomography in geosciences: A review of the current technology and applications. Earth-Science Reviews, 123, 1–17.

Cooper, K.M. (2017) What does a magma reservoir look like? the “crystal’s-eye” view. Elements, 13, 23–28.

Cooper, K.M., and Kent, A.J.R. (2014) Rapid remobilization of magmatic crystals kept in cold storage. Nature, 506, 480–3.

Costa, F., and Dungan, M. (2005) Short time scales of magmatic assimilation from diffusion modeling of multiple elements in olivine. Geology, 33, 837–840.

Costa, F., Chakraborty, S., and Dohmen, R. (2003) Diffusion coupling between major and trace elements and a model for the calculation of magma chamber residence times using plagioclase. Geochimica et Cosmochimica Acta, 67, 2189–2200.

Davidson, J., Tepley, F., Palacz, Z., and Meffan-Main, S. (2001) Magma recharge, contamination and residence times revealed by in situ laser ablation isotopic analysis of feldspar in volcanic rocks. Earth and Planetary Science Letters, 184, 427–442.

Davidson, J.P., and Tepley, F.J. (1997) Recharge in Volcanic Systems: Evidence from Isotope Profiles of Phenocrysts. Science, 275, 826–829.

de Silva, S.L., and Gregg, P.M. (2014) Thermomechanical feedbacks in magmatic systems: Implications for growth, longevity, and evolution of large caldera-forming magma reservoirs and their supereruptions. Journal of Volcanology and Geothermal Research, 282, 77–91.

Deer, W.A., Howie, R.A., and Zussman, J. (1966) An Introduction to the Rock-Forming Minerals. An Introduction to the Rock-Forming Minerals.

Denison, D., Carlson, W.D., and Ketcham, R.A. (1997) Three-dimensional quantitative textural analysis of metamorphic rocks using high-resolution computed X-ray tomography : Part I . Methods and techniques. Journal of metamorphic Geology, 15, 29–44.

Eichelberger, J.C. (1975) Origin of andesite and dacite: Evidence of mixing at Glass Mountain in California and at other circum-Pacific volcanoes. Bulletin of the Geological Society of America, 86, 1381–1391.

Forni, F., Petricca, E., Bachmann, O., Mollo, S., De Astis, G., and Piochi, M. (2018) The role of magma mixing/mingling and cumulate melting in the Neapolitan Yellow Tuff caldera-forming eruption (Campi Flegrei, Southern Italy). Contributions to Mineralogy

and Petrology, 173, 1–18.
Gelman, S.E., Gutiérrez, F.J., and Bachmann, O. (2013) On the longevity of large upper crustal silicic magma reservoirs. Geology, 41.
Geurts, P., Ernst, D., and Wehenkel, L. (2006) Extremely randomized trees. Machine Learning, 63, 3–42.
Ginibre, C., Wörner, G., and Kronz, A. (2004) Structure and dynamics of the Laacher See magma chamber (Eifel, Germany) from major and trace element zoning in sanidine: A cathodoluminescence and electron microprobe study. Journal of Petrology, 45, 2197–2223.
Gualda, G.A.R., and Rivers, M. (2006) Quantitative 3D petrography using x-ray tomography: Application to Bishop Tuff pumice clasts. Journal of Volcanology and Geothermal Research, 154, 48–62.
Gualda, G.A.R., Pamukcu, A.S., Claiborne, L.L., and Rivers, M.L. (2010) Quantitative 3D petrography using X-ray tomography 3: Documenting accessory phases with differential absorption tomography. Geosphere, 6, 782–792.
Hanna, R.D., and Ketcham, R.A. (2017) X-ray computed tomography of planetary materials: A primer and review of recent studies. Chemie der Erde - Geochemistry, 77, 547–572.
Higgins, M.D. (2000) Measurement of crystal size distributions. American Mineralogist, 85, 1105–1116.
Icenhower, J., and London, D. (1996) Experimental partioning of Rb, Cs, Sr and ba between Alkali feldspar and peraluminous melt. American Mineralogist, 81, 719–734.
Jähne, B., Haußecker, H., and Geißler, P. (1999) 3D computer vision and applications. Proceedings - International Conference on Pattern Recognition Vol. 1.
Kent, A.J.R., Darr, C., Koleszar, A.M., Salisbury, M.J., and Cooper, K.M. (2010) Preferential eruption of andesitic magmas through recharge filtering. Nature Geoscience, 3, 631–636.
Krimer, D., and Costa, F. (2017) Evaluation of the effects of 3D diffusion, crystal geometry, and initial conditions on retrieved time-scales from Fe–Mg zoning in natural oriented orthopyroxene crystals. Geochimica et Cosmochimica Acta, 196, 271–288.
Lipman, P.W., and McIntosh, W.C. (2008) Eruptive and noneruptive calderas, northeastern San Juan Mountains, Colorado: Where did the ignimbrites come from? Geological Society of America Bulletin, 120, 771–795.
Lubbers, J. (2021) CTPy, GitHub repository, https: // doi.org/10.5281/zenodo.4540942
Lubbers, J., Deering, C., and Bachmann, O. (2020) Genesis of rhyolitic melts in the upper crust : Fractionation and remobilization of an intermediate cumulate at Lake City caldera, Colorado, USA. Journal of Volcanology and Geothermal Research, 392.
Matthews, N.E., Vazquez, J.A., and Calvert, C.T. (2015) Age of the Lava Creek supereruption and magma chamber assembly at Yellowstone based on 40Ar/39Ar and U-Pb dating of sanidine and zircon crystals. Geochemistry, Geophysics, Geosystems.
Mccullough, E.C. (1975) Photon attenuation in computed tomography. Medical Physics, 2, 307–320.
Mcintire, W.I.L. (1963) McIntire_1963_Partition coefficients. Geochimica et Cosmochimica Acta, 27, 1209–1264.
Morgan, D.J., and Blake, S. (2006) Magmatic residence times of zoned phenocrysts: Introduction and application of the binary element diffusion modeling (BEDM) technique. Contributions to Mineralogy and Petrology, 151, 58–70.
Mourey, A.J., and Shea, T. (2019) Forming Olivine Phenocrysts in Basalt: A 3D Characterization of Growth Rates in Laboratory Experiments. Frontiers in Earth Science, 7, 1–16.
Pamukcu, A.S., and Gualda, G.A.R. (2010) Quantitative 3D petrography using X-ray tomography 2: Combining information at various resolutions. Geosphere, 6, 775–781.

Pankhurst, M.J., Dobson, K.J., Morgan, D.J., Loughlin, S.C., Thordarson, T.H., Lee, P.D., and Courtois, L. (2014) Monitoring the magmas fuelling volcanic eruptions in near-real-time using x-ray micro-computed tomography. Journal of Petrology, 55, 671–684.

Pankhurst, M.J., Vo, N.T., Butcher, A.R., Long, H., Wang, H., Nonni, S., Harvey, J., Gucrossed, G.D.S., Fowler, R., Atwood, R., and others (2018) Quantitative measurement of olivine composition in three dimensions using helical-scan X-ray micro-tomography. American Mineralogist, 103, 1800–1811.

Pedregosa, F., Varoquaux, G., Alexandre, G., Michel, V., Thirion, B., Grisel, O., Blondel, M., Prettenhofer, P., Weiss, R., Dubourg, V., and others (2011) Scikit-learn: Machine Learning in Python. Journal of Machine Learning Research, 12, 2825–2830.

Petrelli, M., Caricchi, L., and Perugini, D. (2020) Machine Learning Thermo-Barometry: Application to Clinopyroxene-Bearing Magmas. Journal of Geophysical Research: Solid Earth, 125.

Reddy, S.M., Saxey, D.W., Rickard, W.D.A., Fougerouse, D., Montalvo, S.D., Verberne, R., and van Riessen, A. (2020) Atom Probe Tomography: Development and Application to the Geosciences. Geostandards and Geoanalytical Research, 44, 5–50.

Rickard, W.D.A., Reddy, S.M., Saxey, D.W., Fougerouse, D., Timms, N.E., Daly, L., Peterman, E., Cavosie, A.J., and Jourdan, F. (2020) Novel Applications of FIB-SEM-Based ToF-SIMS in Atom Probe Tomography Workflows. Microscopy and Microanalysis, 26, 750–757.

Roerdink, J.B.T.M., and Meijster, A. (2000) The watershed transform: definitions, algorithms and parallelization strategies. Fundamenta Informaticae, 41, 187–228.

Rout, S.S., Blum-Oeste, M., and Wörner, G. (2021) Long-term temperature cycling in a shallow magma reservoir : insights from sanidine megacrysts at Taápaca volcano , Central Andes ABSTRACT : Journal of Petrology.

Rubin, A.E., Cooper, K.M., Till, C.B., Kent, A.J.R., Costa, F., Bose, M., Gravley, D., Deering, C., and Cole, J. (2017) Rapid cooling and cold storage in a silicic magma reservoir recorded in Individual Crystals. Science, 356, 1154–1156.

Ruprecht, P., and Plank, T. (2013) Feeding andesitic eruptions with a high-speed connection from the mantle. Nature, 500, 68–72.

Schneider, C.A., Rasband, W.S., and Eliceiri, K.W. (2012) NIH Image to ImageJ : 25 years of image analysis. Nature Methods, 9, 671–675.

Shamloo, H.I., and Till, C.B. (2019) Decadal transition from quiescence to supereruption: petrologic investigation of the Lava Creek Tuff, Yellowstone Caldera, WY. Contributions to Mineralogy and Petrology, 174, 1–18.

Shea, T., Costa, F., Krimer, D., and Hammer, J.E. (2015) Accuracy of timescales retrieved from diffusion modeling in olivine: A 3D perspective. American Mineralogist, 100, 2026–2042.

Sheppard, A., Latham, S., Middleton, J., Kingston, A., Myers, G., Varslot, T., Fogden, A., Sawkins, T., Cruikshank, R., Saadatfar, M., and others (2014) Techniques in helical scanning, dynamic imaging and image segmentation for improved quantitative analysis with X-ray micro-CT. Nuclear Instruments and Methods in Physics Research, Section B: Beam Interactions with Materials and Atoms, 324, 49–56.

Simonetti, A., Shore, M., and Bell, K. (1996) Diopside phenocrysts from nephelinite lavas, Napak volcano, eastern Uganda: Evidence for magma mixing. Canadian Mineralogist, 34, 411–421.

Singer, B.S., Dungan, M.A., and Layne, G.D. (1995) Textures and Sr,Ba,Mg,Fe,K, and Ti compositional profiles in volcanic plagioclase: Clues to the dynamics of calc-alkaline magma chambers. American Mineralogist, 80, 833–840.

Spear, F.S., and Daniel, C.G. (2003) Three-dimensional imaging of garnet porphyroblast sizes and chemical zoning: Nucleation and growth history in the garnet zone. American

Mineralogist, 88, 245.
Streck, M.J., Dungan, M.A., Bussy, F., and Malavassi, E. (2005) Mineral inventory of continuously erupting basaltic andesites at Arenal volcano, Costa Rica: Implications for interpreting monotonous, crystal-rich, mafic arc stratigraphies. Journal of Volcanology and Geothermal Research, 140, 133–155.
Szymanowski, D., Wotzlaw, J.-F., Ellis, B.S., Bachmann, O., Guillong, M., and von Quadt, A. (2017) Protracted near-solidus storage and pre-eruptive rejuvenation of large magma reservoirs. Nature Geoscience, 10.
Szymanowski, D., Ellis, B.S., Wotzlaw, J.-F., and Bachmann, O. (2019) Maturation and rejuvenation of a silicic magma reservoir: High-resolution chronology of the Kneeling Nun Tuff. Earth and Planetary Science Letters, 510, 103–115.
Tajčmanová, L., Abart, R., Wirth, R., Habler, G., and Rhede, D. (2012) Intracrystalline microstructures in alkali feldspars from fluid-deficient felsic granulites: A mineral chemical and TEM study. Contributions to Mineralogy and Petrology, 164, 715–729.
Tepley, F.J., Davidson, J.P., Tilling, R.I., and Arth, J.G. (2000) Magma mixing, recharge, and eruption histories recorded in plagioclase phenocrysts from El Chichon Volcano, Mexico, 41, 1397–1411.
Till, C.B., Vazquez, J.A., and Boyce, J.W. (2015) Months between rejuvenation and volcanic eruption at Yellowstone caldera, Wyoming. Geology, 43, 695–698.
Tsuchiyama, A., Nakano, T., Uesugi, K., Uesugi, M., Takeuchi, A., Suzuki, Y., Noguchi, R., Matsumoto, T., Matsuno, J., Nagano, T., and others (2013) Analytical dual-energy microtomography: A new method for obtaining three-dimensional mineral phase images and its application to Hayabusa samples. Geochimica et Cosmochimica Acta, 116, 5–16.
Uesugi, M., Uesugi, K., and Oka, M. (2010) Non-destructive observation of meteorite chips using quantitative analysis of optimized X-ray micro-computed tomography. Earth and Planetary Science Letters, 299, 359–367.
Van Der Walt, S., Schönberger, J.L., Nunez-Iglesias, J., Boulogne, F., Warner, J.D., Yager, N., Gouillart, E., and Yu, T. (2014) Scikit-image: Image processing in python. PeerJ, 2014, 1–18.
Van Grieken, R., and Markowicz, A. (2002) Handbook of X-Ray Spectrometry, Second Edition. Marcel Dekker, Inc.
Varslot, T., Kingston, A., Sheppard, A., and Sakellariou, A. (2011) Fast high-resolution micro-CT with exact reconstruction methods. Developments in X-Ray Tomography VII, 7804, 780413.
Vincent, L., and Soille, P. (1991) Watersheds in Digital Spaces: An Efficient Algorithm Based on Immersion Simulations. IEEE Transactions on Pattern Analysis and Machine Intelligence, 13, 583–598.
Wildenschild, D., and Sheppard, A.P. (2013) X-ray imaging and analysis techniques for quantifying pore-scale structure and processes in subsurface porous medium systems. Advances in Water Resources, 51, 217–246.
Willmott, P. (2011) An Introduction to Synchrotron Radiation. An Introduction to Synchrotron Radiation.
Wirth, R. (2009) Focused Ion Beam (FIB) combined with SEM and TEM: Advanced analytical tools for studies of chemical composition, microstructure and crystal structure in geomaterials on a nanometre scale. Chemical Geology, 261, 217–229.
Wolff, J.A., Ellis, B.S., Ramos, F.C., Starkel, W.A., Boroughs, S., Olin, P.H., and Bachmann, O. (2015) Remelting of cumulates as a process for producing chemical zoning in silicic tuffs: A comparison of cool, wet and hot, dry rhyolitic magma systems. Lithos, 236–237, 275–286.
Wolff, J.A., Forni, F., Ellis, B.S., and Szymanowski, D. (2020) Europium and barium

enrichments in compositionally zoned felsic tuffs: A smoking gun for the origin of chemical and physical gradients by cumulate melting. Earth and Planetary Science Letters, 540, 116251.

Zhang, Y. (2010) Diffusion in minerals and melts: Theoretical background. Reviews in Mineralogy and Geochemistry, 72, 5–59.

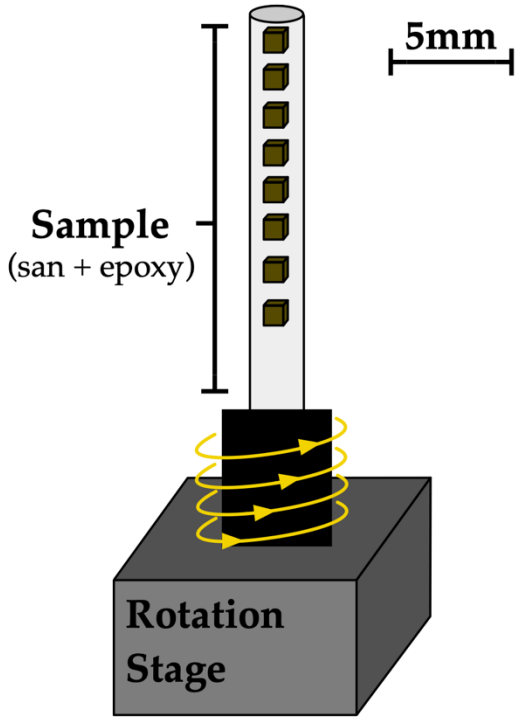

Figure 4.1: Schematic of the sample setup used in the microtomographic scanning. Sanidine grains were mounted vertically in a thin epoxy rod and placed in the sample holder on the helical rotation stage. This allowed for a source to sample distance of 5mm, and the helical trajectory subsequently allowed for numerous grains to be scanned in one single (long) scan at high resolution.

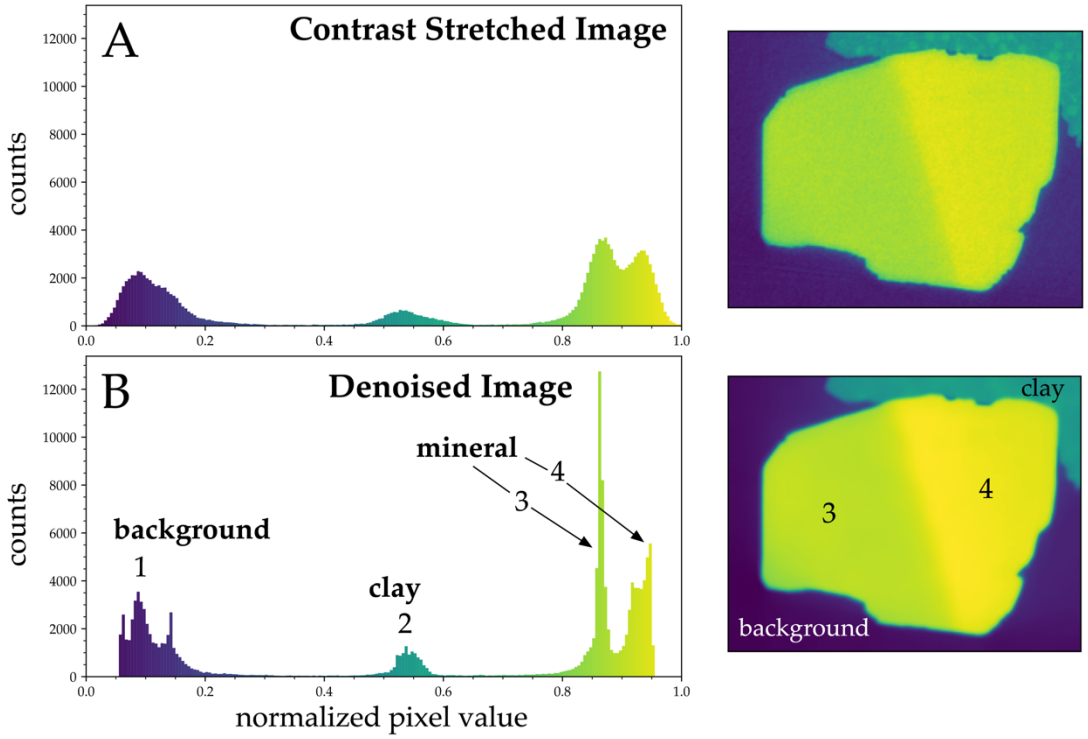

Figure 4.2: Individual CT slices extracted from the 3D dataset and their corresponding histograms. A) raw, unfiltered data that shows changes in pixel value within the mineral, however there is significant overlap between the mineral peaks (3 and 4). B) same slice processed using a non-local means filter (using Python's scikit-image). The slice histogram now has resolvable peaks that better correspond to distinct mineral regions and allows for reliable image segmentation, and subsequent quantification.

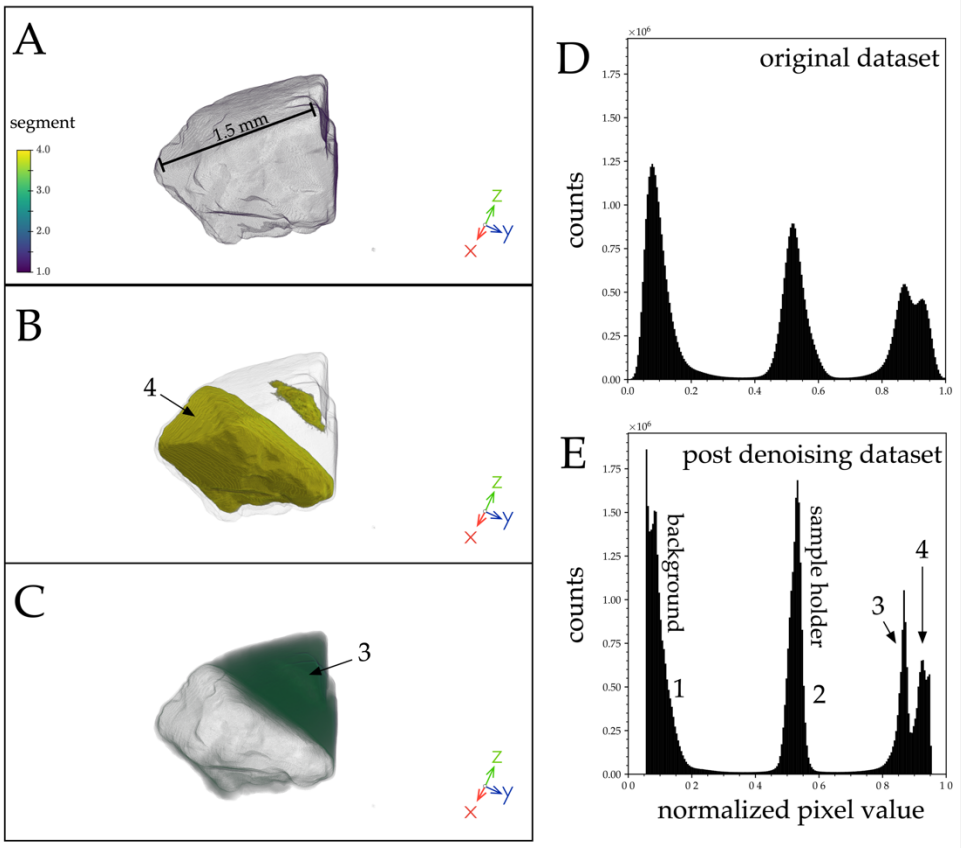

Figure 4.3: 3D rendering of a segmented sanidine from the Kneeling Nun Tuff and the same grain shown in Figure 1KNT. A, B, and C all have the same orientation. A) Whole mineral. B) Mineral zone that corresponds to peak 4 in the post denoising histogram. C) Mineral zone that corresponds to peak 3 in the post denoising histogram. E) Raw CT data histogram and D) denoised histogram justifying the segments used to train the watershed algorithm.

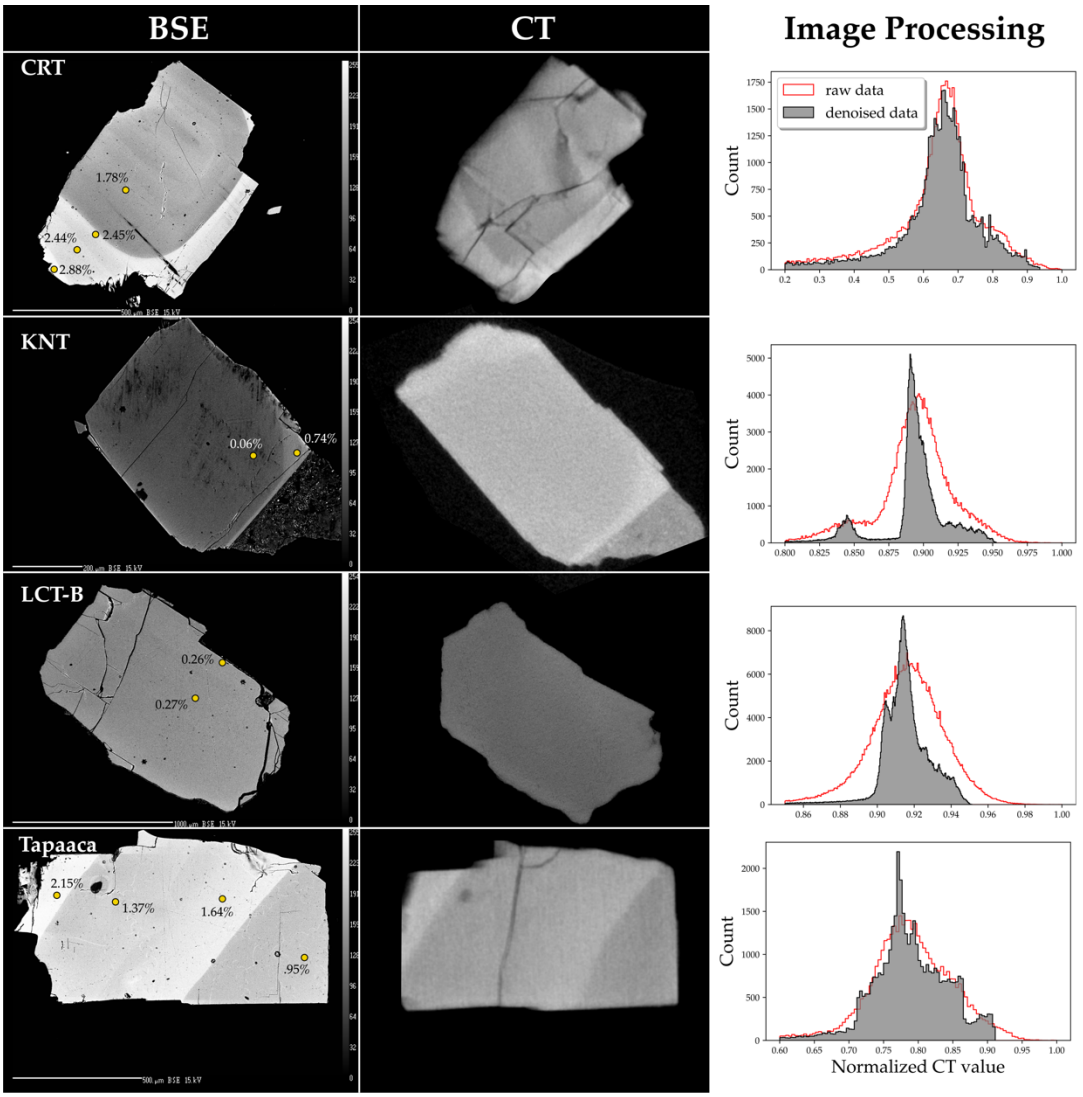

Figure 4.4: Representative sanidine grains from each system studied comparing BSE (left) and CT (middle) grayscale images for similar 2D slices through the same grain. Yellow spots annotated on BSE images indicate locations for EPMA spot analyses and BaO concentrations are listed next to each spot. The right panel shows histograms of normalized CT grayscale values for both raw data (red line) and denoised data (black line with gray fill) for each grain and illustrates its ability to sufficiently remove Gaussian noise such that mineral zoning in CT can be quantified via image segmentation methods.

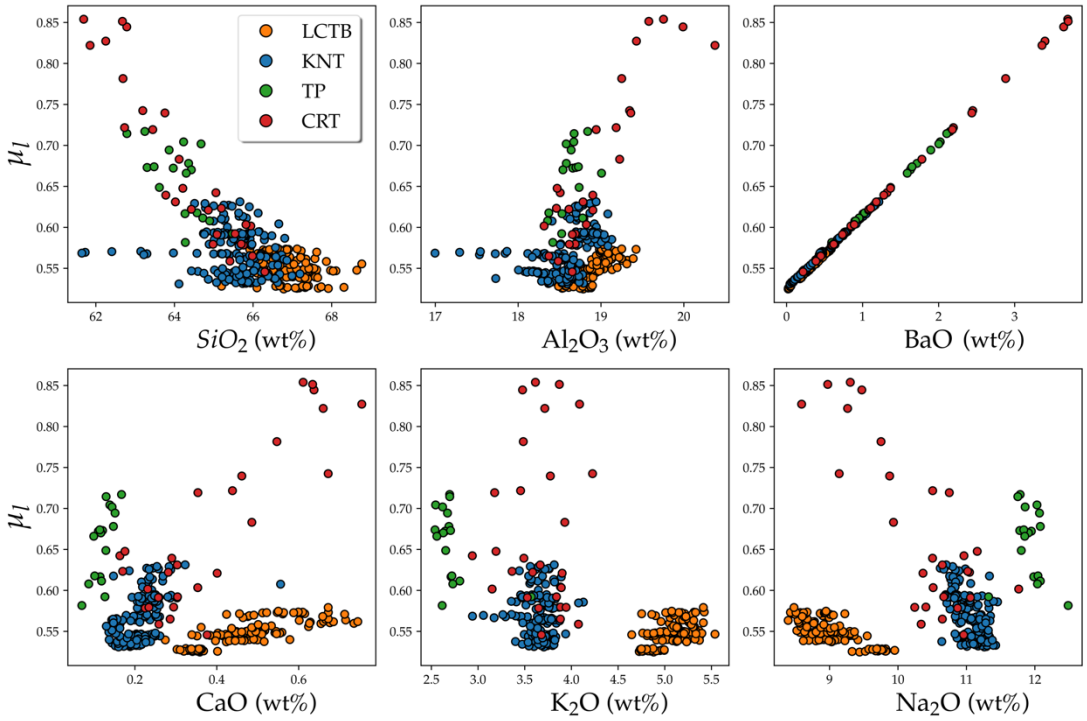

Figure 4.5: Calculated linear attenuation coefficient (μ) plotted against major element compositions for each analysis. While the Carpenter Ridge Tuff displays weak linear correlations between μ and CaO and Na2O, BaO shows strong linear correlations with μ for all sanidines studied in this project.

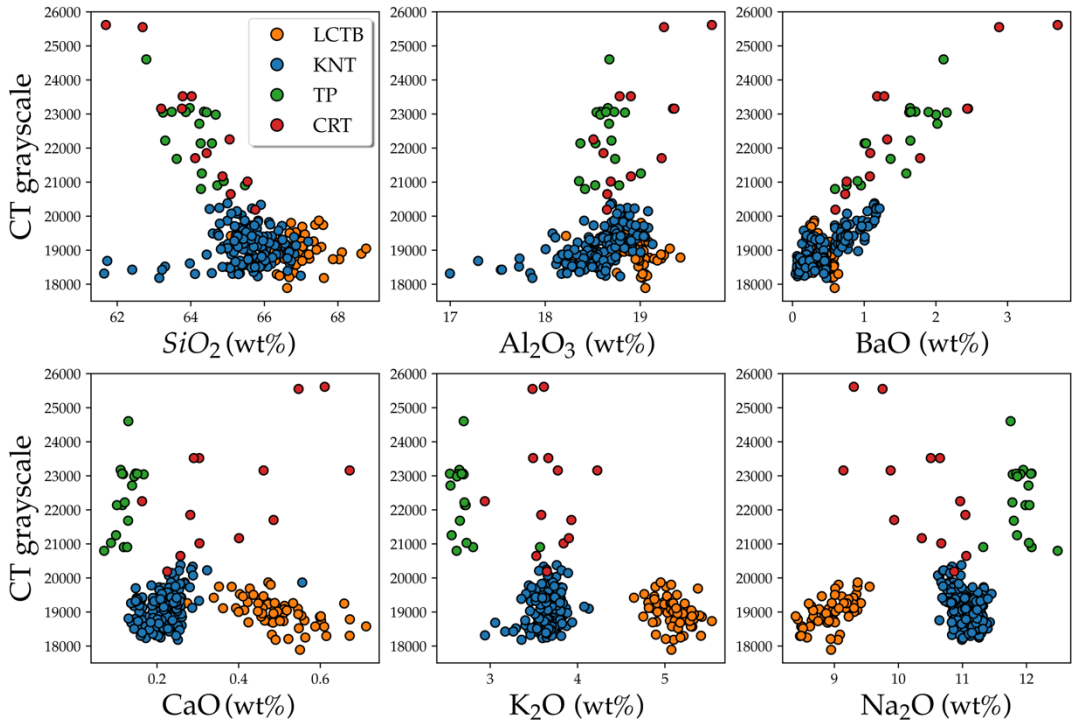

Figure 4.6: Observed CT grayscale for the same location on a given sanidine that EPMA analyses were completed, plotted against major element compositions for the same location. The shape of the observed CT grayscale vs. major element relationships qualitatively looks similar to that described by the μ vs. major element relationships shown in Figure 4. This is in agreement with Denison et al. (1997), which shows that CT grayscale is linearly related to μ.

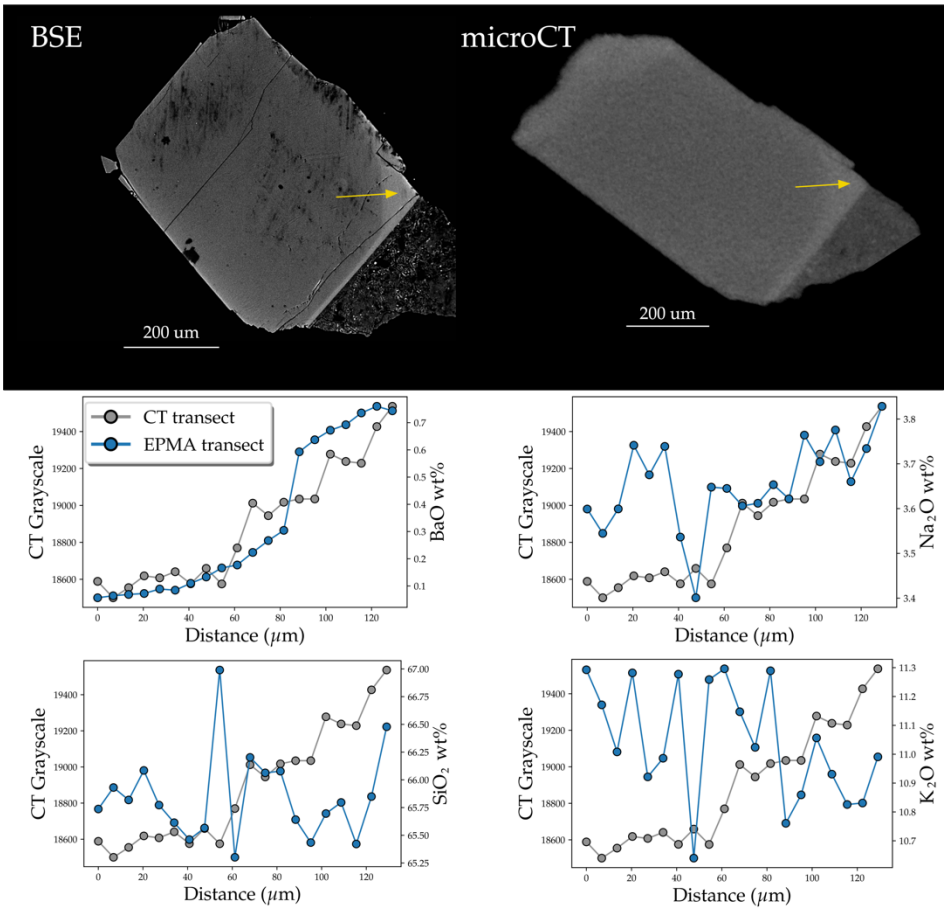

Figure 4.7: Comparison of BSE image and CT grayscale image for the same plane through a KNT sanidine. Yellow lines illustrate location of the EPMA and CT transects that are plotted below. Both show the same relative changes in magnitude and have similar slopes. This further adds to the relationships shown in Figure 4 by adding in a spatial component and shows that CT grayscale is largely controlled by Ba concentrations throughout the mineral.

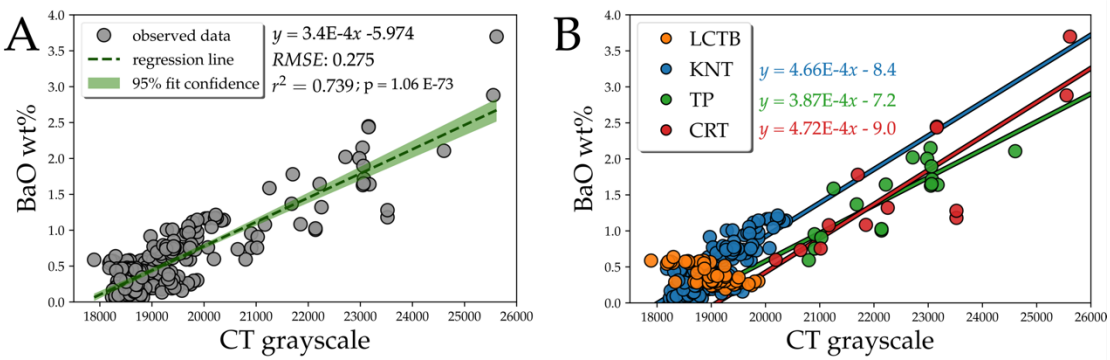

Figure 4.8 A) Regression for Ba vs. CT relationship for all sanidines studied in this experiment. B) Regression for Ba vs. CT for each individual eruption studied in this experiment. Note there is no regression for the LCTB, as it displayed too narrow a range in BaO concentrations. While KNT, TP, and CRT sanidines all show a linear correlation between BaO and CT grayscale, the parameters that define each relationship vary slightly, suggesting that although BaO is largely responsible for controlling X-ray attenuation in sanidine, its influence on each system is not the same.

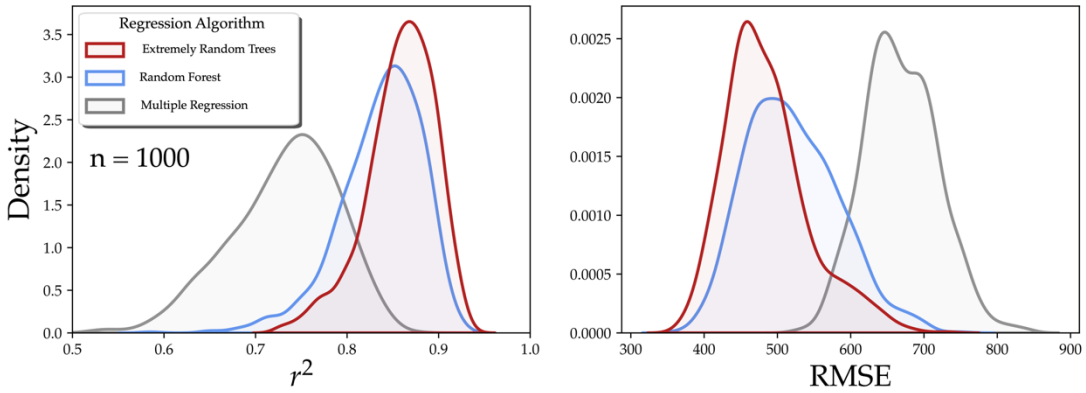

Figure 4.9: R2 and Root Mean Squared Error (RMSE) of predicted CT grayscale results of a Monte Carlo simulation in which each machine learning algorithm for predicting CT values was run 1000 times. For every iteration, the splitting, training, and validation steps for each algorithm were randomized so as to remove bias of any one iteration on the overall interpretation of a given algorithm's accuracy and precision. The Extremely Random Trees (ERT) regression algorithm performs the best by both R2 (mean = 0.86) and RMSE (mean = 487) metrics, therefore making it the preferred algorithm for predicting CT grayscale in this study.

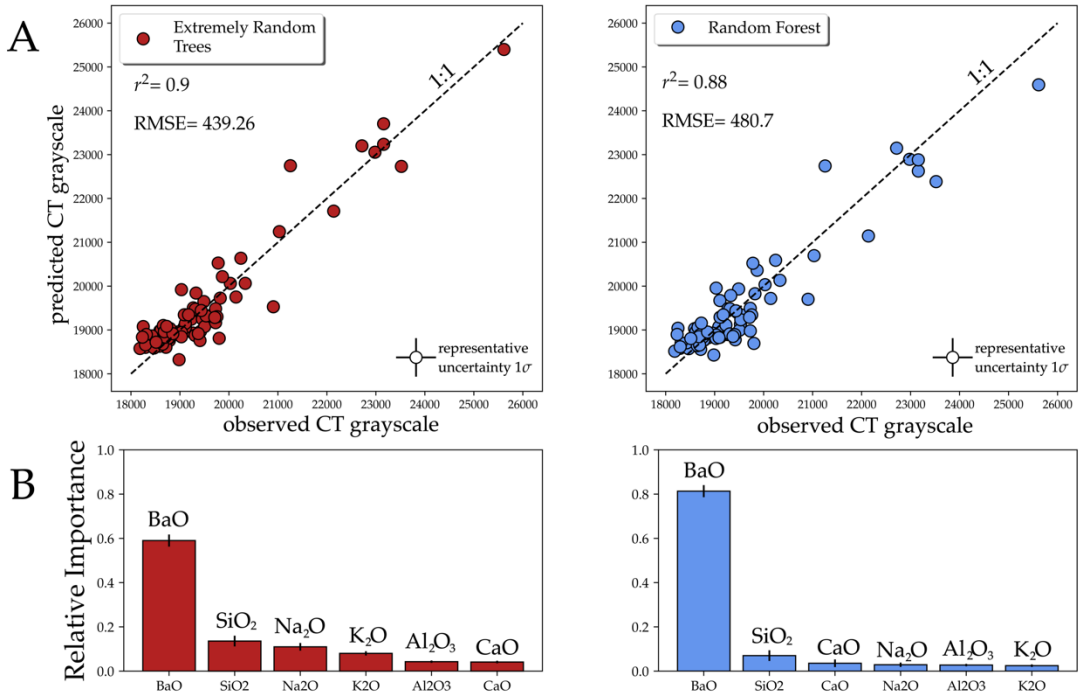

Figure 4.10 A) scatter plot of predicted vs. observed CT grayscale values from the ERT (left) and random forest (right) algorithms for one of the random iterations of the Monte Carlo simulation shown in Figure 8 illustrating that they: 1) accurately predict the observed CT values (e.g., falls along a 1:1 predicted vs. observed line); 2) produces low RMSE values relative to the overall attenuation signal (i.e., < 3%). B) bar charts displaying the relative importance of each feature used in the regression algorithms. The height of the bars is the mean value of each feature's importance from the Monte Carlo simulation and error bars are 1σ uncertainties for each mean value. Note, the total height of all the bars is equal to 1. Single feature values closer to 0 are not as useful at predicting the target and values closer to 1 are extremely useful at predicting the target. Barium displays the highest feature importance in both algorithms and accounts for the majority of information required to accurately predict CT grayscale values, suggesting it is largely responsible for controlling X-ray attenuation in sanidine.

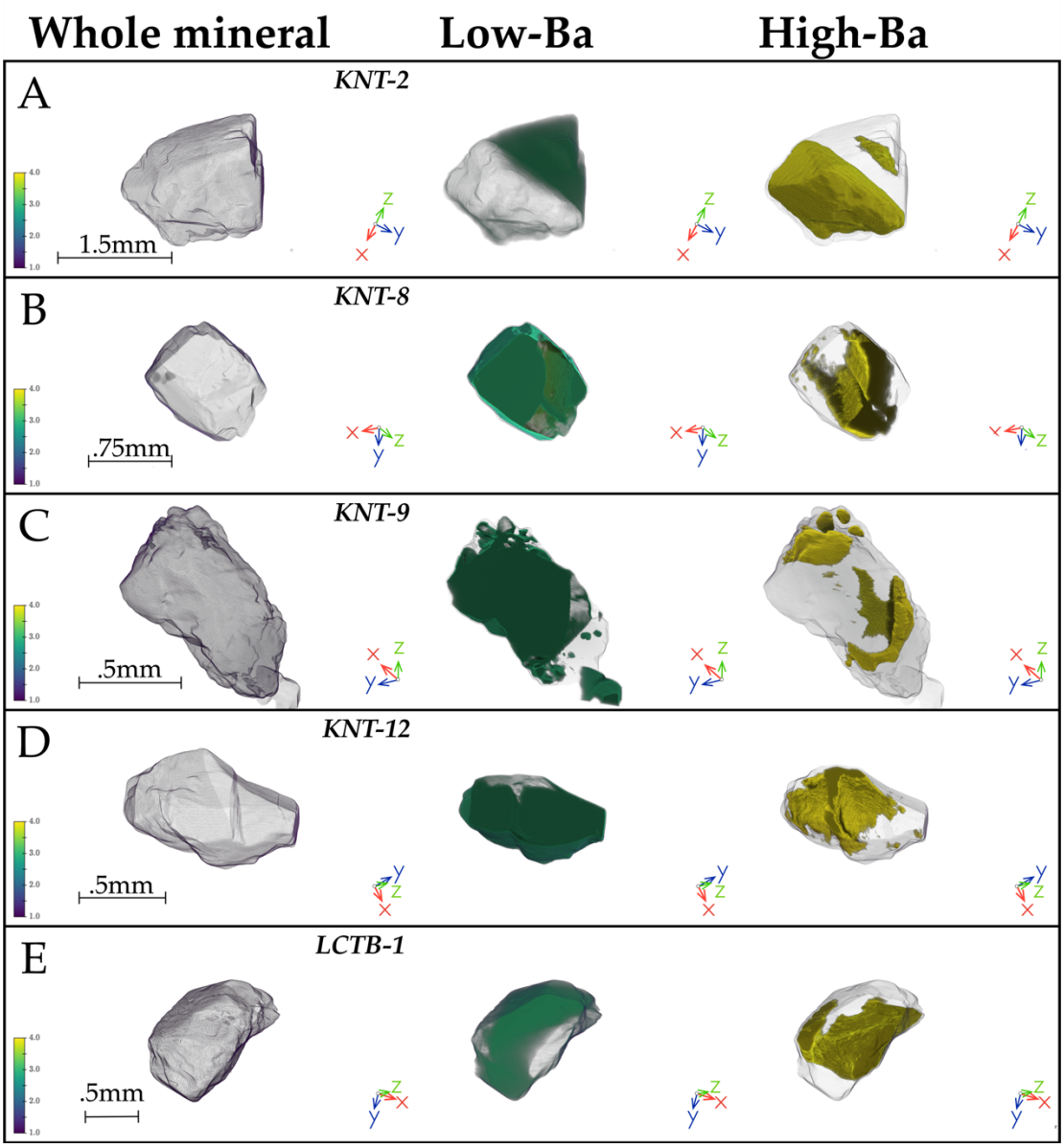

Figure 4.113D volume reconstructions of chosen sanidines segmented in this study. Left column is entire mineral outline, center column green isosurfaces represent extent of zones classified as "low-Ba" within the grain, and right column yellow isosurfaces outline extent of areas within the grain classified as "high-Ba". Rows A-D are grains from the Kneeling Nun Tuff and row E is a Lava Creek Tuff – B sanidine. Note that zoning patterns are frequently: 1) not always concentric and 2) not always on the rims of the grain.

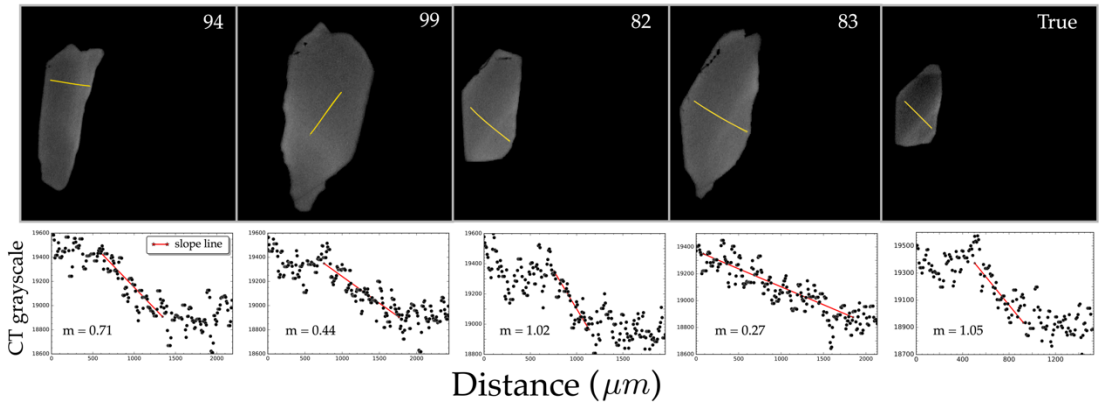

Figure 4.12: Selected random slices and their corresponding CT grayscale profile perpendicular to observed zoning from grain LCTB – 1 shown in Figure 4.10E. Grayscale profiles display a wide range of widths and slopes, illustrating the effect that random slicing through a grain has on the interpretation of chemical zoning.

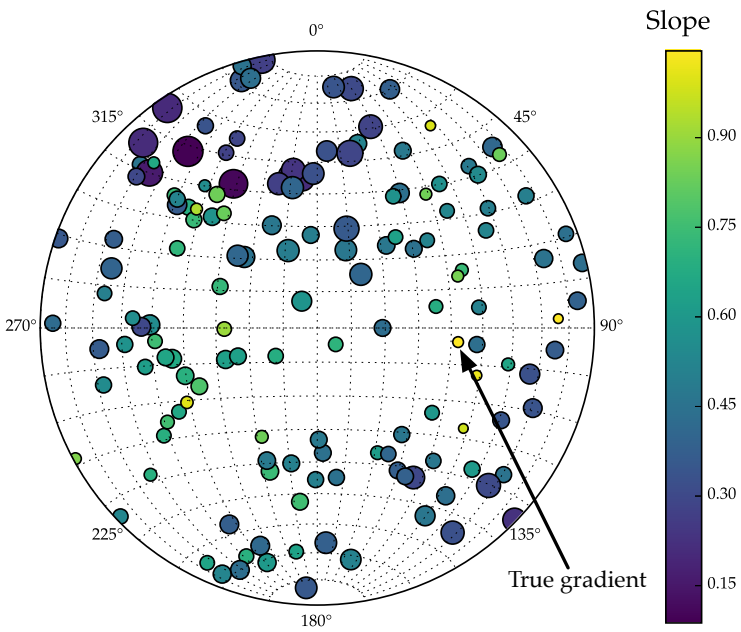

Figure 4.13: Stereonet of 150 random slices through crystal LCTB – 1 shown in Figure 4.10E, where each pole to the plane for a given random slice is a spot on the stereonet. Here, degrees are in arbitrary 3D space, not cardinal directions. Colors of each spot are mapped to the slope of the concentration gradient, while the size of each spot is mapped to the width. Overall, shallower slopes and longer profile widths are associated with slices that are more parallel to the true gradient orientation (e.g., upper left on the stereonet).

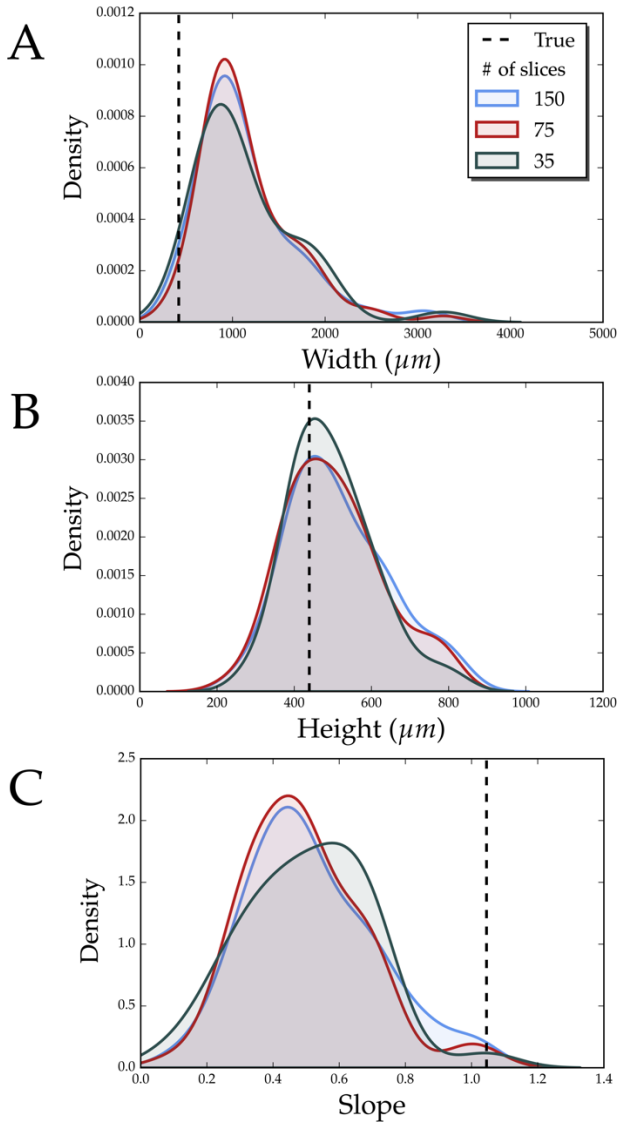

Figure 4.14: Breakdown of random slicing exercise in which 35, 75, and 150 random slices were generated through the center of grain LCTB-1, shown in Figure 4.10E. Slices were through the center of the grain so as to ensure that the concentration gradient was intersected by the slice. A) Kernel density estimates (KDE) of concentration gradient widths illustrating how the true width of a concentration gradient is overestimated by majority of slices B) KDE plot for gradient heights. Here, the random slicing exercise suggests that the mean of random slicing more accurately portrays the height of a given concentration gradient C) KDE plot for gradient slopes. Similar to A, the majority of slices do not reflect the true slope of a given concentration gradient and the majority of slopes generated from random slicing are significantly less than the true slope of the concentration gradient.

Table 4.1: Standards utilized in EPMA experiment calibration for each element measured, along with the relative standard error and detection limit for each element measured. ALBI and SANI standards are synthetic albite and sanidine standards made by Astimex Scientific Ltd and NMNH standards are from the collection at the Smithsonian Museum of Natural History. Established concentrations can be found in the Appendix 1.

Standard	Element	Relative Standard Error (%)	Detection limit (μg/g)
ALBI	Na	0.40	334
SANI	Si	0.12	684
SANI	Al	0.14	336
SANI	K	0.17	438
SANI	Ba	0.28	309
NMNH 115900	Ca	21.61	357
NMNH 113498-1	Fe	4.77	812

Table 4.2 List of programs/software used in this research and what each was used for.

Program/Software	**Use**
Avizo ®	Dataset cropping, 2D slicing of dataset (both random and non-random)
Fiji/ImageJ (Schneider et al. 2012):	Image measurement functions (i.e. linear grayscale profiles, ROI histograms), adjusting image brightness/contrast
Python/JupyterLab ©	Dataset cropping, image denoising, image segmentation, image statistics, interactive volume reconstructions. Utilizes the package scikit-image (Van Der Walt et al. 2014) and volume reconstructions require package K3D-jupyter ©

CHAPTER FIVE: OPEN-SOURCE DATA PROCESSING FOR LA-ICP-MS SPOT DATA: LASERTRAM AND LASERCALC

Jordan Lubbers
Adam Kent
Chris Russo

ABSTRACT

We present an open-source user friendly and web-hosted graphical user interface (GUI) pair for the reduction of laser ablation inductively coupled plasma mass spectrometry (LA-ICP-MS): Laser Time Resolved Analysis Module (LaserTRAM) and LaserCalc. In the first sections we present the background math that governs the calculations and in the second half we provide a walkthrough on how to use the programs to calculate concentrations from LA-ICP-MS spot analyses of silicate minerals.

INTRODUCTION

Laser ablation inductively coupled plasma mass spectrometry (LA-ICP-MS) is a now a commonplace tool for the gathering of trace element (i.e., < .1 wt%) in the fields of igneous petrology and geochemistry. The last two decades have seen significant advances in both instrument capabilities and operating software allowing users to generate large volumes of *in situ* geochemical data in comparatively little time to previous methodologies (i.e., micro-drilling) while still maintaining high degrees of accuracy and precision. This has led to researchers generating significantly more trace element data in their projects and, ultimately, tackling questions that can only be answered with larger datasets pushing their fields forward into a more "data-driven" age.

Raw data output from LA-ICP-MS, however, is in the form of counts per second (cps), not elemental concentrations (Figure 5.1). When integrated over a certain period of time (e.g., the duration of an analysis), a total number of counts for a given analyte per spot analysis can be quantified. This number is a function of many things, but namely: the number of analytes being analyzed, the dwell time of the ICP-MS on each analyte, and the total analysis time. While important to understand the so-called "ins and outs" of LA-ICP-MS, to help maximize the quality of data output from the instrument, they are not requisite for calculating concentrations from raw data. Currently, there are several proprietary and open-source software tools (e.g., SILLS - Guillong et al., 2008; Iolite - Paton et al., 2011; LAtools - Branson et al., 2019; TERMITE - Mischel et al., 2017; GLITTER) and countless other "in house" spreadsheet-based tools for LA-ICP-MS data reduction. All have their strengths and weaknesses, however, there is yet to be a powerful, web-hosted Graphical User Interface (GUI).

This document outlines how data gathered from a Photon Machines Analyte G2193 ArF Excimer laser system connected to a ThermoFisher Scientific iCAP-RQ ICP-MS is converted from raw counts per second data into concentrations ($\mu g \cdot g^{-1}$) using a pair of

programs: Laser Time Resolved Analysis Module (LaserTRAM) and LaserCalc. LaserTRAM and LaserCalc, however, will work with data generated via virtually any common LA-ICP-MS setup provided they are in the right input format. At the end there is also a short walk through on how to use them both. In brief, each has a specific role in the process of LA-ICP-MS data reduction:

- LaserTRAM: takes raw counts per second data and user input decisions to determine an interval of interest for each spot analysis. It then determines the ratio of each analyte to a chosen internal standard analyte to correct for potential changes in ablation rate.
- LaserCalc: uses the output from LaserTRAM (i.e., the analyte normalized ratios) and accepted standard reference material values to calculate elemental concentrations of the unknown materials in the experiment.

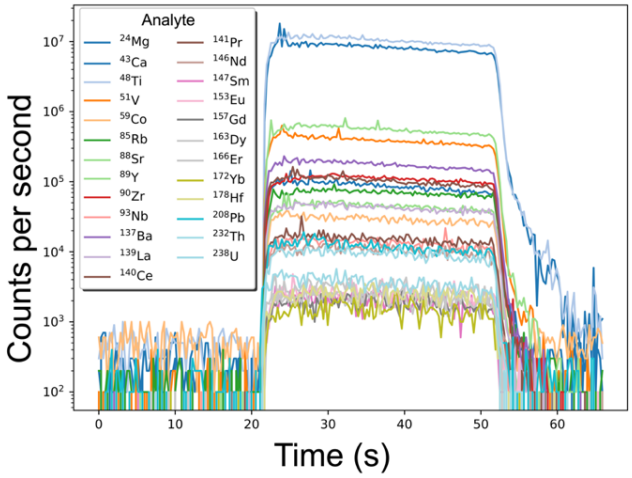

Figure 5.1: Example of raw data for a single spot analysis from standard reference material BCR-2G showing the possibility of measuring > 25 analytes in a given experiment. The plateau in the middle is the signal that corresponds to the ablated material being measured by the ICP-MS, while the lower cps values on either side are background levels for each analyte.

GOVERNING EQUATIONS

We calculate the concentration of analyte (i) in an unknown material (u) using the following relationship, initially described by Longerich et al., (1996):

$$1. \quad C_i{}^u = \frac{R_i{}^u}{S}$$

Where $C_i{}^u$ and $R_i{}^u$ are the concentration of analyte and count rate of analyte (i) in the unknown material, respectively, and S is the normalized sensitivity. When using naturally occuring internal standards, S can be defined as:

$$2. \quad S = \frac{R_i{}^{std}}{C_i{}^{std}} \left[\frac{R_n{}^u}{R_n{}^{std}} \frac{C_n{}^{std}}{C_n{}^u} \right]$$

Here, R_i^{std} and C_i^{std} are the count rate and and concentration of analyte (i) in the calibration standard, R_n^{u} and R_n^{std} are the mean count rates of the internal standard in the unknown material and calibration standard, C_n^{u} and C_n^{std} are the concentrations of the internal standard in the unknown material and calibration standard. Kent and Ungerer (2006), e-arrange this relationship such that the count rate expressions always contain unknown analytes in the numerator:

$$3. \quad C_i{}^u = C_n{}^u \frac{\left[\frac{C_i{}^{std}}{C_n{}^{std}}\right]}{\left[\frac{R_i{}^{std}}{R_n{}^{std}}\right]} \frac{R_i{}^u}{R_n{}^u}$$

This allows for easy calculations implementing data that has been normalized to an internal standard analyte and is the equation used by LaserCalc to calculate final concentrations.

DETERMINING NORMALIZED RATIOS

The purpose of LaserTRAM is to give the user complete control over how much of an analysis gets used in calculating concentrations. When a given interval of interest has been chosen, every analyte is normalized to a chosen internal standard. LaserTRAM commonly uses either ^{43}Ca or ^{29}Si as internal standards for silicate minerals, however it has the capability to use any analyte that has been measured. The raw data first has the background subtracted from it. Background is determined by taking the median counts per second value for each analyte over a user-specified background range. Once data have been background subtracted, each normalized ratio is calculated the following way:

$$4. \quad N_i = median\left[\frac{cps_i}{cps_{is}}\right]$$

where cps_i is the background subtracted counts per second data for analyte (i) and cps_{is} is the background subtracted counts per second data for the internal standard. Since counts per second is analogous to count rate above in Equation 3 we can simplify the above relationship to now reflect our N_i values:

$$5. \quad C_i{}^u = C_n{}^u \frac{\left[\frac{C_i{}^{std}}{C_n{}^{std}}\right]}{N_i{}^{std}} N_i{}^u$$

Here, N_i^{std} and N_i^{u} are the normalized counts per second value of analyte (i) in the calibration standard and unknown, respectively. The uncertainty for any given normalized ratio is expressed as:

$$6. \quad SE = \frac{\sigma_{N_i}}{\sqrt{n}}$$

σ_N is the standard deviation of a given analyte's normalized ratio for the interval and n is the number of time steps in the interval chosen (i.e., cycles through the mass range). The relative standard error is then:

$$7. \quad RSE_i{}^u = \left[\frac{SE}{N_i}\right] 100$$

Detection limits for each analyte are 3 standard deviations above the mean of the background levels as defined earlier. This then means that you have 99.7% confidence of that analyte being above background levels. This is standard practice in LA-ICP-MS data reduction. To reflect this in data output, normalized ratios below detection limit are coded to show up as negative ratios in LaserTRAM that then get turned into "b.d.l." values in LaserCalc.

DRIFT CORRECTION

To check for drift in calibration standard normalized ratios over time, a linear regression is applied to each analyte where the dependent variable is the count rate normalized to the internal standard and the independent variable is the analysis number (Figure 5.2). This regression and the observed data then receive a Root Mean Squared Error (RMSE) value. A linear drift correction is applied to an analyte only if the relative RMSE value for a given analyte is less than the RSE. Here RSE is defined as:

$$8. \quad RSE_i{}^{std} = \left[\frac{\frac{\sigma_i}{\sqrt{n}}}{\mu_i}\right] 100$$

where σ_i and μ_i are the standard deviation and mean of all of the calibration standard normalized ratios respectively and n_i is the total number of calibration standard analyses for analyte (i). In brief, drift correction only happens if there is a sufficiently large linear change in normalized count rates over time that will drive the RMSE of the regression to lower values while the standard error of the mean will increase. This drift correction then uses the regression parameters (e.g., slope and intercept) to calculate a normalized count rate for the calibration standard at the point in time where an unknown was analyzed:

$$9. \quad C_i{}^u = C_n{}^u \frac{\left[\frac{c_i{}^{std}}{c_n{}^{std}}\right]}{[m_i x + b_i]} N_i{}^u$$

where m is the regression slope, x is the analysis number, and b is the intercept for analyte (i).

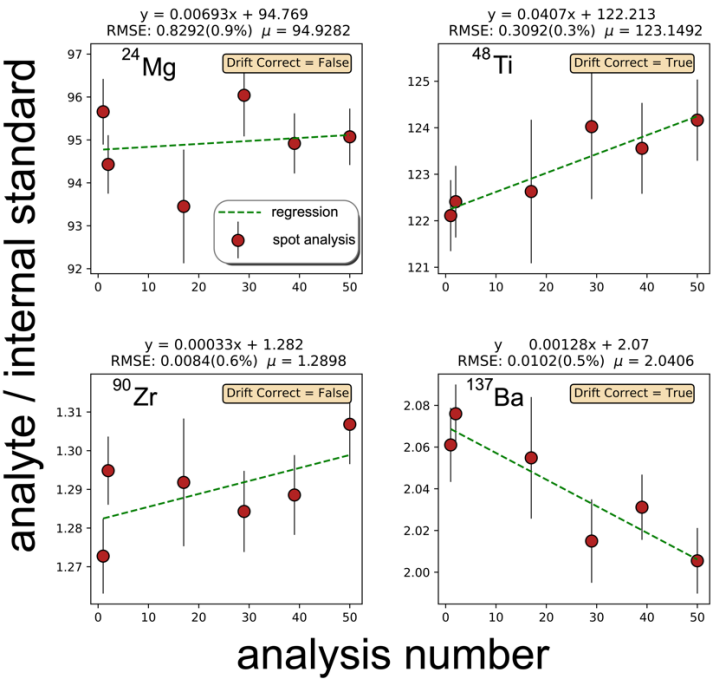

Figure 5.2: Drift correction test for selected analytes in Figure 5.1 illustrating analytes that are both drift corrected and not drift corrected in LaserCalc.

UNCERTAINTIES

Uncertainties in calculated concentrations are calculated according to standard error propagation of uncertainties in products and quotients:

$$10.\ \frac{\sigma_q}{|q|} = \sqrt{\left(\frac{\sigma_x}{|x|}\right)^2 + \left(\frac{\sigma_y}{|y|}\right)^2 + \left(\frac{\sigma_z}{|z|}\right)^2 + \cdots \left(\frac{\sigma_n}{|n|}\right)^2}$$

Because the formula for calculating concentrations of a given analyte in an unknown material is just a series of nested quotients and products, we can explain the overall uncertainty of a given analyte as:

$$11.\ \sigma_{C_i} = {C_i}^u \sqrt{\left(\frac{\sigma_{C_u^n}}{{C_u}^n}\right)^2 + \left(\frac{\sigma_{C_i^{std}}}{{C_i}^{std}}\right)^2 + \left(\frac{\sigma_{C_n^{std}}}{{C_n}^{std}}\right)^2 + \left({RSE_i}^{std}\right)^2 + ({RSE_i}^u)^2}$$

For analytes where drift correction has been applied, RSE_i^{std} is replaced with:

$$100\left[\frac{RMSE_i}{\mu_i}\right]$$

Where $RMSE_i$ is the Root Mean Squared Error as specified in the Drift correction section.

USING LASERTRAM AND LASERCALC

Here we outline the general workflow for using LaserTRAM and LaserCalc. LaserTRAM

1. When LaserTRAM opens it will look like the following:

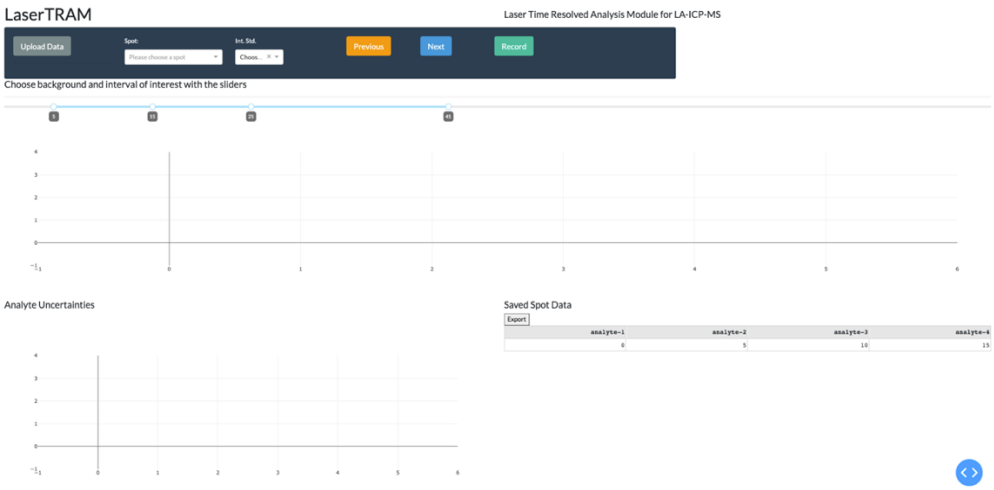

Figure 5.3: Empty LaserTRAM window upon opening the program.

2. Use the Upload Data button in the upper left to search your Finder/File Explorer for the requisite experiment data. This data should be a spreadsheet or csv file that has columns denoting time, cps values for each time step, and a column for which spot each time step belongs to:

	A	B	C	D	E	F	G	H	I	J	K	L	M	N	O	P
1	SampleLabel	Time	24Mg	43Ca	48Ti	51V	59Co	85Rb	88Sr	89Y	90Zr	93Nb	137Ba	139La	140Ce	141Pr
2	BCR-2G_1	12.48	200.0016	0	300.0036	100.0004	600.0144	200.0016	0	0	0	0	0	0	0	0
3	BCR-2G_1	297.54	100.0004	600.0144	500.01	0	300.0036	200.0016	0	0	0	0	0	0	0	0
4	BCR-2G_1	582.79	0	700.0196	300.0036	100.0004	600.0144	0	0	0	0	0	0	0	0	0
5	BCR-2G_1	868	0	700.0196	600.0144	100.0004	600.0144	100.0004	0	0	0	0	0	0	0	0
6	BCR-2G_1	1153.05	100.0004	100.0004	400.0064	0	100.0004	200.0016	0	0	0	0	0	0	0	0
7	BCR-2G_1	1438.06	200.0016	300.0036	700.0196	0	600.0144	0	0	0	0	0	0	0	0	0
8	BCR-2G_1	1723.18	100.0004	0	500.01	100.0004	700.0196	0	0	0	0	0	0	0	0	0
9	BCR-2G_1	2008.27	100.0004	200.0016	900.0324	200.0016	100.0004	100.0004	0	0	0	0	100.0004	0	0	0
10	BCR-2G_1	2293.49	200.0016	500.01	400.0064	200.0016	200.0016	200.0016	0	0	0	0	0	0	0	0
11	BCR-2G_1	2578.56	200.0016	100.0004	500.01	100.0004	300.0036	100.0004	0	0	0	0	0	0	0	0
12	BCR-2G_1	2863.63	100.0004	300.0036	100.0004	0	700.0196	200.0016	0	0	0	0	0	0	0	0
13	BCR-2G_1	3148.71	0	300.0036	1000.04	200.0016	400.0064	0	0	0	0	0	0	0	0	0
14	BCR-2G_1	3433.67	200.0016	100.0004	300.0036	0	1000.04	100.0004	0	0	0	0	0	0	0	0
15	BCR-2G_1	3718.81	100.0004	100.0004	100.0004	0	500.01	200.0016	0	0	0	0	0	0	0	0
16	BCR-2G_1	4003.92	300.0036	300.0036	400.0064	0	600.0144	200.0016	0	0	0	0	0	0	0	0
17	BCR-2G_1	4289.1	200.0016	300.0036	800.0256	100.0004	1000.04	100.0004	0	0	0	0	0	0	0	0
18	BCR-2G_1	4574.18	100.0004	300.0036	700.0196	0	300.0036	100.0004	0	0	0	0	0	0	0	0
19	BCR-2G_1	4859.24	200.0016	200.0016	400.0064	100.0004	600.0144	200.0016	0	0	0	0	0	0	0	0

Figure 5.4: Example of data format required for LaserTRAM.

Pending the size of the file it may take a few seconds to load the data into LaserTRAM, however, when it is done loading the “Saved Spot Data” table will now reflect the analyte list of your experiment, as well as the Internal Standard dropdown at the top.

3. Choose internal standard by selecting an analyte from the “Int. Std.” dropdown menu. This analyte is what all other analytes will be normalized to in order to correct for differences in ablation rate throughout the duration of the analysis. This should be the same analyte for the entire duration of the experiment.
4. You may now go to the spot dropdown and choose which spot you would like to start with. Once a spot is chosen all of the plots will populate:

Figure 5.5: LaserTRAM interface with populated graphs after choosing a spot analysis from the dropdown menu.

The upper left plot is the raw data signal with counts per second on the y-axis and time on the x-axis. The red region is controlled by the left-most nodes on the slider bar above the plot and can be changed by simply dragging them to the desired location. It represents the region in the analysis that the median background cps values for each analyte is determined. This should stay the same for the entire experiment. Similarly, the green area is controlled by the right-most nodes on the slider bar and represents the portion of the analysis to be used in calculating normalized ratios to be used for concentrations later on. They represent time durations for where the region starts and stops. The plot in the upper right shows the normalized ratios for each analyte for the chosen green interval. As the slider nodes are changed this plot will update accordingly. The relative standard error for each analyte's normalized ratio is displayed in the plot on the lower left. The annotated number above each bar is the median value for each analyte over the chosen green interval and follows standard SI notation (https://www.npl.co.uk/si-units).

A brief note on the plots. They are all fully interactive (e.g., you can pan, zoom, view hover data). The various interactive plot features can be accessed via the toolbar that appears when you hover in the upper right of the plot

Figure 5.6: Toolbar used for manipulating graphs in LaserTRAM.

5. Choose intervals like listed above by dragging the sliders to their desired location. Both the normalized data plot and the uncertainties plot will update in real time as this is done allowing for complete control on not only which part of the analysis is used, but also allowing for the tracking of the uncertainties. This is useful for geologic materials that are

known to have either glass or mineral inclusions throughout that may not be apparent on the surface yet still incorporated into the analysis as it ablates into the sample. If an analyte is below detection limit as defined earlier, there will be no bar in the uncertainties plot.

6. When the desired interval is chosen, simply press “Record” at the top. This will save the background and analysis interval information, internal standard analyte and its counts per second, and normalized ratios with their uncertainties for every analyte. It will be displayed in the “Saved Spot Data” table in the lower right with each spot having its own row:

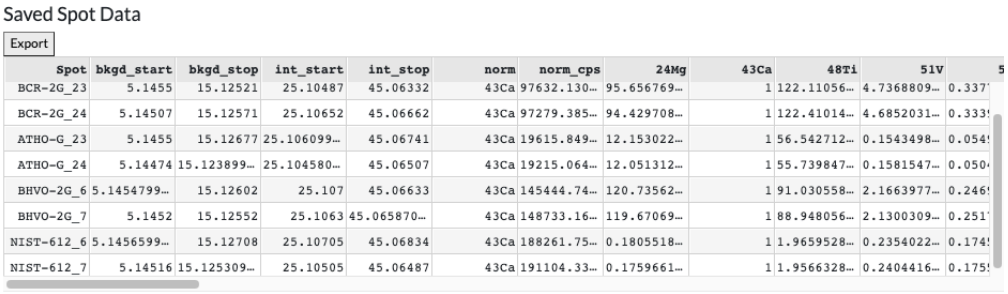
Saved Spot Data

Export

Spot	bkgd_start	bkgd_stop	int_start	int_stop	norm	norm_cps	24Mg	43Ca	48Ti	51V	5
BCR-2G_23	5.1455	15.12521	25.10487	45.06332	43Ca	97632.130…	95.656769…	1	122.11056…	4.7368809…	0.337
BCR-2G_24	5.14507	15.12571	25.10652	45.06662	43Ca	97279.385…	94.429708…	1	122.41014…	4.6852031…	0.333
ATHO-G_23	5.1455	15.12677	25.106099…	45.06741	43Ca	19615.849…	12.153022…	1	56.542712…	0.1543498…	0.054
ATHO-G_24	5.14474	15.123899…	25.104580…	45.06507	43Ca	19215.064…	12.051312…	1	55.739847…	0.1581547…	0.050
BHVO-2G_6	5.1454799…	15.12602	25.107	45.06633	43Ca	145444.74…	120.73562…	1	91.030558…	2.1663977…	0.246
BHVO-2G_7	5.1452	15.12552	25.1063	45.065870…	43Ca	148733.16…	119.67069…	1	88.948056…	2.1300309…	0.251
NIST-612_6	5.1456599…	15.12708	25.10705	45.06834	43Ca	188261.75…	0.1805518…	1	1.9659528…	0.2354022…	0.174
NIST-612_7	5.14516	15.125309…	25.10505	45.06487	43Ca	191104.33…	0.1759661…	1	1.9566328…	0.2404416…	0.175

Figure 5.7: Example of the table generated as the user saves information for each spot.

Use the scroll bars to pan left, right, up, and down in the table.

7. Now, the only thing left to do is to apply steps 5 and 6 for every spot in the experiment. This can be done multiple ways:
    a. Using the spot dropdown to select any other spot in the list
    b. Using the “Previous” and “Next” buttons (preferred). These buttons will move you one more spot in the dropdown list either backwards (“Previous”) or forwards (“Next”). As you progress the “Saved Spot Data” table will populate with more and more rows.
8. When finished, hit the “Export” button above the “Saved Spot Data” table and save the data as an excel spreadsheet. The output format will mimic the table and look like this:

	A	B	C	D	E	F	G	H	I	J	K	L
1	Spot	bkgd_start	bkgd_stop	int_start	int_stop	norm	norm_cps	24Mg	43Ca	48Ti	51V	59Co
2												
3	BCR-2G_23	5.1455	15.12521	25.10487	45.06332	43Ca	97632.1301	95.6567691	1	122.110565	4.73688096	0.33774677
4	BCR-2G_24	5.14507	15.12571	25.10652	45.06662	43Ca	97279.3851	94.4297084	1	122.410147	4.6852032	0.33391564
5	ATHO-G_23	5.1455	15.12677	25.1061	45.06741	43Ca	19615.8494	12.1530224	1	56.5427124	0.15434986	0.05495174
6	ATHO-G_24	5.14474	15.1239	25.10458	45.06507	43Ca	19215.0649	12.0513123	1	55.7398479	0.15815476	0.05040951
7	BHVO-2G_6	5.14548	15.12602	25.107	45.06633	43Ca	145444.743	120.73563	1	91.0305586	2.16639775	0.24694046
8	BHVO-2G_7	5.1452	15.12552	25.1063	45.06587	43Ca	148733.167	119.670692	1	88.9480563	2.13003098	0.25173916
9	NIST-612_6	5.14566	15.12708	25.10705	45.06834	43Ca	188261.757	0.18055181	1	1.96595289	0.23540226	0.17451422
10	NIST-612_7	5.14516	15.12531	25.10505	45.06487	43Ca	191104.331	0.17596613	1	1.95663283	0.24044167	0.17553116
11	LT012_1	5.14542	15.12528	25.1056	45.06642	43Ca	4951.09923	14.3041598	1	26.8043874	-9999	-9999
12	LT012_2	5.14502	15.12473	25.10502	45.0654	43Ca	1950.21462	15.2007113	1	26.0653857	-9999	-9999
13	LT012_3	5.14544	15.12629	25.10735	45.06746	43Ca	2800.38085	14.94736	1	24.7838925	-9999	-9999
14	LT012_4	5.14557	15.12635	25.10648	45.06729	43Ca	5201.20667	14.0652648	1	25.7288949	0.06812647	-9999
15	LT012_5	5.14501	15.12585	25.10615	45.06627	43Ca	4751.01681	14.8798168	1	27.2697938	-9999	-9999
16	LT012_6	5.14495	15.12545	25.10667	45.06689	43Ca	4500.88217	13.7169734	1	23.9301401	-9999	-9999
17	LT012_7	5.14522	15.125	25.10524	45.0653	43Ca	6651.92914	14.9481188	1	25.3774383	0.04346609	-9999
18	LT012_8	5.14499	15.12504	25.10442	45.065	43Ca	3500.57409	14.0353983	1	24.2609587	-9999	-9999
19	LT012_9	5.14501	15.1248	25.10467	45.06382	43Ca	1000.056	15.3746161	1	26.7878598	-9999	-9999
20	LT012_10	5.14527	15.12445	25.10512	45.06604	43Ca	3850.68551	13.0901371	1	24.0778752	-9999	-9999

Figure 5.8: Example output generated from LaserTRAM. This completely mimics the data table generated in the GUI.

Note: Negative values in this table correspond to analytes being below detection limit for a given spot.

LaserCalc

1. When LaserCalc opens it will look like the following:

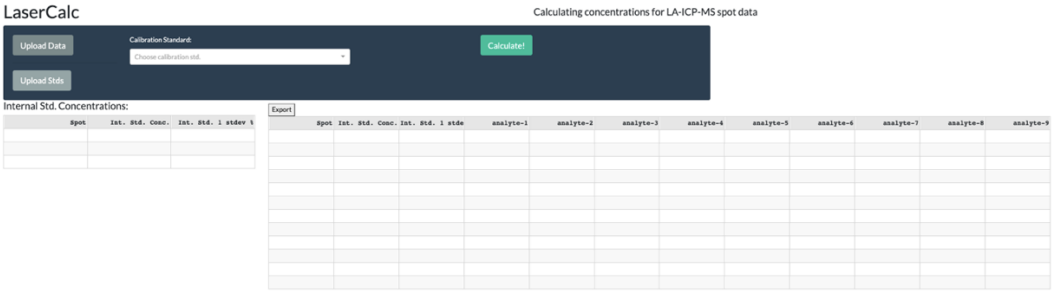

Figure 5.9: LaserCalc interface upon loading the program.

2. To import your work from LaserTRAM, use the “Upload Data” button in the upper left. This will prompt you to go into your Finder/File Explorer and select the proper file. When imported the table on the left will populate with columns denoting spot as well as internal standard concentrations and uncertainties:

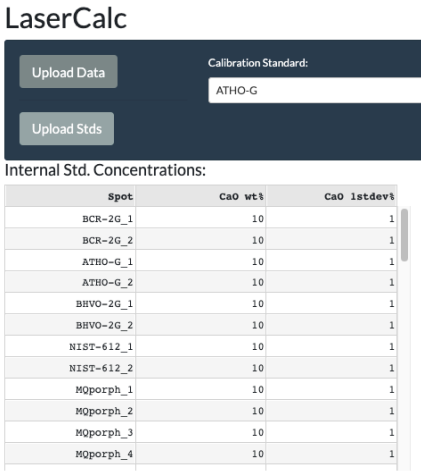

Spot	CaO wt%	CaO 1stdev%
BCR-2G_1	10	1
BCR-2G_2	10	1
ATHO-G_1	10	1
ATHO-G_2	10	1
BHVO-2G_1	10	1
BHVO-2G_2	10	1
NIST-612_1	10	1
NIST-612_2	10	1
MQporph_1	10	1
MQporph_2	10	1
MQporph_3	10	1
MQporph_4	10	1

Figure 5.10: Populated Internal Std. Concentrations table after output from LaserTRAM is loaded into LaserCalc. Adjust the values to reflect internal standard concentrations and relative uncertainties.

The "Internal Std. Concentrations" table now contains arbitrary concentration and uncertainty values for the internal standard for each spot (e.g., 10 wt% and 1% RSE). These are analogous to the C_n^u and C_n^{std} parameters in the relationship described above.

3. Import the spreadsheet with preferred concentrations for standard reference materials as defined by the GEOREM database (http://georem.mpch-mainz.gwdg.de/sample_query_pref.asp). This file can be found here: https://drive.google.com/file/d/1g9ZimiT6OIvWteqqXTYHiLSUxrK2RtqV/view?usp=sharing
4. Choose your desired calibration standard via the dropdown at the top. This populates based on the spot names in your experiment and compares them to those found in the uploaded standards data spreadsheet. Therefore, standards must have the proper GEOREM name (i.e., ATHO-G, BCR-2G, NIST-612, etc.) somewhere in their label.
5. For all non-standard reference materials in your data that are not listed in the uploaded standards sheet, edit the table on left to reflect the concentration of the internal standard and its relative standard error for each spot. For example, in silicate minerals this is usually in the form of electron probe data. All standard reference materials will use the preferred data listed in the uploaded spreadsheet.
6. When you are done editing the "Internal Std. Concentrations" table, double check your work and hit "Calculate!" This will calculate concentrations based on the relationship defined above by Kent and Ungerer (2006). The table on the right will now switch to say "Calculated Concentrations":

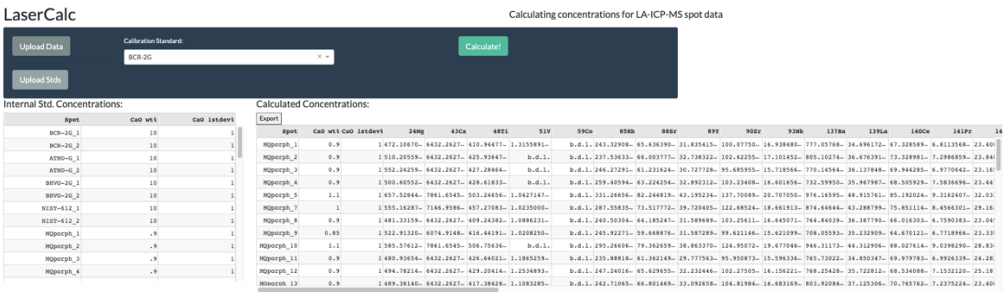

Figure 5.11: Populated Calculated Concentrations table after "Calculate!" button is clicked. Table will update in real time to reflect values in Internal Std. Concentrations table as they change.

The “Internal Std. Concentrations” table and “Calculated Concentrations” table are now linked. As you change values in the “Internal Std. Concentrations” table the “Calculated Concentrations” table will now immediately update to reflect those changes. The “Calculated Concentrations” table is also now sorted and tosses all the standard reference material analyses at the bottom instead of being interspersed through the table. Analytes that are below detection limit for a given spot now have “b.d.l.” in their respective cell.

You may now also toggle between potential calibration standards using the “Calibration Standard” dropdown to explore how different calibration standards affect calculated concentrations. Upon changing the value in the dropdown, the calculated concentrations will update immediately, and you do not have to press the “Calculate!” button again.

7. Similar to LaserTRAM, to export the data, simply hit the “Export” button at the top of the “Calculated Concentrations” table and save your output as an Excel spreadsheet.

REFERENCES

Branson, O., Fehrenbacher, J.S., Vetter, L., Sadekov, A.Y., Eggins, S.M., Spero, H.J., 2019. LAtools: A data analysis package for the reproducible reduction of LA-ICPMS data. Chem. Geol. 504, 83–95. https://doi.org/10.1016/j.chemgeo.2018.10.029

Guillong, M., Meier, D.L., Allan, M.M., Heinrich, C.A., Yardley, B.W.D., 2008. SILLS: A MATLAB-BASED PROGRAM FOR THE REDUCTION OF LASER ABLATION ICP-MS DATA OF HOMOGENEOUS MATERIALS AND INCLUSIONS. Mineral. Soc. Canada Short Course 328–333.

Kent, A.J.R., Ungerer, C.A., 2006. Analysis of light lithophile elements (Li, Be, B) by laser ablation ICP-MS: Comparison between magnetic sector and quadrupole ICP-MS. Am. Mineral. 91, 1401–1411. https://doi.org/10.2138/am.2006.2030

Longerich, H.P., Jackson, S.E., Günther, D., 1996. Laser ablation inductively coupled plasma mass spectrometric transient signal data acquisition and analyte concentration calculation. J. Anal. At. Spectrom. 11, 899–904. https://doi.org/10.1039/JA9961100899

Mischel, S.A., Mertz-Kraus, R., Jochum, K.P., Scholz, D., 2017. TERMITE: An R script for fast reduction of laser ablation inductively coupled plasma mass spectrometry data and its application to trace element measurements. Rapid Commun. Mass Spectrom. 31, 1079–1087. https://doi.org/10.1002/rcm.7895

Paton, C., Hellstrom, J., Paul, B., Woodhead, J., Hergt, J., 2011. Iolite: Freeware for the visualisation and processing of mass spectrometric data. J. Anal. At. Spectrom. 26, 2508–2518. https://doi.org/10.1039/c1ja10172b

CHAPTER SIX: GENERAL CONCLUSIONS

The results from these studies illustrate the importance of interpreting chemical zoning in igneous minerals as it pertains to storage conditions of large bodies of silicic magma within the crust.

In chapter 2 we applied diffusion modeling of Mg and Sr in plagioclase from the 2.08 Ma, 630 km^3, Cerro Galán Ignimbrite (CGI) to investigate the long-term thermochemical magma storage conditions of large silicic magma reservoirs. Our results indicate that, although bulk-rock geochemistry implies a magmatic system that is chemically homogeneous at the time of eruption, plagioclase are recording diverse crystallization environments throughout their crystallization history that largely do not reflect those at the time of eruption. Furthermore, despite this evidence for long-term storage within the reservoir, CGI plagioclase are only recording timescales of decades to centuries at temperatures required to produce eruptible volumes of magma.

In chapter 3, like chapter 2, we applied diffusion modeling of Mg and Sr in plagioclase to the 74 ka, 2800 km^3, Youngest Toba Tuff (YTT) eruption. We also utilized Sr in amphibole diffusion and amphibole-based thermometry to constrain not only the thermal evolution of the YTT magmatic system but also the system responsible for originally crystallizing the xenocrystic amphibole. We found that similar to the CGI magmatic system, eruptible volumes of magma are only present within the YTT for decades, illustrating that despite long residence times within the upper crust, large silicic magma systems are dominated by periods of storage whereby they are at temperatures incapable of producing and storing large volumes of magma.

Chapter 4 developed a technique to quantify and observe chemical zoning in sanidine in 3D using micro computed tomography (microCT). We showed that microCT grayscale was largely a function of Ba concentration in sanidine. As Ba in sanidine is useful in quantifying petrogenetic processes, we stress that this technique has the capability to be heavily utilized in future igneous petrology studies that use tools that interpret mineral zoning (e.g., diffusion chronometry), as it mitigates 2D sectioning effects that are commonly large sources of uncertainty.

Chapter 5 provides the documentation and a tutorial for a new, open-source, web hosted graphical user interface (GUI) for the reduction of LA-ICP-MS spot data. It gives the user complete control over the portion of signal utilized in concentrations, provides drift correction functionality to account for changes in ICP-MS sensitivity over time, and allows the user to rapidly compare concentrations calculated from different calibration standards. The goal

of this project was to mitigate the frequent “black box” behavior of other LA-ICP-MS data reduction methods such that users have a better idea of the assumptions that go into generating trace element data critical to their experiments.

BIBLIOGRAPHY

Andersen, N.L., Jicha, B.R., Singer, B.S., and Hildreth, W., 2017, Incremental heating of Bishop Tuff sanidine reveals preeruptive radiogenic Ar and rapid remobilization from cold storage: v. 114, p. 12407–12412, doi: 10.1073/pnas.1709581114.

Anderson, A.T., 1976, Magma mixing: petrological process and volcanological tool: Journal of Volcanology and Geothermal Research, v. 1, p. 3–33, doi: 10.1016/0377-0273(76)90016-0.

Annen, C., Blundy, J.D., Leuthold, J., and Sparks, R.S.J., 2015, Construction and evolution of igneous bodies: Towards an integrated perspective of crustal magmatism: Lithos, v. 230, p. 206–221, doi: 10.1016/j.lithos.2015.05.008.

Annen, C., Blundy, J.D., and Sparks, R.S.J., 2006, The genesis of intermediate and silicic magmas in deep crustal hot zones: Journal of Petrology, v. 47, p. 505–539, doi: 10.1093/petrology/egi084.

Bachmann, O., and Bergantz, G.W., 2008a, Deciphering Magma Chamber Dynamics from Styles of Compositional Zoning in Large Silicic Ash Flow Sheets: Reviews in Mineralogy and Geochemistry, v. 69, p. 651–674, doi: 10.2138/rmg.2008.69.17.

Bachmann, O., and Bergantz, G.W., 2004, On the Origin of Crystal-poor Rhyolites: Extracted from Batholithic Crystal Mushes: Journal of Petrology, v. 45, p. 1565–1582, doi: 10.1093/petrology/egh019.

Bachmann, O., and Bergantz, G.W., 2008b, Rhyolites and their source mushes across tectonic settings: Journal of Petrology, v. 49, p. 2277–2285, doi: 10.1093/petrology/egn068.

Bachmann, O., Deering, C.D., Lipman, P.W., and Plummer, C., 2014, Building zoned ignimbrites by recycling silicic cumulates: insight from the 1,000 km3 Carpenter Ridge Tuff, CO: Contributions to Mineralogy and Petrology, v. 167, p. 1025, doi: 10.1007/s00410-014-1025-3.

Bachmann, O., and Dungan, M.A., 2002, Temperature-induced Al-zoning in hornblendes of the Fish Canyon magma, Colorado: American Mineralogist, v. 87, p. 1062–1076, doi: 10.2138/am-2002-8-903.

Bachmann, O., Dungan, M.A., and Lipman, P.W., 2002, The Fish Canyon Magma Body , San Juan Volcanic Field , Colorado : Rejuvenation and Eruption of an Upper-Crustal Batholith: v. 43, p. 1469–1503.

Bachmann, O., and Huber, C., 2016, Silicic magma reservoirs in the Earth's crust: American Mineralogist, v. 101, p. 2377–2404, doi: 10.2138/am-2016-5675.

Bacon, C.R., and Lowenstern, J.B., 2005, Late Pleistocene granodiorite source for recycled zircon and phenocrysts in rhyodacite lava at Crater Lake, Oregon: Earth and Planetary Science Letters, v. 233, p. 277–293, doi: 10.1016/j.epsl.2005.02.012.

Barbee, O., Chesner, C., and Deering, C., 2020, Quartz in Toba rhyolites show textures symptomatic of rapid crystallization: American Mineralogist, v. 105, p. 194–226, doi: 10.2138/am-2020-6947.

Barboni, M., Boehnke, P., Schmitt, A.K., Harrison, T.M., Shane, P., Bouvier, A.-S., and Baumgartner, L., 2016, Warm storage for arc magmas: Proceedings of the National Academy of Sciences, v. 113, p. 13959–13964, doi: 10.1073/pnas.1616129113.

Bindeman, I.N., Davis, A.M., and Drake, M.J., 1998a, Ion microprobe study of plagioclase- basalt partition experiments at natural concentration levels of trace elements: Geochimica et Cosmochimica Acta, v. 62, p. 1175–1193, doi: 10.1016/S0016-7037(98)00047-7.

Bindeman, I.N., Davis, A., and Drake, M., 1998b, Ion microprobe study of plagioclase-basalt partition experiments at natural concentration levels of trace elements: v. 62, p. 1175–1193.

Bindeman, I.N., and Melnik, O.E., 2016, Zircon survival, rebirth and recycling during crustal melting, magma crystallization, and mixing based on numerical modelling: Journal of Petrology, v. 57, p. 437–460, doi: 10.1093/petrology/egw013.

Blundy, J., Cashman, K., and Humphreys, M., 2006, Magma heating by decompression-driven crystallization beneath andesite volcanoes: Nature, v. 443, p. 76–80, doi: 10.1038/nature05100.

Boehnke, P., Watson, E.B., Trail, D., Harrison, T.M., and Schmitt, A.K., 2013, Zircon saturation re-revisited: Chemical Geology, v. 351, p. 324–334, doi: 10.1016/j.chemgeo.2013.05.028.

Bowen, N.L., 1915, The Later Stages of the Evolution of the Igneous Rocks: v. 23.

Bowen, N.L., 1913, The Melting Phenomena of the Plagioclase Feldspars: American Journal of Science,.

Boyce, J.W., and Hervig, R.L., 2008, Magmatic degassing histories from apatite volatile stratigraphy: Geology, v. 36, p. 63–66, doi: 10.1130/G24184A.1.

Brabander, D.J., and Giletti, B.J., 1995, Strontium diffusion kinetics in amphiboles and significance to thermal history determinations: Geochimica et Cosmochimica Acta, v. 59, p. 2223–2238, doi: 10.1016/0016-7037(95)00102-6.

Bradshaw, R.W., 2017, Crystal Records of the Origin, Evolution, and Thermal Histories of Magmas: Oregon State University, Man.

Bradshaw, R.W., and Kent, A.J.R., 2017, The analytical limits of modeling short diffusion timescales: Chemical Geology, v. 466, p. 667–677, doi: 10.1016/j.chemgeo.2017.07.018.

Branson, O., Fehrenbacher, J.S., Vetter, L., Sadekov, A.Y., Eggins, S.M., and Spero, H.J., 2019, LAtools: A data analysis package for the reproducible reduction of LA-ICPMS data: Chemical Geology, v. 504, p. 83–95, doi: 10.1016/j.chemgeo.2018.10.029.

Breiman, L., 2001, Random forests, in Schapire, R.E. ed., Machine Learning, Kluwer Academic Publishers, p. 5–32.

Buades, A., Coll, B., and Morel, J.M., 2005, A non-local algorithm for image denoising, in Proceedings - 2005 IEEE Computer Society Conference on Computer Vision and Pattern Recognition, CVPR 2005, v. II, p. 60–65, doi: 10.1109/CVPR.2005.38.

Budd, D.A., Troll, V.R., Deegan, F.M., Jolis, E.M., Smith, V.C., Whitehouse, M.J., Harris, C., Freda, C., Hilton, D.R., Halldórsson, S.A., and Bindeman, I.N., 2017, Magma reservoir dynamics at Toba caldera, Indonesia, recorded by oxygen isotope zoning in quartz: Scientific Reports, v. 7, p. 1–11, doi: 10.1038/srep40624.

Caricchi, L., and Blundy, J., 2015, Experimental petrology of monotonous intermediate magmas: Geological Society Special Publication, v. 422, p. 105–130, doi: 10.1144/SP422.9.

Cashman, K. V., Sparks, R.S.J., and Blundy, J.D., 2017, Vertically extensive and unstable magmatic systems: A unified view of igneous processes: Science, v. 355, doi: 10.1126/science.aag3055.

Castillo, P.R., 2012, Adakite petrogenesis: Lithos, v. 134–135, p. 304–316, doi: 10.1016/j.lithos.2011.09.013.

Chakraborty, S., 2008, Diffusion in Solid Silicates: A Tool to Track Timescales of Processes Comes of Age: Annual Review of Earth and Planetary Sciences, v. 36, p. 153–190, doi: 10.1146/annurev.earth.36.031207.124125.

Chamberlain, K.J., Morgan, D.J., and Wilson, C.J.N., 2014, Timescales of mixing and mobilisation in the Bishop Tuff magma body : perspectives from diffusion chronometry: Contributions to Mineralogy and Petrology, doi: 10.1007/s00410-014-1034-2.

Chambers, M., Memeti, V., Eddy, M.P., and Schoene, B., 2020, Half a million years of magmatic history recorded in a K-feldspar megacryst of the tuolumne intrusive complex, California, USA: Geology, v. 48, p. 400–404, doi: 10.1130/G46873.1.

Chantler, C.T., 2000, Detailed Tabulation of Atomic Form Factors, Photoelectric Absorption and Scattering Cross Section, and Mass Attenuation Coefficients in the Vicinity of Absorption Edges in the Soft X-Ray (Z=30-36,Z=60-89,E=0.1 keV-10 keV), Addressing Convergence Issues of: J. Phys. Chem. Ref. Data, v. 29, p. 597–1048.

Cherniak, D.J., 2002, Ba diffusion in feldspar: Geochimica et Cosmochimica Acta, v. 66, p. 1641–1650, doi: 10.1016/S0016-7037(01)00866-3.

Cherniak, D.J., 2010, Cation diffusion in feldspars: Reviews in Mineralogy and Geochemistry, v. 72, p. 691–733, doi: 10.2138/rmg.2010.72.15.

Cherniak, D.J., and Watson, E.B., 1994, A study of strontium diffusion in plagioclase using Rutherford backscattering spectroscopy: Geochimica et Cosmochimica Acta, v. 58, p. 5179–5190, doi: 10.1016/0016-7037(94)90303-4.

Chesner, C.A., 1998, Petrogenesis of the Toba Tuffs, Sumatra, Indonesia: Journal of Petrology, v. 39, p. 397–438, doi: 10.1093/petroj/39.3.397.

Chesner, C.A., 2012, The Toba Caldera Complex: Quaternary International, v. 258, p. 5–18, doi: 10.1016/j.quaint.2011.09.025.

Chesner, C.A., and Luhr, J.F., 2010, A melt inclusion study of the Toba Tuffs, Sumatra, Indonesia: Journal of Volcanology and Geothermal Research, v. 197, p. 259–278, doi: 10.1016/j.jvolgeores.2010.06.001.

Chesner, C., and Rose, Wi., 1991, Stratigraphy of the Toba Tuffs and the evolution of the Toba Caldera Complex, Sumatra, Indonesia: Bulletin of Volcanology, v. 53, p. 343–356.

Claiborne, L.L., Miller, C.F., Flanagan, D.M., Clynne, M.A., and Wooden, J.L., 2010, Zircon reveals protracted magma storage and recycling beneath Mount St. Helens: Geology, v. 38, p. 1011–1014, doi: 10.1130/G31285.1.

Cnudde, V., and Boone, M.N., 2013, High-resolution X-ray computed tomography in geosciences: A review of the current technology and applications: Earth-Science Reviews, v. 123, p. 1–17, doi: 10.1016/j.earscirev.2013.04.003.

Cooper, K.M., 2017, What does a magma reservoir look like? the “crystal’s-eye” view: Elements, v. 13, p. 23–28, doi: 10.2113/gselements.13.1.23.

Cooper, K.M., and Kent, A.J.R., 2014, Rapid remobilization of magmatic crystals kept in cold storage.: Nature, v. 506, p. 480–3, doi: 10.1038/nature12991.

Cooper, K.M., and Reid, M.R., 2003, Re-examination of crystal ages in recent Mount St. Helens lavas: Implications for magma reservoir processes: Earth and Planetary Science Letters, v. 213, p. 149–167, doi: 10.1016/S0012-821X(03)00262-0.

Cooper, K.M., and Reid, M.R., 2008, Uranium-series Crystal Ages: Reviews in Mineralogy and Geochemistry, v. 69, p. 479–544, doi: 10.2138/rmg.2008.69.13.

Cooper, K., Reid, M., Murrell, M., and D.a., C., 2001, Crystal and magma residence at Kilauea Volcano: Earth and Planetary Science Letters, v. 184, p. 703–718, http://scholar.google.com/scholar?hl=en&btnG=Search&q=intitle:Crystal+and+magma+residence+at+Kilauea+Volcano+,+Hawaii#8.

Costa, F., Chakraborty, S., and Dohmen, R., 2003, Diffusion coupling between major and trace elements and a model for the calculation of magma chamber residence times using plagioclase: Geochimica et Cosmochimica Acta, v. 67, p. 2189–2200, doi: 10.1016/S0016-7037(00)01345-5.

Costa, F., Dohmen, R., and Chakraborty, S., 2008, Time Scales of Magmatic Processes from Modeling the Zoning Patterns of Crystals: Reviews in Mineralogy and Geochemistry, v. 69, p. 545–594, doi: 10.2138/rmg.2008.69.14.

Costa, F., and Dungan, M., 2005, Short time scales of magmatic assimilation from diffusion modeling of multiple elements in olivine: Geology, v. 33, p. 837–840, doi: 10.1130/G21675.1.

Costa, F., Shea, T., and Ubide, T., 2020, Diffusion chronometry and the timescales of magmatic processes: Nature Reviews Earth & Environment, v. 1, p. 201–214, doi: 10.1038/s43017-020-0038-x.

Couperthwaite, F.K., Thordarson, T., Morgan, D.J., Harvey, J., and Wilson, M., 2020, Diffusion Timescales of Magmatic Processes in the Moinui Lava Eruption at Mauna Loa, Hawai`i, as Inferred from Bimodal Olivine Populations: Journal of Petrology, v. 61, doi: 10.1093/petrology/egaa058.

Crank, J., 1975, The Mathematics of Diffusion: Oxford, England, Oxford University Press.

Davidson, J.P., and Tepley, F.J., 1997, Recharge in Volcanic Systems: Evidence from Isotope Profiles of Phenocrysts: Science, v. 275, p. 826–829, doi: 10.1126/science.275.5301.826.

Davidson, J., Tepley, F., Palacz, Z., and Meffan-Main, S., 2001, Magma recharge, contamination and residence times revealed by in situ laser ablation isotopic analysis of feldspar in volcanic rocks: Earth and Planetary Science Letters, v. 184, p. 427–442, doi: 10.1016/S0012-821X(00)00333-2.

Deer, W.A., Howie, R.A., and Zussman, J., 1966, An Introduction to the Rock-Forming Minerals:, doi: 10.1180/dhz.

Deering, C.D., Cole, J.W., and Vogel, T.A., 2008, A rhyolite compositional continuum governed by lower crustal source conditions in the taupo volcanic zone, New Zealand: Journal of Petrology, v. 49, p. 2245–2276, doi: 10.1093/petrology/egn067.

Deering, C.D., Gravley, D.M., Vogel, T.A., Cole, J.W., and Leonard, G.S., 2010, Origins of cold-wet-oxidizing to hot-dry-reducing rhyolite magma cycles and distribution in the Taupo Volcanic Zone, New Zealand: Contributions to Mineralogy and Petrology, v. 160, p. 609–629, doi: 10.1007/s00410-010-0496-0.

Degruyter, W., and Huber, C., 2014, A model for eruption frequency of upper crustal silicic magma chambers: Earth and Planetary Science Letters, v. 403, p. 117–130, doi: 10.1016/j.epsl.2014.06.047.

Denison, D., Carlson, W.D., and Ketcham, R.A., 1997, Three-dimensional quantitative textural analysis of metamorphic rocks using high-resolution computed X-ray tomography : Part I . Methods and techniques: Journal of metamorphic Geology, v. 15, p. 29–44.

Dingwell, D.B., 1998, Recent experimental progress in the physical description of silicic magma relevant to explosive volcanism: Geological Society, London, Special Publications, v. 145, p. 9–26, doi: 10.1144/GSL.SP.1996.145.01.02.

Dohmen, R., and Blundy, J., 2014, A PREDICTIVE THERMODYNAMIC MODEL FOR ELEMENT PARTITIONING BETWEEN PLAGIOCLASE AND MELT AS A FUNCTION OF PRESSURE , TEMPERATURE AND COMPOSITION: v. 314, p. 1319–1372, doi: 10.2475/09.2014.04.

Drake, M.J., 1976, Plagioclase-melt equilibria: Geochimica et Cosmochimica Acta, v. 40, p. 457–465.

Drew, S.T., Ducea, M.N., and Schoenbohm, L.M., 2009, Mafic volcanism on the Puna Plateau, NW Argentina: Implications for lithospheric composition and evolution with an emphasis on lithospheric foundering: Lithosphere, v. 1, p. 305–318, doi: 10.1130/L54.1.

Druitt, T.H., Costa, F., Deloule, E., Dungan, M., and Scaillet, B., 2012, Decadal to monthly timescales of magma transfer and reservoir growth at a caldera volcano: Nature, v. 482, p. 77–80, doi: 10.1038/nature10706.

Dufek, J., and Bergantz, G.W., 2005, Lower crustal magma genesis and preservation: A stochastic framework for the evaluation of basalt-crust interaction: Journal of Petrology, v. 46, p. 2167–2195, doi: 10.1093/petrology/egi049.

Eichelberger, J.C., 1975, Origin of andesite and dacite: Evidence of mixing at Glass Mountain in California and at other circum-Pacific volcanoes: Bulletin of the Geological Society of America, v. 86, p. 1381–1391, doi: 10.1130/0016-7606(1975)86<1381:OOAADE>2.0.CO;2.

Folkes, C.B., De Silva, S.L., Schmitt, A.K., and Cas, R.A.F., 2011, A reconnaissance of U-Pb zircon ages in the Cerro Galán system, NW Argentina: Prolonged magma residence, crystal recycling, and crustal assimilation: Journal of Volcanology and Geothermal Research, v. 206, p. 136–147, doi: 10.1016/j.jvolgeores.2011.06.001.

Folkes, C.B., de Silva, S.L., Wright, H.M., and Cas, R.A.F., 2011, Geochemical homogeneity of a long-lived, large silicic system; evidence from the Cerro Galán caldera, NW Argentina: Bulletin of Volcanology, v. 73, p. 1455–1486, doi: 10.1007/s00445-011-0511-y.

Folkes, C.B., Wright, H.M., Cas, R.A.F., de Silva, S.L., Lesti, C., and Viramonte, J.G., 2011, A re-appraisal of the stratigraphy and volcanology of the Cerro Galán volcanic system, NW Argentina: Bulletin of Volcanology, v. 73, p. 1427–1454, doi: 10.1007/s00445-011-0459-y.

Forni, F., Petricca, E., Bachmann, O., Mollo, S., De Astis, G., and Piochi, M., 2018, The role of magma mixing/mingling and cumulate melting in the Neapolitan Yellow Tuff caldera-forming eruption (Campi Flegrei, Southern Italy): Contributions to Mineralogy and Petrology, v. 173, p. 1–18, doi: 10.1007/s00410-018-1471-4.

Gardner, J.E., Layer, P.W., and Rutherford, M.J., 2002, Phenocrysts versus xenocrysts in the youngest Toba Tuff: Impications for the petrogenesis of 2800 km3 of magma: Geology, v. 30, p. 347–350, doi: 10.1130/0091-7613(2002)030<0347:PVXITY>2.0.CO;2.

Gelman, S.E., Gutiérrez, F.J., and Bachmann, O., 2013, On the longevity of large upper crustal silicic magma reservoirs: Geology, v. 41, doi: 10.1130/G34241.1.

Geurts, P., Ernst, D., and Wehenkel, L., 2006, Extremely randomized trees: Machine Learning, v. 63, p. 3–42, doi: 10.1007/s10994-006-6226-1.

Giletti, B.J., and Casserly, J.E.D., 1994, Strontium diffusion kinetics in plagioclase feldspars: Geochimica et Cosmochimica Acta, v. 58, p. 3785–3793, doi: 10.1016/0016-7037(94)90363-8.

Ginibre, C., Wörner, G., and Kronz, A., 2004, Structure and dynamics of the Laacher See magma chamber (Eifel, Germany) from major and trace element zoning in sanidine: A cathodoluminescence and electron microprobe study: Journal of Petrology, v. 45, p. 2197–2223, doi: 10.1093/petrology/egh053.

Giordano, D., Russell, J.K., and Dingwell, D.B., 2008, Viscosity of magmatic liquids : A model: v. 271, p. 123–134, doi: 10.1016/j.epsl.2008.03.038.

Glazner, A.F., Coleman, D.S., and Bartley, J.M., 2008, The tenuous connection between high-silica rhyolites and granodiorite plutons: Geology, v. 36, p. 183–186, doi: 10.1130/G24496A.1.

Van Grieken, R., and Markowicz, A., 2002, Handbook of X-Ray Spectrometry, Second Edition: Marcel Dekker, Inc, doi: 10.1201/9780203908709.

Grocke, S.B., Andrews, B.J., and de Silva, S.L., 2017, Experimental and petrological constraints on long-term magma dynamics and post-climactic eruptions at the Cerro Galán caldera system, NW Argentina: Journal of Volcanology and Geothermal Research, v. 347, p. 296–311, doi: 10.1016/j.jvolgeores.2017.09.021.

Grove, T.L., Baker, M.B., and Kinzler, R.J., 1984, Coupled CaAl-NaSi diffusion in plagioclase feldspar: Experiments and applications to cooling rate speedometry: Geochimica et Cosmochimica Acta, v. 48, p. 2113–2121, doi: 10.1016/0016-7037(84)90391-0.

Gualda, G.A.R., and Ghiorso, M.S., 2015, MELTS-Excel: A Microsoft Excel-based MELTS interface for research and teaching of magma properties and evolution: Geochemistry, Geophysics, Geosystems, v. 16, p. 315–324, doi: 10.1002/2014GC005545.

Gualda, G.A.R., Ghiorso, M.S., Lemons, R. V., and Carley, T.L., 2012, Rhyolite-MELTS: A modified calibration of MELTS optimized for silica-rich, fluid-bearing magmatic systems: Journal of Petrology, v. 53, p. 875–890, doi: 10.1093/petrology/egr080.

Gualda, G.A.R., Gravley, D.M., Connor, M., Hollmann, B., Pamukcu, A.S., Bégué, F., Ghiorso, M.S., and Deering, C.D., 2018, Climbing the crustal ladder: Magma storage-depth evolution during a volcanic flare-up: Science Advances, v. 4, p. 1–10, doi: 10.1126/sciadv.aap7567.

Gualda, G.A.R., Pamukcu, A.S., Claiborne, L.L., and Rivers, M.L., 2010, Quantitative 3D petrography using X-ray tomography 3: Documenting accessory phases with differential absorption tomography: Geosphere, v. 6, p. 782–792, doi: 10.1130/GES00568.1.

Gualda, G.A.R., and Rivers, M., 2006, Quantitative 3D petrography using x-ray tomography: Application to Bishop Tuff pumice clasts: Journal of Volcanology and Geothermal Research, v. 154, p. 48–62, doi: 10.1016/j.jvolgeores.2005.09.019.

Guillong, M., Meier, D.L., Allan, M.M., Heinrich, C.A., and Yardley, B.W.D., 2008, SILLS: A MATLAB-BASED PROGRAM FOR THE REDUCTION OF LASER ABLATION ICP-MS DATA OF HOMOGENEOUS MATERIALS AND INCLUSIONS: Mineralogical Society of Canada Short Course, p. 328–333.

Hanna, R.D., and Ketcham, R.A., 2017, X-ray computed tomography of planetary materials: A primer and review of recent studies: Chemie der Erde - Geochemistry, v. 77, p. 547–572, doi: 10.1016/j.chemer.2017.01.006.

Hartung, E., Weber, G., and Caricchi, L., 2019, The role of H2O on the extraction of melt from crystallising magmas: Earth and Planetary Science Letters, v. 508, p. 85–96, doi: 10.1016/j.epsl.2018.12.010.

Higgins, M.D., 2000, Measurement of crystal size distributions: American Mineralogist, v. 85, p. 1105–1116.

Hildreth, W., 1981, Gradients in Silicic Magma Chambers Implications for Lithospheric Magmatism: Journal of Geophysical Research, v. 86, p. 10153–10192.

Holland, T., and Blundy, J., 1994, Non-ideal interactions in calcic amphiboles and their bearing on amphibole-plagioclase thermometry: Contributions to Mineralogy and Petrology, v. 116, p. 433–447, doi: 10.1007/BF00310910.

Huber, C., Bachmann, O., and Dufek, J., 2012, Crystal-poor versus crystal-rich ignimbrites: A competition between stirring and reactivation: Geology, v. 40, p. 115–118, doi: 10.1130/G32425.1.

Huber, C., Townsend, M., Degruyter, W., and Bachmann, O., 2019, Optimal depth of subvolcanic magma chamber growth controlled by volatiles and crust rheology: Nature Geoscience, v. 12, p. 762–768, doi: 10.1038/s41561-019-0415-6.

Icenhower, J., and London, D., 1996, Experimental partioning of Rb, Cs, Sr and ba between Alkalifeldspar and peraluminous melt: American Mineralogist, v. 81, p. 719–734, doi: 10.2138/am-1996-5-619.

Jaeger, J.C., 1964, Thermal Effects of Intrusions: Reviews of Geophysics, v. 2.

Jähne, B., Haußecker, H., and Geißler, P., 1999, 3D computer vision and applications: v. 1.

Jaxybulatov, K., Shapiro, N.M., Koulakov, I., Mordret, A., Landès, M., and Sens-Schönfelder, C., 2014, A large magmatic sill complex beneath the Toba caldera: Science, v. 346, p. 617–619, doi: 10.1126/science.1258582.

Jellinek, A.M., and DePaolo, D.J., 2003, A model for the origin of large silicic magma chambers: Precursors of caldera-forming eruptions: Bulletin of Volcanology, v. 65, p. 363–381, doi: 10.1007/s00445-003-0277-y.

Kaiser, J.F., de Silva, S., Schmitt, A.K., Economos, R., and Sunagua, M., 2017, Million-year melt–presence in monotonous intermediate magma for a volcanic–plutonic assemblage in the Central Andes: Contrasting histories of crystal-rich and crystal-poor super-sized silicic magmas: Earth and Planetary Science Letters, v. 457, p. 73–86, doi: 10.1016/j.epsl.2016.09.048.

Karakas, O., Degruyter, W., Bachmann, O., and Dufek, J., 2017, Lifetime and size of shallow magma bodies controlled by crustal-scale magmatism: Nature Geoscience, v. 10, p. 446–450, doi: 10.1038/ngeo2959.

Kay, S.M., Coira, B., and Viramonte, J., 1994, Young mafic back arc volcanic rocks as indicators of continental lithospheric delamination beneath the Argentine Puna plateau, central Andes: v. 99.

Kay, S.M., Coira, B., Wörner, G., Kay, R.W., and Singer, B.S., 2011, Geochemical, isotopic and single crystal 40Ar/39Ar age constraints on the evolution of the Cerro Galán ignimbrites: Bulletin of Volcanology, v. 73, p. 1487–1511, doi: 10.1007/s00445-010-0410-7.

Kent, A.J.R., Blundy, J., Cashman, K. V., Copper, K.M., Donnelly, C., Pallister, J.S., Reagan, M., Rowe, M.C., and Thornber, C.R., 2007, Vapor transfer prior to the October 2004 eruption of Mount St. Helens, Washington: Geology, v. 35, p. 231–234, doi: 10.1130/G22809A.1.

Kent, A.J.R., and Cooper, K.M., 2018, How well do zircons record the thermal evolution of magmatic systems ? v. 46, p. 1–4, doi: doi.org/10.1130/G39690.1.

Kent, A.J.R., Darr, C., Koleszar, A.M., Salisbury, M.J., and Cooper, K.M., 2010, Preferential eruption of andesitic magmas through recharge filtering: Nature Geoscience, v. 3, p. 631–636, doi: 10.1038/ngeo924.

Kent, A.J.R., Rowe, M.C., Thornber, C.R., and Pallister, J.S., 2008, Trace element and Pb isotope composition of plagioclase from dome samples from the 2004-2005 eruption of Mount St. Helens, Washington: US Geological Survey Professional Paper, p. 809–826, doi: 10.3133/pp175035.

Kent, A.J.R., and Ungerer, C.A., 2006, Analysis of light lithophile elements (Li, Be, B) by laser ablation ICP-MS: Comparison between magnetic sector and quadrupole ICP-MS: American Mineralogist, v. 91, p. 1401–1411, doi: 10.2138/am.2006.2030.

Kern, J.M., de Silva, S.L., Schmitt, A.K., Kaiser, J.F., Iriarte, A.R., and Economos, R., 2016, Geochronological imaging of an episodically constructed subvolcanic batholith: U-Pb in zircon chronochemistry of the Altiplano-Puna Volcanic Complex of the Central Andes: Geosphere, v. 12, p. 1054–1077, doi: 10.1130/GES01258.1.

Klemetti, E.W., Deering, C.D., Cooper, K.M., and Roeske, S.M., 2011, Magmatic perturbations in the Okataina Volcanic Complex, New Zealand at thousand-year timescales recorded in single zircon crystals: Earth and Planetary Science Letters, v. 305, p. 185–194, doi: 10.1016/j.epsl.2011.02.054.

Knaack, C., Cornelius, S., and Hooper, P., 1994, Trace element analyses of rocks and minerals by ICP-MS.:

Krimer, D., and Costa, F., 2017, Evaluation of the effects of 3D diffusion, crystal geometry, and initial conditions on retrieved time-scales from Fe–Mg zoning in natural oriented orthopyroxene crystals: Geochimica et Cosmochimica Acta, v. 196, p. 271–288, doi: 10.1016/j.gca.2016.09.037.

LaTourrette, T., and Wasserburg, G.J., 1998, Mg diffusion in anorthite: implications for the formation of early solar system planetesimals: Earth and Planetary Science Letters, v. 158, p. 91–108, doi: 10.1016/S0012-821X(98)00048-X.

Laumonier, M., Karakas, O., Bachmann, O., Gaillard, F., Lukács, R., Seghedi, I., Menand, T., and Harangi, S., 2019, Evidence for a persistent magma reservoir with large melt content beneath an apparently extinct volcano: Earth and Planetary Science Letters, v. 521, p. 79–90, doi: 10.1016/j.epsl.2019.06.004.

Leake, B.E., Woolley, A.R., Arps, C.E.S., Birch, W.D., Gilbert, M.C., Grice, J.D., Hawthorne, F.C., Kato, A., Kisch, H.J., Krivovichev, V.G., Linthout, K., Laird, J., Mandarino, J.A., Maresch, W. V., et al., 1997, Nomenclature of amphiboles: Report of the subcommittee on amphiboles of the international mineralogical association, commission on new minerals and mineral names: Canadian Mineralogist, v. 35, p. 219–246.

Lipman, P.W., and McIntosh, W.C., 2008, Eruptive and noneruptive calderas, northeastern San Juan Mountains, Colorado: Where did the ignimbrites come from? Geological Society of America Bulletin, v. 120, p. 771–795, doi: 10.1130/B26330.1.

Liu, M., and Yund, R.A., 1992, NaSi-CaAl interdiffusion in plagioclase: American Mineralogist, v. 77, p. 275–283.

Longerich, H.P., Jackson, S.E., and Günther, D., 1996, Laser ablation inductively coupled plasma mass spectrometric transient signal data acquisition and analyte concentration calculation: Journal of Analytical Atomic Spectrometry, v. 11, p. 899–904, doi: 10.1039/JA9961100899.

Lubbers, J., Deering, C., and Bachmann, O., 2020, Genesis of rhyolitic melts in the upper crust : Fractionation and remobilization of an intermediate cumulate at Lake City caldera, Colorado, USA: Journal of Volcanology and Geothermal Research, v. 392, doi: 10.1016/j.jvolgeores.2019.106750.

Lundstrom, C.C., and Glazner, A.F., 2016, Silicic magmatism and the volcanic-plutonic connection: Elements, v. 12, doi: 10.2113/gselements.12.2.91.

Mader, H.M., Llewellin, E.W., and Mueller, S.P., 2013, The rheology of two-phase magmas: A review and analysis: Journal of Volcanology and Geothermal Research, v. 257, p. 135–158, doi: 10.1016/j.jvolgeores.2013.02.014.

Marsh, B.D., 1981, On the crystallinity, probability of occurrence, and rheology of lava and magma: Contributions to Mineralogy and Petrology, v. 78, p. 85–98, doi: 10.1007/BF00371146.

Mason, B.G., Pyle, D.M., and Oppenheimer, C., 2004, The size and frequency of the largest explosive eruptions on Earth: Bulletin of Volcanology, v. 66, p. 735–748, doi: 10.1007/s00445-004-0355-9.

Matthews, N.E., Vazquez, J.A., and Calvert, C.T., 2015, Age of the Lava Creek supereruption and magma chamber assembly at Yellowstone based on 40Ar/39Ar and U-Pb dating of sanidine and zircon crystals: Geochemistry, Geophysics, Geosystems, doi: 10.1002/2015GC005881.Received.

Mccullough, E.C., 1975, Photon attenuation in computed tomography: Medical Physics, v. 2, p. 307–320, doi: 10.1118/1.594199.

Mcintire, W.I.L., 1963, McIntire_1963_Partition coefficients: Geochimica et Cosmochimica Acta, v. 27, p. 1209–1264.

Mischel, S.A., Mertz-Kraus, R., Jochum, K.P., and Scholz, D., 2017, TERMITE: An R script for fast reduction of laser ablation inductively coupled plasma mass spectrometry data and its application to trace element measurements: Rapid communications in mass spectrometry : RCM, v. 31, p. 1079–1087, doi: 10.1002/rcm.7895.

Morgan, D.J., and Blake, S., 2006, Magmatic residence times of zoned phenocrysts: Introduction and application of the binary element diffusion modelling (BEDM) technique: Contributions to Mineralogy and Petrology, v. 151, p. 58–70, doi: 10.1007/s00410-005-0045-4.

Mourey, A.J., and Shea, T., 2019, Forming Olivine Phenocrysts in Basalt: A 3D Characterization of Growth Rates in Laboratory Experiments: Frontiers in Earth Science, v. 7, p. 1–16, doi: 10.3389/feart.2019.00300.

Mucek, A.E., Danišík, M., De Silva, S.L., Schmitt, A.K., Pratomo, I., and Coble, M.A., 2017, Post-supereruption recovery at Toba Caldera: Nature Communications, v. 8, p. 1–9, doi: 10.1038/ncomms15248.

Mutch, E.J.F., Maclennan, J., Shorttle, O., Rudge, J.F., and Neave, D.A., 2021, DFENS: Diffusion Chronometry Using Finite Elements and Nested Sampling: Geochemistry, Geophysics, Geosystems, v. 22, p. 1–28, doi: 10.1029/2020GC009303.

Nielsen, R., Ustunisik, G., Weinsteiger, A., Tepley, F., Johnston, D., and Kent, A.J.R., 2017, Trace element partitioning between plagioclase and melt: An investigation of the impact of experimental and analytical procedures: Geochemistry, Geophysics, Geosystems, v. 18, p. 1580–1593, doi: 10.1002/2017GC006821.

Van Orman, J.A., Cherniak, D.J., and Kita, N.T., 2014, Magnesium diffusion in plagioclase: Dependence on composition, and implications for thermal resetting of the 26Al-26Mg early solar system chronometer: Earth and Planetary Science Letters, v. 385, p. 79–88, doi: 10.1016/j.epsl.2013.10.026.

Ortiz, A., Suzaño, N., Hauser, N., Becchio, R., and Nieves, A., 2019, New hints on the evolution of the Eastern Magmatic Belt, Puna Argentina. SW Gondwana margin: Zircon U-Pb ages and Hf isotopes in the Pachamama Igneous-Metamorphic Complex: Journal of South American Earth Sciences, v. 94, p. 102246, doi: 10.1016/j.jsames.2019.102246.

Pamukcu, A.S., and Gualda, G.A.R., 2010, Quantitative 3D petrography using X-ray tomography 2: Combining information at various resolutions: Geosphere, v. 6, p. 775–781, doi: 10.1130/GES00565.1.

Pankhurst, M.J., Dobson, K.J., Morgan, D.J., Loughlin, S.C., Thordarson, T.H., Lee, P.D., and Courtois, L., 2014, Monitoring the magmas fuelling volcanic eruptions in near-real-time using x-ray micro-computed tomography: Journal of Petrology, v. 55, p. 671–684, doi: 10.1093/petrology/egt079.

Pankhurst, M.J., Vo, N.T., Butcher, A.R., Long, H., Wang, H., Nonni, S., Harvey, J., Gucrossed, G.D.S., Fowler, R., Atwood, R., Walshaw, R., and Lee, P.D., 2018, Quantitative measurement of olivine composition in three dimensions using helical-scan X-ray micro-tomography: American Mineralogist, v. 103, p. 1800–1811, doi: 10.2138/am-2018-6419.

Paton, C., Hellstrom, J., Paul, B., Woodhead, J., and Hergt, J., 2011, Iolite: Freeware for the visualisation and processing of mass spectrometric data: Journal of Analytical Atomic Spectrometry, v. 26, p. 2508–2518, doi: 10.1039/c1ja10172b.

Pearce, N.J.G., Westgate, J.A., Gualda, G.A.R., Gatti, E., and Muhammad, R.F., 2020, Tephra glass chemistry provides storage and discharge details of five magma reservoirs which fed the 75 ka Youngest Toba Tuff eruption, northern Sumatra: Journal of Quaternary Science, v. 35, p. 256–271, doi: 10.1002/jqs.3149.

Pedregosa, F., Varoquaux, G., Alexandre, G., Michel, V., Thirion, B., Grisel, O., Blondel, M., Prettenhofer, P., Weiss, R., Dubourg, V., Vanderplas, J., Passos, A., Cournapeau, D., Brucher, M., et al., 2011, Scikit-learn: Machine Learning in Python: Journal of Machine Learning Research, v. 12, p. 2825–2830.

Petford, N., Cruden, A.R., McCaffrey, K.J.W., and Vigneresse, J.L., 2000, Granite magma formation , transport and emplacement in the Earth ' s crust: v. 408, p. 1–15.

Petrelli, M., Caricchi, L., and Perugini, D., 2020, Machine Learning Thermo-Barometry: Application to Clinopyroxene-Bearing Magmas: Journal of Geophysical Research: Solid Earth, v. 125.

Putirka, K., 2016, Amphibole thermometers and barometers for igneous systems and some implications for eruption mechanisms of felsic magmas at arc volcanoes: American Mineralogist, v. 101, p. 841–858, doi: 10.2138/am-2016-5506.

Putirka, K.D., 2008, Thermometers and Barometers for Volcanic Systems: Reviews in Mineralogy and Geochemistry, v. 69, p. 61–120, doi: 10.2138/rmg.2008.69.3.

Ratajeski, K., Sisson, T.W., and Glazner, A.F., 2005, Experimental and geochemical evidence for derivation of the El Capitan Granite, California, by partial melting of hydrous gabbroic lower crust: Contributions to Mineralogy and Petrology, v. 149, p. 713–734, doi: 10.1007/s00410-005-0677-4.

Reddy, S.M., Saxey, D.W., Rickard, W.D.A., Fougerouse, D., Montalvo, S.D., Verberne, R., and van Riessen, A., 2020, Atom Probe Tomography: Development and Application to the Geosciences: Geostandards and Geoanalytical Research, v. 44, p. 5–50, doi: 10.1111/ggr.12313.

Reid, M.R., and Vazquez, J.A., 2017, Fitful and protracted magma assembly leading to a giant eruption, Youngest Toba Tuff, Indonesia: Geochemistry, Geophysics, Geosystems, v. 18, p. 156–177, doi: 10.1002/2016GC006641.

Rickard, W.D.A., Reddy, S.M., Saxey, D.W., Fougerouse, D., Timms, N.E., Daly, L., Peterman, E., Cavosie, A.J., and Jourdan, F., 2020, Novel Applications of FIB-SEM-Based ToF-SIMS in Atom Probe Tomography Workflows: Microscopy and Microanalysis, v. 26, p. 750–757, doi: 10.1017/S1431927620000136.

Roerdink, J.B.T.M., and Meijster, A., 2000, The watershed transform: definitions, algorithms and parallelization strategies: Fundamenta Informaticae, v. 41, p. 187–228, doi: 10.3233/FI-2000-411207.

Rose, Wi., and Chesner, C., 1987, Dispersal of ash in the great Toba eruption, 75 ka: Geology, v. 15, p. 913–917.

Rout, S.S., Blum-Oeste, M., and Wörner, G., 2021, Long-term temperature cycling in a shallow magma reservoir : insights from sanidine megacrysts at Taápaca volcano , Central Andes ABSTRACT : Journal of Petrology, doi: https://doi.org/10.1093/petrology/egab010.

Rubin, A.E., Cooper, K.M., Till, C.B., Kent, A.J.R., Costa, F., Bose, M., Gravley, D., Deering, C., and Cole, J., 2017, Rapid cooling and cold storage in a silicic magma reservoir recorded in Individual Crystals: Science, v. 356, p. 1154–1156, doi: 10.1126/science.aam8720.

Rudnick, R.L., and Fountain, D.M., 1995, Nature and composition of the continental crust: A lower-crustal perspective: Reviews of Geophysics, v. 33, p. 267–309, doi: Doi 10.1029/95rg01302.

Ruprecht, P., and Plank, T., 2013, Feeding andesitic eruptions with a high-speed connection from the mantle: Nature, v. 500, p. 68–72, doi: 10.1038/nature12342.

Ruth, D.C.S., Costa, F., Bouvet De Maisonneuve, C., Franco, L., Cortés, J.A., and Calder, E.S., 2018, Crystal and melt inclusion timescales reveal the evolution of magma migration before eruption: Nature Communications, v. 9, doi: 10.1038/s41467-018-05086-8.

Scaillet, B., Holtz, F., and Pichavant, M., 1998a, Phase equilibrium constraints on the viscosity of silicic: v. 103.

Scaillet, B., Holtz, F., and Pichavant, M., 1998b, Phase equilibrium constraints on the viscosity of silicic magmas: 1. Volcanic-plutonic comparison: Journal of Geophysical Research: Solid Earth, v. 103, p. 27257–27266, doi: 10.1029/98jb02469.

Schneider, C.A., Rasband, W.S., and Eliceiri, K.W., 2012, NIH Image to ImageJ : 25 years of image analysis: Nature Methods, v. 9, p. 671–675, doi: 10.1038/nmeth.2089.

Self, S., 2006, The effects and consequences of very large explosive volcanic eruptions: Philosophical Transactions of the Royal Society A: Mathematical, Physical and Engineering Sciences, v. 364, p. 2073–2097, doi: 10.1098/rsta.2006.1814.

Shamloo, H.I., and Till, C.B., 2019, Decadal transition from quiescence to supereruption: petrologic investigation of the Lava Creek Tuff, Yellowstone Caldera, WY: Contributions to Mineralogy and Petrology, v. 174, p. 1–18, doi: 10.1007/s00410-019-1570-x.

Shamloo, H.I., Till, C.B., and Hervig, R.L., 2021, Multi-mode Magnesium Diffusion in Sanidine: Applications for Geospeedometry in Magmatic Systems: Geochimica et Cosmochimica Acta, v. 298, p. 55–69, doi: 10.1016/j.gca.2021.01.044.

Shea, T., Costa, F., Krimer, D., and Hammer, J.E., 2015, Accuracy of timescales retrieved from diffusion modeling in olivine: A 3D perspective: American Mineralogist, v. 100, p. 2026–2042, doi: 10.2138/am-2015-5163.

Sheppard, A., Latham, S., Middleton, J., Kingston, A., Myers, G., Varslot, T., Fogden, A., Sawkins, T., Cruikshank, R., Saadatfar, M., Francois, N., Arns, C., and Senden, T., 2014, Techniques in helical scanning, dynamic imaging and image segmentation for improved quantitative analysis with X-ray

micro-CT: Nuclear Instruments and Methods in Physics Research, Section B: Beam Interactions with Materials and Atoms, v. 324, p. 49–56, doi: 10.1016/j.nimb.2013.08.072.

Sigl, M., Winstrup, M., McConnell, J.R., Welten, K.C., Plunkett, G., Ludlow, F., Büntgen, U., Caffee, M., Chellman, N., Dahl-Jensen, D., Fischer, H., Kipfstuhl, S., Kostick, C., Maselli, O.J., et al., 2015, Timing and climate forcing of volcanic eruptions for the past 2,500 years: Nature, v. 523, p. 543–549, doi: 10.1038/nature14565.

de Silva, S.L., and Gregg, P.M., 2014, Thermomechanical feedbacks in magmatic systems: Implications for growth, longevity, and evolution of large caldera-forming magma reservoirs and their supereruptions: Journal of Volcanology and Geothermal Research, v. 282, p. 77–91, doi: 10.1016/j.jvolgeores.2014.06.001.

Simonetti, A., Shore, M., and Bell, K., 1996, Diopside phenocrysts from nephelinite lavas, Napak volcano, eastern Uganda: Evidence for magma mixing: Canadian Mineralogist, v. 34, p. 411–421.

Singer, B.S., Dungan, M.A., and Layne, G.D., 1995, Textures and Sr,Ba,Mg,Fe,K, and Ti compositional profiles in volcanic plagioclase: Clues to the dynamics of calc-alkaline magma chambers: American Mineralogist, v. 80, p. 833–840, doi: 10.2138/am-1995-7-819.

Spear, F.S., and Daniel, C.G., 2003, Three-dimensional imaging of garnet porphyroblast sizes and chemical zoning: Nucleation and growth history in the garnet zone: American Mineralogist, v. 88, p. 245.

Streck, M.J., 2008, Mineral Textures and Zoning as Evidence for Open System Processes: Reviews in Mineralogy and Geochemistry, v. 69, p. 595–622, doi: 10.2138/rmg.2008.69.15.

Streck, M.J., Dungan, M.A., Bussy, F., and Malavassi, E., 2005, Mineral inventory of continuously erupting basaltic andesites at Arenal volcano, Costa Rica: Implications for interpreting monotonous, crystal-rich, mafic arc stratigraphies: Journal of Volcanology and Geothermal Research, v. 140, p. 133–155, doi: 10.1016/j.jvolgeores.2004.07.018.

Streck, M.J., and Grunder, A.L., 2008, Phenocryst-poor rhyolites of bimodal, tholeiitic provinces: The Rattlesnake Tuff and implications for mush extraction models: Bulletin of Volcanology, v. 70, p. 385–401, doi: 10.1007/s00445-007-0144-3.

Szymanowski, D., Ellis, B.S., Wotzlaw, J.-F., and Bachmann, O., 2019, Maturation and rejuvenation of a silicic magma reservoir: High-resolution chronology of the Kneeling Nun Tuff: Earth and Planetary Science Letters, v. 510, p. 103–115, doi: 10.1016/j.epsl.2019.01.007.

Szymanowski, D., Wotzlaw, J.-F., Ellis, B.S., Bachmann, O., Guillong, M., and von Quadt, A., 2017, Protracted near-solidus storage and pre-eruptive rejuvenation of large magma reservoirs: Nature Geoscience, v. 10, doi: 10.1038/ngeo3020.

Tajčmanová, L., Abart, R., Wirth, R., Habler, G., and Rhede, D., 2012, Intracrystalline microstructures in alkali feldspars from fluid-deficient felsic granulites: A mineral chemical and TEM study: Contributions to Mineralogy and Petrology, v. 164, p. 715–729, doi: 10.1007/s00410-012-0772-2.

Takeuchi, S., 2004, Precursory dike propagation control of viscous magma eruptions: Geology, v. 32, p. 1001–1004, doi: 10.1130/G20792.1.

Takeuchi, S., 2011, Preeruptive magma viscosity: An important measure of magma eruptibility: Journal of Geophysical Research: Solid Earth, v. 116, doi: 10.1029/2011JB008243.

Taylor, S., and McLennan, S., 1995, The Geochemical Evolution of the Continental Crust: Reviews of Geophysics, v. 33, p. 241–265, doi: 10.1029/95RG00262.

Tepley, F.J., Davidson, J.P., Tilling, R.I., and Arth, J.G., 2000, Magma mixing, recharge, and eruption histories recorded in plagioclase phenocrysts from El Chichon Volcano, Mexico: v. 41, p. 1397–1411.

Tierney, C.R., Reid, M.R., Vazquez, J.A., and Chesner, C.A., 2019, Diverse late-stage crystallization and storage conditions in melt domains from the Youngest Toba Tuff revealed by age and compositional heterogeneity in the last increment of accessory phase growth: Contributions to Mineralogy and Petrology, v. 174, p. 1–21, doi: 10.1007/s00410-019-1566-6.

Tierney, C.R., Schmitt, A.K., Lovera, O.M., and de Silva, S.L., 2016, Voluminous plutonism during volcanic quiescence revealed by thermochemical modeling of zircon: Geology, v. 44, p. 683–686, doi: 10.1130/G37968.1.

Till, C.B., Vazquez, J.A., and Boyce, J.W., 2015a, Months between rejuvenation and volcanic eruption at Yellowstone caldera, Wyoming: Geology, v. 43, p. 695–698, doi: 10.1130/G36862.1.

Till, C.B., Vazquez, J.A., and Boyce, J.W., 2015b, Months between rejuvenation and volcanic eruption at Yellowstone caldera, Wyoming Supplementary Data: Geology, p. 3–7, doi: 10.1038/ngeo1638.Kuiper.

Tsuchiyama, A., Nakano, T., Uesugi, K., Uesugi, M., Takeuchi, A., Suzuki, Y., Noguchi, R., Matsumoto, T., Matsuno, J., Nagano, T., Imai, Y., Nakamura, T., Ogami, T., Noguchi, T., et al., 2013, Analytical dual-energy microtomography: A new method for obtaining three-dimensional mineral phase images and its application to Hayabusa samples: Geochimica et Cosmochimica Acta, v. 116, p. 5–16, doi: 10.1016/j.gca.2012.11.036.

Turcotte, D., and Schubert, G., 2002, Geodynamics: Cambridge University Press, 456 p.

Uesugi, M., Uesugi, K., and Oka, M., 2010, Non-destructive observation of meteorite chips using quantitative analysis of optimized X-ray micro-computed tomography: Earth and Planetary Science Letters, v. 299, p. 359–367, doi: 10.1016/j.epsl.2010.09.016.

Varslot, T., Kingston, A., Sheppard, A., and Sakellariou, A., 2011, Fast high-resolution micro-CT with exact reconstruction methods: Developments in X-Ray Tomography VII, v. 7804, p. 780413, doi: 10.1117/12.860298.

Vazquez, J.A., and Reid, M.R., 2004, Probing the accumulation history of the voluminous Toba magma: Science, v. 305, p. 991–994, doi: 10.1126/science.1096994.

Vigneresse, J.L., Barbey, P., and Cuney, M., 1996, Rheological Transitions During Partial Melting and Crystallization with Application to Felsic Magma Segregation and Transfer: Journal of Petrology, v. 37, p. 1579–1600.

Vincent, L., and Soille, P., 1991, Watersheds in Digital Spaces: An Efficient Algorithm Based on Immersion Simulations: IEEE Transactions on Pattern Analysis and Machine Intelligence, v. 13, p. 583–598, doi: https://doi.org/10.1109/34.87344.

Walker, B.A., Klemetti, E.W., Grunder, A.L., Dilles, J.H., Tepley, F.J., and Giles, D., 2013, Crystal reaming during the assembly, maturation, and waning of an eleven-million-year crustal magma cycle: Thermobarometry of the Aucanquilcha Volcanic Cluster: Contributions to Mineralogy and Petrology, v. 165, p. 663–682, doi: 10.1007/s00410-012-0829-2.

Van Der Walt, S., Schönberger, J.L., Nunez-Iglesias, J., Boulogne, F., Warner, J.D., Yager, N., Gouillart, E., and Yu, T., 2014, Scikit-image: Image processing in python: PeerJ, v. 2014, p. 1–18, doi: 10.7717/peerj.453.

Watson, E.B., and Harrison, T.M., 1983, Zircon saturation revisited: temperature and composition effects in a variety of crustal magma types: Earth and Planetary Science Letters, v. 64, p. 295–304, doi: 10.1016/0012-821X(83)90211-X.

Wildenschild, D., and Sheppard, A.P., 2013, X-ray imaging and analysis techniques for quantifying pore-scale structure and processes in subsurface porous medium systems: Advances in Water Resources, v. 51, p. 217–246, doi: 10.1016/j.advwatres.2012.07.018.

Willmott, P., 2011, An Introduction to Synchrotron Radiation:, doi: 10.1002/9781119970958.

Wilson, C.J.N., Cooper, G.F., Chamberlain, K.J., Barker, S.J., Myers, M.L., Kemp, F.I.-, and Farrell, J., 2021, No single model for supersized eruptions and their magma bodies: Nature Reviews Earth & Environment, doi: 10.1038/s43017-021-00191-7.

Wirth, R., 2009, Focused Ion Beam (FIB) combined with SEM and TEM: Advanced analytical tools for studies of chemical composition, microstructure and crystal structure in geomaterials on a nanometre scale: Chemical Geology, v. 261, p. 217–229, doi: 10.1016/j.chemgeo.2008.05.019.

Wolff, J.A., 2017, On the syenite-trachyte problem: v. 45, p. 1067–1070.

Wolff, J.A., Ellis, B.S., Ramos, F.C., Starkel, W.A., Boroughs, S., Olin, P.H., and Bachmann, O., 2015, Remelting of cumulates as a process for producing chemical zoning in silicic tuffs: A comparison of cool, wet and hot, dry rhyolitic magma systems: Lithos, v. 236–237, p. 275–286, doi: 10.1016/j.lithos.2015.09.002.

Wolff, J.A., Forni, F., Ellis, B.S., and Szymanowski, D., 2020, Europium and barium enrichments in compositionally zoned felsic tuffs: A smoking gun for the origin of chemical and physical gradients by cumulate melting: Earth and Planetary Science Letters, v. 540, p. 116251, doi: 10.1016/j.epsl.2020.116251.

Wotzlaw, J.F., Schaltegger, U., Frick, D.A., Dungan, M.A., Gerdes, A.G., and G??nther, D., 2013, Tracking the evolution of large-volume silicic magma reservoirs from assembly to supereruption: Geology, v. 41, p. 867–870, doi: 10.1130/G34366.1.

Wright, H.M.N., Folkes, C.B., Cas, R.A.F., and Cashman, K. V., 2011, Heterogeneous pumice populations in the 2.08-Ma Cerro Galán Ignimbrite: Implications for magma recharge and ascent preceding a large-volume silicic eruption: Bulletin of Volcanology, v. 73, p. 1513–1533, doi: 10.1007/s00445-011-0525-5.

Zhang, Y., 2010, Diffusion in minerals and melts: Theoretical background: Reviews in Mineralogy and Geochemistry, v. 72, p. 5–59, doi: 10.2138/rmg.2010.72.2.

APPENDICES

Appendix A:

Supplemental figures for chapter 2

Data from this chapter are available in the online version of this dissertation

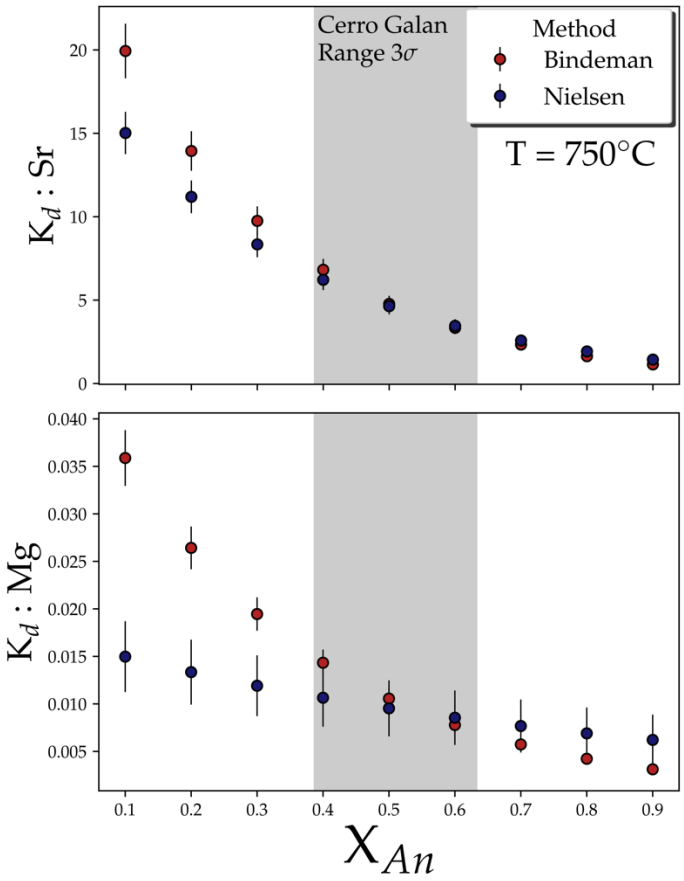

Figure A.1: Comparing partition coefficients calculated using Bindeman et al., (1998) and Nielsen et al., (2017)

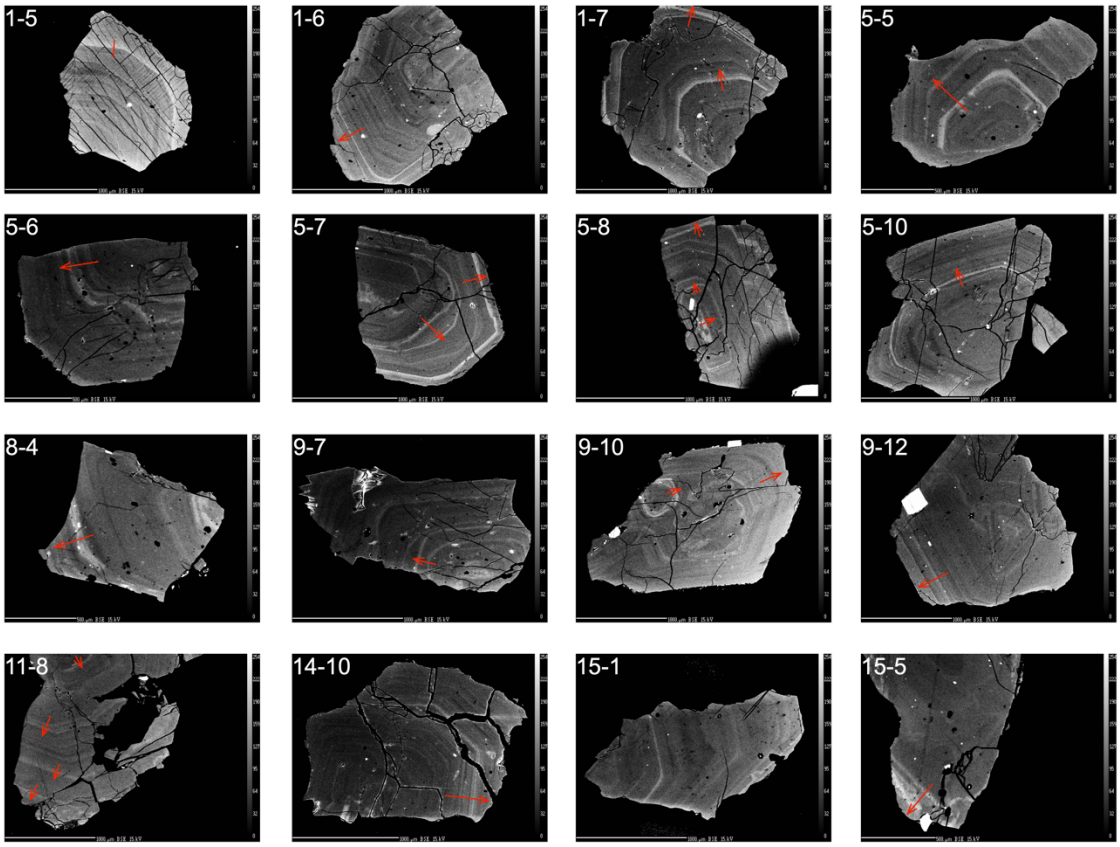

Figure A.2 Plagioclase BSE images

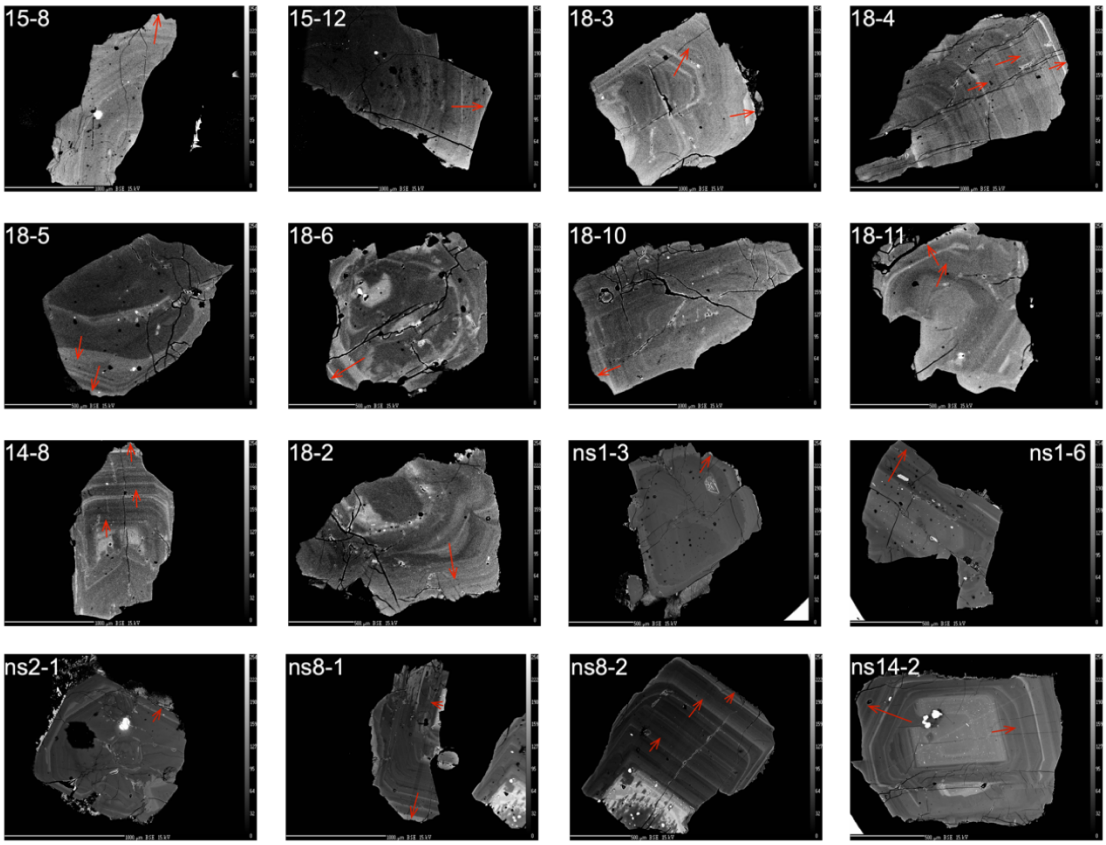

Figure A.2 (continued)

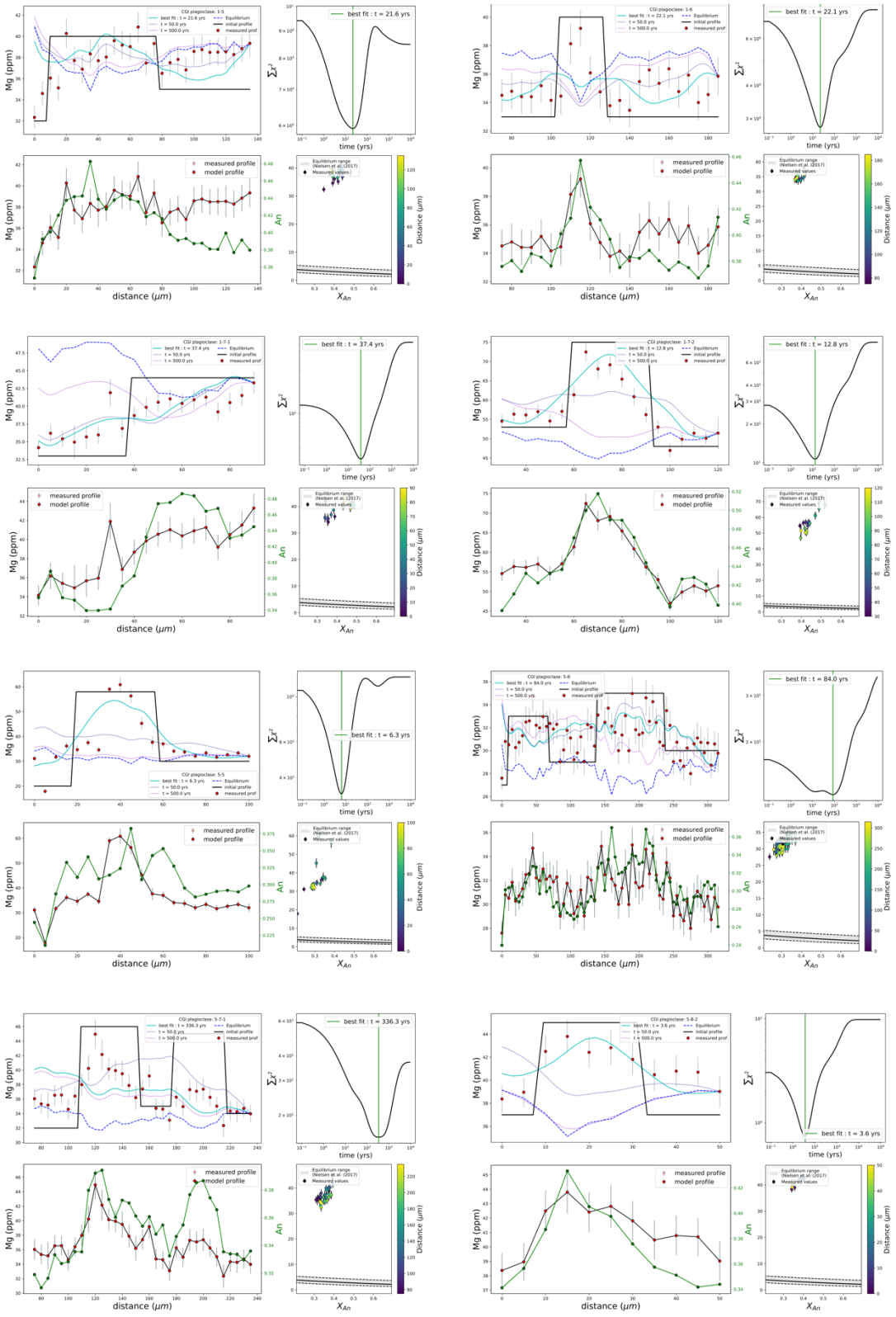

Figure A.3: Individual Mg diffusion models for each grain shown in A.1

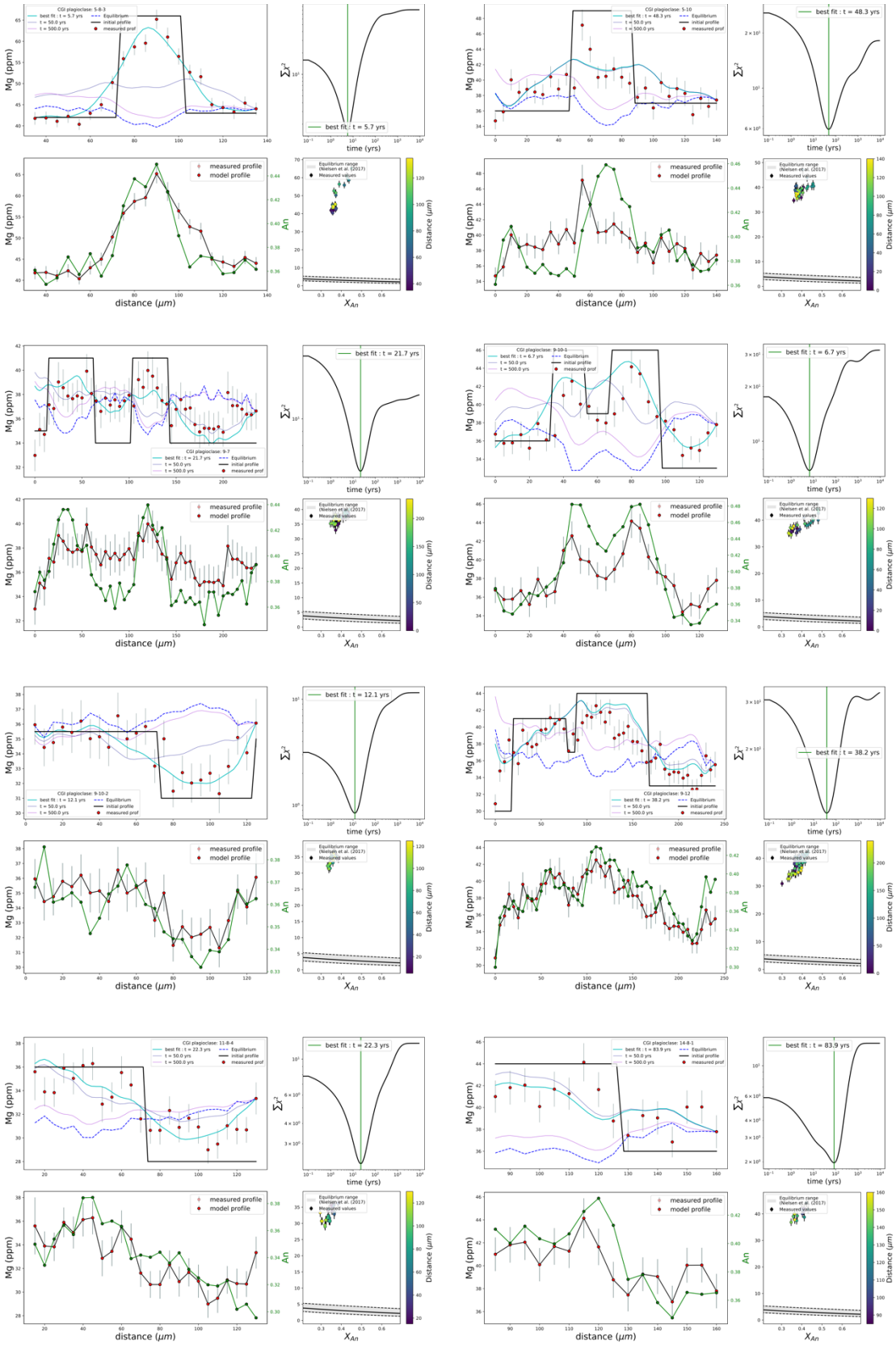

Figure A.3 (continued)

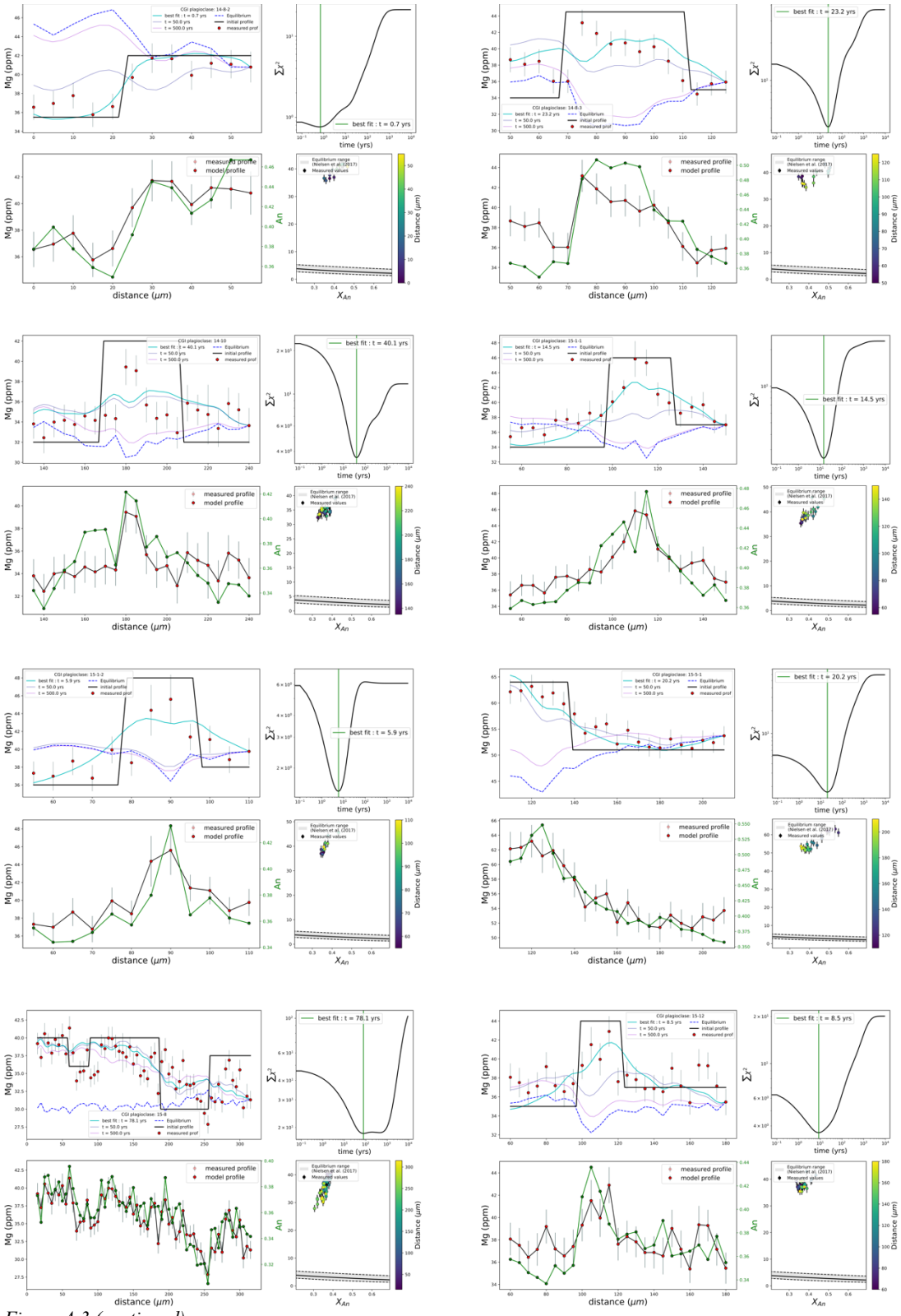

Figure A.3 (continued)

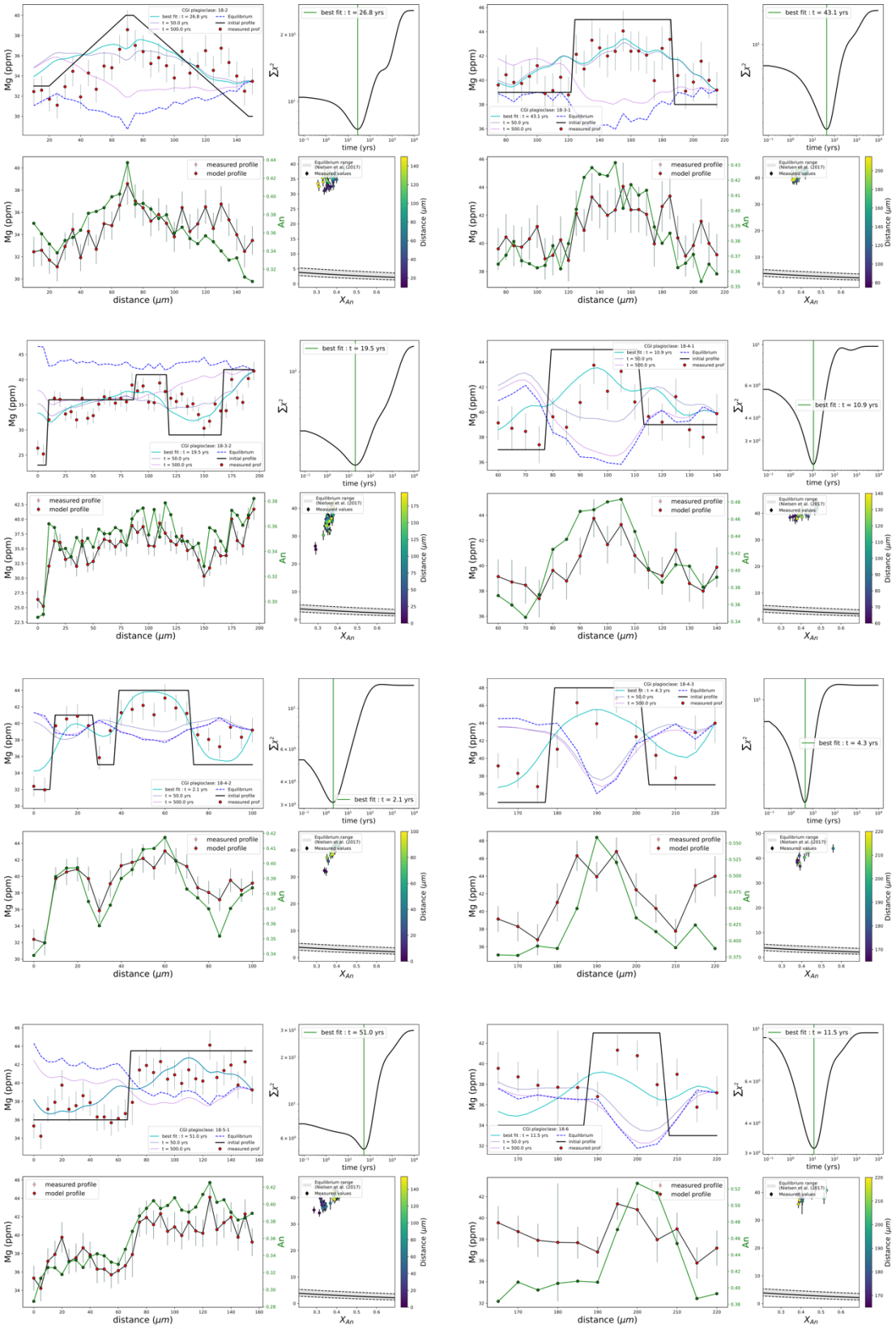

Figure A.3 (continued)

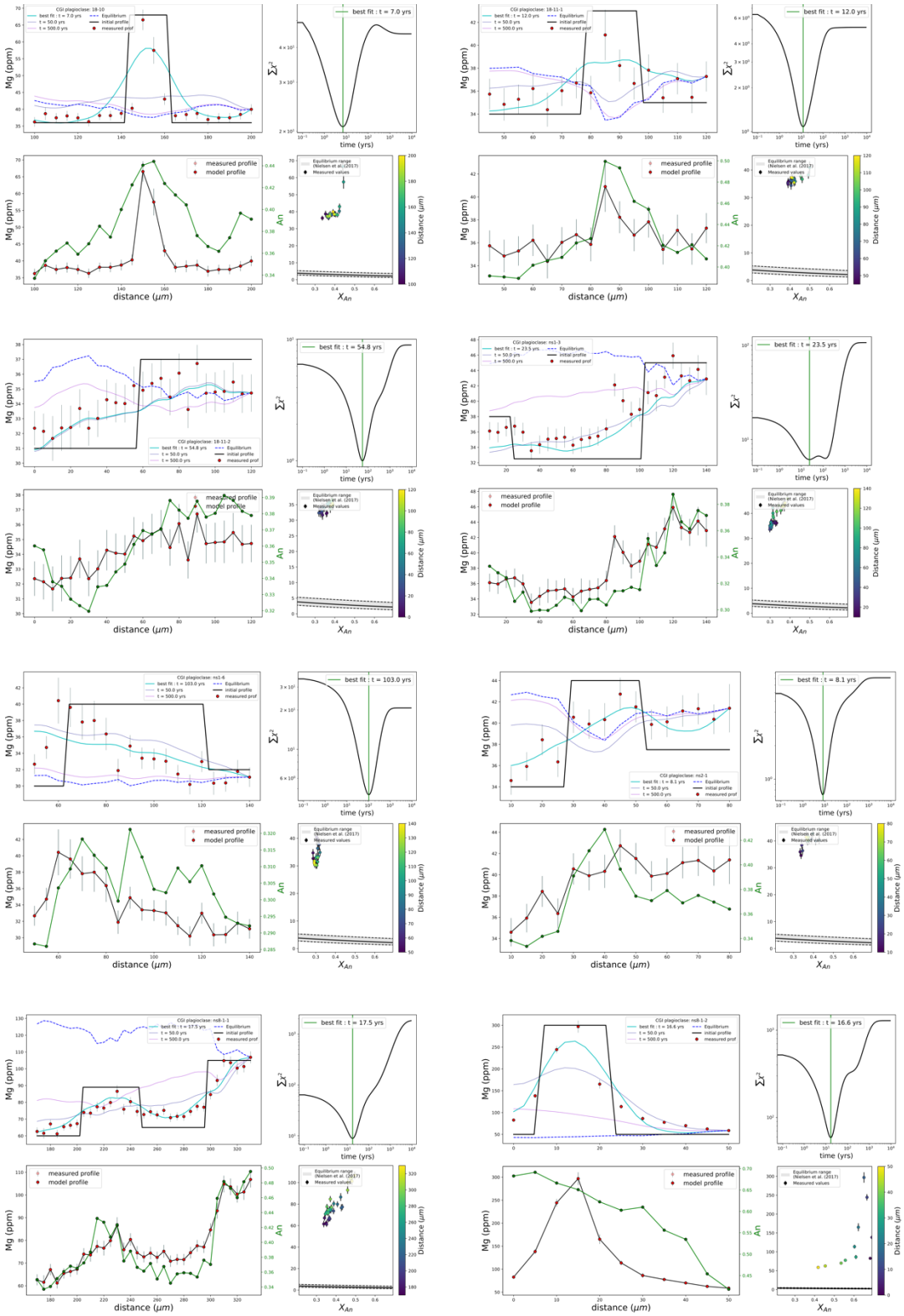

Figure A.3 (continued)

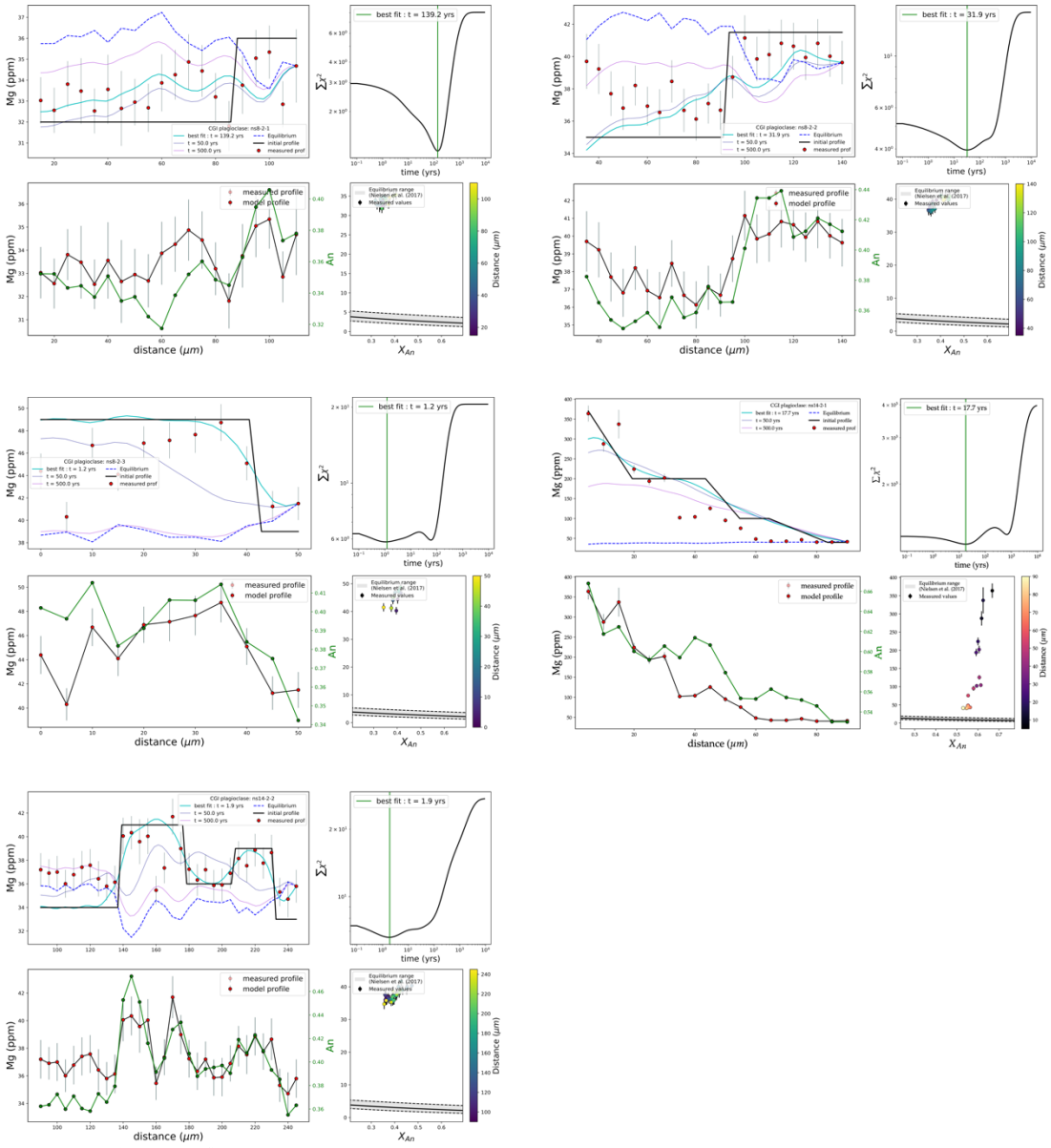

Figure A.3 (continued)

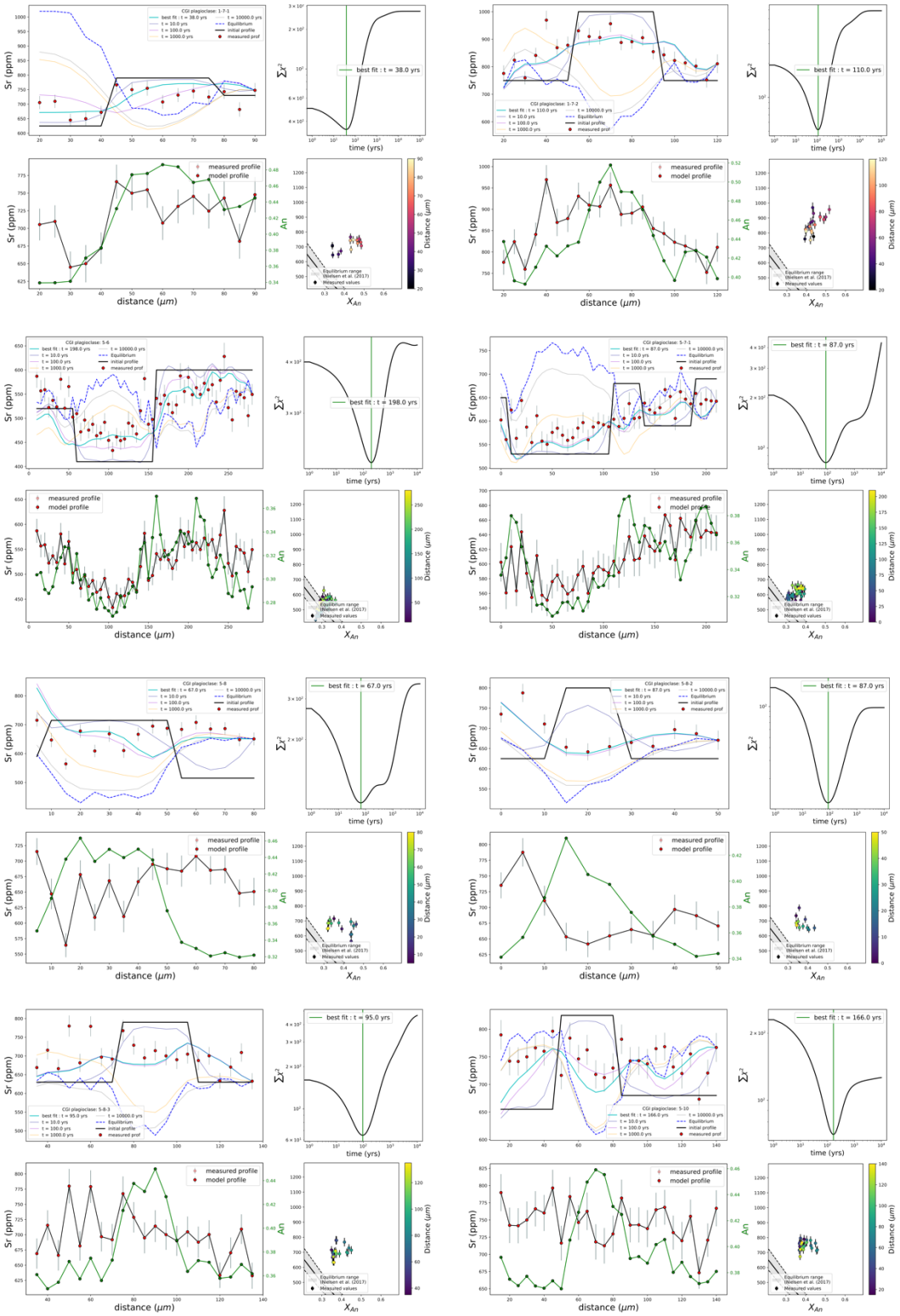

Figure A.4: Individual Sr diffusion models for each grain shown in A.1

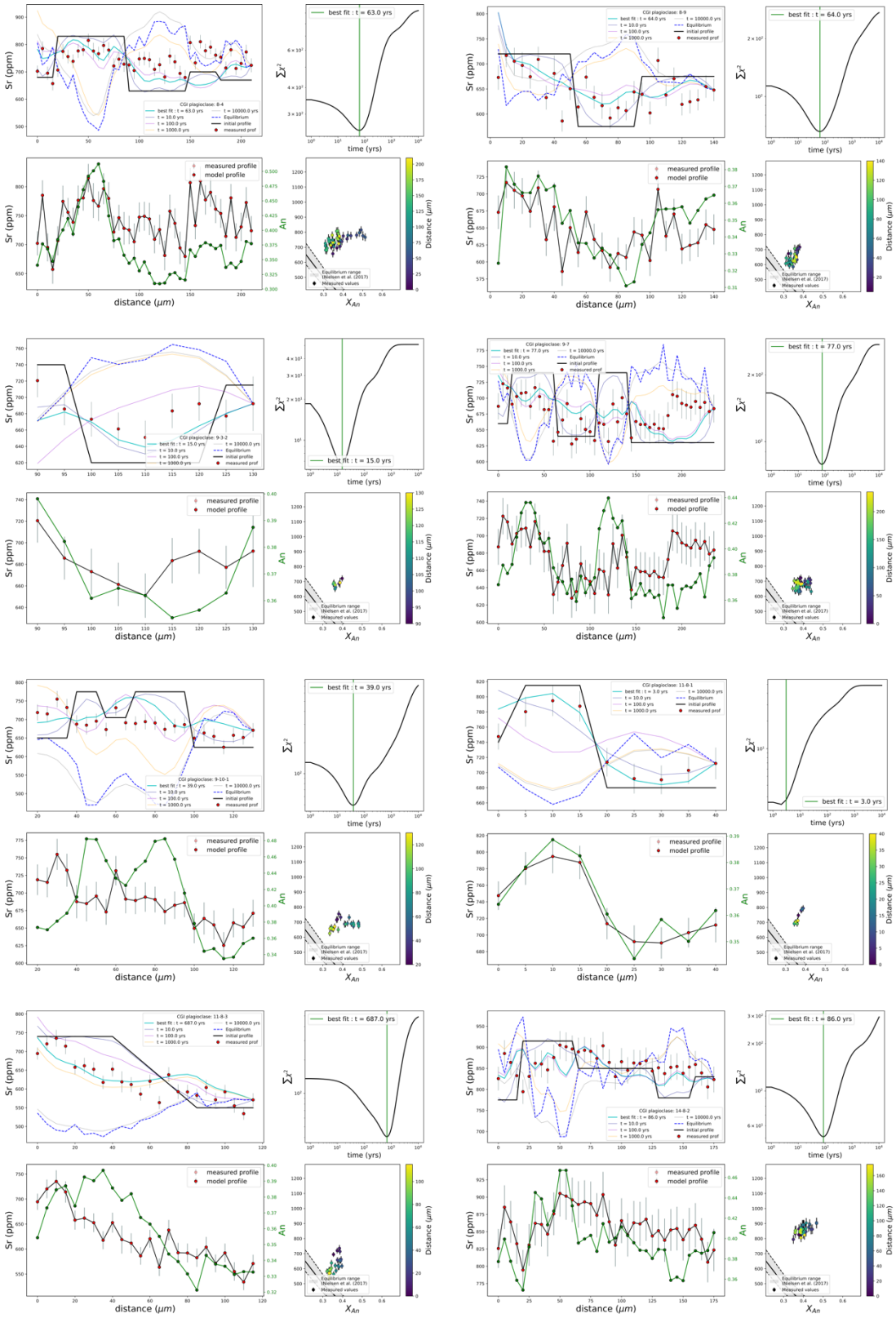

Figure A.4 (continued)

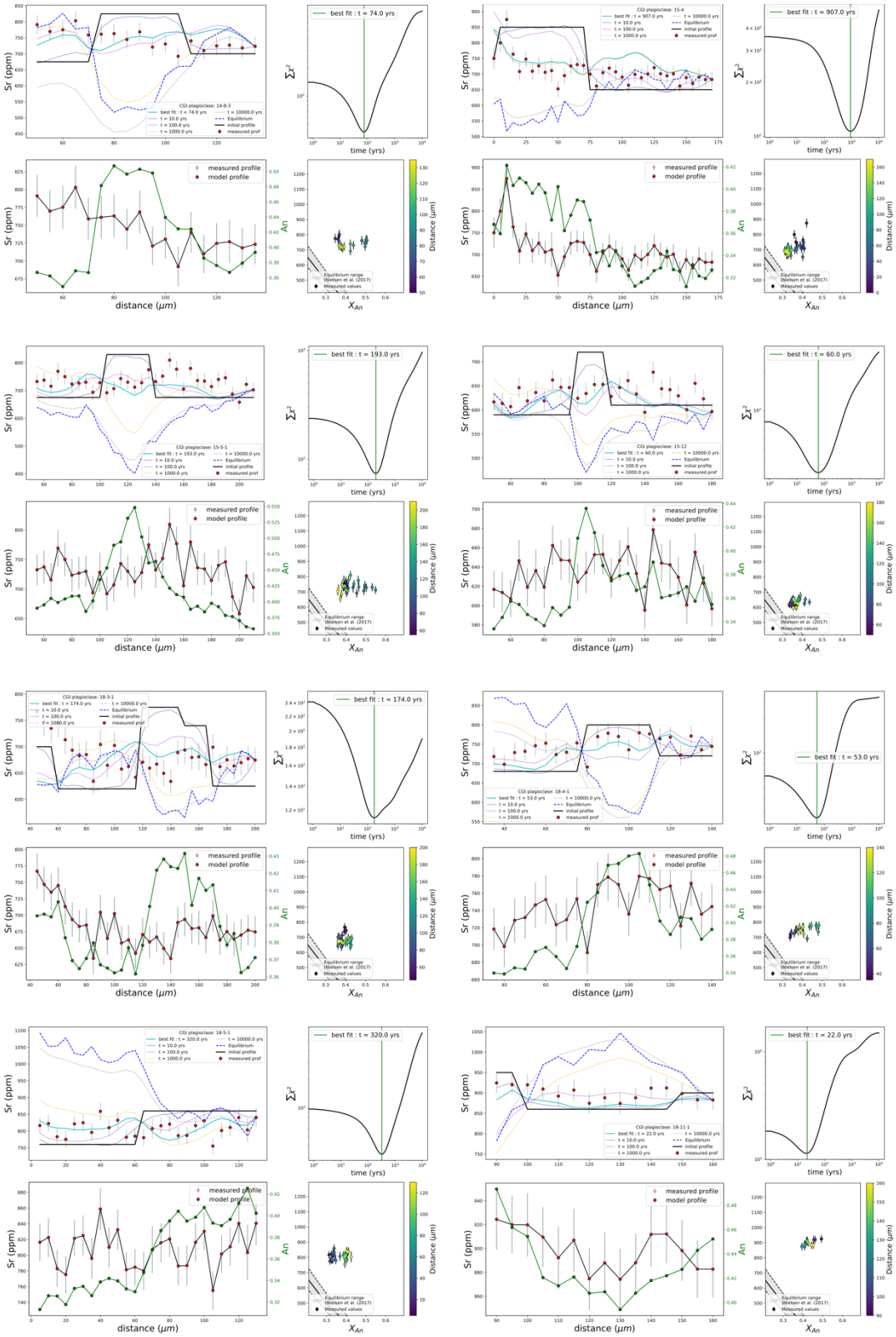

Figure A.4 (continued)

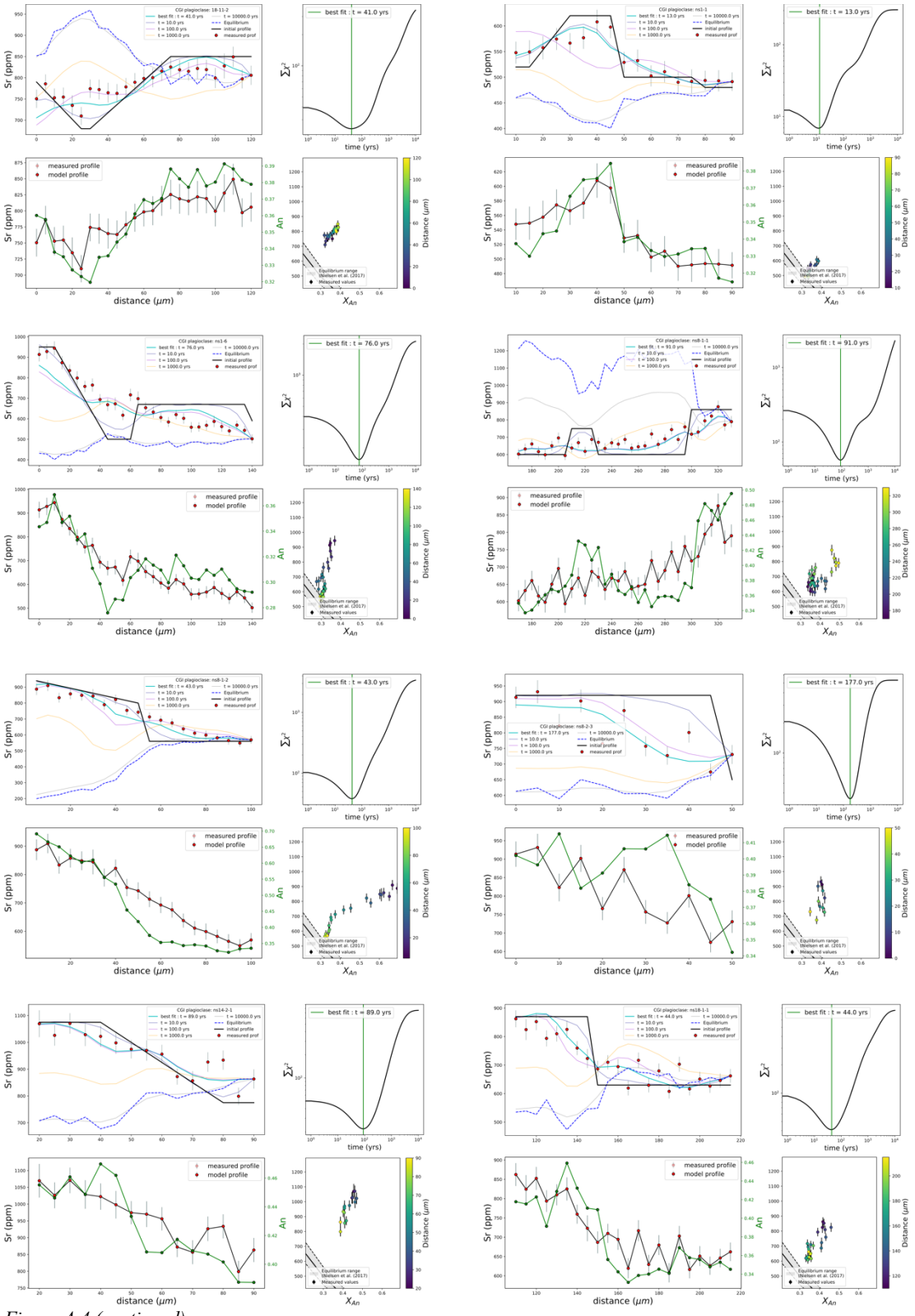

Figure A.4 (continued)

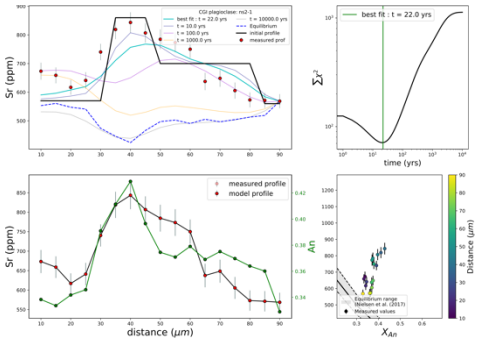

Figure A.4 (continued)

Appendix B:
Supplemental figures for chapter 3

Data from this chapter are available in the online version of this dissertation

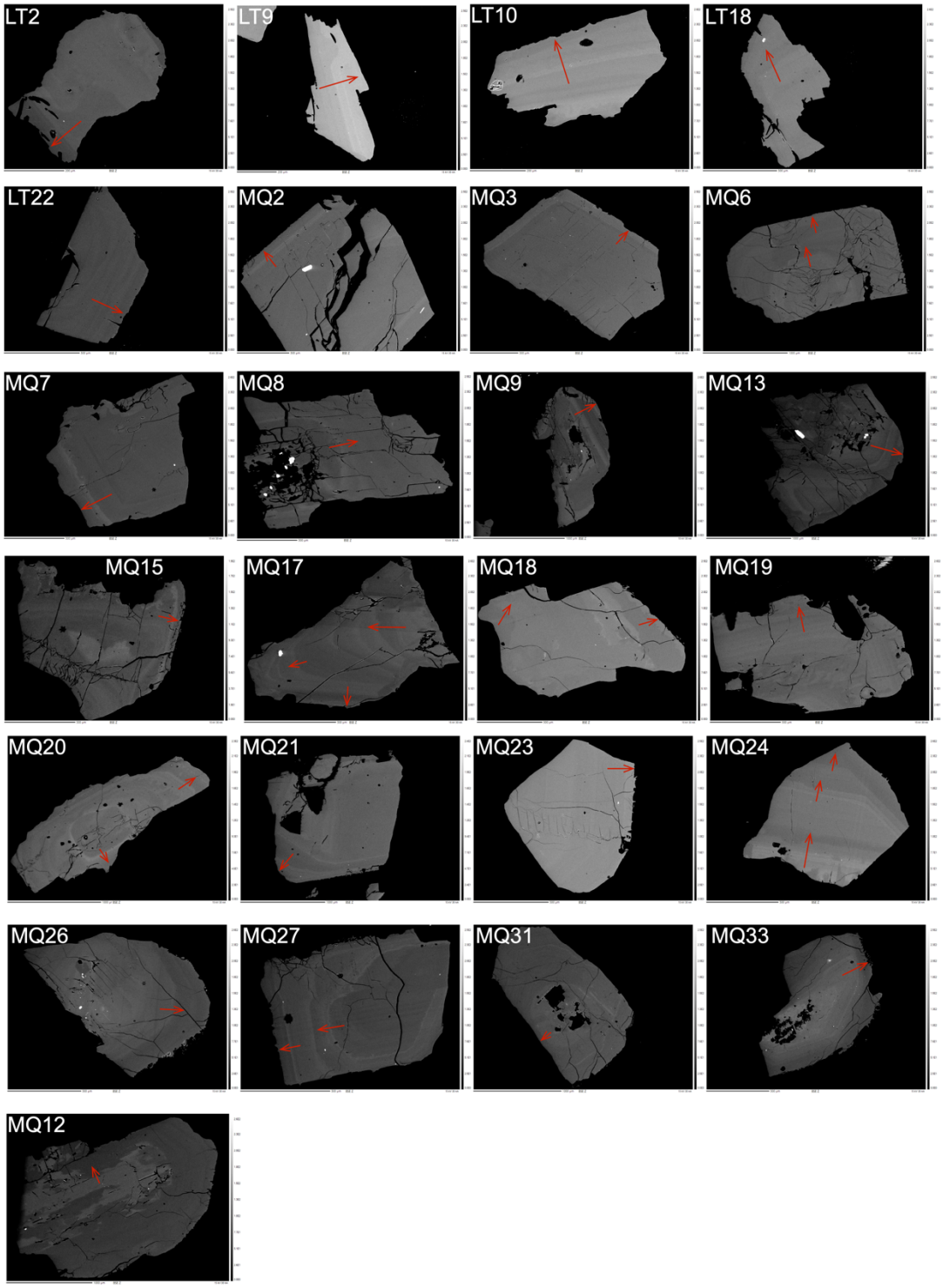

Figure B.1: Plagioclase BSE images

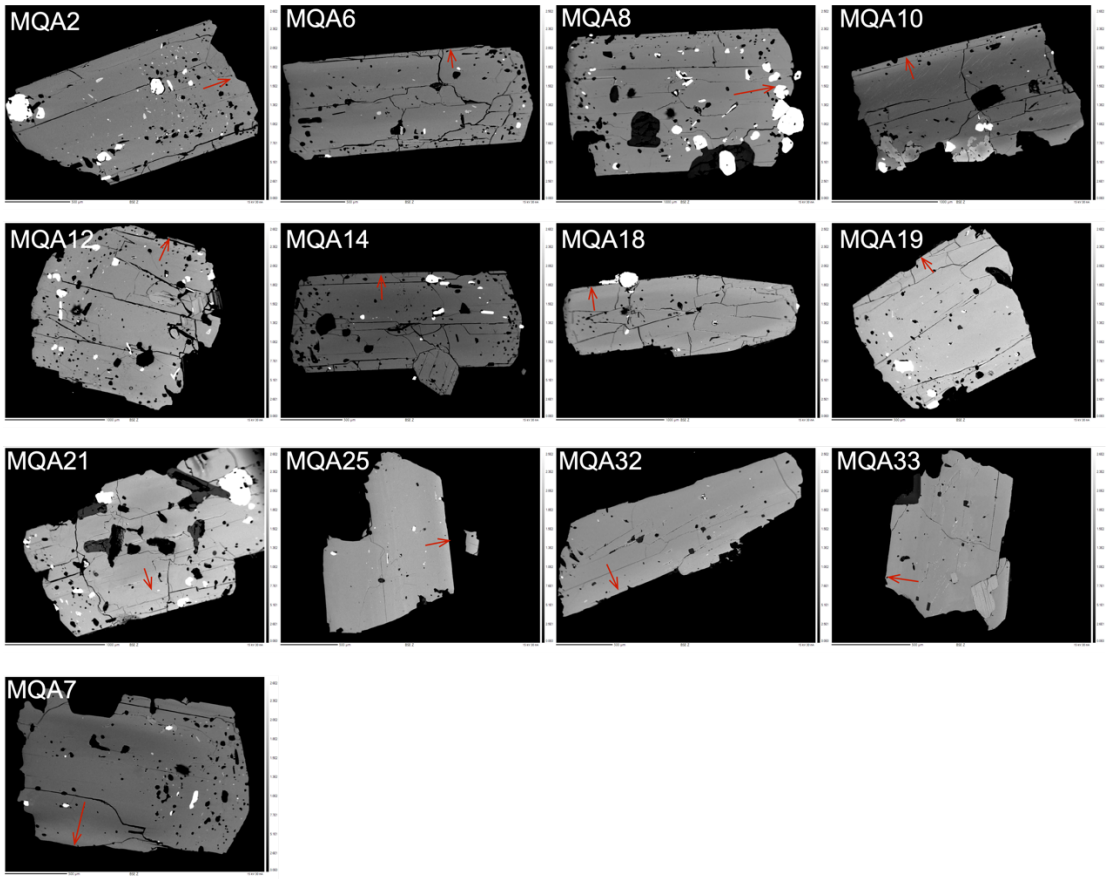

Figure B.2: Amphibole BSE images

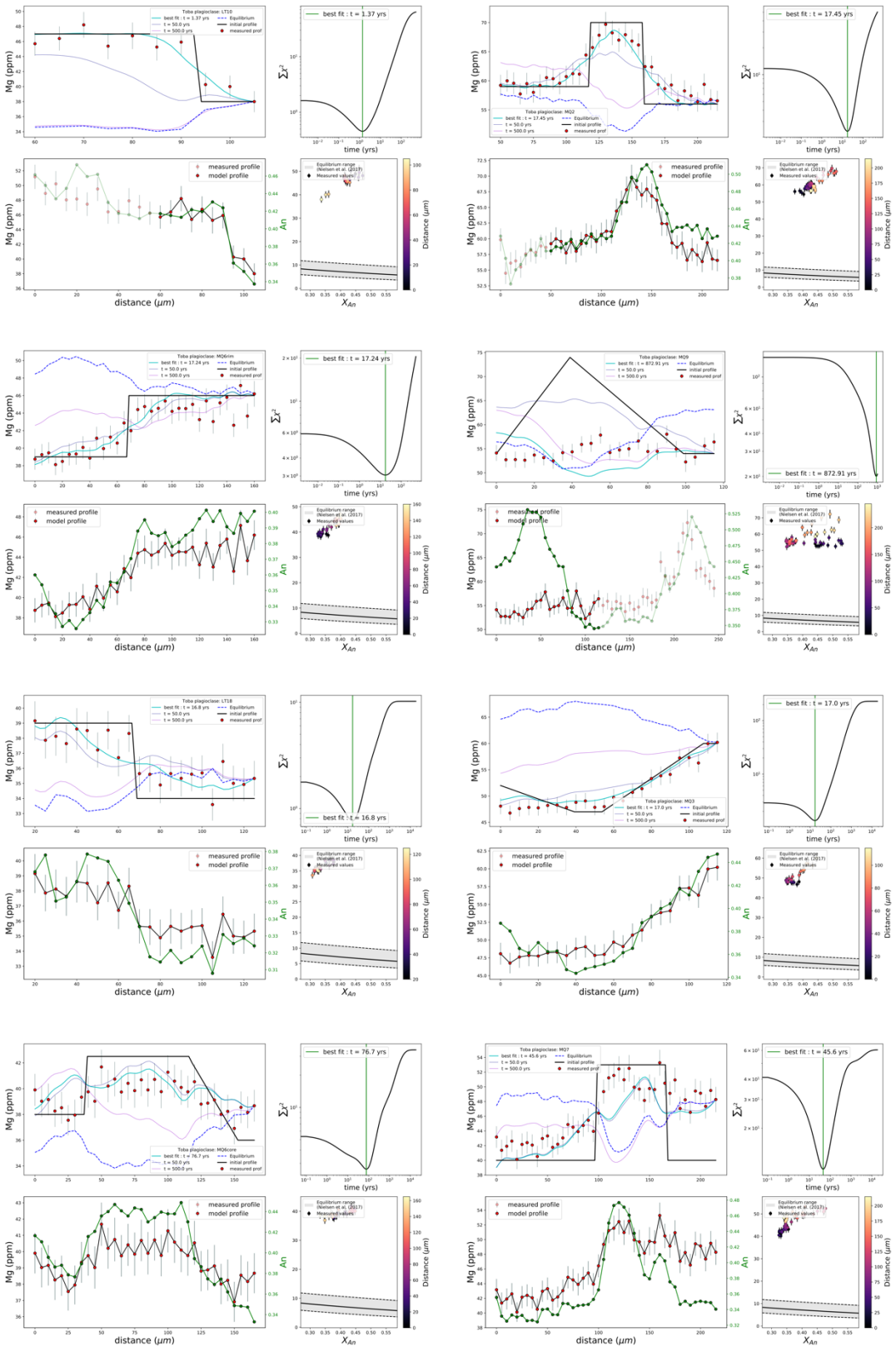

Figure B.3: Individual Mg in plagioclase diffusion models for grains shown in B.1

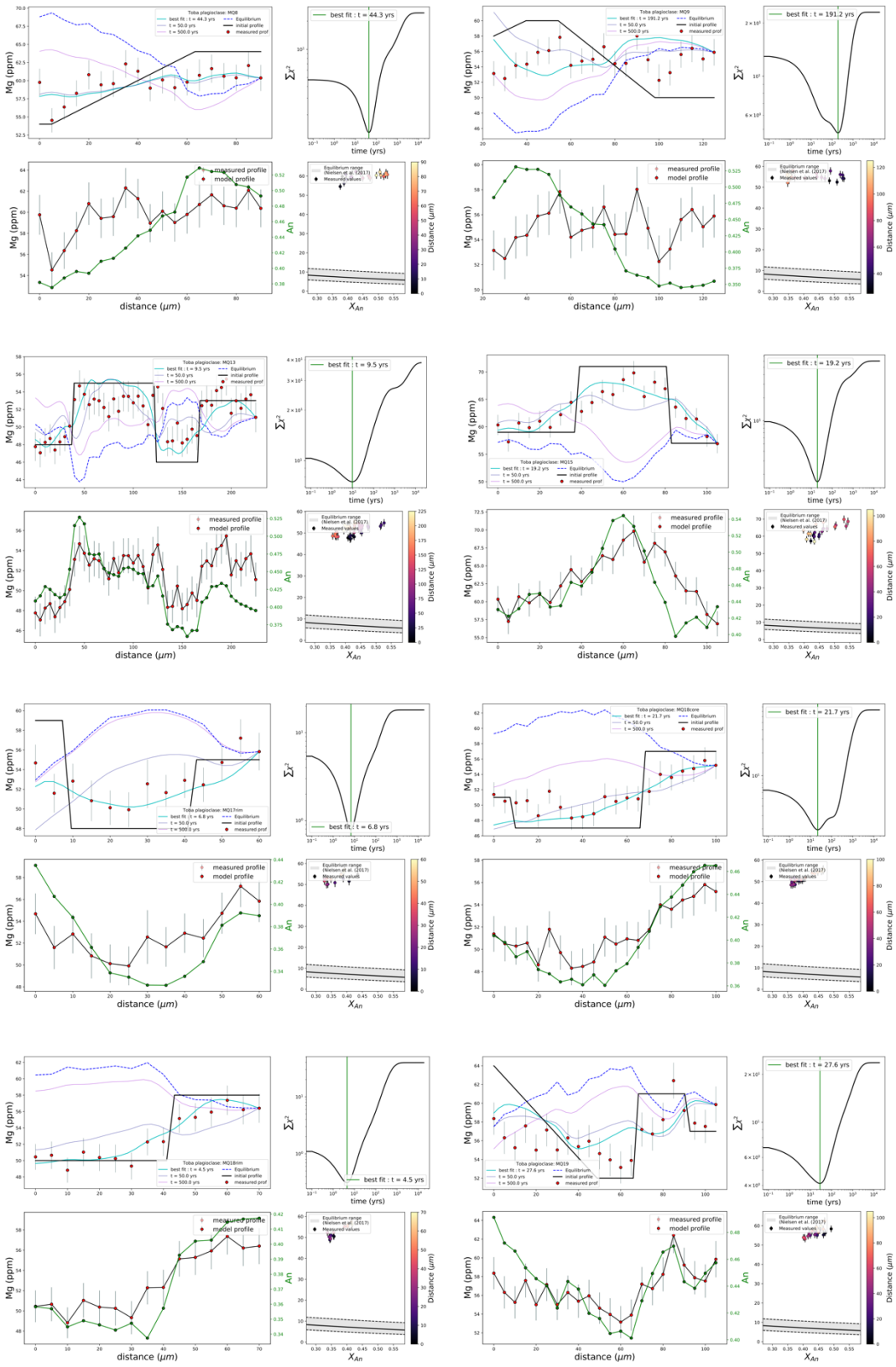

Figure B.3 (continued)

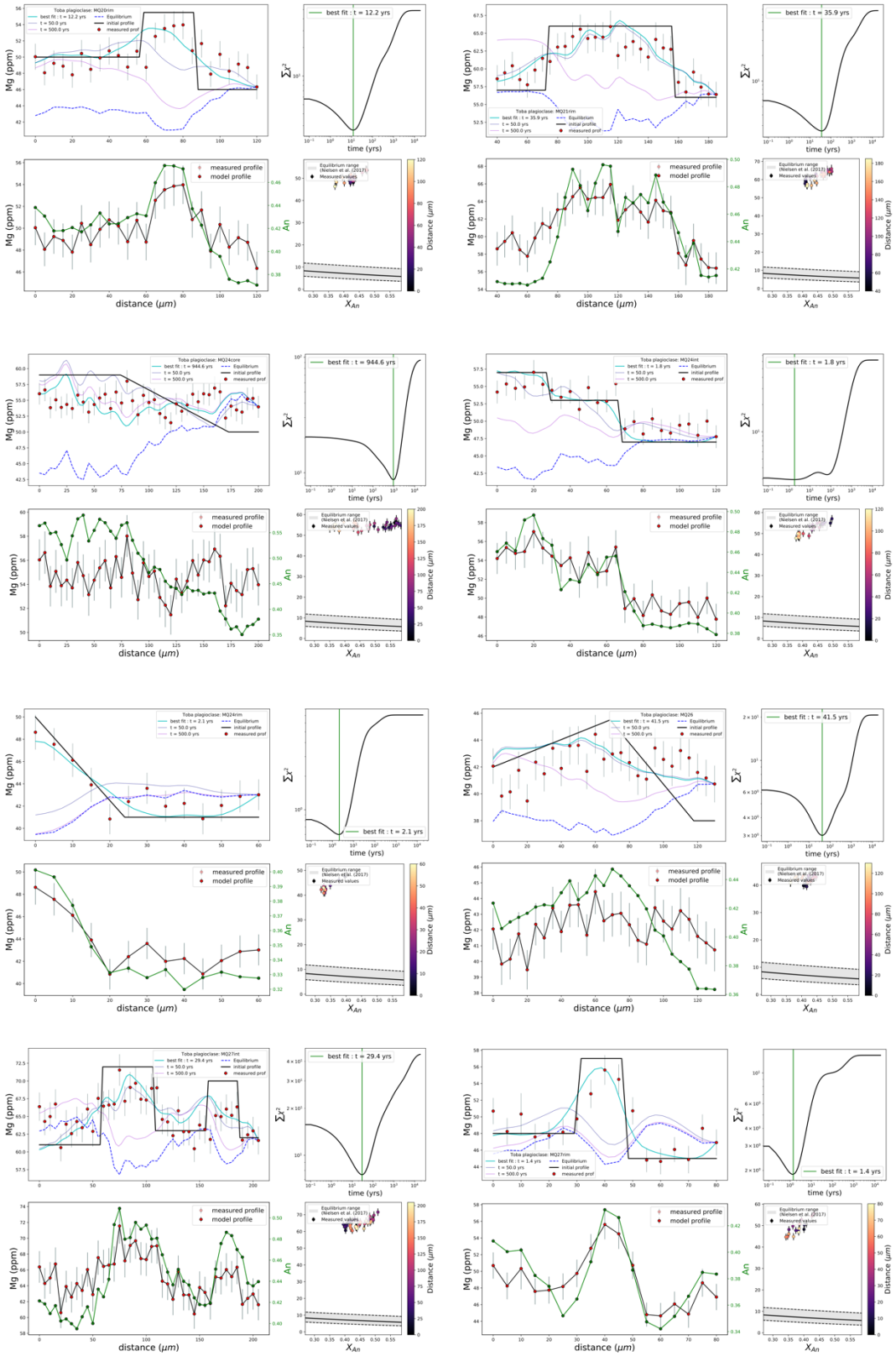

Figure B.3 (continued)

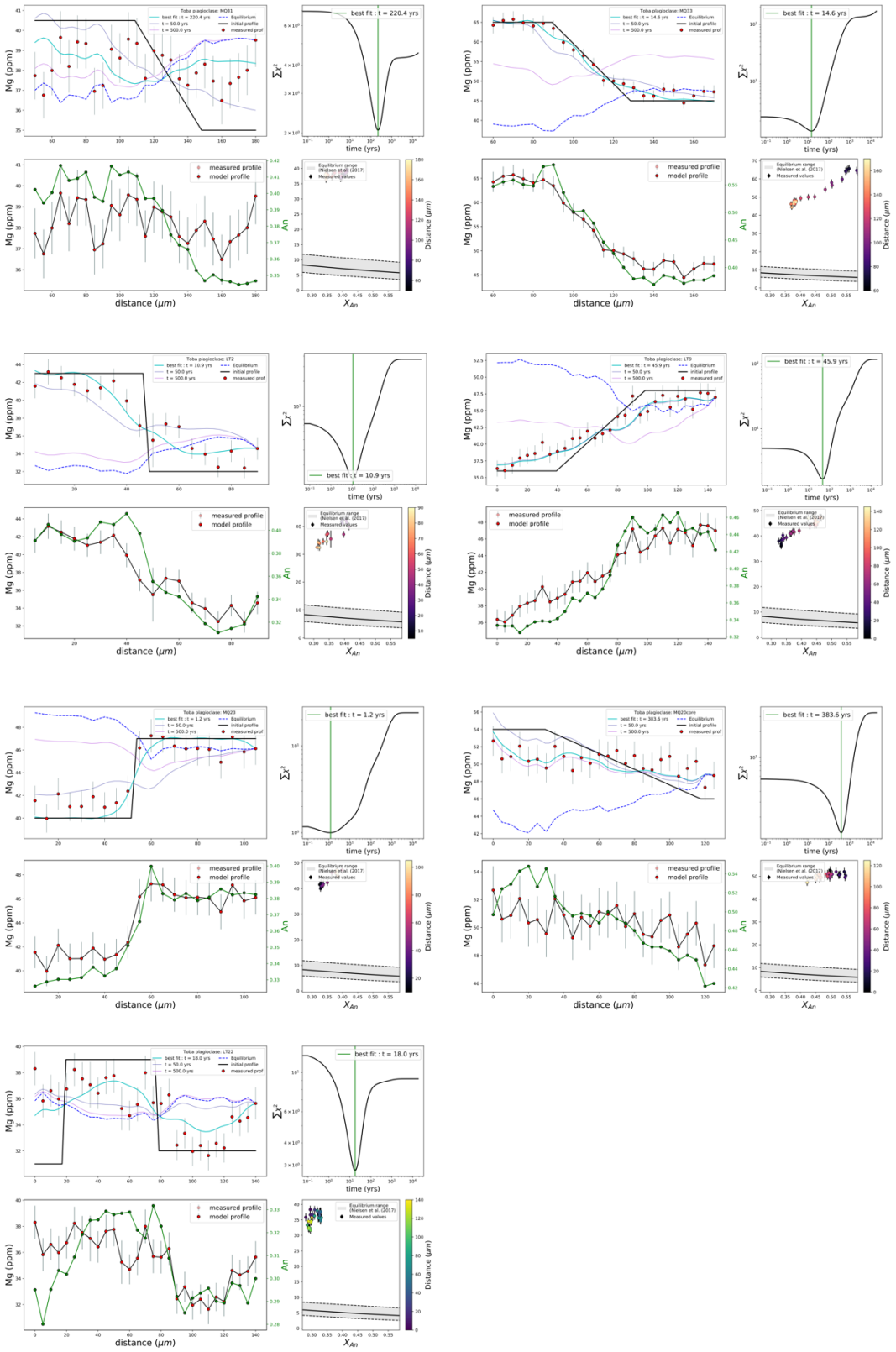

Figure B.3 (continued)

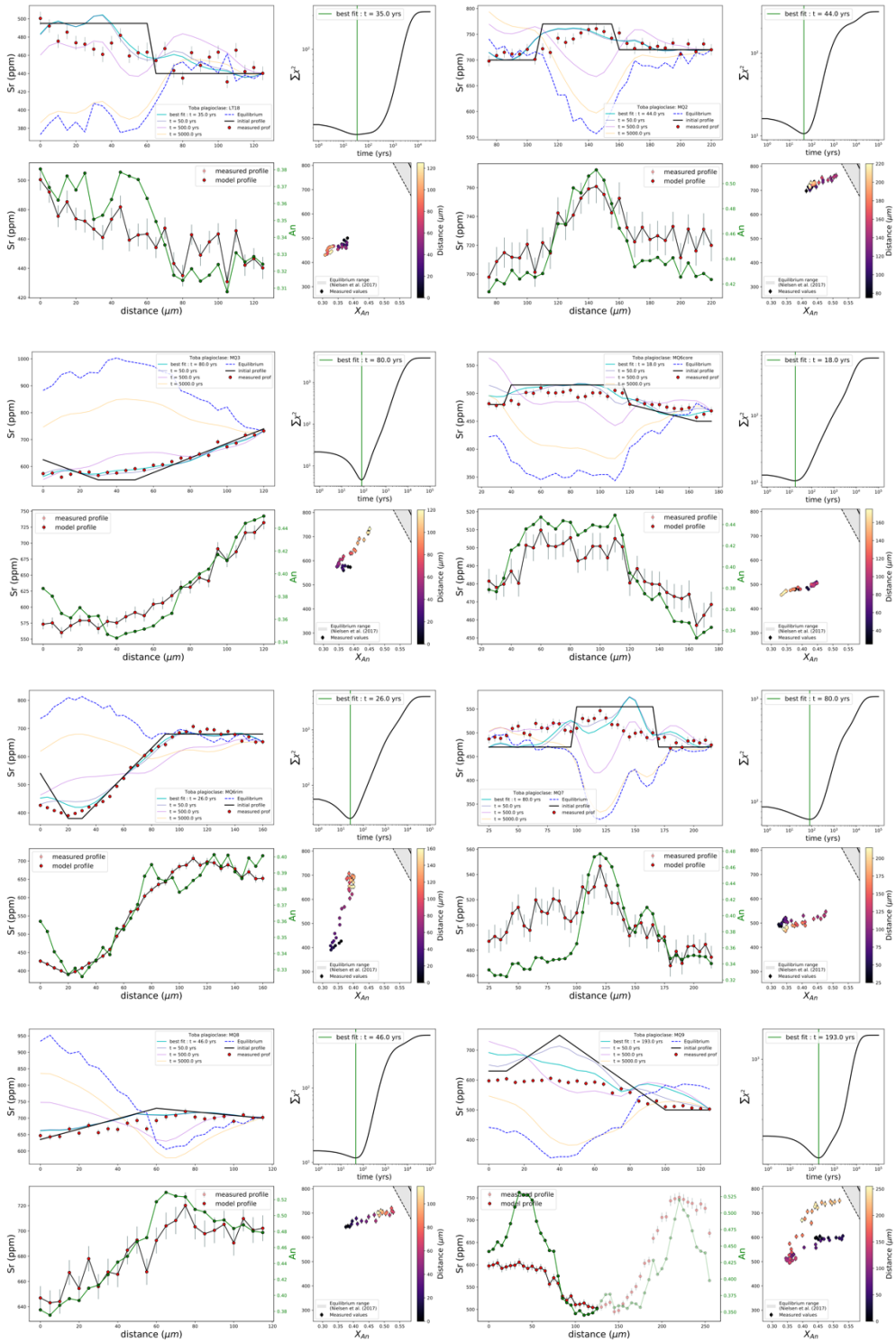

Figure B.4: Individual Sr in plagioclase diffusion models for all the grains shown in B.1

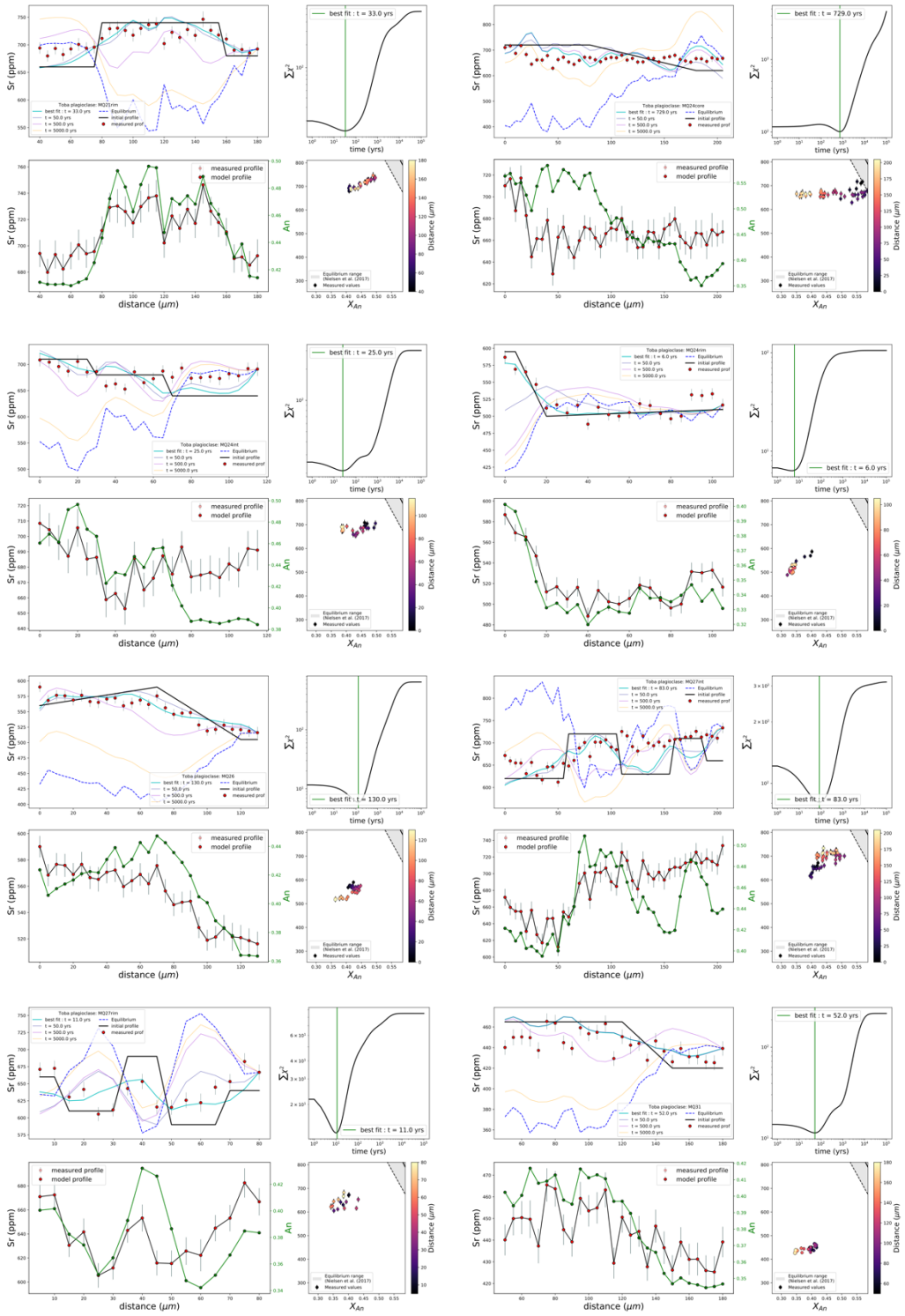

Figure B.4 (continued)

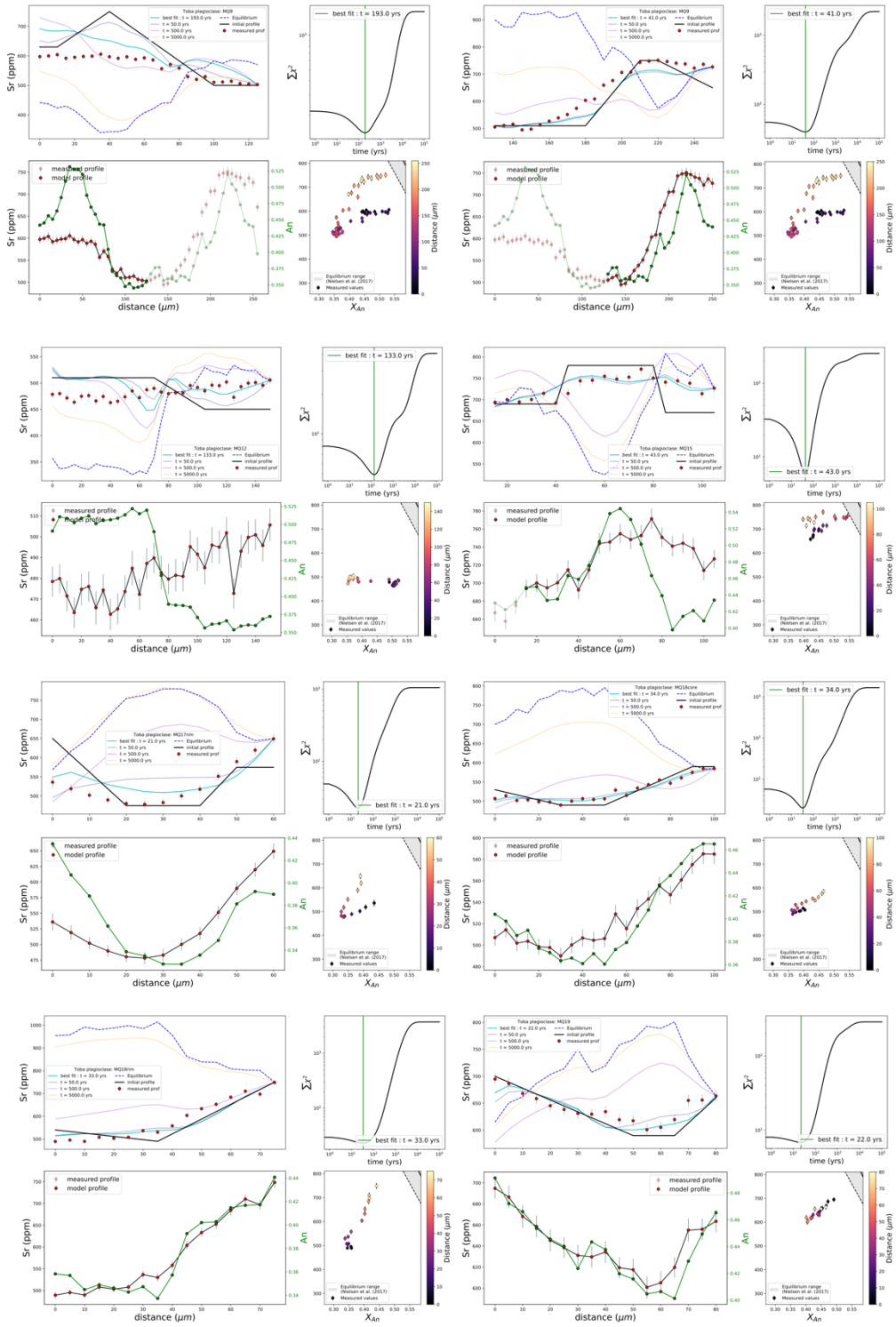

Figure B.4 (continued)

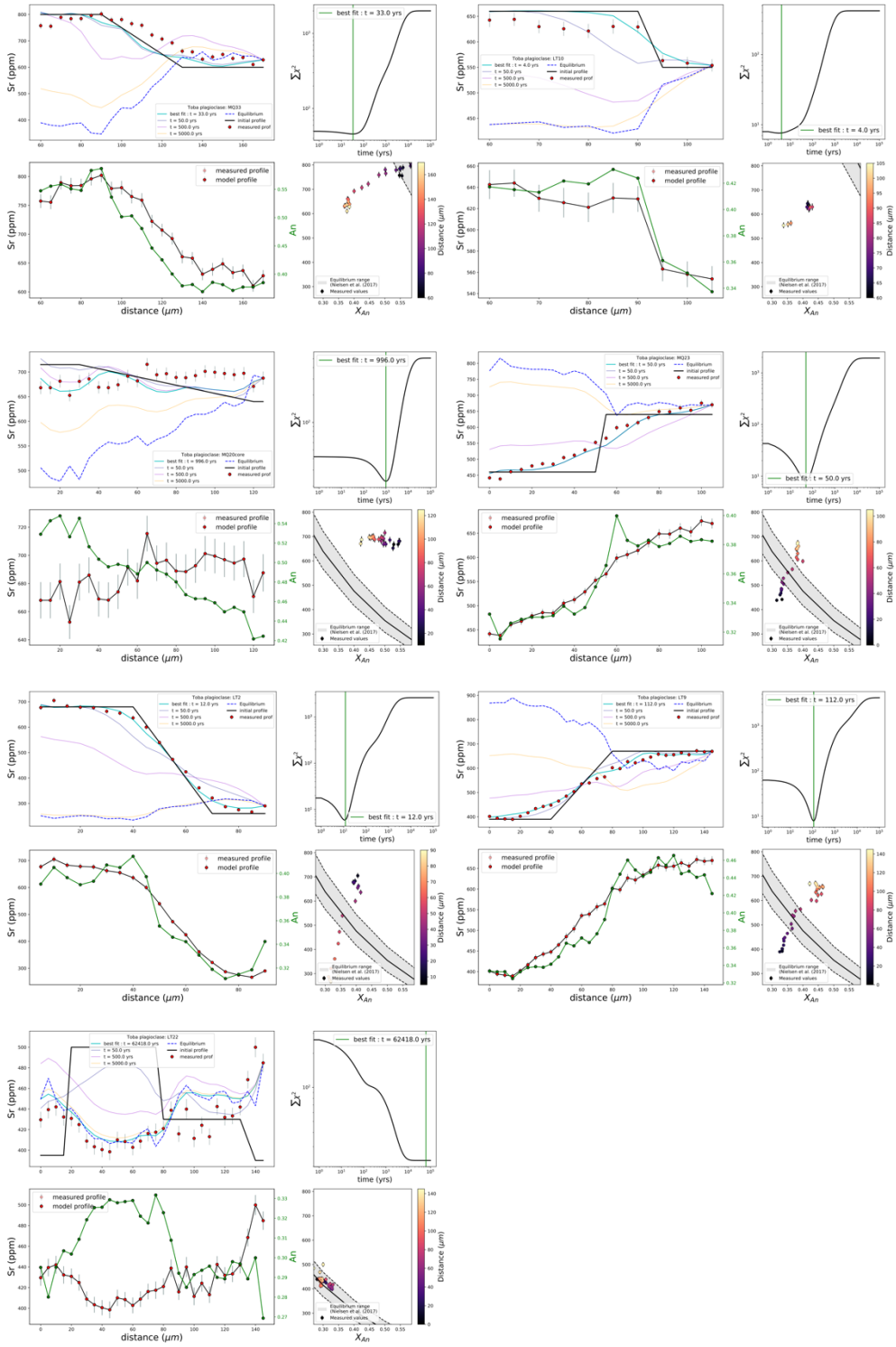

Figure B.4 (continued)

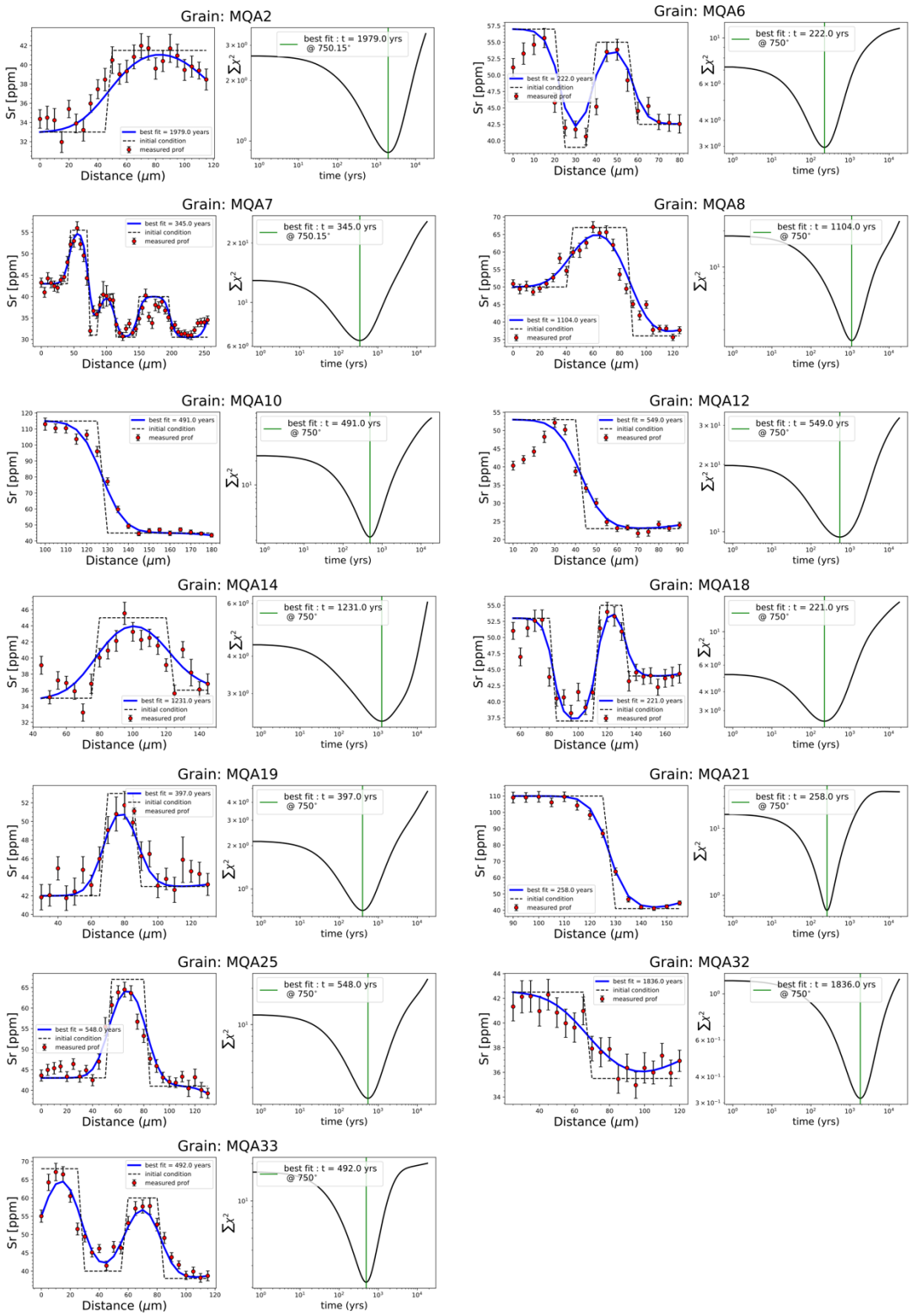

Figure B.5: Individual Sr in amphibole diffusion models for grains shown in B.2

Appendix C:
Supplemental figures for chapter 4

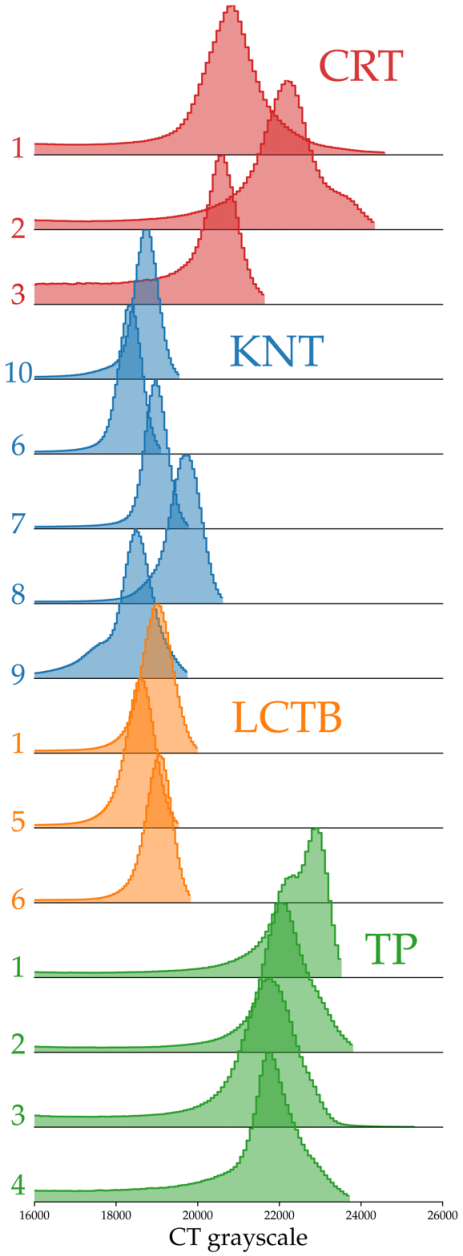

Figure C.1: Raw data histograms for all grains in this study. Regions of histogram below 16,000 grayscale values are cropped off as they pertain to sample holder and background.